APPLIED NEUROIMAGING EDITOR'S PICK 2021

EDITED BY: Jan Kassubek
PUBLISHED IN: Frontiers in Neurology

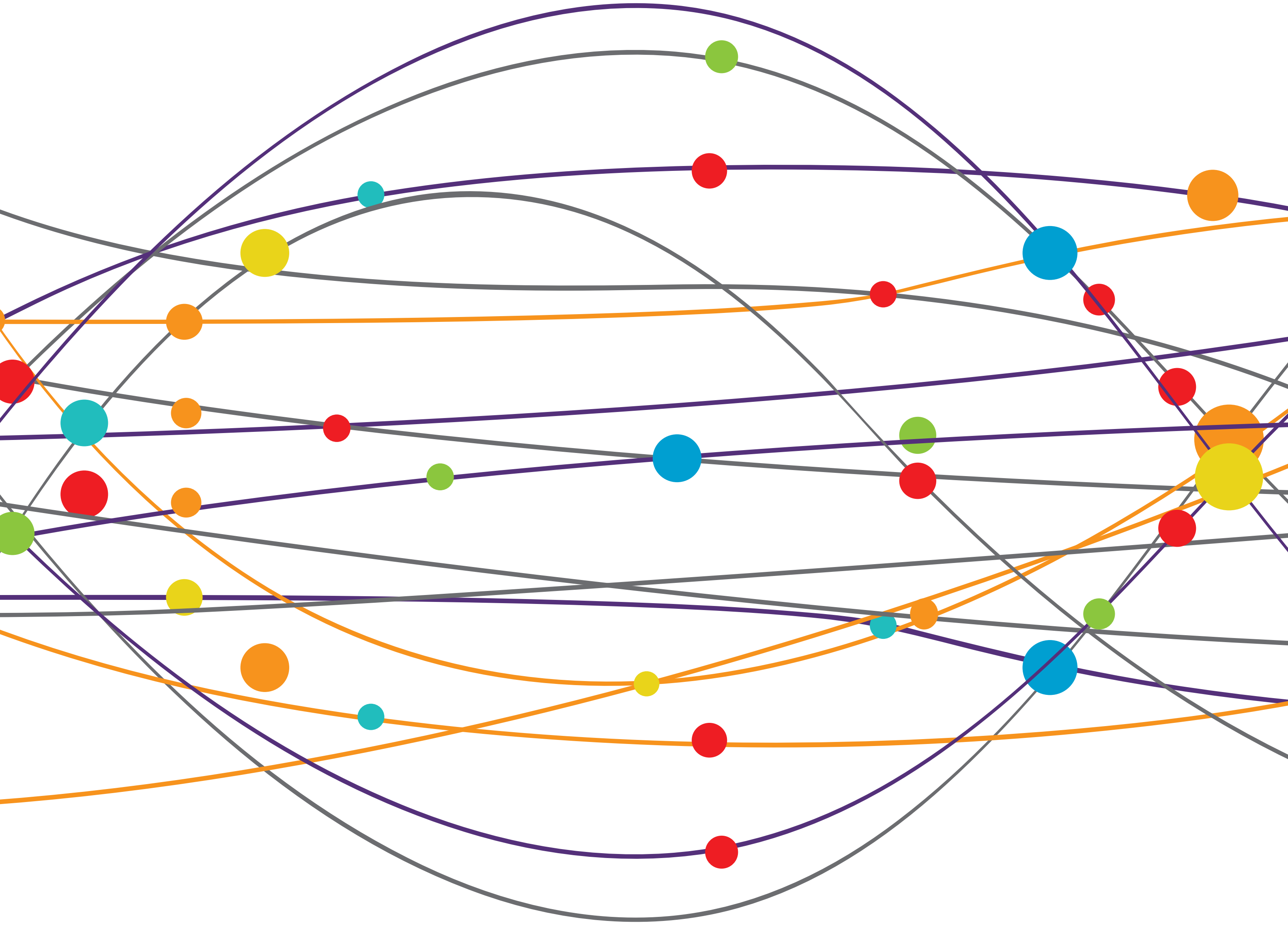

frontiers Research Topics

ISSN 1664-8714
ISBN 978-2-88971-341-7
DOI 10.3389/978-2-88971-341-7

About Frontiers

Frontiers is more than just an open-access publisher of scholarly articles: it is a pioneering approach to the world of academia, radically improving the way scholarly research is managed. The grand vision of Frontiers is a world where all people have an equal opportunity to seek, share and generate knowledge. Frontiers provides immediate and permanent online open access to all its publications, but this alone is not enough to realize our grand goals.

Frontiers Journal Series

The Frontiers Journal Series is a multi-tier and interdisciplinary set of open-access, online journals, promising a paradigm shift from the current review, selection and dissemination processes in academic publishing. All Frontiers journals are driven by researchers for researchers; therefore, they constitute a service to the scholarly community. At the same time, the Frontiers Journal Series operates on a revolutionary invention, the tiered publishing system, initially addressing specific communities of scholars, and gradually climbing up to broader public understanding, thus serving the interests of the lay society, too.

Dedication to Quality

Each Frontiers article is a landmark of the highest quality, thanks to genuinely collaborative interactions between authors and review editors, who include some of the world's best academicians. Research must be certified by peers before entering a stream of knowledge that may eventually reach the public - and shape society; therefore, Frontiers only applies the most rigorous and unbiased reviews.
Frontiers revolutionizes research publishing by freely delivering the most outstanding research, evaluated with no bias from both the academic and social point of view.
By applying the most advanced information technologies, Frontiers is catapulting scholarly publishing into a new generation.

What are Frontiers Research Topics?

Frontiers Research Topics are very popular trademarks of the Frontiers Journals Series: they are collections of at least ten articles, all centered on a particular subject. With their unique mix of varied contributions from Original Research to Review Articles, Frontiers Research Topics unify the most influential researchers, the latest key findings and historical advances in a hot research area! Find out more on how to host your own Frontiers Research Topic or contribute to one as an author by contacting the Frontiers Editorial Office: frontiersin.org/about/contact

APPLIED NEUROIMAGING EDITOR'S PICK 2021

Topic Editor:
Jan Kassubek, University of Ulm, Germany

Citation: Kassubek, J., ed. (2021). Applied Neuroimaging Editor's Pick 2021. Lausanne: Frontiers Media SA. doi: 10.3389/978-2-88971-341-7

Table of Contents

frontiers in Neurology

PERSPECTIVE
published: 09 May 2019
doi: 10.3389/fneur.2019.00425

10Kin1day: A Bottom-Up Neuroimaging Initiative

Martijn P. van den Heuvel[1,2]*, *Lianne H. Scholtens*[1,2], *Hannelore K. van der Burgh*[3], *Federica Agosta*[4], *Clara Alloza*[5,6], *Celso Arango*[6], *Bonnie Auyeung*[7] *on behalf of Cambridge Child Development Project*†, *Simon Baron-Cohen*[7], *Silvia Basaia*[4], *Manon J. N. L. Benders*[8], *Frauke Beyer*[9], *Linda Booij*[10], *Kees P. J. Braun*[11], *Geraldo Busatto Filho*[12], *Wiepke Cahn*[2], *Dara M. Cannon*[13], *Tiffany M. Chaim-Avancini*[12], *Sandra S. M. Chan*[14], *Eric Y. H. Chen*[15], *Benedicto Crespo-Facorro*[16], *Eveline A. Crone*[17], *Udo Dannlowski*[18], *Sonja M. C. de Zwarte*[2], *Bruno Dietsche*[19], *Gary Donohoe*[20], *Stefan Du Plessis*[21], *Sarah Durston*[2], *Covadonga M. Díaz-Caneja*[6], *Ana M. Díaz-Zuluaga*[22], *Robin Emsley*[21], *Massimo Filippi*[4], *Thomas Frodl*[23], *Martin Gorges*[24], *Beata Graff*[25], *Dominik Grotegerd*[18], *Dariusz Gąsecki*[26], *Julie M. Hall*[27], *Laurena Holleran*[20], *Rosemary Holt*[7] *on behalf of Cambridge Child Development Project*†, *Helene J. Hopman*[28], *Andreas Jansen*[29], *Joost Janssen*[6], *Krzysztof Jodzio*[30], *Lutz Jäncke*[31], *Vasiliy G. Kaleda*[32], *Jan Kassubek*[24], *Shahrzad Kharabian Masouleh*[33], *Tilo Kircher*[29], *Martijn G. J. C. Koevoets*[2], *Vladimir S. Kostic*[34], *Axel Krug*[29], *Stephen M. Lawrie*[35], *Irina S. Lebedeva*[36], *Edwin H. M. Lee*[15], *Tristram A. Lett*[37], *Simon J. G. Lewis*[27], *Franziskus Liem*[38], *Michael V. Lombardo*[7] *on behalf of Cambridge Child Development Project*†, *Carlos Lopez-Jaramillo*[39], *Daniel S. Margulies*[40], *Sebastian Markett*[41], *Paulo Marques*[42], *Ignacio Martínez-Zalacaín*[43], *Colm McDonald*[13], *Andrew M. McIntosh*[35], *Genevieve McPhilemy*[13], *Susanne L. Meinert*[18], *José M. Menchón*[43], *Christian Montag*[44], *Pedro S. Moreira*[42], *Pedro Morgado*[42], *David O. Mothersill*[20], *Susan Mérillat*[38], *Hans-Peter Müller*[24], *Leila Nabulsi*[13], *Pablo Najt*[13], *Krzysztof Narkiewicz*[25], *Patrycja Naumczyk*[30], *Bob Oranje*[2], *Victor Ortiz-Garcia de la Foz*[45], *Jiska S. Peper*[17], *Julian A. Pineda*[46], *Paul E. Rasser*[47], *Ronny Redlich*[18], *Jonathan Repple*[18], *Martin Reuter*[41], *Pedro G. P. Rosa*[48], *Amber N. V. Ruigrok*[7], *Agnieszka Sabisz*[49], *Ulrich Schall*[47], *Soraya Seedat*[21], *Mauricio H. Serpa*[50], *Stavros Skouras*[51], *Carles Soriano-Mas*[52], *Nuno Sousa*[42], *Edyta Szurowska*[49], *Alexander S. Tomyshev*[53], *Diana Tordesillas-Gutierrez*[54], *Sofie L. Valk*[55], *Leonard H. van den Berg*[3], *Theo G. M. van Erp*[56], *Neeltje E. M. van Haren*[2,57], *Judith M. C. van Leeuwen*[58], *Arno Villringer*[59], *Christiaan H. Vinkers*[60], *Christian Vollmar*[61], *Lea Waller*[62], *Henrik Walter*[63], *Heather C. Whalley*[35], *Marta Witkowska*[30], *A. Veronica Witte*[9], *Marcus V. Zanetti*[64,65], *Rui Zhang*[66] *and Siemon C. de Lange*[1,2]

[1] Connectome Lab, CTG, CNCR, VU Amsterdam, Amsterdam, Netherlands, [2] UMC Utrecht Brain Center, Department of Psychiatry, University Medical Center Utrecht, Utrecht, Netherlands, [3] Department of Neurology, UMC Utrecht Brain Center, University Medical Center Utrecht, Utrecht, Netherlands, [4] Neuroimaging Research Unit, Institute of Experimental Neurology, Division of Neuroscience, IRCCS San Raffaele Scientific Institute, Vita-Salute San Raffaele University, Milan, Italy, [5] Division of Psychiatry, University of Edinburgh, Edinburgh, United Kingdom, [6] Department of Child and Adolescent Psychiatry, IiSGM, CIBERSAM, School of Medicine, Hospital General Universitario Gregorio Marañón, Universidad Complutense, Madrid, Spain, [7] Department of Psychiatry, Autism Research Centre, University of Cambridge, Cambridge, United Kingdom, [8] Department of Neonatology, UMC Utrecht Brain Center, Wilhelmina Children's Hospital, University Medical Center Utrecht, Utrecht, Netherlands, [9] Department of Neurology, CRC "Obesity Mechanisms", Subproject A1, Max Planck Institute for Human Cognitive and Brain Sciences, University of Leipzig, Leipzig, Germany, [10] Department of Psychology, Concordia University, Montreal, QC, Canada, [11] Department of Child Neurology, UMC Utrecht Brain Center, Wilhelmina Children's Hospital, University Medical Center Utrecht, Utrecht, Netherlands, [12] Laboratory of Psychiatric Neuroimaging (LIM21), Faculdade de Medicina, Instituto de Psiquiatria, Hospital das Clinicas HCFMUSP, Universidade de São Paulo, São Paulo, Brazil, [13] Clinical Neuroimaging Laboratory, Centre for Neuroimaging and Cognitive Genomics (NICOG), NCBES Galway Neuroscience Centre, College of Medicine Nursing and Health Sciences, National University of Ireland Galway, Galway, Ireland, [14] Department of Psychiatry, Faculty of Medicine, Chinese University of Hong Kong, Hong Kong, China, [15] Department of Psychiatry, University of Hong Kong, Hong Kong, China, [16] Psychiatry Unit, Department of Medicine and Psychiatry, Hospital Universitario Marques de Valdecilla, IDIVAL, CIBERSAM, Hosptial Universitario Virgen del Rocío, Universidad de Seville, Seville, Spain, [17] Brain and Development Research Center, Leiden University, Leiden, Netherlands, [18] Department of Psychiatry, University of Münster, Münster, Germany, [19] Department of Psychiatry, University of Marburg, Marburg, Germany

OPEN ACCESS

Edited by:
Christian Gaser,
Friedrich Schiller University Jena,
Germany

Reviewed by:
Olga Tymofiyeva,
University of California, San Francisco,
United States
Hanbo Chen,
Tencent Holdings Limited, China

***Correspondence:**
Martijn P. van den Heuvel
martijn.vanden.heuvel@vu.nl

† Bonnie Auyeung, Rosemary Holt and Michael V. Lombardo wrote the paper on behalf of the Cambridge Child Development Project

Specialty section:
This article was submitted to
Applied Neuroimaging,
a section of the journal
Frontiers in Neurology

Received: 13 December 2018
Accepted: 08 April 2019
Published: 09 May 2019

[20] *Cognitive Genetics and Cognitive Therapy Group, Neuroimaging and Cognitive Genomics Centre and NCBES Galway Neuroscience Centre, School of Psychology and Discipline of Biochemistry, National University of Ireland, Galway, Ireland,* [21] *Department of Psychiatry, Stellenbosch University, Cape Town, South Africa,* [22] *Research Group in Psychiatry GIPSI, Department of Psychiatry, Faculty of Medicine, Universidad de Antioquia, Medellín, Colombia,* [23] *Department of Psychiatry and Psychotherapy, University Hospital, Otto von Guericke University, Magdeburg, Germany,* [24] *Department of Neurology, University of Ulm, Ulm, Germany,* [25] *Department of Hypertension and Diabetology, Medical University of Gdańsk, Gdańsk, Poland,* [26] *Department of Neurology of Adults, Medical University of Gdańsk, Gdańsk, Poland,* [27] *Parkinson's Disease Research Clinic, Brain and Mind Centre, University of Sydney, Sydney, NSW, Australia,* [28] *Department of Medicine and Therapeutics, Chinese University of Hong Kong, Hong Kong, China,* [29] *Department of Psychiatry and Center for Mind, Brain and Behaviour, University of Marburg, Marburg, Germany,* [30] *Institute of Psychology, University of Gdańsk, Gdańsk, Poland,* [31] *Division of Neuropsychology, University of Zurich, Zurich, Switzerland,* [32] *Department of Endogenous Mental Disorders, Mental Health Research Center, Moscow, Russia,* [33] *Institute for Neuroscience and Medicine 7, Forschungszentrum Jülich, Jülich, Germany,* [34] *Clinic of Neurology, School of Medicine, University of Belgrade, Belgrade, Serbia,* [35] *Division of Psychiatry, University of Edinburgh, Edinburgh, United Kingdom,* [36] *Laboratory of Neuroimaging and Multimodal Analysis, Mental Health Research Center, Moscow, Russia,* [37] *Department of Psychiatry and Psychotherapy, Division of Mind and Brain Research, Charité - Universitätsmedizin Berlin, Berlin, Germany,* [38] *University Research Priority Program "Dynamics of Healthy Aging", University of Zurich, Zurich, Switzerland,* [39] *Mood Disorders Program, Research Group in Psychiatry GIPSI, Department of Psychiatry, Faculty of Medicine, Hospital Universitario San Vicente Fundación, Universidad de Antioquia, Medellín, Colombia,* [40] *Frontlab, Centre National de la Recherche Scientifique, Institut du Cerveau et de la Moelle Épinière, UMR 7225, Paris, France,* [41] *Department of Psychology, Humboldt Universität zu Berlin, Berlin, Germany,* [42] *School of Medicine, Life and Health Sciences Research Institute (ICVS), University of Minho, Braga, Portugal,* [43] *Department of Psychiatry, Bellvitge Biomedical Research Institute-IDIBELL and CIBERSAM, Barcelona, Spain,* [44] *Department of Molecular Psychology, Institute of Psychology and Education, Ulm University, Ulm, Germany,* [45] *Psychiatry Unit, Department of Medicine and Psychiatry, IDIVAL, CIBERSAM, Hospital Universitario Marques de Valdecilla, Santander, Spain,* [46] *Research Group, Instituto de Alta Tecnología Médica, Universidad de Antioquia, Medellín, Colombia,* [47] *Priority Centre for Brain and Mental Health Research, The University of Newcastle, Newcastle, NSW, Australia,* [48] *Laboratory of Psychiatric Neuroimaging (LIM21), Faculdade de Medicina, Instituto de Psiquiatria, Hospital das Clinicas HCFMUSP, Universidade de São Paulo, São Paulo, Brazil,* [49] *2nd Department of Radiology, Medical University of Gdańsk, Gdańsk, Poland,* [50] *Laboratory of Psychiatric Neuroimaging (LIM21), Departamento de Psiquiatria, Faculdade de Medicina, Universidade de São Paulo, São Paulo, Brazil,* [51] *BarcelonaBeta Brain Research Center, Pasqual Maragall Foundation, Barcelona, Spain,* [52] *Department of Psychiatry (IDIBELL and CIBERSAM) and Department of Psychobiology and Methodology in Health Sciences (UAB), Bellvitge Biomedical Research Institute-IDIBELL, CIBERSAM and Universitat Autònoma de Barcelona, Barcelona, Spain,* [53] *Laboratory of Neuroimaging and Multimodal Analysis, Mental Health Research Center, Moscow, Russia,* [54] *Neuroimaging Unit, Technological Facilities, Valdecilla Biomedical Research Institute IDIVAL, CIBERSAM, Santander, Spain,* [55] *Institute for Neuroscience and Medicine 7/Institute of Systems Neuroscience, Forschungszentrum Jülich - Heinrich Heine Universitaet Duesseldorf, Jülich, Germany,* [56] *Clinical Translational Neuroscience Laboratory, Department of Psychiatry and Human Behavior, University of California, Irvine, Irvine, CA, United States,* [57] *Department of Child and Adolescent Psychiatry/Psychology, Erasmus Medical Center, Rotterdam, Netherlands,* [58] *Donders Institute for Brain, Cognition, and Behaviour, Radboud University Medical Center, Nijmegen, Netherlands,* [59] *Departments of Neurology, Cognitive Neurology, Max Planck Institute for Human Cognitive and Brain Sciences, University of Leipzig, Leipzig, Germany,* [60] *Departments of Psychiatry, Anatomy and Neurosciences, Amsterdam UMC, Amsterdam, Netherlands,* [61] *Department of Neurology, Epilepsy Centre, University of Munich Hospital, Munich, Germany,* [62] *Division of Mind and Brain Research, Department of Psychiatry and Psychotherapy CCM, Charité Universitätsmedizin Berlin, Corporate Member of Berlin Institute of Health, Freie Universität Berlin, Humboldt-Universität zu Berlin, Berlin, Germany,* [63] *Division of Mind and Brain Research, Department of Psychiatry and Psychotherapy CCM, Charité - Universitätsmedizin Berlin, Corporate Member of Berlin Institute of Health, Freie Universität Berlin, Humboldt-Universität zu Berlin, Berlin, Germany,* [64] *Laboratory of Psychiatric Neuroimaging (LIM21), Faculdade de Medicina, Instituto de Psiquiatria, Hospital das Clinicas HCFMUSP, São Paulo, Brazil,* [65] *Instituto de Ensino e Pesquisa, Hospital Sírio-Libanês, Universidade de São Paulo, São Paulo, Brazil,* [66] *Department of Neurology, Max Planck Institute for Human Cognitive and Brain Sciences, Leipzig, Germany*

We organized 10Kin1day, a pop-up scientific event with the goal to bring together neuroimaging groups from around the world to jointly analyze 10,000+ existing MRI connectivity datasets during a 3-day workshop. In this report, we describe the motivation and principles of 10Kin1day, together with a public release of 8,000+ MRI connectome maps of the human brain.

Keywords: MRI, connectome analysis, diffusion weighted MRI, brain, network

Ongoing grand-scale projects like the European Human Brain Project (1), the US Brain Initiative (2), the Human Connectome Project (3), the Chinese Brainnetome (4) and exciting world-wide neuroimaging collaborations such as ENIGMA (5) herald the new era of *big neuroscience*. In conjunction with these major undertakings, there is an emerging trend for bottom-up initiatives, starting with small-scale projects built upon existing collaborations and infrastructures. As described by Mainen et al. (6), these initiatives are centralized around self-organized groups of researchers working on the same challenges and sharing interests and specialized expertise. These projects could scale and open up to a larger audience and other disciplines over time, eventually lining up and merging their findings with other programs to make the bigger picture.

10KIN1DAY

One type of event that fits well with this grass-roots collaboration philosophy are short gatherings of scientists around a single theme, bringing together expertise and tools to jointly analyze existing neuroscience data. We organized 10Kin1day, an MRI connectome event, with the goal to bring together an international group of researchers in the field of neuroimaging and consistently analyze MRI connectivity data of the human cerebrum. We organized the event around five founding principles:

- use existing neuroimaging data, available from many research groups around the world; we focused on diffusion MRI data and aimed to bring together 10,000+ datasets
- analyze data from varying cohorts and imaging protocols, using a single, straightforward analysis strategy to encourage across-group collaborations and multisite studies
- perform all processing during a short workshop, with only basic expertise of analysis needed
- provide education on how to analyze resulting connectome data, so participants can continue to work on their projects after the event
- each participant analyzes their own data and is free to decide what to do with their analyzed results

THE 10K WORKSHOP

Over 50 participants from 40 different neuroimaging groups gathered in The Netherlands for a 3-day event. Participants brought and worked on their own datasets, varying from MRI data on healthy human brain organization, cross-sectional and longitudinal brain development, aging, cognitive psychology, as well as MRI data of a wide range of neurological and psychiatric brain disorders (including among others: Schizophrenia, Mood Disorders, Alzheimer's Disease, Mild Cognitive Impairment, Amyotrophic Lateral Sclerosis, Frontotemporal Dementia, Epilepsy and Parkinson's Disease). Written informed consent of the included healthy controls and/or patients was obtained by each of the participating researchers at their local institute. 10 TB online storage space and 50,000+ CPU hours was reserved on the Cartesius supercomputer of the collaborative Information and Communication Technology (ICT) organization for Dutch education and research (SURF, https://surfsara.nl/) to analyze the data during the workshop. Workshop participants performed data quality checks on their data 1 week before the event after which they uploaded the MRI data (Diffusion Weighted Images (DWI) and pre-processed T1 data, see Materials and Methods) to their own user account on the supercomputer. During the workshop, participants were brought up to speed on DWI processing, connectome construction (see section Materials and Methods for details on the performed analysis), and running parallel jobs on a supercomputer. Together, a total of 15,947 MRI datasets were processed into anatomical connectome maps, with each output dataset including connectivity matrices with different types of connection weights and multiple parcellation resolutions (**Figures 1A,B**). Data processing was paralleled by interactive educational talks and workshops on connectome analysis.

OPEN DATA

In line with the collaborative nature of the event, the 10K group discussed making the connectome maps available to the scientific community for non-commercial use, free of restrictions. We include herein the resulting individual connectome maps of 8,000+ connectome datasets across an age range of 0–90 years, with five different edge weights [number of traced streamlines (NOS), streamline density (SD), fiber length, fractional anisotropy (FA), and mean diffusivity (MD)] at three parcellation resolutions (80+ cortical and subcortical regions, 100+ and 200+ cortical regions, see section Materials and Methods for details). Connectome maps are presented anonymously and blinded for participation site, together with basic demographics (age in bins of 5 years, gender, patient/control status, **Figure 1**). Data is presented under the Non-Commercial Common Creative (CC BY-NC) license, free for all scientists to use in a non-commercial setting. A download request can be made at dutchconnectomelab.org for a download link to the data. Data for download includes connectivity matrices with five connectivity weights (NOS, FA, MD, fiber length, SD) at three atlas resolutions, information on the cortical and subcortical nodes, blinded group site and subject demographics (gender, age in 5 year bins, case/control).

CONCLUDING WORDS

We performed a few first analyses on the joint dataset, including cross-site consistency, comparison to Human Connectome Project (HCP) data and a first examination of effects of age (see Materials and Methods for more detail). We observed a high average consistency across sites with an average cross-site overlap of 92% (sd:0.0251) and a cross-site correlation of FA weights $r = 0.88$ (sd:0.0958), as well as a high consistency of the 10K group averaged matrix with data derived from the high-quality HCP, with at least 69% of pathways identified in HCP also observed in the 10K set and with 98% of all non-existing connections in HCP verified in the 10K set (**Figure 1C**). Furthermore, the distribution of weights across reconstructed connections is highly similar across the two datasets (FA weights, $r = 0.93$, $p < 0.0001$, **Figure 1C**). Age analysis shows clear developmental patterns of cortical morphology (**Figure 1E**) and white matter microstructure across age. Analysis of inverse MD showed rapid growth of microstructure in early years, with continuing development throughout adolescence, peaking around the beginning of the third decade, followed by a steady pattern of decline throughout aging (**Figure 1D**).

We acknowledge that there are many shortcomings to the presented MRI connectome dataset. Besides general, inherent limitations of diffusion MRI (7), the presented dataset is a

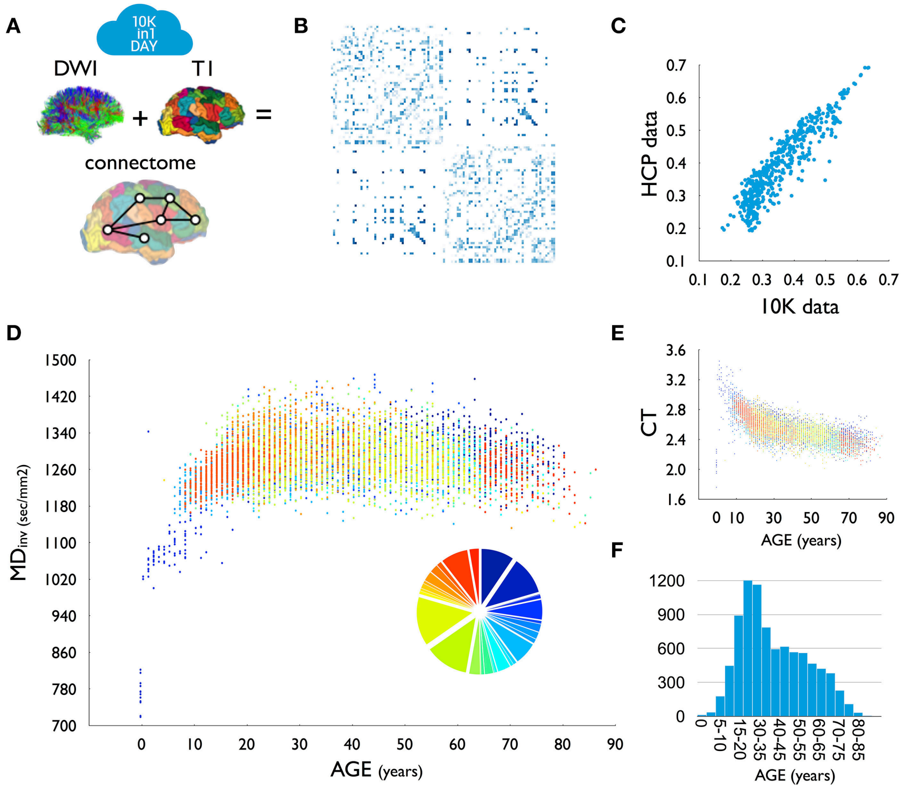

FIGURE 1 | (A) For each dataset, DWI tractography was combined with T1-based parcellation of cerebral brain regions to reconstruct a brain network. **(B)** Group-averaged (group threshold 33%) FA matrix of the 10K dataset. **(C)** High overlap ($r = 0.93$) between group-averaged FA values as derived from high-resolution HCP data and the 10K dataset. **(D)** Relationship between age and average inverse mean diffusivity (MD, sec/mm2) across the 10K dataset. Colors indicate the different included datasets. Insert shows a pie diagram of the size of included datasets, color coded to set participation. One dataset (set_634413) was excluded from this plot, showing (across the age span) deviating FA (lower) and MD (higher) values than the other datasets (see methods). Due to the high total n, excluding this dataset did not change the relationship with age. **(E)** Relationship between age and average cortical thickness (CT). **(F)** Age distribution of the presented data as in **(D,E)**. T1, anatomical MRI; DWI, diffusion weighted imaging; CT, cortical thickness.

collation of data from a wide variety of groups, acquired with different scanners, different scanning protocols, varying data quality etcetera, and includes data from a mixture of different patient and control populations. While these limitations place constraints on the type of investigations that one can perform with such collated multi-site datasets, we are optimistic that the 10K dataset can be used as a large reference dataset for future studies, enabling many technical and neuroscientific research questions to be addressed (e.g., **Figure 1**). As such, we hope that the presented data will be of use to the neuroscience community in the examination of the human connectome. Above all, we hope that our report will inspire others to organize exciting 10Kin1day-type of events in the near future, bringing together existing neuroimaging data and further catalyze open neuroimaging research of the healthy and diseased brain.

MATERIALS AND METHODS

A total of 42 groups (52 participants) participated in the workshop, some working on multiple datasets. Each dataset included a diffusion MRI scan and T1 MRI scan processed using FreeSurfer (8). Datasets across groups included data from 1.5 and 3 Tesla MRI with varying scanner protocols and number of applied DWI gradients. Data included MRI data of healthy participants and patients with a neurological or psychiatric disorder. Twenty-three groups were able to make their data available, making a total of 8,000+ connectome maps publicly available through means of this report. Reconstructed connectome maps are presented anonymously, coded for participation site and disease condition(s). Basic demographics of the datasets are included in the download set.

DWI Preprocessing

DWI datasets were corrected for susceptibility and eddy current distortions using the open tools from the FMRIB Software Library (FSL, http://fsl.fmrib.ox.ac.uk). Depending on their DWI dataset, participants preprocessed their data using the FSL *eddy_correct* or *eddy* tool. For those DWI sets that included a subset of scans with an opposite k-space read out, an additional field distortion map was formed and applied to the DWI images (9).

Cortical Parcellation

Before the event, the participants created FreeSurfer files based on their T1 images, with this output being subjected to varying degrees of quality control. The resulting parcellations of the cerebrum were used to select the regions of interest for the connectome reconstruction. The 68 cortical regions of FreeSurfer's standard Desikan-Killiany Atlas (10, 11) as well as 14 subcortical regions were selected as network regions. Additionally, FreeSurfer files were used to further parcellate the cortex into 114 and 219 regions, respectively using the Cammoun atlas (12).

Fiber Reconstruction

After preprocessing of the DWI data, in-house developed scripts were used to fit a diffusion tensor to the diffusion signal in each voxel of the white matter mask (selected based on the white matter segmentation map of the FreeSurfer files) using robust tensor fitting (13). Simple Diffusion Tensor Imaging (DTI) reconstruction was used due to its robustness and relatively low sensitivity to false positive reconstructions compared to more advanced reconstruction methods (14), and thus potentially being the least distorting solution for connectome reconstruction and analysis based on MR imaging data (15). Decomposition of the tensor into eigenvectors and eigenvalues was used to select the main diffusion direction in each voxel, and to compute fractional anisotropy (FA) and mean diffusivity (MD) (16). Deterministic fiber tractography was used to construct large-scale white matter pathways. Eight seeds (evenly distributed across the voxel) started in each white matter voxel, and fiber streamlines were formed by following the main diffusion direction from voxel to voxel using the *fiber assignment by continuous tracking* (FACT) algorithm (17), until one of the stopping criteria was met. A streamline was stopped when (1) it hit a voxel with an FA<0.1, (2) went out of the brain mask, or (3) made a turn >45 degrees.

Connectome Reconstruction

A connectome map was made by combining the (sub)cortical parcellation map and the set of reconstructed fibers using commonly described procedures [see (18–21)]. For each of the Cammoun Desikan-Killiany parcellation maps (i.e., 14+68, 14+114, and 14+219 regions, respectively), the total collection of reconstructed fiber streamlines was used to assess the level of connectivity between each pair of (sub)cortical regions, represented as the *connectivity matrix CIJ*. (Sub)cortical regions were selected as the nodes of the reconstructed network, and for each combination of region *i* and region *j* where fiber streamlines touched both regions a connection (i.e., network edge) was included in cell *CIJ(i,j)* in the connectivity matrix. Five different types of strength of a connection were computed and included as edge strength: (1) the number of reconstructed streamlines (NOS) between region *i* and *j*, (2) the average FA of the voxels traversed by the reconstructed streamlines, (3) the average MD of the reconstructed streamlines, (4) the average length of the reconstructed streamlines and (5) streamline density computed as the number of reconstructed streamlines corrected for the average volume of region *i* and region *j* (18, 19).

Outliers

A total of 15,947 connectome maps were analyzed across the participating groups. Of the datasets that could be shared, 197 were detected as outliers (and were subsequently removed from the dataset). Outliers were detected automatically by testing per dataset and for each connectome map their average connection strength and their distance to the group average prevalence map. The average connection strength of a connectome map was calculated for each of the five connection weights as the mean of the strengths over all existing (nonzero) connections. To measure the presence of odd connections or absence of common connections in a connectome map, we constructed a group prevalence matrix for each dataset, counting per node pair how many times an edge was observed across the group of subjects in the dataset. For each connectome map the total prevalence of all observed connections and the total prevalence of all non-observed connections was computed. Outliers were identified as connectome maps that displayed on any of the 7 measures (5 weight and 2 prevalence measures) a score below Q1 – 2×IQR or above Q3 + 2×IQR, with Q1 and Q3 referring to the first and third quartile, respectively and IQR the interquartile range IQR = Q3 – Q1. This resulted in the detection of 189 outliers in total, which were excluded from the dataset. One complete dataset (set_634413, n=584) showed across all included individual sets an average lower FA / higher MD as compared to the other datasets and this set was excluded from the age curves shown in **Figure 1**. Due to the high overall sample size, including or excluding this dataset did not change the shape of the final plot.

Cross-Site Comparison

Datasets across sites were compared by computing for each site a group average connectome map (group threshold 60%) and comparing the group average connectivity matrices across each of the sites. Cross-site overlap was computed as the percentage of overlap of the binary matrices and as the correlation between the non-zero elements of the FA group-average matrices.

Comparison to HCP

To test the validity of the 10K dataset, we compared the group average matrix of the 10K set to the group average matrix of data from the Human Connectome Project (HCP) (3). First, for the 10K dataset, a group average FA matrix was computed, by including those edges that were observed in at least 33% of the group (i.e., a group threshold of 33%, >2700 subjects showing a particular network edge). Average weight values of the included edges were taken as the non-zero mean of those edges across the group of subjects. Second, a similar group average FA matrix was derived from previously analyzed HCP data (22) (n = 487 datasets). In brief, HCP analysis included the following steps [see (22) for more detailed information on the HCP data analysis]. For each of the HCP DWI datasets a connectome was reconstructed based on the minimally pre-processed data of HCP. Given the high quality of the HCP data, analysis here included reconstruction of multiple diffusion directions, allowing for the reconstruction of more complex fiber configurations (e.g., crossing fibers) (22). Similarly as for the 10K data, across the total set of 487 datasets, an average FA group matrix was computed, including those network edges that were observed in at least 33% of the total population (i.e., >160 datasets) and taking the non-zero mean of FA values across the group of subjects. Comparison between the 10K set and the HCP dataset was computed by means of (1) counting the number of existing connections and non-existing connections in the 10K dataset as observed in the HCP dataset and (2) by correlating the FA weights of the set of edges as observed in both datasets.

ETHICS STATEMENT

This study was carried out in accordance with the recommendations of the ethical committee boards of each independent institute. The protocol was approved by the ethical committee boards of each independent institute. Informed consent of all participants was acquired by the independent research groups.

AUTHOR CONTRIBUTIONS

All authors contributed to the acquisition and/or analysis of the MRI data. MvdH wrote the first draft of the manuscript. All authors revised the manuscript and contributed intellectual content.

FUNDING

The 10Kin1day workshop was generously sponsored by the Neuroscience and Cognition program Utrecht (NCU) of the Utrecht University (https://www.uu.nl/en/research/neuroscience-and-cognition-utrecht), the ENIGMA consortium (http://enigma.ini.usc.edu), and personal grants: MvdH: NWO-VIDI (452-16-015), MQ Fellowship; SB-C: the Wellcome Trust; Medical Research Council UK; NIHR CLAHRC for Cambridgeshire and Peterborough Foundation National Health Services Trust; Autism Research Trust; LB: New Investigator Award, Canadian Institutes of Health Research; Dara Cannon: Health Research Board (HRB), Ireland (grant code HRA-POR-2013-324); SC: Research Grant Council (Hong Kong)-GRF 14101714; Eveline Crone: ERC-2010-StG-263234; UD: DFG, grant FOR2107 DA1151/5-1, DA1151/5-2, SFB-TRR58, Project C09, IZKF, grant Dan3/012/17; SD: MRC-RFA-UFSP-01-2013 (Shared Roots MRC Flagship grant); TF: Marie Curie Programme, International Training Programme, r'Birth; DG: National Science Centre (UMO-2011/02/A/NZ5/00329); BG: National Science Centre (UMO-2011/02/A/NZ5/00329); JH: Western Sydney University Postgraduate Research Award; LH: Science Foundation Ireland, ERC; HH: Research Grant Council (Hong Kong)-GRF 14101714; LJ: Velux Stiftung, grant 369 & UZH University Research Priority Program Dynamics of Healthy Aging; AJ: DFG, grant FOR2107 JA 1890/7-1; KJ: National Science Centre (UMO-2013/09/N/HS6/02634); VK: The Russian Foundation for Basic Research (grant code 15-06-05758 A); TK: DFG, grant FOR2107 KI 588/14-1, DFG, grant FOR2107 KI 588/15-1; AK: DFG, grant FOR2107 KO 4291/4-1, DFG, grant FOR2107 KO 4291/3-1; IL: The Russian Foundation for Basic Research (grant code 15-06-05758 A); EL: Health and Medical Research Fund - 11121271; SiL: NHMRC-ARC Dementia Fellowship 1110414, NHMRC Dementia Research Team Grant 1095127, NHMRC Project Grant 1062319; CL-J: 537-2011, 2014-849; AM: Wellcome Trust Strategic Award (104036/Z/14/Z), MRC Grant MC_PC_17209; CM: Heisenberg-Grant, German Research Foundation, DFG MO 2363/3-2; PM: Foundation for Science and Technology, Portugal - PDE/BDE/113601/2015; KN: National Science Centre (UMO-2011/02/A/NZ5/00329); PN: National Science Centre (UMO-2013/09/N/HS6/02634); JiP: NWO-Veni 451-10-007; PaR: PER and US would like to thank the Schizophrenia Research Institute and the Chief-Investigators of the Australian Schizophrenia Research Bank V. Carr, U. Schall, R. Scott, A. Jablensky, B. Mowry, P. Michie, S. Catts, F. Henskens, and C. Pantelis; AS: National Science Centre (UMO-2011/02/A/NZ5/00329); SS: European Union's Horizon 2020 research and innovation programme under the Marie Skłodowska-Curie grant agreement No 707730; CS-M: Carlos III Health Institute (PI13/01958), Carlos III Health Institute (PI16/00889), Carlos III Health Institute (CPII16/00048); ES: National Science Centre (UMO-2011/02/A/NZ5/00329); AT: The Russian Foundation for Basic Research (grant code 15-06-05758 A); DT-G: PI14/00918, PI14/00639; Leonardo Tozzi: Marie Curie Programme, International Training Programme, r'Birth; SV: IMPRS Neurocom stipend; TvE: National Center for Research Resources at the National Institutes of Health (grant numbers: NIH 1 U24 RR021992 (Function Biomedical Informatics Research Network), NIH 1 U24 RR025736-01 (Biomedical Informatics Research Network Coordinating Center; http://www.birncommunity.org) and the NIH Big Data to Knowledge (BD2K) award (U54 EB020403 to Paul Thompson). NvH: NWO-VIDI (452-11-014); MW: National Science Centre (UMO-2011/02/A/NZ5/00329); Veronica O'Keane: Meath Foundation; AV and AW: CRC Obesity Mechanism (SFB 1052) Project A1 funded by DFG. The funding sources had no role in the study design, data collection, analysis, and interpretation of the data.

ACKNOWLEDGMENTS

We further like to thank Joanna Goc, Veronica O'Keane, Devon Shook, and Leonardo Tozzi for their participation and/or support of the 10K project. HCP data was provided by the Human Connectome Project, WU-Minn Consortium (Principal Investigators: David Van Essen and Kamil Ugurbil; 1U54MH091657) funded by the 16 NIH Institutes and Centers that support the NIH Blueprint for Neuroscience Research; and by the McDonnell Center for Systems Neuroscience at Washington University.

REFERENCES

1. Amunts K, Ebell C, Muller J, Telefont M, Knoll A, Lippert T. The Human Brain Project: Creating a European Research Infrastructure to Decode the Human Brain. *Neuron.* (2016) 92:574–81. doi: 10.1016/j.neuron.2016.10.046
2. Insel TR, Landis SC, Collins FS. Research priorities. *NIH BRAIN Init Sci.*(2013) 340:687–8. doi: 10.1126/science.1239276
3. Van Essen DC, Smith SM, Barch DM, Behrens TE, Yacoub E, Ugurbil K. The WU-Minn Human Connectome Project: an overview. *Neuroimage.* (2013) 80:62–79. doi: 10.1016/j.neuroimage.2013.05.041
4. Jiang T. Brainnetome: a new -ome to understand the brain and its disorders. *Neuroimage.* (2013) 80:263–72. doi: 10.1016/j.neuroimage.2013.04.002
5. Thompson PM, Andreassen OA, Arias-Vasquez A, Bearden CE, Boedhoe PS, Brouwer RM, et al. ENIGMA and the individual: Predicting factors that affect the brain in 35 countries worldwide. *Neuroimage.* (2017) 145:389–408. doi: 10.1016/j.neuroimage.2015.11.057
6. Mainen ZF, Hausser M, Pouget A. A better way to crack the brain. *Nature.* (2016) 539:159–61. doi: 10.1038/539159a
7. Mori S, Zhang JY. Principles of diffusion tensor imaging and its applications to basic neuroscience research. *Neuron.* (2006) 51:527–39. doi: 10.1016/j.neuron.2006.08.012
8. Fischl B, Dale AM. Measuring the thickness of the human cerebral cortex from magnetic resonance images. *Proc Natl Acad Sci USA.* (2000) 97:11050–5. doi: 10.1073/pnas.200033797
9. Andersson JL, Skare S, Ashburner J. How to correct susceptibility distortions in spin-echo echo-planar images: application to diffusion tensor imaging. *Neuroimage.* (2003) 20:870–88. doi: 10.1016/S1053-8119(03)00336-7
10. Desikan RS, Ségonne F, Fischl B, Quinn BT, Dickerson BC, Blacker D, et al. An automated labeling system for subdividing the human cerebral cortex on MRI scans into gyral based regions of interest. *NeuroImage.* (2006) 31:968–80. doi: 10.1016/j.neuroimage.2006.01.021
11. Fischl B, van der Kouwe A, Destrieux C, Halgren E, Ségonne F, Salat DH, et al. Automatically parcellating the human cerebral cortex. *Cereb Cortex.* (2004) 14:11–22. doi: 10.1093/cercor/bhg087
12. Cammoun L, Gigandet X, Meskaldji D, Thiran JP, Sporns O, Do KQ, et al. Mapping the human connectome at multiple scales with diffusion spectrum MRI. *J Neurosci Methods.* (2012) 203:386–97. doi: 10.1016/j.jneumeth.2011.09.031
13. Chang LC, Jones DK, Pierpaoli C. RESTORE: robust estimation of tensors by outlier rejection. *Magn Reson Med.* (2005) 53:1088–95. doi: 10.1002/mrm.20426
14. Maier-Hein KH, Neher, PF, Houde, J-C, Côté, M-A, Garyfallidis E, Zhong J, et al. The challenge of mapping the human connectome based on diffusion tractography. *Nat Commun.* (2017) 8:1349. doi: 10.1038/s41467-017-01285-x
15. Zalesky A, Fornito A, Cocchi L, Gollo LL, van den Heuvel MP, Breakspear M. Connectome sensitivity or specificity: which is more important? *Neuroimage.* (2016) 15:407–420. doi: 10.1016/j.neuroimage.2016.06.035
16. Beaulieu C, Allen PS. Determinants of anisotropic water diffusion in nerves. *Magn Reson Med.* (1994) 31:394–400. doi: 10.1002/mrm.1910310408
17. Mori S, Barker PB. Diffusion magnetic resonance imaging: its principle and applications. *Anat Rec.* (1999) 257:102–9. doi: 10.1002/(SICI)1097-0185(19990615)257:3<102::AID-AR7>3.0.CO;2-6
18. Hagmann P, Cammoun L, Gigandet X, Meuli R, Honey CJ, Wedeen VJ, et al. Mapping the structural core of human cerebral cortex. *PLoS Biol.* (2008) 6:e159. doi: 10.1371/journal.pbio.0060159
19. van den Heuvel MP, Kahn RS, Goni J, Sporns O. High-cost, high-capacity backbone for global brain communication. *Proc Natl Acad Sci USA.* (2012) 109:11372–7. doi: 10.1073/pnas.1203593109
20. van den Heuvel MP, Mandl RC, Stam CJ, Kahn RS, Hulshoff Pol HE. Aberrant frontal and temporal complex network structure in schizophrenia: a graph theoretical analysis. *J Neurosci.* (2010) 30:15915–26. doi: 10.1523/JNEUROSCI.2874-10.2010
21. van den Heuvel MP, Sporns O. Rich-club organization of the human connectome. *J Neurosci.* (2011) 31:15775–86. doi: 10.1523/JNEUROSCI.3539-11.2011
22. van den Heuvel MP, Scholtens LH, de Reus MA, Kahn RS. Associated microscale spine density and macroscale connectivity disruptions in schizophrenia. *Biol Psychiatry.* (2016) 80:293–301. doi: 10.1016/j.biopsych.2015.10.005

Conflict of Interest Statement: The authors declare that the research was conducted in the absence of any commercial or financial relationships that could be construed as a potential conflict of interest.

Citation: van den Heuvel MP, Scholtens LH, van der Burgh HK, Agosta F, Alloza C, Arango C, Auyeung B, Baron-Cohen S, Basaia S, Benders MJNL, Beyer F, Booij L, Braun KPJ, Filho GB, Cahn W, Cannon DM, Chaim-Avancini TM, Chan SSM, Chen EYH, Crespo-Facorro B, Crone EA, Dannlowski U, de Zwarte SMC, Dietsche B, Donohoe G, Du Plessis S, Durston S, Díaz-Caneja CM, Díaz-Zuluaga AM, Emsley R, Filippi M, Frodl T, Gorges M, Graff B, Grotegerd D, Gąsecki D, Hall JM, Holleran L, Holt R, Hopman HJ, Jansen A, Janssen J, Jodzio K, Jäncke L, Kaleda VG, Kassubek J, Kharabian Masouleh S, Kircher T, Koevoets MGJC, Kostic VS, Krug A, Lawrie SM, Lebedeva IS, Lee EHM, Lett TA, Lewis SJG, Liem F, Lombardo MV, Lopez-Jaramillo C, Margulies DS, Markett S, Marques P, Martínez-Zalacaín I, McDonald C, McIntosh AM, McPhilemy G, Meinert SL, Menchón JM, Montag C, Moreira PS, Morgado P, Mothersill DO, Mérillat S, Müller H-P, Nabulsi L, Najt P, Narkiewicz K, Naumczyk P, Oranje B, Ortiz-Garcia de la Foz V, Peper JS, Pineda JA, Rasser PE, Redlich R, Repple J, Reuter M, Rosa PGP, Ruigrok ANV, Sabisz A, Schall U, Seedat S, Serpa MH, Skouras S, Soriano-Mas C, Sousa N, Szurowska E, Tomyshev AS, Tordesillas-Gutierrez D, Valk SL, van den Berg LH, van Erp TGM, van Haren NEM, van Leeuwen JMC, Villringer A, Vinkers CH, Vollmar C, Waller L, Walter H, Whalley HC, Witkowska M, Witte AV, Zanetti MV, Zhang R and de Lange SC (2019) 10Kin1day: A Bottom-Up Neuroimaging Initiative. Front. Neurol. 10:425. doi: 10.3389/fneur.2019.00425

frontiers in Neurology

BRIEF RESEARCH REPORT
published: 27 August 2019
doi: 10.3389/fneur.2019.00851

MRI Atlas of the Human Deep Brain

Jean-Jacques Lemaire[1]*, Antonio De Salles[2], Guillaume Coll[1], Youssef El Ouadih[1], Rémi Chaix[1], Jérôme Coste[1], Franck Durif[3], Nikos Makris[4] and Ron Kikinis[4,5,6]

[1] Service de Neurochirurgie, CHU Clermont-Ferrand, Université Clermont Auvergne, Centre National de la Recherche Scientifique, Engineering School SIGMA Clermont, Clermont-Ferrand, France, [2] Department of Neurosurgery, Radiation Oncology, HCOR Neuroscience, São Paulo, Brazil, [3] Service de Neurologie, Centre National de la Recherche Scientifique, CHU Clermont-Ferrand, Université Clermont Auvergne, Engineering School SIGMA Clermont, Clermont-Ferrand, France, [4] Surgical Planning Laboratory, Center for Morphometric Analysis, A. Martinos Center for Biomedical Imaging, Harvard Medical School, Massachusetts General Hospital, Brigham and Women's Hospital, Boston, MA, United States, [5] Robert Greenes Distinguished Director of Biomedical Informatics, Brigham and Women's Hospital, Boston, MA, United States, [6] Computer Science Department, Fraunhofer MEVIS, University of Bremen, Bremen, Germany

Mastering detailed anatomy of the human deep brain in clinical neurosciences is challenging. Although numerous pioneering works have gathered a large dataset of structural and topographic information, it is still difficult to transfer this knowledge into practice, even with advanced magnetic resonance imaging techniques. Thus, classical histological atlases continue to be used to identify structures for stereotactic targeting in functional neurosurgery. Physicians mainly use these atlases as a template co-registered with the patient's brain. However, it is possible to directly identify stereotactic targets on MRI scans, enabling personalized targeting. In order to help clinicians directly identify deep brain structures relevant to present and future medical applications, we built a volumetric MRI atlas of the deep brain (MDBA) on a large scale (infra millimetric). Twelve hypothalamic, 39 subthalamic, 36 telencephalic, and 32 thalamic structures were identified, contoured, and labeled. Nineteen coronal, 18 axial, and 15 sagittal MRI plates were created. Although primarily designed for direct labeling, the anatomic space was also subdivided in twelfths of AC-PC distance, leading to proportional scaling in the coronal, axial, and sagittal planes. This extensive work is now available to clinicians and neuroscientists, offering another representation of the human deep brain ([https://hal.archives-ouvertes.fr/] [hal-02116633]). The atlas may also be used by computer scientists who are interested in deciphering the topography of this complex region.

Keywords: atlas, MRI, human, thalamus, hypothalamus, subthalamus, deep brain, stereotaxis

OPEN ACCESS

Edited by:
Hans-Peter Müller,
University of Ulm, Germany

Reviewed by:
Kenichi Oishi,
Johns Hopkins University,
United States
Nicola Amoroso,
University of Bari Aldo Moro, Italy

****Correspondence:***
Jean-Jacques Lemaire
jjlemaire@chu-clermontferrand.fr

Specialty section:
This article was submitted to
Applied Neuroimaging,
a section of the journal
Frontiers in Neurology

Received: *22 May 2019*
Accepted: *23 July 2019*
Published: *27 August 2019*

Citation:
Lemaire J-J, De Salles A, Coll G, El Ouadih Y, Chaix R, Coste J, Durif F, Makris N and Kikinis R (2019) MRI Atlas of the Human Deep Brain. Front. Neurol. 10:851. doi: 10.3389/fneur.2019.00851

INTRODUCTION

The term "deep brain" (DB) describes the combination of subcortical structures including the mesencephalon. It is anatomically a highly complex region with clinical importance in a number of diseases. Several specialized atlases have been created to orient deep brain interventions. The atlases of the human deep brain most used in clinical neurosurgery relies on histological studies (1–4). They are both, anatomic books, and stereotactic atlases. They are co-registerable with patient brains through landmarks; such as the widely used anterior (AC) and posterior (PC) white commissures. Other proportional grid systems derived from landmarks, are also still largely used (5, 6). These atlases provide probabilistic coordinates of structural related functional targets. Rigid registration of an atlas to a patient's brain MRI refines the quality of probabilistic targeting (7). This approach is called indirect stereotactic identification of structures (2), because the structures of interest were not directly visible before the existence of the MRI.

The deep brain geometry limited variability coupled with the relative facility to construct proportional diagrams made the indirect visualization approach used worldwide in stereotactic and functional neurosurgery, including radiosurgery (8).Yet an increasing number of surgical teams transitioned to use both, MRI landmarks and/or directly visualization of targeted structures for implantation of DB stimulation (DBS) (9–15). We proposed direct targeting of pallidal structures visualized on MRI without the use of AC-PC referencing (16), and since used this approach routinely (17).

Recent advances of MRI technologies have resulted in a dramatic increase in both, spatial resolution and contrast resolution, consequently the ability to identify clinically relevant structures in the deep brain. Our group begun to manually segmenting the DB using *ex vivo* high field MRI in the early 2000's (18). Because of its complex architecture, it took over 10 years to comprehensively label the majority of relevant structures. We reported intermediate stages of this atlas over the years (19–22). Herein we present a clinical MRI Deep Brain Atlas (MDBA) built from a unique anatomic specimen offering for the first time the most advanced version with detailed volumetric representation. Though mainly developed to identify structures of the deep brain on MRI for neurosurgical practices, it also offers to neuroscientists another representation of the topographic organization of the deep brain.

MATERIALS AND METHODS

Specimen, Raw Image Data, and Initial Contouring of Structures

The brain specimen was obtained from a 65 year-old male subject who died of non-neurological cause. It was studied following our institutional rules and guidelines. After long term fixation in 10% formaldehyde, a block measuring about 60-mm in each direction was scanned at 4.7 Tesla (Bruker, Ettlingen, Germany) with a 3D T1-weighted spin echo sequence (about 14 h of acquisition), resulting in 250 μm isotropic voxels (256^3 matrix). The image data was initially manually contoured and labeled using a neurosurgical software (Iplan, BrainLab, Munich, Germany). MRI cartography and labeling relied on the analysis of different signals and patterns of the deep brain structures (19). The signal intensity of a voxel reflects the microarchitecture, i.e., cell density, and anisotropy of bundles of axons (the higher number of anisotropic bundles, the lower signal), as well as the cells contents, notably the ferromagnetic load of neurons (the higher ferromagnetic charge, the lower signal). In addition, at the resolution available in our data set, the common separation of brain tissue into white and gray matters is not binary in the deep brain. For instance, at large scale (centimetric) the thalamus is made of gray matter; at small scale (millimetric) the thalamus is made of gray matter nuclei such as the ventromedial posterior nucleus, of white fascicles such as the mammillothalamic fascicle, and of mixed structures such as intralaminar nuclei or the reticular nucleus crossed by numerous white matter fibers. The cartography was performed structure by structure, starting from the most readily identifiable ones, such as the subthalamic nucleus. In parallel to the progressive mapping of the 4.7-Tesla data set, the updated version was tested in clinical practice for direct targeting in functional neurosurgery as an neuroanatomic aid (23, 24). The different nuclei of the hypothalamus were parcellated into different structures according to proportional topography and structural connectivity (21, 25).

Building of the MRI Deep Brain Atlas

The objects, i.e., the anatomic structures, were exported as surface (stl format) from the surgical software. Surfaces were transformed in binary maps for voxel-based representation and co-registered with a modified MRI data set (Thermo Scientific™ Amira™, v 6.4, Hillsboro, OR, USA). The raw image data set were realigned along AC-PC line, slices being resampled accordingly; leading to a new image data set of 0.125 × 0.125

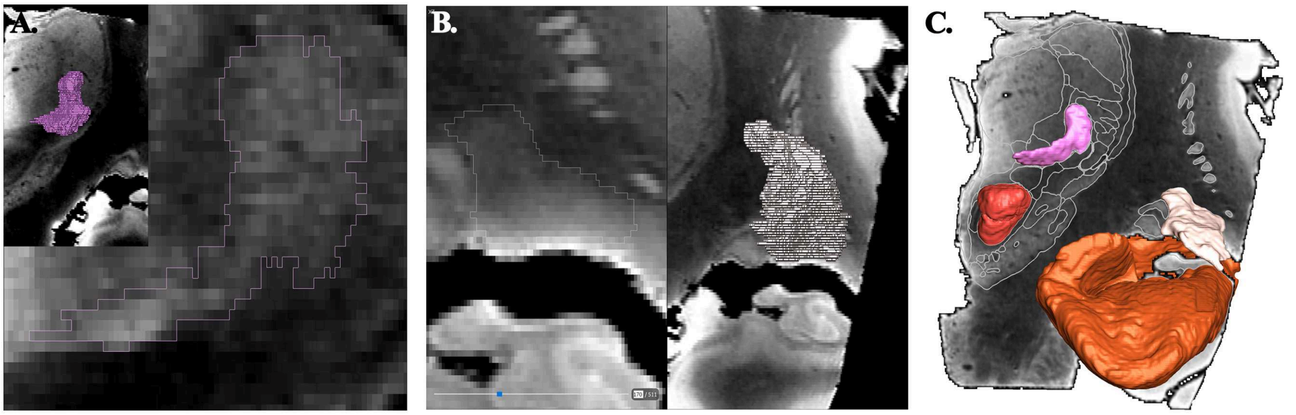

FIGURE 1 | Principle of contouring and voxel objects (frontal view; coronal slices). **(A)** ventrocaudal medial nucleus of thalamus (pink). **(B)** retrolenticular-reticularoïd zone (light beige). **(C)** smoothed surfaces of voxel objects, ventrocaudal medial nucleus of thalamus, retrolenticular-reticularoïd zone, red nucleus (red), and hippocampal formation (light brown).

× 0.256 mm^3 voxels (512 × 512 × 256 matrix; 8-bit grayscale ranging from 0 to 255). The resampled MRI images were cleaned (removed of cerebrospinal-fluid spaces, vessels and nerves of the subarachnoid space; Photoshop CC, Adobe, San Jose, CA, USA,) and then filtered (unsharp masking and sigmoid intensity remapping; 16-bit grayscale; Thermo Scientific^{TM} Amira^{TM}, v 6.4, Hillsboro, OR, USA). All imported objects were manually re-segmented accounting to the new high geometric resolution and highest contrast between adjacent structures using multi-objects contouring tools (Thermo Scientific^{TM} Amira^{TM}, v 6.4, Hillsboro, OR, USA) (**Figure 1A**). Contours of unnamed structures were identified and labeled during this process (**Figure 1B**). A unique color (HSV color model) was attributed to each object. The surface representation of voxel objects was smoothed with a Gaussian filter (Thermo Scientific^{TM} Amira^{TM}, v 6.4, Hillsboro, OR, USA) (**Figure 1C**).

Labeling of Structures

The structures were labeled according to clinically known classical names (1, 2, 26–37) and ontologies (38–40). These structures were essentially nuclear, i.e., where neuronal bodies are concentrated; in addition, small white matter fascicles embedded were included (e.g., thalamic fascicle), but we did not label the large capsule fascicles, namely the internal, external and extreme capsules. Complementary information, such as homonyms and French names were also added. Acronyms were created to reduce the text size of labels on plates. Structures not precisely identified or still unnamed were detailed and labeled according to the location and the aspect on MRI. For instance: (i) the retrolenticular reticularoid zone was observed laterally to the area or zone of Wernicke, hence in a retrolenticular position, Because of its reticular appearance (low signal intensity) it was named reticularoid (**Figure 2**); (ii) the subthalamic tegmental field covered the historical Forel's H field, and was segregated into anterior, dorsal, medial, lateral and central zones; (iii) the area of reticular appearance, i.e., with an apparent low density of cells, which is placed posteriorly and below the pallidum, was named the posterior subpallidal area. The information is available as **Supplementary Table**.

The structures were also specified according to four subregions of the deep brain, although these subdivisions are still not formally set (33, 40), namely the hypothalamus, the thalamus, the subthalamus or prethalamus and the telencephalon (**Supplementary Table**). The labeling was not fully extensive, as we focused on structures identifiable on MRI for the thalamus, subthalamus, and telencephalon, or inferred from diagrams for the hypothalamus (e.g., the suprachiasmatic and supraoptic nuclei were not separated).

MDBA Plates

For each MRI slice and related maps, structural (MRI slice) and topographic (maps) data were distributed on a double page or plate.

Topographic maps were created from cross sections of objects intersecting with cutting planes (Thermo Scientific^{TM} Amira^{TM}, v 6.4, Hillsboro, OR, USA), displaying colored surface and

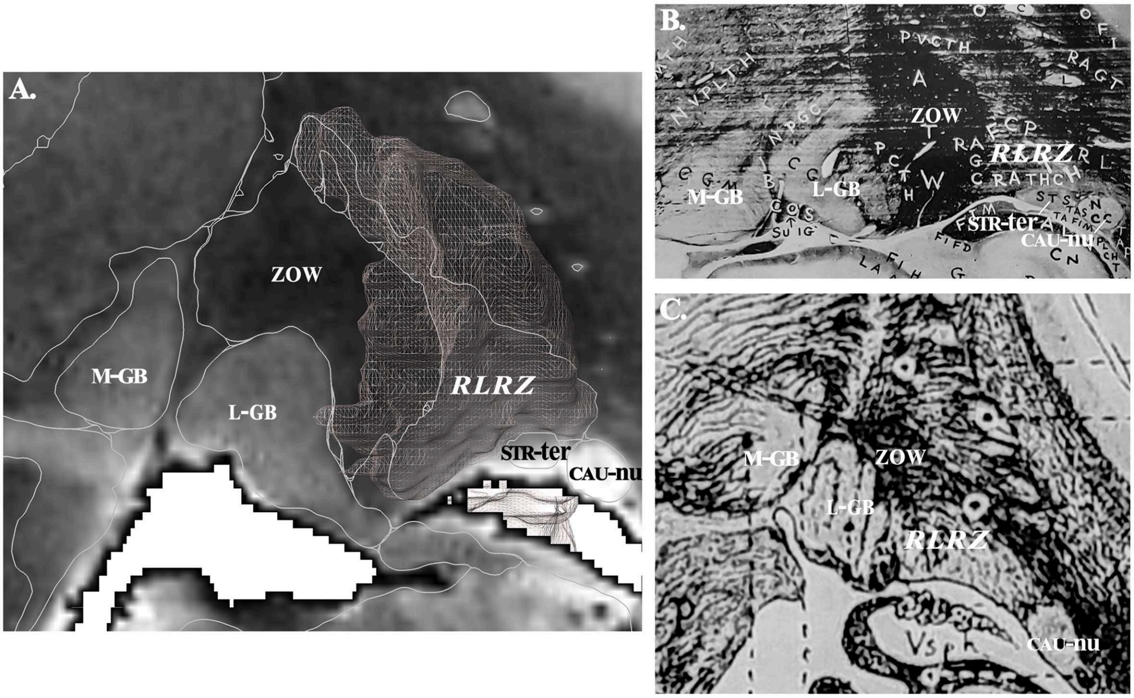

FIGURE 2 | (A) Contouring and labeling of the retrolenticular reticularoid zone (*RLRZ*; the voxel object is overlaid) on MRI slice (see MDBA plate 10); medial geniculate body, M-GB; lateral geniculate body, L-GB; stria terminalis, STR-ter; caudate nucleus, CAU-nu. **(B)** Same region according to Riley (36); the *RLRZ* is visible (histologic preparation) but not identified. **(C)** Same region according to Dejerine (26); the RLRZ is visible (artist drawing) but not identified.

contours of structures overlaid on MRI slices (**Figure 3**). The MRI slices were not scaled, as they were assumed to be used for direct comparison with patient MRI datasets. Furthermore, the aspect of signal of structures is very similar to that observed in images routinely used in clinical practice, even if the latter have a lower spatial resolution, which is supramillimetric. The contours of structures were overlaid (white line) on each MRI slice, facilitating the identification of structures on the patients' individual imagery. The contrast of each MRI slice was enhanced by automatic adjustment of tones (Photoshop CC, Adobe, San Jose, CA, USA), in a slice by slice fashion, minimizing heterogeneity of signals due to the presence of extremely high (white) and low (black) values within the volume of acquisition (a legacy of the original MRI acquisition).

The anatomic space, scaled in millimeters and oriented along vertical and horizontal AC-PC plans, was subdivided in twelfth of AC-PC distance according to Guiot et al. (5), Benabid et al. (6), leading to proportional scaling in the coronal (C), axial (A), and sagittal (S) planes (**Figure 4**). AC-PC distance was rounded to 27 mm; 1/12th of AC-PC was rounded to 2.25 mm; the midpoint between AC and PC (MI) was rounded to 13.5 mm. The height of the thalamus was 18 mm. The proportional grid system numbers were used to name the slices and related maps. Hence, for one unique location in a plane, both absolute (overlay of absolute millimeter distance grid) and relative (overlay of proportional distance grid) positions were available. Three particular sections served as reference positions. The axial section going through the AC-PC horizontal plane was named A0-AC-PC; sections above that plane were named superior (AS), and below, inferior (AI). The coronal section going through AC (perpendicular to AC-PC horizontal plane) was named C0-AC. All plates in front of AC were named CF, whereas the ones located posteriorly (or rear) to AC were named CR; at the MI point, the coronal section was named CR6-MI (the 6th coronal plane posterior to AC); at PC, CR12-PC (the 12th coronal plane posterior to AC). The sagittal section going through the vertical AC-PC plane was named S0-ACPC.

On each plate whatever the orientation, one MRI slice and related position graphs and maps, were arranged for localization and comparison purposes. The relative position of any given MRI slice and related maps was overlaid on proportional grids on A0-ACPC, CR6-MI, or S4, according to its orientation. Two related maps of the MRI slice were displayed: the first is the map of structures at the specific location with the contours and labels (acronyms), on which is overlaid a millimetric grid (absolute location); the second map is made of the same structures but colored according to the four subregions, including the overlay of a proportional grid as well. This second map was colored using luminance gradients of the specific color of the subregion as follows. The hypothalamus was colored in yellow, the thalamus in blue, the subthalamus in brown, and the telencephalon in green.

RESULTS

Twelve hypothalamic, 39 subthalamic, 36 telencephalic and 32 thalamic structures were identified, contoured and

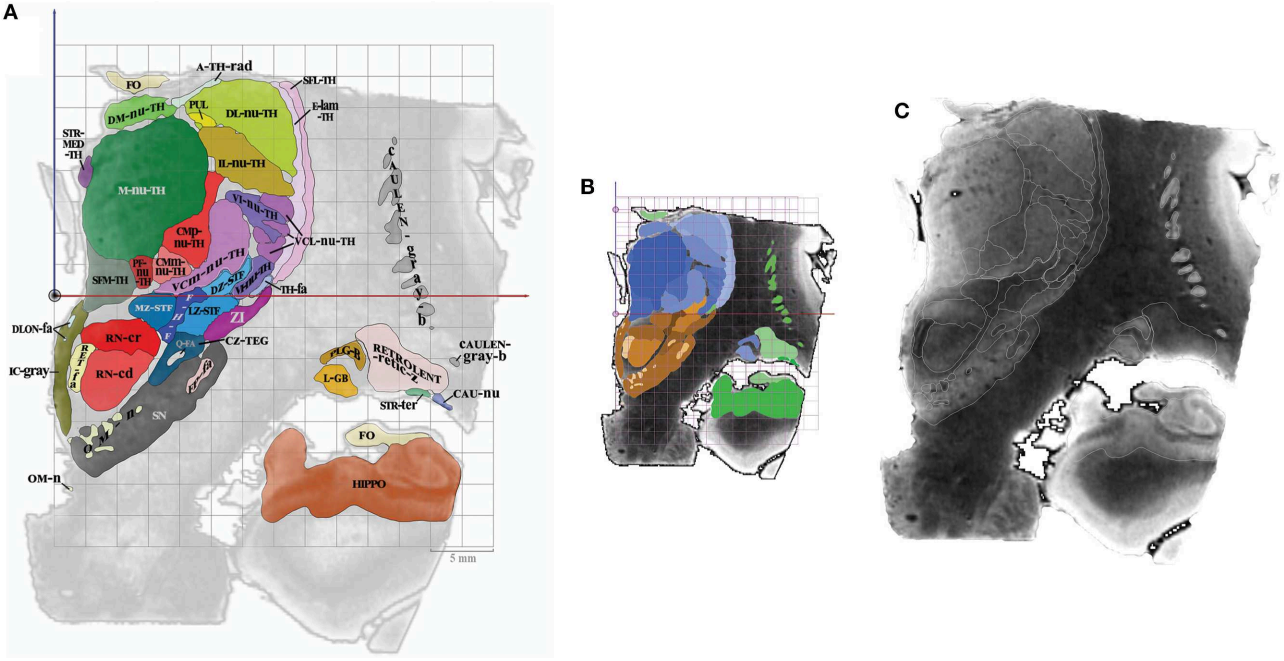

FIGURE 3 | (A) Colored surfaces and acronyms, plate CR8 (millimeter scale), the ACPC line is depicted as a black circle. **(B)** Same plate, colors are specified according to subregions (proportional and millimeter scales); thalamus (blue gradation), subthalamus (brown gradation) and telencephalon (green gradation). **(C)** Same plate, MRI slice and white contours of structures (no scale).

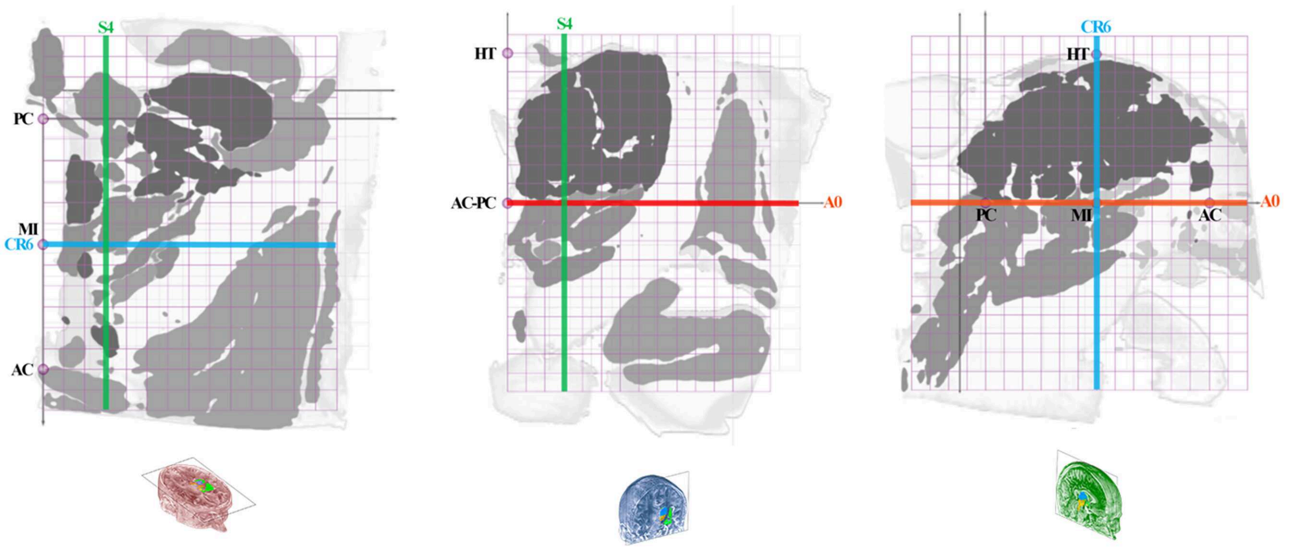

FIGURE 4 | Position of slices (colored lines: axial, red; coronal, blue; sagittal, green) on the axial ACPC plan (A0-ACPC; left row), coronal MI plan (CR6-MI; intermediate row) and 9-mm lateral sagittal plan (S4; right row); proportional grid (purple) in 12th of ACPC distance; HT, thalamus height.

TABLE 1 | MDBA plates.

Coronal			Axial			Sagittal		
Acronym	**Relative position (1/12th of ACPC)**	**Location (mm)**	**Acronym**	**Relative position (1/12th of ACPC)**	**location (mm)**	**Acronym**	**Relative position (1/12th of ACPC)**	**Location (mm)**
CF2	2 in front of AC	−4.5	AS8	8 above ACPC	18	S0-ACPC	0 of ACPC	0
CF1	1 in front of AC	−2.2	AS7	7 above ACPC	15.5	S1	1 of ACPC	2.3
CO-AC	0 of AC	0	AS6	6 above ACPC	13.5	S2	2 of ACPC	4.5
CR1	1 rear to AC	2.2	AS5	5 above ACPC	11.3	S3	3 of ACPC	6.8
CR2	2 rear to AC	4.5	AS4	4 above ACPC	9	S4	4 of ACPC	9
CR3	3 rear to AC	6.7	AS3	3 above ACPC	6.8	S5	5 of ACPC	11.3
CR4	4 rear to AC	9	AS2	2 above ACPC	4.5	S6	6 of ACPC	13.5
CR5	5 rear to AC	11.2	AS1	1 above ACPC	2.3	S7	7 of ACPC	15.8
CR6-MI	6 rear to AC	13.5	A0-ACPC	0 of ACPC	0	S8	8 of ACPC	18
CR7	7 rear to AC	15.7	AI1	1 below ACPC	−2.3	S9	9 of ACPC	20.3
CR8	8 rear to AC	18	AI2	2 below ACPC	−4.5	S10	10 of ACPC	22.5
CR9	9 rear to AC	20.2	AI3	3 below ACPC	−6.8	S11	11 of ACPC	24.8
CR10	10 rear to AC	22.5	AI4	4 below ACPC	−9	S12	12 of ACPC	27
CR11	11 rear to AC	24.7	AI5	5 below ACPC	−11.3	S13	13 of ACPC	29.3
CR12-PC	12 rear to AC	27	AI6	6 below ACPC	−13.5	S14	14 of ACPC	31.5
CR13	13 rear to AC	29.2	AI7	7 below ACPC	−15.8			
CR14	14 rear to AC	31.4	AI8	8 below ACPC	−18			
CR15	15 rear to AC	33.7	AI9	9 below ACPC	−20.3			
CR16	16 rear to AC	35.9						

labeled ($n = 119$; **Supplementary Table**). Nineteen coronal, 18 axial, and 15 sagittal MRI plates were created ($n = 52$; **Table 1**). The acronyms were classified in alphabetic order by subregion. The 52 plates generated for this study can be found in the https://hal.archives-ouvertes.fr/ [hal-02116633].

DISCUSSION

The MDBA with 119 structures and 52 plates provides an extensive 3D MRI structural analysis of the human deep brain mainly for clinical applications, but also researchers interested in direct visual identification of neuroanatomical structures.

The simple principle of cartography from reconstructed slices of one anatomic specimen without destruction of tissue greatly facilitates the 3D structural analysis, which is also dramatically improved by high spatial resolution with infra millimetric voxels. Although the result of parcellation according to T1-weighted contrast harvested a lot of data, further approaches using others MRI contrast, such as inversion-recovery sequences, or multimodal imaging with DTI, should refine the information.

The large scale maps of MDBA with 250-μm side voxels is compatible with the recent human DTI data sets with isotropic voxels of 400 μm (41) up to 60 μm (42), as well as with high resolution probabilistic atlases (43, 44) and could help in the labeling process of the deep brain. Indeed the MDBA gives high level of structural details of white and gray matter structures substantially enhancing the current structural knowledge within this region. Although it can be used both at the individual level and in series, it is intrinsically a detailed data set of a unique specimen which must interpreted in this strict context as a topological descriptor of the deep brain architecture. Anyway this topological descriptor, could be the support of advanced probabilistic atlases enabling to integrate the variability, still not mastered, of the deep brain, through large cohorts of subjects.

Our approach has shown that it is feasible to identify the details of individual MRI anatomy. Whereas, the atlas-with proportional scales is still largely used for stereotactic targeting, nevertheless there must be kept in mind such unsolved issues as inhomogeneity of ontologies, weak cross-correspondences between atlases (45) and between set of slices within atlases questions (20). On the other hand it can be assumed that machine learning approaches (46) could significantly enhance these anatomical uncertainties, therefore dramatically change paradigms to solve these challenges. This is expected as the learning databases are rapidly becoming stronger. For instance the MDBA could be used in the work flow of learning methods including decision-based approaches whether supervised or not (47–49) to interpret the results. In the interim, the MDBA can assist significantly those who are willing to better master the deep brain architecture, which is particularly important for clinicians implanting devices in the deep brain. In this latter condition, practitioners can use the atlas like classical histological atlases from the proportional grid plates, and at the same time they can adjust or specify directly the targets from the MRI plates. Furthermore, the MDBA is of considerable value to study injured and deformed brains as indirect methods are unreliable due to the hampered landmarks in the injured brain (50). The MDBA also improves scientific knowledge of the deep brain structural aspect as revealed by current MRI. In this sense, it fuels the panoply of MRI-based brain atlases used for research and clinical purposes, notably in computer science (see e.g., https://en.wikibooks.org/wiki/SPM/Atlases). Furthermore, the MDBA creates a link to pioneering data (see **Supplementary Table**), which otherwise would remain into oblivion. Moreover, the MDBA serves as a new tool in the continuous effort of mastering the structural and functional anatomy of the human brain using either direct or indirect methods of cartography. Last but not least, it can also be used for teaching, learning and training purposes, taking advantage of current publicly available free website-based programs (https://www.openanatomy.org/).

DATA AVAILABILITY

One dataset generated for this study can be found in the [https://hal.archives-ouvertes.fr/] [hal-02116633].

AUTHOR CONTRIBUTIONS

J-JL designed and realized the MDBA and wrote the first draft of the manuscript. AD contributed substantially to the interpretation of anatomical data of the MDBA and wrote sections of the manuscript. GC, YE, RC, JC, and FD contributed substantially to the interpretation of anatomical data of the MDBA. NM and RK contributed to the conception the work and wrote sections of the manuscript. All authors contributed to manuscript revision, read and approved the submitted version.

FUNDING

NIH grants P41 EB015902, P41 EB015898, and U24 CA180918 to RK.

ACKNOWLEDGMENTS

We deeply thank all who contributed and aided during this long term work.

SUPPLEMENTARY MATERIAL

The Supplementary Material for this article can be found online at: https://www.frontiersin.org/articles/10.3389/fneur.2019.00851/full#supplementary-material

REFERENCES

1. Schaltenbrand G, Wahren W. *Atlas for Stereotaxy of the Human Brain*. Stuttgart, NY: Thieme (1977).
2. Talairach J, David M, Tournoux P, Corredor H, Kvasina. *Atlas D'anatomie Stéréotaxique*. Repérage Radiologique Indirect Des Noyaux Gris Centraux Des Régions Mésencéphalo-Sous-Optiques et Hypothalamiques de l'homme. Paris: Masson et Cie (1957).
3. Mai JK, Assheuer J, Paxinos G. *Atlas of the Human Brain*. London: Academic Press (1977).
4. Yelnik J, Bardinet E, Dormont D, Malandain G, Ourselin S, Tandé D., et al. A three-dimensional, histological and deformable atlas of the human basal ganglia. I. atlas construction based on immunohistochemical and MRI data. *NeuroImage*. (2007) 34:618–638. doi: 10.1016/j.neuroimage.2006.09.026
5. Guiot G, Derome P, Trigo JC. Intention tremor: the best indication for stereotaxic surgery. *La Presse Med*. (1967) 75:2513–8.

6. Benabid AL, Koudsie A, Benazzouz A, Le Bas JF, Pollak P. Imaging of subthalamic nucleus and ventralis intermedius of the thalamus. *Mov Disord.* (2002) 17 (Suppl 3):S123–9. doi: 10.1002/mds.10153
7. Bardinet E, Bhattacharjee M, Dormont D, Pidoux B, Malandain G, Schüpbach M., et al. A three-dimensional histological atlas of the human basal ganglia. II. atlas deformation strategy and evaluation in deep brain stimulation for Parkinson disease. *J Neurosurg.* (2009) 110:208–19. doi: 10.3171/2008.3.17469
8. Tuleasca C, Najdenovska E, Régis J, Witjas T, Girard N, Champoudry J., et al. Ventrolateral motor thalamus abnormal connectivity in essential tremor before and after thalamotomy: a resting-state functional magnetic resonance imaging study. *World Neurosurg.* (2018) 113:e453–64. doi: 10.1093/neuros/nyy303.210
9. Brunenberg EJ, Moeskops P, Backes WH, Pollo C, Cammoun L, Vilanova A., et al. Structural and resting state functional connectivity of the subthalamic nucleus: identification of motor STN parts and the hyperdirect pathway. *PLoS ONE.* (2012) 7:e39061. doi: 10.1371/journal.pone.0039061
10. Cho ZH, Min HK, Oh SH, Han JY, Park CW, Chi JG., et al. Direct visualization of deep brain stimulation targets in Parkinson Disease with the use of 7-tesla magnetic resonance imaging. *J Neurosurg.* (2010) 113:639–47. doi: 10.3171/2010.3.JNS091385
11. Cho ZH, Min HK, Oh SH, Han JY, Park CW, Chi JG., et al. Evaluating indirect subthalamic nucleus targeting with validated 3-tesla magnetic resonance imaging. *Stereotact Funct Neurosurg.* (2014) 92:337–45. doi: 10.1159/000366286
12. Lefranc M, Derrey S, Merle P, Tir M, Constans JM, Montpellier D., et al. High-resolution 3-dimensional T2*-weighted angiography (HR 3-D SWAN): an optimized 3-T magnetic resonance imaging sequence for targeting the subthalamic nucleus. *Neurosurgery*. (2014) 74:615–26. doi: 10.1227/NEU.0000000000000319
13. O'Gorman RL, Shmueli K, Ashkan K, Samuel M, Lythgoe DJ, Shahidiani A., et al. Optimal MRI methods for direct stereotactic targeting of the subthalamic nucleus and globus pallidus. *Eur. Radiol.* (2011) 21:130–6. doi: 10.1007/s00330-010-1885-5
14. Vertinsky AT, Coenen VA, Lang DJ, Kolind S, Honey CR, Li D., et al. Localization of the subthalamic nucleus: optimization with susceptibility-weighted phase MR imaging. *Am J Neuroradiol.* (2009) 30:1717–24. doi: 10.3174/ajnr.A1669
15. Xiao Y, Jannin P, D'Albis T, Guizard N, Haegelen C, Lalys F., et al. Investigation of morphometric variability of subthalamic nucleus, red nucleus, and substantia nigra in advanced Parkinson's disease patients using automatic segmentation and PCA-based analysis. *Hum Brain Mapp.* (2014) 35:4330–44. doi: 10.1002/hbm.22478
16. Lemaire JJ, Durif F, Boire JY, Debilly B, Irthum B, Chazal J. Direct stereotactic MRI location in the globus pallidus for chronic stimulation in Parkinson's disease. *Acta Neurochirurgica*. (1999) 141:759–65. doi: 10.1007/s007010050372
17. Zerroug A, Gabrillargues J, Coll G, Vassal F, Jean B, Chabert E., et al. Personalized mapping of the deep brain with a white matter attenuated inversion recovery (WAIR) sequence at 1.5-Tesla: experience based on a series of 156 patients. *Neuro-Chirurgie*. (2016) 62:183–9. doi: 10.1016/j.neuchi.2016.01.009
18. Lemaire J-J, Caire F, Bonny J-M, Kemeny J-L, Villéger A, Chazal J. Contribution of 4.7-tesla MRI in the analysis of MRI anatomy of the human subthalamic area. *Acta Neurochirurgica*. (2004) 146 (Suppl): 906–7.
19. Lemaire JJ, Sakka L, Ouchchane L, Caire F, Gabrillargues J, Bonny JM. Anatomy of the human thalamus based on spontaneous contrast and microscopic voxels in high-field magnetic resonance imaging. *Neurosurgery*. (2010) 66 (3 Suppl Operative):161–72. doi: 10.1227/01.NEU.0000365617.41061.A3
20. Lemaire JJ, Coste J, Ouchchane L, Caire F, Nuti C, Derost P., et al. Brain mapping in stereotactic surgery: a brief overview from the probabilistic targeting to the patient-based anatomic mapping. *NeuroImage.* (2007) 37:S109–15. doi: 10.1016/j.neuroimage.2007.05.055
21. Lemaire JJ, Nezzar H, Sakka L, Boirie Y, Fontaine D, Coste A., et al. Maps of the adult human hypothalamus. *Surg Neurol Int.* (2013) 4 (Suppl 3):S156–63. doi: 10.4103/2152-7806.110667
22. Fontaine D, Deudon A, Lemaire JJ, Razzouk M, Viau P, Darcourt J., et al. Symptomatic treatment of memory decline in alzheimer's disease by deep brain stimulation: a feasibility study. *J Alzheimer's Dis.* (2013) 34:315–23. doi: 10.3233/JAD-121579
23. Batisse-Lignier M, Rieu I, Guillet C, Pujos E, Morio B, Lemaire JJ., et al. Deep brain stimulation of the subthalamic nucleus regulates postabsorptive glucose metabolism in patients with Parkinson's disease. *J Clin Endocrinol Metabol.* (2013) 98:E1050–4. doi: 10.1210/jc.2012-3838
24. Ulla M, Thobois S, Lemaire JJ, Schmitt A, Derost P, Broussolle E, et al. Manic behaviour induced by deep-brain stimulation in Parkinson's disease: evidence of substantia nigra implication? *J Neurol Neurosurg Psychiatry*. (2006) 77:1363–66. doi: 10.1136/jnnp.2006.096628
25. Lemaire JJ, Frew AJ, McArthur D, Gorgulho AA, Alger JR, Salomon N., et al. White matter connectivity of human hypothalamus. *Brain Res.* (2011) 1371 :43–64. doi: 10.1016/j.brainres.2010.11.072
26. Dejerine J. *Anatomie Des Centres Nerveux (Tomes 1 and 2* Paris: Rueff et Cie (1901)
27. Duvernoy HM, Cabanis EA, Iba-Zizen MT, Tamraz J, Guyot J. *Le Cerveau Humain: Surfaces, Coupes Sériées Tridimentionelles et IRM*. Paris: Springer-Verlag (1992).
28. Guillain G, Ivan B. *Anatomie Topographique Du Système Nerveux Central*. Paris: Masson et Cie (1926).
29. Haymaker W, Anderson, Nauta WJH. *The Hypothalamus*. *Thomas Books*. Springfield, IL: Charles C. Thomas (1969).
30. Laget P. *Elements de Neuro-Anatomie Fonctionnelle*. Paris: Masson (1973).
31. Morel A, Magnin M, Jeanmonod D. Multiarchitectonic and stereotactic atlas of the human thalamus. *J Comparat Neurol.* (1997) 387:588–630.3
32. Morel A, Magnin M, Jeanmonod D. *Duvernoy's Atlas of the Human Brain Stem and Cerebellum*. Austria: Springer Wien NewYork (2009)
33. Nieuwenhuys R, Voogd J, Huijzen C. *The Human Central Nervous System*. Berlin, Heidelberg, NY: Springer-Verlag (2008).
34. Olszewski J, Baxter D. *Cytoarchitecture of the Brain Stem*. Basel: Karger (1954).
35. Parent A. *Carpenter's Human Neuroanatomy*. Baltimore: Williams & Wilkins (1996).
36. Riley HA. *An Atlas of the Basal Ganglia, Brain Stem and Spinal Cord*. Baltimore: Williams & Wilkins (1953).
37. Toni R, Malaguti A, Benfenati F, Martini L. The human hypothalamus: a morpho-functional perspective. *J Endocrinol Invest.* (2004) 27 (6 Suppl):73–94.
38. *Terminologia Anatomica TA*. (1998). Available online at: https://www.unifr.ch/ifaa/Public/EntryPage/ViewTAOnLine.html (accessed January 29, 2019)
39. *BrainInfo*. (2019). Available online at: http://braininfo.rprc.washington.edu/ (accessed January 29, 2019)
40. Ten Donkelaar HJ, Broman J, Neumann PE, Puelles L, Riva A, Tubbs RS., et al.FIPAT. *Terminologia Neuroanatomica*. FIPAT.library.dal.ca. (2017). Available online at: http://fipat.library.dal.ca/wp-content/uploads/2017/02/FIPAT-TNA-Ch1.pdf (accessed August 16, 2019)
41. Roebroeck A, Miller KL, Aggarwal M. *Ex vivo* diffusion MRI of the human brain: technical challenges and recent advances. *NMR Biomed.* (2019) 32:e3941. doi: 10.1002/nbm.3941
42. Sengupta S, Fritz FJ, Harms RL, Hildebrand S, Tse DHY, Poser BA., et al. High resolution anatomical and quantitative MRI of the entire human occipital lobe *ex vivo* at 9.4 T. *NeuroImage.* (2018) 168:162–71. doi: 10.1016/j.neuroimage.2017.03.039
43. Najdenovska E, Alemán-Gómez Y, Battistella G, Descoteaux M, Hagmann P, Jacquemont S., et al. *In-vivo* probabilistic atlas of human thalamic nuclei based on diffusion- weighted magnetic resonance imaging. *Sci. Data.* (2018) 5:180270. doi: 10.1038/sdata.2018.270
44. Pauli WM, Nili AN, Tyszka JM. A high-resolution probabilistic in vivo atlas of human subcortical brain nuclei. *Sci Data.* (2018) 5:180063. doi: 10.1038/sdata.2018.63
45. Mai JK, Majtanik M. Toward a common terminology for the thalamus. *Front Neuroanat.* (2018) 12:114. doi: 10.3389/fnana.2018.00114

46. Akkus Z, Galimzianova A, Hoogi A, Rubin DL, Erickson BJ. Deep learning for brain MRI segmentation: state of the art and future directions. *J Digit Imag.* (2017) 30:449–59. doi: 10.1007/s10278-017-9983-4
47. Suk HI, Lee SW, Shen D. Hierarchical feature representation and multimodal fusion with deep learning for AD/MCI diagnosis. *NeuroImage.* (2014) 101:569–582. doi: 10.1016/j.neuroimage.2014.06.077
48. Liu M, Zhang D, Shen D. Hierarchical fusion of features and classifier decisions for Alzheimer's disease diagnosis. *Hum Brain Mapp.* (2014) 35:1305–1319. doi: 10.1002/hbm.22254
49. Amoroso N, La Rocca M, Bruno S, Maggipinto T, Monaco A, Bellotti R., et al. Multiplex networks for early diagnosis of Alzheimer's disease. *Front. Aging Neurosci.* (2018) 10:365 doi: 10.3389/fnagi.2018.00365
50. Lemaire JJ, Sontheimer A, Pereira B, Coste J, Rosenberg S, Sarret C., et al. Deep brain stimulation in five patients with severe disorders of consciousness. *Ann Clin Transl Neurol.* (2018) 5:1372–84. doi: 10.1002/acn3.648

Conflict of Interest Statement: The authors declare that the research was conducted in the absence of any commercial or financial relationships that could be construed as a potential conflict of interest.

frontiers in Neurology

ORIGINAL RESEARCH
published: 18 October 2019
doi: 10.3389/fneur.2019.01082

Characterization of Contrast-Enhancing and Non-contrast-enhancing Multiple Sclerosis Lesions Using Susceptibility-Weighted Imaging

Philipp Eisele[1], Katja Fischer[2], Kristina Szabo[1], Michael Platten[1] and Achim Gass[1]*

[1] *Department of Neurology, Universitätsmedizin Mannheim, University of Heidelberg, Mannheim, Germany,* [2] *Department of Neurology, Klinikum der Stadt Ludwigshafen, Ludwigshafen, Germany*

Susceptibility-weighted magnetic resonance imaging (MRI) (SWI) offers additional information on conventional MRI contrasts. Central veins can be identified within lesions, and recently, it has been suggested that multiple sclerosis (MS) lesions with slowly expanding demyelination, so-called smoldering lesions, can be identified by a phase rim surrounding the lesion. We analyzed post-contrast SWI in regard to intrinsic lesion characteristics in a cohort of MS patients. A total of 294 MS patients were evaluated using a 3-T MRI. A comprehensive MRI protocol was used including post-contrast SWI. Lesions of at least 5 mm in size were analyzed on conventional MRI and SWI with a structured reporting scheme with a focus on SWI lesion characteristics. A total of 1,323 lesions were analyzed: 1,246/1,323 (94%) were non-enhancing and 77/1,323 (6%) were contrast-enhancing (CE) lesions. In CE lesions, the following patterns were seen: contrast enhancement was nodular in 34/77, ring-shaped enhancement was present in 33/77, and areas of peripheral enhancement were present in 10/77. In CE lesions, an association with central veins was found in 38/77 (50%). In 75/1,246 (6%) non-enhancing lesions, a central dark dot in keeping with a central vein was seen, whereas 162/1,246 (13%) showed peripheral hypointense dots/rims, 199/1,246 (16%) showed scattered hypointense dots mainly within the lesion area, and in 374/1,246 (30%), no SWI hypointensity was detected. Furthermore, 436/1,246 (35%) lesions showed isointensity to the surrounding tissue and were not visible on SWI. SWI is able to offer additional aspects of MS pathology also when used after the application of a contrast agent. Veins connected to lesions, a potentially useful marker in the differential diagnosis of MS, were seen in about 50% of enhancing lesions. Susceptibility artifacts, suggested to mark the presence of myelin-laden macrophages and smoldering inflammation, were visible in 28% of lesions as hypointense dots in and in the periphery of the lesion. Given those results, SWI may provide practical useful additional information in the evaluation of the lesion status in MS patients.

Keywords: multiple sclerosis, lesions, MRI, susceptibility-weighted imaging, central vein

OPEN ACCESS

Edited by:
Jan Kassubek,
University of Ulm, Germany

Reviewed by:
Yulin Ge,
New York University, United States
Ronald Peeters,
University Hospitals Leuven, Belgium

***Correspondence:**
Achim Gass
achim.gass@medma.uni-heidelberg.de

Specialty section:
This article was submitted to Applied Neuroimaging, a section of the journal Frontiers in Neurology

Received: *22 June 2019*
Accepted: *25 September 2019*
Published: *18 October 2019*

Citation:
Eisele P, Fischer K, Szabo K, Platten M and Gass A (2019) Characterization of Contrast-Enhancing and Non-contrast-enhancing Multiple Sclerosis Lesions Using Susceptibility-Weighted Imaging. Front. Neurol. 10:1082. doi: 10.3389/fneur.2019.01082

INTRODUCTION

Conventional magnetic resonance imaging (MRI) techniques play an important role in the diagnosis and monitoring of disease evolution in multiple sclerosis (MS). Review of MS lesion characteristics can provide insight into the acute and chronic pathology. Hyperintense lesions on T2-weighted (T2-w) images are thought to represent a heterogeneous pathology such as edema, gliosis, axonal loss, and demyelination (1). New T2 lesions on follow-up MRI are commonly employed in the search for a recent inflammatory disease activity. In addition, the presence of contrast enhancement on post-contrast T1-weighted (T1w) images and occasionally hyperintensity on diffusion weighted MRI can also indicate acute inflammatory changes (2–5). Recently, susceptibility-weighted imaging (SWI), a velocity-compensated three-dimensional gradient echo sequence (6), has been shown to be sensitive to iron on the form of ferritin, hemosiderin, and deoxyhemoglobin (7). It is sensitive to iron accumulation in the normal-appearing brain tissue, in lesions, and in the vessel walls of veins in MS (8). Iron is supposed to cause damage to oligodendroctyes and myelin by oxidative stress in the form of free radicals (9). Furthermore, areas of active myelin breakdown also show susceptibility effects in the form of dark dots or rims (10–12). The susceptibility effects in those lesions are due to the presence of iron-laden activated microglia/macrophages and reactive astrocytes at the lesion edge (6, 8–11, 13). These lesions have been suggested to represent areas of so-called smoldering inflammation (10, 11, 13). Furthermore, it has been demonstrated that these lesions may increase in size during longer observation periods. Such gradual slowly evolving increases in lesion size can also be identified when analyzing serial T1w MRI as it has recently been demonstrated (14). This type of lesion has also generated high clinical interest, as it is conceivable that it contributes to gradual clinical worsening in MS.

Commonly, SWI is acquired before contrast agent injection, and only a few studies evaluated contrast-enhancing (CE) lesions on SWI after contrast application (15, 16). We investigated characteristics of active CE and non-enhancing lesions detected on contrast-enhanced SWI.

MATERIALS AND METHODS

Subjects

We performed a retrospective, cohort analysis of MRI in MS patients in our MS database over a 3-year interval. Inclusion criteria were diagnosis of MS according to the McDonald diagnostic criteria (17) and being at least 18 years of age. Exclusion criteria were presence of neurological conditions other than MS, cardiovascular or respiratory disease, contraindication to MRI, and pregnancy or breastfeeding.

MRI Studies

All MRI studies were performed on a 3.0-T MR system [MAGNETOM Skyra, Siemens, Erlangen, Germany, 20-channel head coil, 50-cm field of view [FOV]]. A standardized protocol was used in all patients: (1) axial, coronal, and sagittal localizing sequences followed by axial oblique contiguous 5-mm slices aligned with the inferior borders of the corpus callosum; (2) T2-w images (TR 4,000 ms/TE 78 ms, FOV 220 mm, slice thickness 3 mm, voxel size 0.4 × 0.4 × 3.0 mm); (3) fluid-attenuated inversion recovery (FLAIR) images (TI 2,500 ms/TR 8,500 ms/TE 136 ms, FOV 220 mm, slice thickness 3 mm, voxel size 0.4 × 0.4 × 3.0 mm); (4) T1w images (TR 225 ms/TE 2.5 ms, FOV 220 mm, slice thickness 3 mm, voxel size 0.7 × 0.7 × 3.0 mm); (5) T2*-w images (TR 594 ms/TE 19.9 ms, FOV 220 mm, slice thickness 3 mm, voxel size 0.4 × 0.4 × 3.0 mm); and (6) identical to (4) T1w images 10 min after manual injection of single-dose contrast agent of 0.1 mmol/kg body weight (Dotarem, Guerbet) followed by (7) susceptibility-weighted imaging (TR 27 ms, TE 20 ms, FOV 220 mm, slice thickness 1.50 mm, voxel-size 0.9 × 0.9 × 1.5 mm). SWI and mini-IP images were generated automatically by the scanner software provided by the manufacturer.

To exclude a possible influence of the contrast agent on diagnostic image quality, vascular enhancement, and parenchymal signal alterations in 10 patients were additionally examined with SWI before and after contrast agent injection.

Data Processing and Analysis

Image interpretation was performed on a standard picture archiving and communication system workstation. Two readers experienced in the diagnostic and clinical reading of MS studies examined MR images jointly. Readers were unaware of clinical data and patient identification information. A structured reporting scheme was used. For lesion identification, FLAIR images were used as the "gold standard." Only brain lesions with a diameter >5 mm on axial slices entered further analysis.

With the use of post-contrast T1w images, lesions were classified as CE lesions (group 1) or non-enhancing lesions (group 2), according to previously published criteria (18). All lesions were further classified on T1w images as T1 hypointense (19) or T1 isointense. In a second step after lesion identification on conventional MR images, SW images were analyzed for the corresponding lesion characteristics. As CE is seen also on SW images, CE lesions in group 1 were categorized as follows: (1) ring-shaped CE lesions, (2) lesions with partial peripheral contrast enhancement, or (3) nodular homogenous contrast enhancement. All lesions of group 1 (CE lesions) and group 2 (non-enhancing lesions) were categorized in regard to hypointense features potentially visible on SW images: (i) lesions with central veins, (ii) lesions with peripheral hypointense dots/rims, (iii) lesions with scattered hypointense dots within the lesion, and (iv) isointense lesions not seen on SWI. These categories were employed similar to previously suggested lesion characteristics (10, 11, 13).

Standard Protocol Approval

This study was approved by the local institutional review board and performed in accordance with the ethical standards laid down in the 1964 Declaration of Helsinki and its later amendments. Patient consent was waived owing to the retrospective nature of the study and the lack of patient interaction.

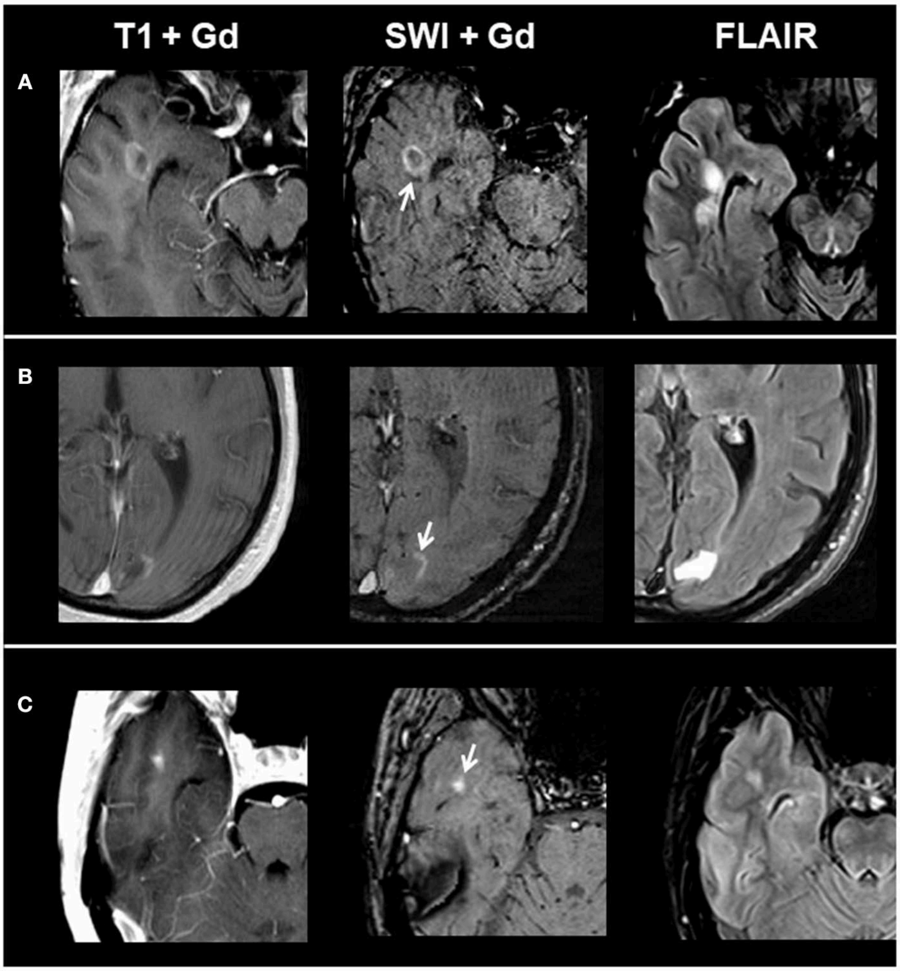

FIGURE 1 | From left to right: representative post-contrast T1, post-contrast SWI, and FLAIR images of acute contrast-enhancing lesion subtypes. **(A)** Ring-shaped contrast enhancement, **(B)** peripheral contrast enhancement, and **(C)** homogenous contrast enhancement. SWI, susceptibility-weighted magnetic resonance imaging; FLAIR, fluid-attenuated inversion recovery.

RESULTS

A total of 294 patients [226 women and 68 men; mean age 36 years (range 18–69 years)] were included in the study. Two hundred seventy-nine patients had relapsing–remitting MS, and 15 patients had secondary progressive MS. The median Expanded Disability Status Scale (EDSS) was 2.0 (range 0–7). Two hundred twenty-four patients were on best individually selected treatment with interferon-beta, glatiramer acetate, dimethyl fumarate, fingolimod, or natalizumab. Seventy-six patients had an acute relapse at the time of MRI. Forty-four patients showed CE lesions on post-contrast T1w images.

Overall, we identified 1,323 lesions on conventional MRI: 77 CE lesions (group 1) and 1,246 non-enhancing lesions (group 2) (915 T1 hypointense lesions and 331 T1 isointense lesions). On T1 and SWI, 33/77 CE lesions presented with ring-shaped contrast enhancement, 10/77 with peripheral contrast enhancement, and 34/77 with homogenous contrast enhancement. When comparing post-contrast T1w and susceptibility-weighted images in respect to contrast enhancement, we found matching enhancement characteristics in all lesions. **Figure 1** shows exemplary images of acute lesion

TABLE 1 | MRI characteristics of contrast-enhancing lesions.

	SWI lesions	Lesions associated with veins on SWI	T1 hypointense lesions
Ring-shaped enhancing lesions on SWI	33	20 (60%)	33 (100%)
Peripheral enhancing lesions on SWI	10	4 (40%)	9 (90%)
Homogenous enhancing lesions on SWI	34	14 (40%)	34 (100%)
Total	77	38 (50%)	76 (98%)

SWI, susceptibility-weighted magnetic resonance imaging.

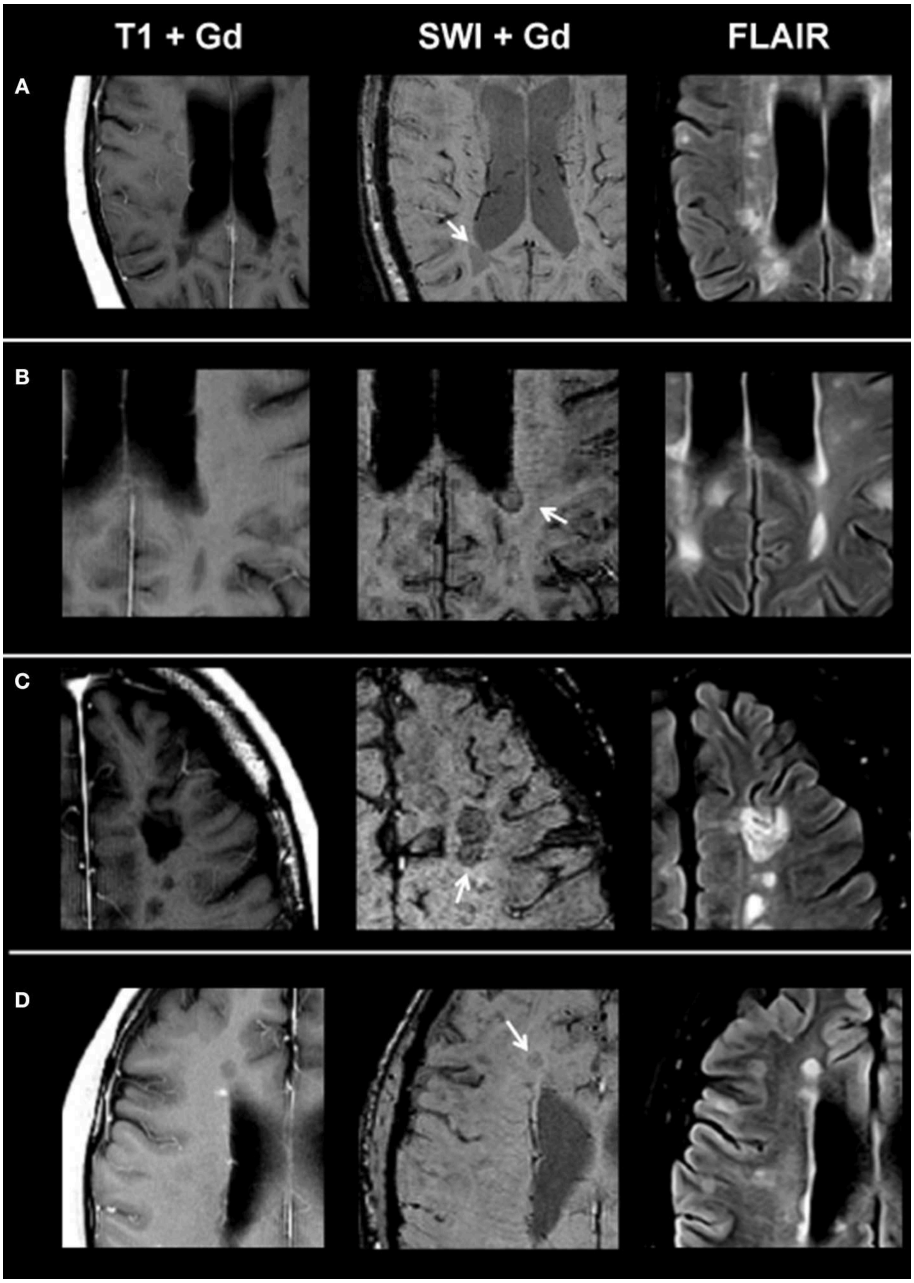

FIGURE 2 | From left to right: representative post-contrast T1, post-contrast SWI, and FLAIR images of non-enhancing lesion subtypes. **(A)** Homogenously hypointense lesion, **(B)** ring-shaped distribution of susceptibility dots, **(C)** scattered distribution of susceptibility dots, and **(D)** lesion with a central dark region. SWI, susceptibility-weighted magnetic resonance imaging; FLAIR, fluid-attenuated inversion recovery.

subtypes identified on SWI, and **Table 1** provides an overview on signal characteristics of CE lesions.

On SWI, lesions in the non-enhancing lesion group 2 showed the following phenotypes: 374/1,246 lesions were homogenously hypointense without dark susceptibility dots, 162/1,246 showed ring-shaped distribution of susceptibility dots, 199/1,246 showed scattered distribution of susceptibility dots, 75/1,246 showed a central dot suggestive of a central vein, and 436/1,246 were not visible on SWI. **Figure 2** demonstrates exemplary images of chronic lesion subtypes identified on SWI, and **Table 2** provides an overview on signal characteristics.

In the subgroup of the 10 patients examined with SWI before and after contrast agent injection, we identified 35 non-enhancing lesions: 6/35 lesions were homogenously hypointense without dark susceptibility dots, 7/35 showed ring-shaped distribution of susceptibility dots, 5/35 showed scattered distribution of susceptibility dots, 2/35 showed a central dot suggestive of a central vein, and 15/35 were not visible on

TABLE 2 | MRI characteristics of non-contrast-enhancing lesions.

	SWI lesions	Lesions associated with veins on SWI	T1 hypointense lesions
Homogenous hypointense lesions	374	172 (46%)	307 (82%)
Ring-shaped distribution of susceptibility dots	162	82 (51%)	138 (85%)
Scattered distribution of susceptibility dots	199	86 (43%)	145 (73%)
Lesions with a central dark region in SWI	75	26 (35%)	46 (61%)
Lesions not visible in SWI	436	–	279 (64%)
Total	1,246	366 (29%)	915 (73%)

SWI, susceptibility-weighted magnetic resonance imaging.

SWI. When comparing pre-contrast and post-contrast SWI, the contrast agent facilitated the visibility of small veins already seen in pre-contrast images but had no influence on the total number of veins detectable or diagnostic image quality and parenchymal signal alterations. **Figure 3** demonstrates an example of an MS patient presenting a non-enhancing T1 hypointense lesion on pre-contrast and post-contrast SWI. In this subgroup, no CE lesions were present.

DISCUSSION

SWI is a relatively new MRI technique that has shown promise to provide additional information to established MRI methods in the diagnostic workup and monitoring of MS patients. We limited the analysis of SWI characteristics to lesions of at least 5 mm in diameter in order to be able to differentiate intrinsic lesion characteristics. As a consequence, the results obtained in this study may not or only partly apply to smaller lesions. The results of this study bring out several interesting points.

SWI can demonstrate features of lesions otherwise not visible. Central dots in keeping with central veins can be readily identified, which can help to confirm a typical MS feature as it has been described pathologically. This feature may have value for the differential diagnosis of MS and is currently being evaluated in regard to its potential to facilitate an early diagnosis (20). CE lesions represent a key feature in MS and are thought to demonstrate blood–brain-barrier permeability changes often facilitating the fulfillment of dissemination in time in the diagnosis of MS or demonstrating an ongoing disease activity despite immune treatment. To date, few studies have performed SWI after contrast application. A standard dose of gadolinium (0.1 mmol/kg) appears to provide optimal image quality for clinical application of contrast-enhanced SWI (15). An earlier study applied SWI before and after contrast agent injection in 31 healthy subjects. They found no signal contamination or quality degradation on SWI after application of a contrast agent (16). Other studies have demonstrated an increased detection of small veins in brain neoplasms (21) and MS (22–24). In our study, investigation of SWI after contrast injection facilitated the visibility of small veins already seen in pre-contrast SWI but had no influence on the total number of veins detectable in this subgroup of patients. We found in the CE lesion group that 50% of lesions are associated veins. This underlines one of the characteristics of MS lesions, and when considered together, a combination of (i) the location of a lesion, (ii) contrast enhancement, and (iii) a typical associated vein may have the potential to become highly informative and specific elements in the diagnosis of MS lesions. In this regard, CE SWI contains potentially valuable information for the characterization of focal MS pathology.

Furthermore, there has been recent interest in signs of smoldering active inflammation/presence of macrophages and demyelination, as this might be a pathological element that could contribute to slowly evolving clinical change (7, 25) that can be seen and may be of interest.

Using SWI, Haacke et al. detected different phenotypes of SWI phenomena in MS (10). This included lesions with scattered susceptibility hypointensities and lesions surrounded by a rim of hypointense signal suggestive of a ring-like shape of elevated iron levels. Our results are in line with those findings. From a histopathological point of view, lesions with a hypointense ring seem to indicate the presence of myelin-laden macrophages that may also participate in continuing smoldering inflammation (12). Current studies highlight the concept of "slowly expanding lesions" that may be best detectable on T1w MRI (12, 26). These lesions maintain some degree of inflammatory and myelin breakdown at the lesion edge after the demyelinating event (12). Various studies have demonstrated that iron accumulates within macrophages and microglia at the edges of these lesions, forming rims (8, 27). Using 7-T post-mortem MRI, a current study investigated iron accumulation at the edge of MS lesions. The authors demonstrated that a hypointense rim detected on SWI correlated histologically with iron accumulation in macrophages and microglia expressing the pro-inflammatory markers CD86 and p22phox at the edge of slowly expanding lesions, whereas non-rim lesions showed a tendency to shrink over time (12). The authors concluded that the presence of iron rims on SWI MRI might be a sign of progressive tissue injury and might serve as a marker of a disease activity in MS patients (12). We detected in 29% of lesions larger than 5-mm indications of smoldering inflammatory pathology in the form of scattered or peripheral susceptibility hypointensities. This number is larger than the absolute number of CE lesions in this study, which may indicate that the presence of this pathological change persists for a longer duration than the duration of contrast enhancement. This would be in line with the observation made in a follow-up study (12). To date, no comparative studies to other pathologies are available, and it is possible that hypointense rim lesions are specific for MS and not seen in other pathologies. This could be addressed in future studies.

One limitation of our study is the cross-sectional nature of the analysis and observations. We are aware that although no serial MRI data were available, this is certainly a limitation when trying to obtain information on dynamic phenomena of lesion evolution.

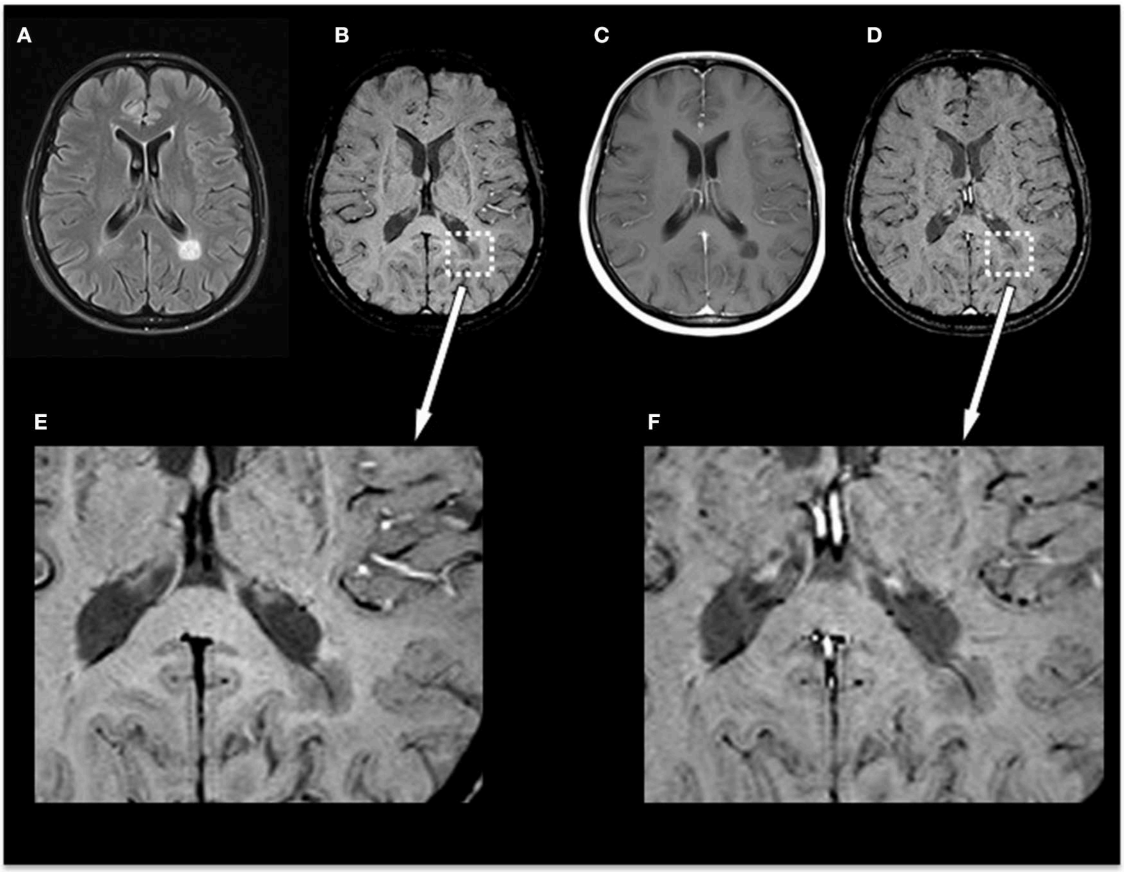

FIGURE 3 | Exemplary MRI of a 44-year-old woman presenting with relapsing–remitting MS. **(A)** T2-FLAIR, **(B)** pre-contrast SWI and magnification **(E)**, **(C)** post-contrast T1-weighted (T1w), and **(D)** post-contrast SWI and magnification **(F)**. Conventional MRI demonstrates a chronic T1-hypointense lesion ("black hole") that appears homogenously hypointense on SWI. Post-contrast SWI **(D)** and magnification **(F)** facilitated the visibility of the penetrating vein already seen in pre-contrast images but had no influence on the total number of veins detectable or diagnostic image quality and parenchymal signal alterations. MS, multiple sclerosis; FLAIR, fluid-attenuated inversion recovery; SWI, susceptibility-weighted magnetic resonance imaging.

Our data add to the growing database of SWI in MS and point to a potential, useful additional information when integrating the information from CE and SWI MRI.

DATA AVAILABILITY STATEMENT

Anonymized data will be made available on request to researchers who meet the criteria for access to confidential data.

ETHICS STATEMENT

The studies involving human participants were reviewed and approved by University Medicine Mannheim Ethics Committee. Patient consent was waived owing to the retrospective nature of the study and the lack of patient interaction.

AUTHOR CONTRIBUTIONS

PE and AG: conceptualization of the study, acquisition, analysis, interpretation of the data, drafting, and revising the manuscript. KP, KS, and MP: analysis and interpretation of the data and revising the manuscript.

ACKNOWLEDGMENTS

We thank Petra Stoiber for technical assistance.

REFERENCES

1. MacKay A, Laule C, Vavasour I, Bjarnason T, Kolind S, Madler B. Insights into brain microstructure from the T2 distribution. *Magn Reson Imaging.* (2006) 24:515–25. doi: 10.1016/j.mri.2005.12.037
2. Kermode AG, Tofts PS, Thompson AJ, MacManus DG, Rudge P, Kendall BE, et al. Heterogeneity of blood-brain barrier changes in multiple sclerosis: an MRI study with gadolinium-DTPA enhancement. *Neurology.* (1990) 40:229–35. doi: 10.1212/WNL.40.2.229
3. Fazekas F, Soelberg-Sorensen P, Comi G, Filippi M. MRI to monitor treatment efficacy in multiple sclerosis. *J Neuroimaging.*

(2007) 17(Suppl 1):50S−5S. doi: 10.1111/j.1552-6569.2007.00138.x

4. Eisele P, Szabo K, Griebe M, Rossmanith C, Forster A, Hennerici M, et al. Reduced diffusion in a subset of acute MS lesions: a serial multiparametric MRI study. *AJNR Am J Neuroradiol.* (2012) 33:1369–73. doi: 10.3174/ajnr.A2975
5. Eisele P, Konstandin S, Szabo K, Ebert A, Rossmanith C, Paschke N, et al. Temporal evolution of acute multiple sclerosis lesions on serial sodium [(23)Na] MRI. *Mult Scler Relat Disord.* (2019) 29:48–54. doi: 10.1016/j.msard.2019.01.027
6. Haacke EM, Mittal S, Wu Z, Neelavalli J, Cheng YC. Susceptibility-weighted imaging: technical aspects and clinical applications, part 1. *AJNR Am J Neuroradiol.* (2009) 30:19–30. doi: 10.3174/ajnr.A1400
7. Haacke EM, Xu Y, Cheng YC, Reichenbach JR. Susceptibility weighted imaging (SWI). *Magn Reson Med.* (2004) 52:612–8. doi: 10.1002/mrm.20198
8. Bagnato F, Hametner S, Yao B, van Gelderen P, Merkle H, Cantor FK, et al. Tracking iron in multiple sclerosis: a combined imaging and histopathological study at 7 Tesla. *Brain.* (2011). 134(Pt 12):3602–15. doi: 10.1093/brain/awr278
9. Schenck JF, Zimmerman EA. High-field magnetic resonance imaging of brain iron: birth of a biomarker? *NMR Biomed.* (2004) 17:433–45. doi: 10.1002/nbm.922
10. Haacke EM, Makki M, Ge Y, Maheshwari M, Sehgal V, Hu J, et al. Characterizing iron deposition in multiple sclerosis lesions using susceptibility weighted imaging. *J Magn Reson Imaging.* (2009) 29:537–44. doi: 10.1002/jmri.21676
11. Grabner G, Dal-Bianco A, Schernthaner M, Vass K, Lassmann H, Trattnig S. Analysis of multiple sclerosis lesions using a fusion of 3.0 T FLAIR and 7.0 T SWI phase: FLAIR SWI. *J Magn Reson Imaging.* (2011) 33:543–9. doi: 10.1002/jmri.22452
12. Dal-Bianco A, Grabner G, Kronnerwetter C, Weber M, Hoftberger R, Berger T, et al. Slow expansion of multiple sclerosis iron rim lesions: pathology and 7 T magnetic resonance imaging. *Acta Neuropathol.* (2017) 133:25–42. doi: 10.1007/s00401-016-1636-z
13. Hagemeier J, Heininen-Brown M, Poloni GU, Bergsland N, Magnano CR, Durfee J, et al. Iron deposition in multiple sclerosis lesions measured by susceptibility-weighted imaging filtered phase: a case control study. *J Magn Reson Imaging.* (2012) 36:73–83. doi: 10.1002/jmri.23603
14. Fox J, Kraemer M, Schormann T, Dabringhaus A, Hirsch J, Eisele P, et al. Individual assessment of brain tissue changes in MS and the effect of focal lesions on short-term focal atrophy development in MS: a voxel-guided morphometry study. *Int J Mol Sci.* (2016) 17:489. doi: 10.3390/ijms17040489
15. Noebauer-Huhmann IM, Pinker K, Barth M, Mlynarik V, Ba-Ssalamah A, Saringer WF, et al. Contrast-enhanced, high-resolution, susceptibility-weighted magnetic resonance imaging of the brain: dose-dependent optimization at 3 tesla and 1.5 tesla in healthy volunteers. *Invest Radiol.* (2006) 41:249–55. doi: 10.1097/01.rli.0000188360.24222.5e
16. El-Koussy M, Schenk P, Kiefer C, Osman OM, Mordasini P, Ozdoba C, et al. Susceptibility-weighted imaging of the brain: does gadolinium administration matter? *Eur J Radiol.* (2012) 81:272–6. doi: 10.1016/j.ejrad.2010.12.021
17. Polman CH, Reingold SC, Banwell B, Clanet M, Cohen JA, Filippi M, et al. Diagnostic criteria for multiple sclerosis: 2010 revisions to the McDonald criteria. *Ann Neurol.* (2011) 69:292–302. doi: 10.1002/ana.22366
18. Barkhof F, Filippi M, van Waesberghe JH, Molyneux P, Rovaris M, Lycklama a Nijeholt G, et al. Improving interobserver variation in reporting gadolinium-enhanced MRI lesions in multiple sclerosis. *Neurology.* (1997) 49:1682–8. doi: 10.1212/WNL.49.6.1682
19. van Waesberghe JH, Kamphorst W, De Groot CJ, van Walderveen MA, Castelijns JA, Ravid R, et al. Axonal loss in multiple sclerosis lesions: magnetic resonance imaging insights into substrates of disability. *Ann Neurol.* (1999) 46:747–54. doi: 10.1002/1531-8249(199911)46:5<747::AID-ANA10>3.0.CO;2-4
20. Cortese R, Magnollay L, Tur C, Abdel-Aziz K, Jacob A, De Angelis F, et al. Value of the central vein sign at 3T to differentiate MS from seropositive NMOSD. *Neurology.* (2018) 90:e1183–90. doi: 10.1212/WNL.0000000000005256
21. Hori M, Ishigame K, Kabasawa H, Kumagai H, Ikenaga S, Shiraga N, et al. Precontrast and postcontrast susceptibility-weighted imaging in the assessment of intracranial brain neoplasms at 1.5 T. *Jpn J Radiol.* (2010) 28:299–304. doi: 10.1007/s11604-010-0427-z
22. Tan IL, van Schijndel RA, Pouwels PJ, van Walderveen MA, Reichenbach JR, Manoliu RA, et al. MR venography of multiple sclerosis. *AJNR Am J Neuroradiol.* (2000) 21:1039–42.
23. Sati P, Thomasson DM, Li N, Pham DL, Biassou NM, Reich DS, et al. Rapid, high-resolution, whole-brain, susceptibility-based MRI of multiple sclerosis. *Mult Scler.* (2014) 20:1464–70. doi: 10.1177/1352458514525868
24. Maggi P, Mazzoni LN, Moretti M, Grammatico M, Chiti S, Massacesi L. SWI enhances vein detection using gadolinium in multiple sclerosis. *Acta Radiol Open.* (2015) 4:2047981614560938. doi: 10.1177/2047981614560938
25. Filippi M, Rocca MA, De Stefano N, Enzinger C, Fisher E, Horsfield MA, et al. Magnetic resonance techniques in multiple sclerosis: the present and the future. *Arch Neurol.* (2011) 68:1514–20. doi: 10.1001/archneurol.2011.914
26. Prineas JW, Kwon EE, Cho ES, Sharer LR, Barnett MH, Oleszak EL, et al. Immunopathology of secondary-progressive multiple sclerosis. *Ann Neurol.* (2001) 50:646–57. doi: 10.1002/ana.1255
27. Frischer JM, Weigand SD, Guo Y, Kale N, Parisi JE, Pirko I, et al. Clinical and pathological insights into the dynamic nature of the white matter multiple sclerosis plaque. *Ann Neurol.* (2015) 78:710–21. doi: 10.1002/ana.24497

Conflict of Interest: PE has received travel allowance from Bayer Health Care. MP has a consultant relationship with Novartis, Merck, and Genentech/Roche; has received non-personal, institutional honoraria from Medac, Merck, Novartis, TEVA, and Genentech/Roche; and has research agreements with Bayer Health Care. AG has received honoraria for lecturing, travel allowance for attending meetings, and financial support for research from Bayer Schering, Biogen Idec, Merck Serono, Novartis, and TEVA Neurosciences and serves on the Editorial Board of Frontiers in Neurology—Applied Neuroimaging and Journal of Neuroimaging.

The remaining authors declare that the research was conducted in the absence of any commercial or financial relationships that could be construed as a potential conflict of interest.

frontiers in Neurology

ORIGINAL RESEARCH
published: 08 April 2020
doi: 10.3389/fneur.2020.00248

Parkinson's Disease Diagnosis Using Neostriatum Radiomic Features Based on T2-Weighted Magnetic Resonance Imaging

Panshi Liu*[1], *Han Wang*[2], *Shilei Zheng*[1], *Fan Zhang*[3] and *Xianglin Zhang*[1]

[1] Department of Radiology, First Affiliated Hospital of Jinzhou Medical University, Jinzhou, China, [2] Medical Imaging Center, Taian Central Hospital, Taian, China, [3] Department of Neurology, First Affiliated Hospital of Jinzhou Medical University, Jinzhou, China

Background: Parkinson's disease (PD) is a neurodegenerative disease in which the neostriatum, including the caudate nucleus (CN) and putamen (PU), has an important role in the pathophysiology. However, conventional magnetic resonance imaging (MRI) lacks sufficient specificity to diagnose PD. Therefore, the study's aim was to investigate the feasibility of using a radiomics approach to distinguish PD patients from healthy controls on T2-weighted images of the neostriatum and provide a basis for the clinical diagnosis of PD.

Methods: T2-weighted images from 69 PD patients and 69 age- and sex-matched healthy controls were obtained on the same 3.0T MRI scanner. Regions of interest (ROIs) were manually placed at the CN and PU on the slices showing the largest respective sizes of the CN and PU. We extracted 274 texture features from each ROI and then used the least absolute shrinkage and selection operator regression to perform feature selection and radiomics signature building to identify the CN and PU radiomics signatures consisting of optimal features. We used a receiver operating characteristic curve analysis to assess the diagnostic performance of two radiomics signatures in a training group and estimate the generalization performance in the test group.

Results: There were no significant differences in the demographic and clinical characteristics between the PD patients and healthy controls. The CN and PU radiomics signatures were built using 12 and 7 optimal features, respectively. The performance of the two radiomics signatures to distinguish PD patients from healthy controls was good. In the training and test groups, the AUCs of the CN radiomics signatures were 0.9410 (95% confidence interval [CI]: 0.8986–0.9833) and 0.7732 (95% CI: 0.6292–0.9173), respectively, and the AUCs of the PU radiomics signature were 0.8767 (95% CI: 0.8066–0.9469) and 0.7143 (95% CI: 0.5540–0.8746), respectively. Vertl_GlevNonU_R appeared simultaneously in both the CN and PU radiomics signatures as an optimal feature. A t-test analysis revealed significantly higher levels of texture values of the CN and PU in the PD patients than healthy controls ($P < 0.05$).

Conclusion: Neostriatum radiomics signatures achieved good diagnostic performance for PD and potentially could serve as a basis for the clinical diagnosis of PD.

Keywords: Parkinson's disease, diagnosis, radiomics, neostriatum, T2-weighted imaging

Edited by:
Fabiana Novellino,
Italian National Research Council, Italy

Reviewed by:
Konstantinos Kalafatakis,
University of Ioannina, Greece
Alessia Sarica,
University of Magna Graecia, Italy

Correspondence:
Xianglin Zhang
zxljr1030@126.com

Specialty section:
This article was submitted to Applied Neuroimaging, a section of the journal Frontiers in Neurology

Received: *26 November 2019*
Accepted: *13 March 2020*
Published: *08 April 2020*

Citation:
Liu P, Wang H, Zheng S, Zhang F and Zhang X (2020) Parkinson's Disease Diagnosis Using Neostriatum Radiomic Features Based on T2-Weighted Magnetic Resonance Imaging. Front. Neurol. 11:248. doi: 10.3389/fneur.2020.00248

INTRODUCTION

Parkinson's disease (PD) is a progressive neurodegenerative disease characterized by rigidity, tremor, slowed movements, and other non-motor symptoms. PD affects 2–3% of elderly people >65 years old worldwide and has a significant impact on patients' quality of life (1). PD mainly causes degeneration of the dopaminergic neurons of the nigrostriatal system (2). As part of the nigrostriatal system, the neostriatum includes both the caudate nucleus (CN) and putamen (PU) (3). Abnormal deposition of cytoplasmic inclusions (Lewy bodies) containing a-synuclein and ubiquitin in the neostriatum has been proven pathologically (4). Additionally, iron deposition in the brain, including the neostriatum, has been proposed as having an important role in the pathophysiology of PD (5, 6). Additionally, converging evidence has demonstrated the existence of striatal microstructural changes (7, 8).

The clinical diagnosis of PD essentially relies on a set of clinical presentations that do not provide high accuracy (9). In neuroimaging, based on the above-mentioned pathophysiological changes in PD, some advanced magnetic resonance imaging (MRI) sequences, such as neuromelanin-sensitive MRI (10) and quantitative susceptibility mapping (11), have been reported to be useful for diagnosis of PD. Resting-state functional MRI and diffusion tensor imaging (DTI) also have demonstrated abnormalities in the neostriatum in PD patients (7, 8, 12). Unfortunately, the limitations of these techniques, such as complicated sequences and time-consuming procedures, have hindered their clinical application. As a basic radiological examination, conventional MRI is widely used in clinical neurology. However, conventional MRI only serves to exclude underlying pathologies (e.g., cerebrovascular disease) and lacks specificity in diagnosis (13).

Radiomics, which use mathematical methods to examine a large set of texture features and extract mineable high-dimensional data from the texture features, can provide non-visual information of medical images, such as microstructural alterations and even pathological changes (14). The "texture features" are the interrelationships of image pixel gray-levels and patterns, which are hard to see directly by radiologists. According to the calculation method, these could be divided into first-, second-, or higher-order features. After texture feature extraction, radiomics use machine learning or advanced statistical methods to analyze the high-dimensional feature data to identify the optimal features. Finally, a radiomics signature, a clinical classifier model consisting of the optimal features, was built (14). In the early years of radiomics, this new approach has been widely applied in oncology fields and has shown potential benefits for tumor grading and pathological classification (15, 16). However, given its power in capturing the microstructural changes in tissues and its correlation with clinical endpoints (17) and age progression (18, 19), the use of radiomics is expected to increase in neurodegenerative disorders (20). Presently, radiomics has been applied to the diagnosis of neurodegenerative diseases, including Alzheimer's disease (AD), amyotrophic lateral sclerosis, and Machado–Joseph disease with conventional MRI (21–25), which have similar pathological changes with PD, such as atrophy, abnormal proteins, or iron deposition in many brain regions. In a longitudinal study, radiomics successfully detected microstructural changes in invisible normal-appearing white matter on conventional T2 fluid-attenuated inversion-recovery (FLAIR) images (18). In addition, recent studies indicated that radiomics features derived from DAT SPECT images can serve as a biomarker for PD progression tracking (26, 27). Notably, a previous texture analysis study demonstrated that texture features based on T2-weighted imaging (T2WI) differed between PD patients and healthy controls in many brain regions (28). However, there is no published study that investigated the diagnosis of PD on conventional MRI by using a radiomics approach.

Therefore, the study aim was to investigate the feasibility of using a radiomics approach for discrimination of PD patients from healthy controls on T2WI, which may provide a basis for the clinical diagnosis of PD and guide management for precision medicine. To this end, we developed two T2WI-based radiomics signatures, each consisting of optimal features for either CN or PU, and then estimated the generalization performance in the test group by using receiver operating characteristic (ROC) analysis.

MATERIALS AND METHODS

Participants

This retrospective study was approved by the Ethics Committee at the First Affiliated Hospital of Jinzhou Medical University, and the requirement for written informed consent was waived by the Ethics Committee. MRI and clinical data were retrospectively and anonymously collected from the Picture Archiving and Communication System and medical records of our hospital. All the data were anonymized and de-identified prior to analysis. The inclusion criteria for PD patients was a clinical diagnosis of idiopathic PD per the UK Parkinson Society Brain Bank criteria (29). The exclusion criteria for PD patients were history of other neurological and psychiatric diseases, secondary or atypical Parkinsonism, history of alcohol and/or drug abuse, and history of head injury. The healthy controls with age and sex matched to the PD patients were recruited from the medical examination center of the hospital. All healthy controls had no history of any neurological or psychiatric disorders, alcohol and/or drug abuse, or head injury. All participants underwent conventional MRI examinations with T2WI on the same 3.0T MRI scanner. The T2W images from each participant were evaluated for artifacts that may have affected the feature extraction. Satisfactory image quality for further analysis was obtained for all participants. Sixty-nine PD patients (40 male; 72.4 ± 9.1 years) and 69 healthy controls (35 male; 70.09 ± 5.6 years) were reviewed, according to the above criteria, from February 2017 to December 2018. The PD patients and healthy controls were randomly allocated to training ($n = 48$) and test groups ($n = 21$) at a proportion of 7:3.

MRI Acquisition

All MRI images were acquired on the same 3.0T Verio Siemens scanner (Siemens, Erlangen, Germany) equipped with an eight-channel head coil. The acquisition parameters were as follows: (1) axial T1 weighted scan (T1WI) [repetition time

(TR)/echo time (TE)/inversion time (TI), 2,000/9/860 ms]; (2) axial T2WI (TR/TE, 6,000/96 ms); (3) axial FLAIR (TR/TE/TI, 8,500/94/2,440 ms); These three sequences shared the following parameters: field of view (FOV), 240 × 204 mm; matrix, 320 × 240 pixels; section thickness, 5 mm; (4) sagittal T1WI (TR/TE/TI, 2,000/9/860 ms; FOV, 240 × 216 mm; matrix, 320 × 240 pixels; section thickness, 5.5 mm) (**Figure 1A**).

Image Selection and Region of Interest (ROI) Delineation

The T2W images were used for feature extraction, and T1W and FLAIR images were used as anatomical references for the ROI delineation and placement. The T2W image quality was evaluated, and the slices for feature extraction were determined by two neurological radiologists (SZ and XZ) who had 9 and 28 years of experience, respectively. To extract the texture features more comprehensively and reduce the partial volume effect due to slice thickness, two slices showing the largest respective sizes of CN and PU in each participant were selected for feature extraction. In cases of disagreement of image selection, consensus was reached through discussion (the outcome of the consensus between the two radiologists can be found in **Supplementary Table 1**).

ROI delineation and texture extraction were performed by using the available MaZda software (MaZda Version 4.6; Technical University of Lodz, Poland). To minimize confounding effects in the image, image gray-level intensity normalization was performed by discarding the image intensities not within $\mu \pm 3\delta$ (μ: mean of gray-level value, δ: standard deviation of gray-level value) (30).

Since different ROI sizes can affect the results of texture extraction (31), to ensure the stability of texture extraction, an ROI was delineated as a rotundity with the same size. In addition, the ROI cannot exceed or coincide the edges of the CN or PU to ensure that it is within the region of the CN or PU. Further, two ROIs were exported as *.roi files with a size of 1,257 pixels and 2,552 pixels for the CN and PU, respectively. Next, we imported the selected CN and PU slices in the MaZda software and then loaded the respective *.roi files. The ROIs were manually placed on the bilateral CN and PU by two neurological radiologists (SZ and XZ, respectively), (**Figure 1B**). Radiologist SZ placed the ROIs again within a 2 weeks interval.

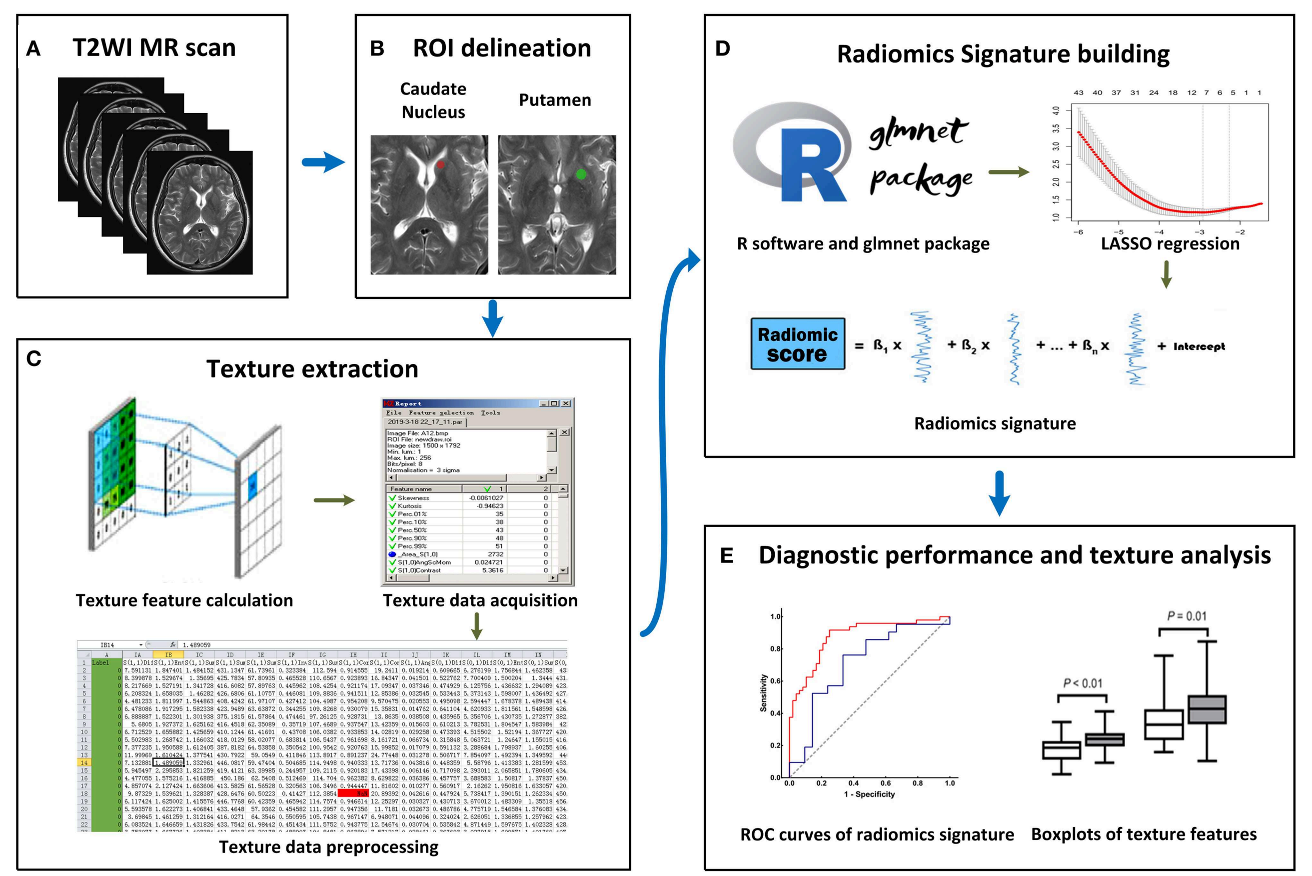

2019-3-18 22_17_11.par

Image File: A12.bmp
ROI File: newdraw.roi
Image size: 1500 x 1792
Min. lum.: 1
Max. lum.: 256
Bits/pixel: 8
Normalisation = 3 sigma

Feature name	1	2
✓ Skewness	-0.0061027	0
✓ Kurtosis	-0.94623	0
✓ Perc.01%	35	0
✓ Perc.10%	38	0
✓ Perc.50%	43	0
✓ Perc.90%	48	0
✓ Perc.99%	51	0
● _Area_S(1,0)	2732	0
✓ S(1,0)AngScMom	0.024721	0
✓ S(1,0)Contrast	5.3616	0

FIGURE 1 | Workflow of this study. **(A)** All T2-weighted imaging (T2WI) images were acquired on the same MRI scanner. **(B)** Regions of interest (ROIs) were manually placed on the bilateral caudate nucleus (CN) and putamen (PU). **(C)** A total of 274 radiomics features were extracted from each ROI. **(D)** On the R software platform with the glmnet package installed, least absolute shrinkage and selection operator (LASSO) regression was used to optimal features selection and radiomics signature building. **(E)** Receiver operating characteristic (ROC) curves were used to evaluate classification performance, and *t*-test analysis and box plots were used to compare the co-occurring optimal feature values.

Texture Extraction

The MaZda software "Analysis" module was used for texture extraction. A total of 274 texture features were extracted from each ROI, and the results were exported as *.sel files (**Figure 1C**).

Radiomics Signatures Building

LASSO regression with filter, which is a sparse learning method suitable for high-dimensional data (32), was used to optimal feature selection and radiomics signatures building. LASSO regression reduced the penalty term lambda to set the coefficients of diagnostic-unrelated features to zero and retain optimal features with non-zero coefficients. To select optimal features in LASSO regression, we employed 10-fold cross-validation with binomial deviance following minimization criteria to determine the optimal penalty term lambda (33). With lambda determined, the radiomics signature was generated by the multivariate LASSO-logistic regression analysis. To be specific, the radiomics signature was a linear equation consisting of an intercept and optimal features multiplied by their respective coefficients. For each participant in the training group, we substituted the optimal feature values into the equation to obtain their radiomics score (**Figure 1D**).

Validation of the Radiomics Signatures

The ROC curve is widely used to evaluate performance of supervised classification (34) and is a common method for the measurement of radiomics signature performance in the field of radiomics research (35). The classification performance of our radiomics signature was measured by a ROC curve and the corresponding AUC in this study, and sensitivity and specificity were also calculated. We plotted the ROC curve of the radiomics score and calculated the AUC, sensitivity, and specificity in the training group. To estimate the generalization performance of our radiomics signatures, we used the same image selection and ROI delineation methods to extract the texture features of the CN and PU in the test group. In the same way, the radiomics score was calculated for each participant in the test group using our radiomics signatures by substituting optimal feature values into the equation. The ROC curve of the test group's radiomics score was plotted to show the generalization performance of the signature, and then the AUC, sensitivity, and specificity were calculated (**Figure 1E**).

Statistical Analysis

All statistical analyses were performed by using SPSS statistical software (Version 20.0; SPSS Inc., Chicago, IL, USA), R software (Version 3.4.3; R Foundation for Statistical Computing, Vienna, Austria), and GraphPad Prism (Version 8.0.2; GraphPad Software, Inc., San Diego, CA). The differences in age, sex, duration of disease, and modified Hoehn–Yahr stage between the study groups were investigated by performing the Chi-square, Student's *t*, and Mann–Whitney *U* tests. LASSO regression was performed by using the "glmnet" package in R software. The Hosmer–Lemeshow test was performed to evaluate the goodness-of-fit of radiomics signatures. ROC curves were used to evaluate the diagnostic classification performance of radiomics signatures. The differences in co-occurring optimal feature values between the PD patients and healthy controls were analyzed by using Student's *t*-test. The inter- and intraobserver agreements of feature extraction reproducibility were evaluated by inter- and intra-class correlation coefficients (ICCs). The interobserver ICC was calculated by using each texture feature for agreement between SZ and XZ, and the intraobserver ICC was calculated by using each texture feature for agreement between two performances by SZ. The threshold for statistical significance was set to $P < 0.05$, and all reported *P*-values were two-sided.

RESULTS

Demographics and Clinical Characteristics

The demographic and clinical characteristics of the participants for the training and test group are shown in **Table 1**. We found no significant differences in age and sex between the healthy controls and PD patients in the training and test groups. Among the PD patients, there were no significant differences in demographic characteristics, modified Hoehn–Yahr stage, and duration of disease between the two groups.

Feature Extraction and Radiomics Signature Building

A total of 274 texture features were extracted from each ROI. The interobserver ICCs ranged from 0.745 to 0.901, and the intraobserver ICCs ranged from 0.776 to 0.924, suggesting favorable reproducibility of feature extraction. **Figure 2** shows the dimensionality reduction after LASSO regression. **Figures 2A,C** shows the trace plots of the texture feature coefficients fit by LASSO. As shown, more coefficients of diagnostic-unrelated features were set to zero with increasing value of the penalty term lambda, which left fewer optimal features with non-zero coefficients in the equation. **Figures 2B,D** shows the determination of the penalty term lambda based on 10-fold cross-validation. To determine the minimization criteria of binomial deviance, we picked the optimized lambda at the left dotted vertical lines: a lambda value of 0.037 with log (lambda) $= -3.310$ and a lambda value of 0.052 with log (lambda) $= -2.963$ were selected for the CN and PU radiomics signatures, respectively. After the dimensionality reduction, there were 12 and seven optimal features with non-zero coefficients remaining in the CN and PU radiomics signatures, respectively (**Table 2**). All optimal features were derived from image histogram, run-length matrix, and co-occurrence matrix texture features (**Table 2**). Finally, two neostriatum radiomics signatures were built on the basis of LASSO-logistic regression analysis; the optimal features, coefficients, and intercept are shown in **Table 2**.

Texture Feature Analysis

Vertl_GlevNonU_R, a second-order run-length matrix texture feature, appeared simultaneously in both the CN and PU signatures as an optimal feature (**Table 2**, marked with an asterisk), which means this feature has high diagnostic value in both CN and PU. The *t*-test analysis revealed significantly higher levels of texture values for both the CN and PU in the PD patients than in the healthy controls ($P < 0.05$) (**Figure 3**).

TABLE 1 | Comparison of demographic and clinical characteristics between patients with PD and healthy controls in the training and test groups.

Characteristics	**Training group**			**Test group**			**HC-Training vs. HC-Test *P* value**	**PD-Training vs. PD-Test *P*-value**
	HC (*n* = 48)	**PD (*n* = 48)**	***P*-value**	**HC (*n* = 21)**	**PD (*n* = 21)**	***P*-value**		
Age (years, mean ± SD)	70.48 ± 5.43	72.91 ± 9.89	0.124[a]	69.19 ± 5.94	71.38 ± 9.54	0.377[a]	0.381[a]	0.544[a]
Gender (male/female)	25/23	27/21	0.838[b]	10/11	13/8	0.535[b]	0.937[b]	0.863[b]
Duration of disease[#] (years, mean ± SD)		4.75 ± 2.92			3.71 ± 2.19			0.111[a]
Modified H&Y stage (median, IQR or mean ± SD)		2.5 (2.0, 3.0)			2.52 ± 0.97			0.711[c]

HC, healthy controls; HC-Training, healthy controls in the training group; HC-Test, healthy controls in the test group; PD, patients with Parkinson's disease; PD-Training, Parkinson's disease patients in the training group; PD-Test, Parkinson's disease patients in the test group; SD, standard deviation; Modified H&Y stage, modified Hoehn–Yahr stage; IQR, interquartile range. [#]*The mean disease duration of PD patients, defined as the time between when a patient subjectively noticed his or her first symptoms and the moment of assessment.* [a]*Two-sample Student's t-test;* [b]*Chi-square test;* [c]*Mann–Whitney U-test.*

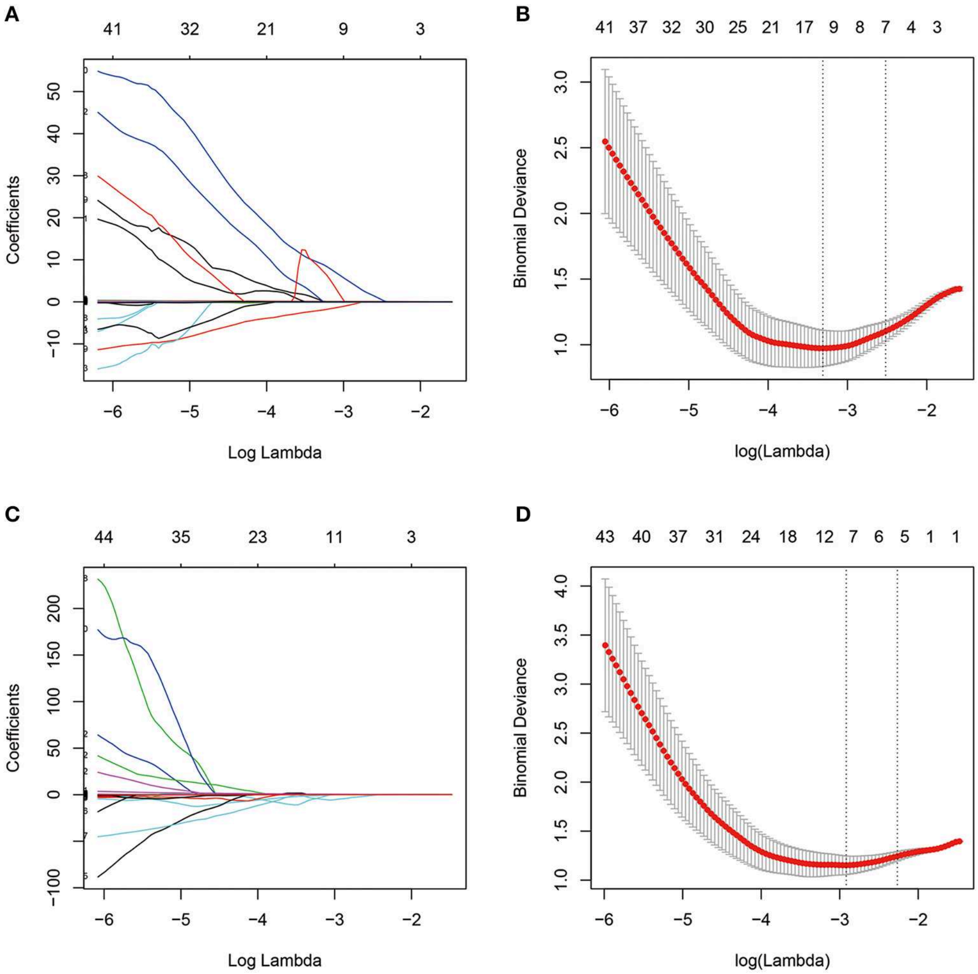

FIGURE 2 | Dimensionality reduction with LASSO regression. **(A,C)** The coefficients of texture features, represented by each colored line, were plotted vs. log (lambda) in the caudate nucleus (CN) and putamen (PU) radiomics signatures, respectively. **(B,D)** The binomial deviances were plotted vs. log (lambda) in the CN and PU radiomics signatures, respectively. Using 10-fold cross-validation, the red points indicate average values of deviance for each lambda, and the left and right dotted vertical lines correspond to lambda in the minimum criteria and the one standard error of the minimum criteria, respectively.

TABLE 2 | Optimal features after the dimensionality reduction.

Optimal features		Coefficient/Intercept
CN radiomics signature		−15.160413946
Histogram	Perc.50%_R	−0.027683304
Run-length matrix	Vertl_GlevNonU_R*	0.112951984
	Vertl_GlevNonU_L	0.019889353
	45dgr_RLNonUni_L	0.001556838
	135dr_RLNonUni_R	0.005421572
Co-occurrence matrix	S (1,0)Correlat_L	8.118174099
	S (1,0)Correlat_R	9.221141623
	S (0,1)SumVarnc_R	0.001540649
	S (1,1)Contrast_R	−2.039856941
	S (1,−1)Contrast_L	−0.142200691
	S (4,−4)InvDfMom_L	0.750813907
	S (5,5)InvDfMom_R	0.462795637
PU radiomics signature		2.705271e + 00
Histogram	Kurtosis_L	4.774812e − 01
	Perc.01%_R	−3.950184e − 02
Run-length matrix	Vertl_GlevNonU_R*	1.979927e − 02
	45dgr_RLNonUni_L	4.756729e − 06
Co-occurrence matrix	S (2,-2)Contrast_L	−1.047061e − 02
	S (5,0)InvDfMom_L	−4.534430e + 00
	S (0,5)Contrast_R	−5.781975e − 03

CN, caudate nucleus; PU, putamen.

**Appeared simultaneously in two neostriatum radiomics signatures.*

Diagnostic Performance of Two Neostriatum Radiomics Signatures

Figure 4A presents the performance of the CN radiomics signature for distinguishing PD from healthy controls in the two groups. In the training group, the AUC, sensitivity, and specificity were 0.9410 (95% confidence interval [CI]: 0.8986–0.9833), 81.25, and 95.83%, respectively. In the test group, the AUC, sensitivity, and specificity were 0.7732 (95% CI: 0.6292–0.9173), 95.24, and 61.90%, respectively. The Hosmer–Lemeshow test showed an acceptable goodness-of-fit of CN radiomics signature in the training and test groups ($P = 0.404$, 0.591, respectively).

Figure 4B shows the performance of the PU radiomics signature for distinguishing PD from healthy controls in the two groups. In the training group, the AUC, sensitivity, and specificity were 0.8767 (95% CI: 0.8066–0.9469), 91.67, and 75.00%, respectively. In the test group, the AUC, sensitivity, and specificity were 0.7143 (95% CI: 0.5540–0.8746), 76.19, and 66.67%, respectively. The Hosmer–Lemeshow test showed an acceptable goodness-of-fit of PU radiomics signature in the training and test groups ($P = 0.285$, 0.508, respectively).

DISCUSSION

Using T2W images with feature extraction and a high-throughput radiomics approach, we showed for the first time that conventional MRI-based radiomics signatures with good diagnostic performance for PD could be built. Our results indicated that neostriatum radiomic features had good potential as diagnostic markers for PD. In addition, we also evaluated the differences in co-occurring optimal feature values between PD patients and healthy controls.

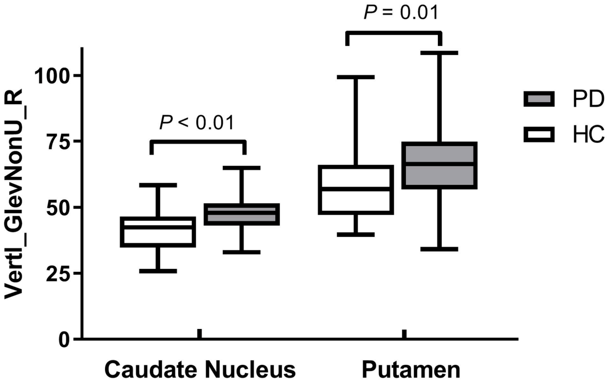

FIGURE 3 | Box plots of optimal feature that appeared simultaneously in two radiomics signatures.

PD is characterized by nigrostriatal degeneration. Although the pathogenesis of PD has not yet been clearly elucidated, iron deposition in the neostriatum has been demonstrated in earlier studies (5, 6). Being paramagnetic, iron can influence T2 relaxation times and, therefore, T2 signals (36–38), which can cause local signal non-uniformity. Moreover, decreases in the T2 signals in the neostriatum have been found in an earlier study (39). Although diagnosis of PD on conventional MRI by measuring the striatum T2 signal is non-specific (40), the local signal non-uniformity might cause changes in the neostriatum textural patterns of T2W images. In addition, pathological and DTI studies have demonstrated the presence of Lewy body deposits and microstructural deficits in the neostriatum of PD patients (4, 7, 8, 41). All of these microstructural changes might be characterized by alteration of textural patterns of T2W images (28) and captured by radiomics approach.

In the current study, according to the calculation method, optimal features (**Table 2**) can be classified into three major categories: the histogram, co-occurrence matrix, and run-length matrix features (42). Further, these major category features were subclassified into two, four, and two minor categories in the histogram, co-occurrence matrix, and run-length matrix features, respectively. As a first-order texture, the histogram only describes the gray-level distribution in the ROI without considering the neighboring pixels as follows: (1) Kurtosis reflects the shape of a histogram and is used to measure the asymmetry of the ROI (43); (2) The Perc indicates the highest gray-level containing a given percentage of pixels in the image (42). The co-occurrence matrix is based on an estimation of the second-order joint conditional probability density functions [p(x,y)]. Each p(x,y) is the probability of a pair of gray values, x and y, in a specified displacement of an image (44). (1) Contrast describes the local variation presented in an image; (2) Correlation describes the image complexity; (3) SumVarnc measures the spread in the sum of the gray-levels of the pixel-pair distribution; (4) InvDfMom

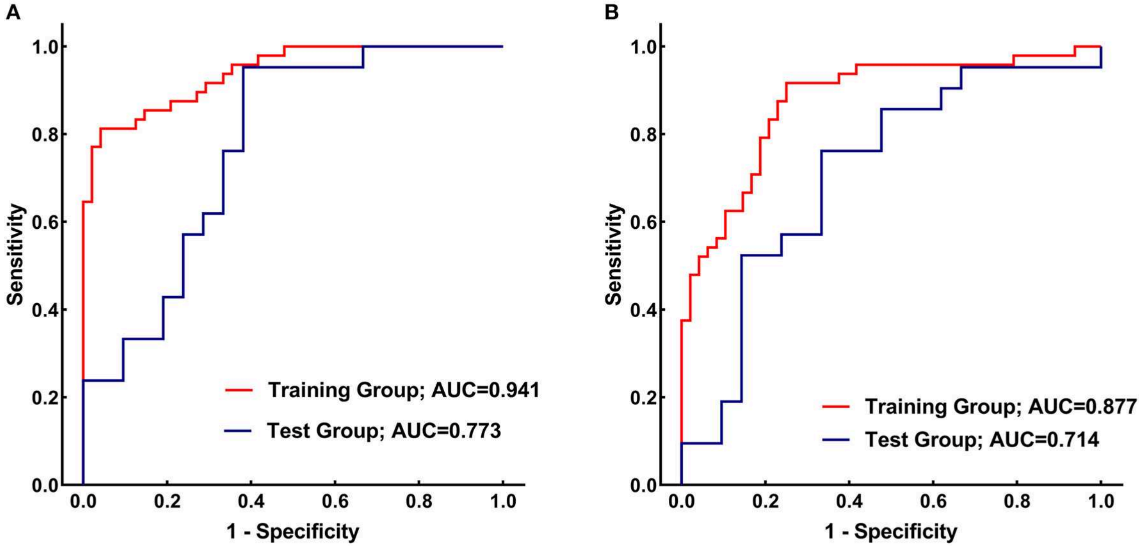

FIGURE 4 | (A) Receiver operating characteristic (ROC) curves of the caudate nucleus (CN) radiomics signature for distinguishing between Parkinson's disease (PD) patients and healthy controls in the training (red) and test (blue) groups. **(B)** ROC curves of the putamen (PU) radiomics signature for distinguishing between PD patients and healthy controls in the training (red) and test (blue) groups.

describes the local degree of homogeneity (45). The gray-level run-length matrix is based on computing the number of same gray-level runs of various lengths in a given direction (in general, the vertical, horizontal, and two-diagonal directions) (44). Both texture features, GlevNonU and RLNonUni, are derived from the run-length feature matrix. Therefore, the GlevNonU and RLNonUni features are a measure of a given direction's homogeneity of the pixel gray-level distribution of the underlying tissue, with higher values representing more inhomogeneity within the gray-levels of the run-length matrix (46). We found that the feature Vertl_GlevNonU_R co-occurred in two signatures, as one of the optimal features, and their feature values in both the CN and PU were significantly higher in the PD patients than in the healthy controls. Thus, combined with the pathological basis, we hypothesized that the significantly higher value of Vertl_GlevNonU_R might be related to the more heterogeneous texture patterns caused by iron deposition in the neostriatum in patients with PD.

Radiomics has been successfully applied to neurodegenerative disease studies. In a recent radiomics study by Feng et al. (23), T1W images from 78 patients with AD and 44 healthy controls were used for radiomics analysis. The corpus callosum was segmented manually, and texture features were obtained after extraction from each subject. After LASSO dimensionality reduction, a diagnostic model containing 11 features was established, which achieved an AUC of 0.72 for diagnosing AD. In another AD study, a support vector machine model demonstrated that hippocampal radiomics features could distinguish AD from healthy controls, with an AUC of 0.93 (22). Similar to these previous studies, we also used a general radiomics approach to extract features and build models of brain regions that had undergone microstructural changes that were not yet visible on conventional MRI. Previous studies above and our results suggested that radiomics could be used as biomarkers for neurodegenerative diseases on conventional MRI. Sikio et al. (28) applied texture analysis to PD for the first time and proved that the texture features of PD patients were changed in multiple brain regions (including the neostriatum), and stated that texture analysis could detect microstructural changes in T2W brain MRI images. However, they only extracted a few co-occurrence matrix features without further mining and modeling. In the current study, we extracted multiple categories of texture features and employed LASSO method to build radiomics signatures for diagnosis. As a popular machine-learning algorithm, LASSO is widely used as a high-dimensional data analysis tool in radiomics research because it is designed to avoid overfitting, so it can analyze large sets of texture features with a relatively small sample size (32). To our knowledge, no reported radiomics study has described the establishment of a PD diagnostic model for conventional MRI. This is the first radiomics study to diagnose PD by using conventional MRI.

Our study had several limitations. First, we built CN and PU radiomics signatures, respectively, rather than as a combined radiomics signature because of an insufficient sample size (the number of observations did not match the number of variables in the matrix, which meant that LASSO regression could not be performed in the "glmnet" package). Second, the sample size was insufficient to perfectly train the radiomics signature, leading to some degree of overfitting, which can be reflected in the AUC loss between the training group, and the test group. Therefore, further studies with greater sample size of training data set are necessary to reduce the degree of overfitting and improve the generalization performance. Third, the manual image selection and ROI determination was labor-intensive and time-consuming in the current study, which hinders the large sample size research progress and clinical application of radiomics. As the training sample size increases in future research, it is crucial to develop automatic or semi-automatic image selection and ROI determination algorithms to improve the research feasibility and to reduce inter-operator variability. Forth, along with age growth, a series of physiological changes in the brain also affect the texture features (47). Although there was no statistically significant difference in age ratios between the two groups, we did not achieve a complete 1:1 match, so the effects of this incomplete match on the research results cannot be completely excluded. Lastly, this was a retrospective study in which all subjects were recruited from a single hospital. In the future, a large-sample multi-center study is needed to evaluate the generalization performance and potential for clinical translation of our radiomics signatures. Moreover, the usefulness of neostriatum radiomic features as imaging markers for PD progression and response to treatment remains to be further investigated.

In conclusion, neostriatum radiomics signatures based on T2W images in this study achieved good diagnostic performance for PD and potentially could serve as a basis for the clinical diagnosis of PD. Moreover, our preliminary results showed the potential of neostriatum radiomic features as imaging markers for PD.

DATA AVAILABILITY STATEMENT

The datasets generated for this study are available on request to the corresponding author.

ETHICS STATEMENT

The studies involving human participants were reviewed and approved by the Ethics Committee at the First Affiliated Hospital of Jinzhou Medical University. The ethics committee waived the requirement of written informed consent for participation.

AUTHOR CONTRIBUTIONS

PL and XZ designed the study. PL, SZ, and FZ collected the raw data. SZ and XZ segmented the ROIs. FZ provided clinical expertise. HW and PL performed the data analysis. PL and SZ wrote the manuscript draft. XZ edited the manuscript and supervised the whole study process. All authors had reviewed this manuscript critically and approved its final submission.

FUNDING

This work was supported by Doctoral Research Startup Fund of Department of Science and Technology of Liaoning Province (No. 2019-BS-099) and Natural Science Foundation of Department of Science and Technology of Liaoning Province (No. 20180551012).

SUPPLEMENTARY MATERIAL

The Supplementary Material for this article can be found online at: https://www.frontiersin.org/articles/10.3389/fneur.2020.00248/full#supplementary-material

REFERENCES

1. Poewe W, Seppi K, Tanner CM, Halliday GM, Brundin P, Volkmann J, et al. Parkinson disease. *Nat Rev Disease Prime*. (2017) 3:17013. doi: 10.1038/nrdp.2017.13
2. Shimohama S, Sawada H, Kitamura Y, Taniguchi T. Disease model: Parkinson's disease. *Trends Mol Med.* (2003) 9:360–5. doi: 10.1016/S1471-4914(03)00117-5
3. Whetsell WO Jr. The mammalian striatum and neurotoxic injury. *Brain Pathol.* (2002) 12:482–7. doi: 10.1111/j.1750-3639.2002.tb00466.x
4. Mori F, Tanji K, Zhang H, Kakita A, Takahashi H, Wakabayashi K. alpha-Synuclein pathology in the neostriatum in Parkinson's disease. *Acta Neuropathol.* (2008) 115:453–9. doi: 10.1007/s00401-007-0316-4
5. Wallis LI, Paley MN, Graham JM, Grunewald RA, Wignall EL, Joy HM, et al. MRI assessment of basal ganglia iron deposition in Parkinson's disease. *J Magn Reson Imaging.* (2008) 28:1061–7. doi: 10.1002/jmri.21563
6. Hopes L, Grolez G, Moreau C, Lopes R, Ryckewaert G, Carriere N, et al. Magnetic Resonance imaging features of the nigrostriatal system: biomarkers of Parkinson's disease stages? *PLoS ONE.* (2016) 11:e0147947. doi: 10.1371/journal.pone.0147947
7. Zhan W, Kang GA, Glass GA, Zhang Y, Shirley C, Millin R, et al. Regional alterations of brain microstructure in Parkinson's disease using diffusion tensor imaging. *Movement Disord.* (2012) 27:90–7. doi: 10.1002/mds.23917
8. Kim HJ, Kim SJ, Kim HS, Choi CG, Kim N, Han S, et al. Alterations of mean diffusivity in brain white matter and deep gray matter in Parkinson's disease. *Neurosci Lett.* (2013) 550:64–8. doi: 10.1016/j.neulet.2013.06.050
9. Caslake R, Moore JN, Gordon JC, Harris CE, Counsell C. Changes in diagnosis with follow-up in an incident cohort of patients with parkinsonism. *J Neurol Neurosurg Psychiatr.* (2008) 79:1202–7. doi: 10.1136/jnnp.2008.144501
10. Prasad S, Stezin A, Lenka A, George L, Saini J, Yadav R, et al. Three-dimensional neuromelanin-sensitive magnetic resonance imaging of the substantia nigra in Parkinson's disease. *Eur J Neurol.* (2018) 25:680–6. doi: 10.1111/ene.13573
11. Sjöström H, Granberg T, Westman E, Svenningsson P. Quantitative susceptibility mapping differentiates between parkinsonian disorders. *Parkinsonism Relat Disord.* (2017) 44:51–7. doi: 10.1016/j.parkreldis.2017.08.029
12. Hacker CD, Perlmutter JS, Criswell SR, Ances BM, Snyder AZ. Resting state functional connectivity of the striatum in Parkinson's disease. *Brain.* (2012) 135:3699–711. doi: 10.1093/brain/aws281
13. Peran P, Cherubini A, Assogna F, Piras F, Quattrocchi C, Peppe A, et al. Magnetic resonance imaging markers of Parkinson's disease nigrostriatal signature. *Brain.* (2010) 133:3423–33. doi: 10.1093/brain/awq212
14. Gillies RJ, Kinahan PE, Hricak H. Radiomics: images are more than pictures, they are data. *Radiology.* (2016) 278:563–77. doi: 10.1148/radiol.2015151169
15. Zhang X, Xu X, Tian Q, Li B, Wu Y, Yang Z, et al. Radiomics assessment of bladder cancer grade using texture features from diffusion-weighted imaging. *J Magn Reson Imaging.* (2017) 46:1281–8. doi: 10.1002/jmri.25669
16. Xie T, Wang Z, Zhao Q, Bai Q, Zhou X, Gu Y, et al. machine learning-based analysis of MR multiparametric radiomics for the subtype classification of breast cancer. *Front. Oncol.* (2019) 9:505. doi: 10.3389/fonc.2019.00505
17. Li Y, Jiang J, Lu J, Jiang J, Zhang H, Zuo C. Radiomics: a novel feature extraction method for brain neuron degeneration disease using 18F-FDG

PET imaging and its implementation for Alzheimer's disease and mild cognitive impairment. *Ther Adv Neurol Disord.* (2019) 12:1756286419838682. doi: 10.1177/1756286419838682

18. Shao Y, Chen Z, Ming S, Ye Q, Shu Z, Gong C, et al. Predicting the development of normal-appearing white matter with radiomics in the aging brain: a longitudinal clinical study. *Front Aging Neurosci.* (2018) 10:393. doi: 10.3389/fnagi.2018.00393
19. Shu ZY, Shao Y, Xu YY, Ye Q, Cui SJ, Mao DW, et al. *Radiomics nomogram based on MRI for predicting white matter hyperintensity progression in elderly adults. J Magn Reson Imaging.* (2019) 51:535–46. doi: 10.1002/jmri.26813
20. Salvatore C, Castiglioni I, Cerasa A. Radiomics approach in the neurodegenerative brain. *Aging Clin Exp Res*, (2019) 1–3. doi: 10.1007/s40520-019-01299-z
21. de Oliveira MS, D'Abreu A, França MC Jr, Lopes-Cendes I, Cendes F, Castellano G. MRI-texture analysis of corpus callosum, thalamus, putamen, and caudate in Machado-Joseph disease. *J Neuroimaging.* (2012) 22:46–52. doi: 10.1111/j.1552-6569.2010.00553.x
22. Feng F, Wang P, Zhao K, Zhou B, Yao H, Meng Q, et al. Radiomic features of hippocampal subregions in Alzheimer's disease and amnestic mild cognitive impairment. *Front Aging Neurosci.* (2018) 10:290. doi: 10.3389/fnagi.2018.00290
23. Feng Q, Chen Y, Liao Z, Jiang H, Mao D, Wang M, et al. Corpus callosum radiomics-based classification model in Alzheimer's disease: a case-control study. *Front Neurol.* (2018) 9:618. doi: 10.3389/fneur.2018.00618
24. Ishaque A, Maani R, Satkunam J, Seres P, Mah D, Wilman AH, et al. Texture analysis to detect cerebral degeneration in amyotrophic lateral sclerosis. *Can J Neurol Sci.* (2018) 45:533–9. doi: 10.1017/cjn.2018.267
25. Zhou H, Jiang J, Lu J, Wang M, Zhang H, Zuo C, et al. Dual-model radiomic biomarkers predict development of mild cognitive impairment progression to Alzheimer's Disease. *Front Neurosci.* (2018) 12:1045. doi: 10.3389/fnins.2018.01045
26. Rahmim A, Huang P, Shenkov N, Fotouhi S, Davoodi-Bojd E, Lu L, et al. Improved prediction of outcome in Parkinson's disease using radiomics analysis of longitudinal DAT SPECT images. *Neuroimage Clin.* (2017) 16:539–44. doi: 10.1016/j.nicl.2017.08.021
27. Tang J, Yang B, Adams MP, Shenkov NN, Klyuzhin IS, Fotouhi S, et al. *Artificial neural network-based prediction of outcome in Parkinson's disease patients using DaTscan SPECT imaging features. Mol Imaging Biol.* (2019) 21:1165–73. doi: 10.1007/s11307-019-01334-5
28. Sikio M, Holli-Helenius KK, Harrison LC, Ryymin P, Ruottinen H, Saunamaki T, et al. MR image texture in Parkinson's disease: a longitudinal study. *Acta Radiol.* (2015) 56:97–104. doi: 10.1177/0284185113519775
29. Hughes AJ, Daniel SE, Kilford L, Lees AJ. Accuracy of clinical diagnosis of idiopathic Parkinson's disease: a clinico-pathological study of 100 cases. *J Neurol Neurosurg Psychiatr.* (1992) 55:181–4. doi: 10.1136/jnnp.55.3.181
30. Collewet G, Strzelecki M, Mariette F. Influence of MRI acquisition protocols and image intensity normalization methods on texture classification. *Magn Reson Imaging.* (2004) 22:81–91. doi: 10.1016/j.mri.2003.09.001
31. Kumar I, Virmani J, Bhadauria H. Optimization of ROI size for development of computer assisted framework for breast tissue pattern characterization using digitized screen film mammograms. In: Dey N, Borra S, Ashour AS, Shi F, editors. *Machine Learning in Bio-Signal Analysis and Diagnostic Imaging*. Cambridge, MA: Elsevier (2019). p. 127–57. doi: 10.1016/B978-0-12-816086-2.00006-0
32. Hepp T, Schmid M, Gefeller O, Waldmann E, Mayr A. approaches to regularized regression - a comparison between gradient boosting and the lasso. *Methods Inf Med.* (2016) 55:422–30. doi: 10.3414/ME16-01-0033
33. Roosen C, Hastie T. *Logistic Response Projection Pursuit*. (1998).
34. Hand DJ, Till RJ. A simple generalisation of the area under the ROC curve for multiple class classification problems. *Mach Learn.* (2001) 45:171–86. doi: 10.1023/A:1010920819831
35. Aerts HJWL, Velazquez ER, Leijenaar RTH, Parmar C, Grossmann P, Carvalho S, et al. Decoding tumour phenotype by noninvasive imaging using a quantitative radiomics approach. *Nat Commun.* (2014) 5:4006. doi: 10.1038/ncomms5644
36. Gomori J, Grossman R. The relation between regional brain iron and T2 shortening. *Am J Neuroradiol.* (1993) 14:1049–50.
37. Thomas L, Boyko O, Anthony D, Burger P. MR detection of brain iron. *Am J Neuroradiol.* (1993) 14:1043–8.
38. Haacke EM, Cheng NY, House MJ, Liu Q, Neelavalli J, Ogg RJ, et al. Imaging iron stores in the brain using magnetic resonance imaging. *Magn Reson Imaging.* (2005) 23:1–25. doi: 10.1016/j.mri.2004.10.001
39. Antonini A, Leenders K, Meier D, Oertel W, Boesiger P, Anliker M. T2 relaxation time in patients with Parkinson's disease. *Neurology.* (1993) 43:697–697. doi: 10.1212/WNL.43.4.697
40. Heim B, Krismer F, De Marzi R, Seppi K. Magnetic resonance imaging for the diagnosis of Parkinson's disease. *J Neural Transm.* (2017) 124:915–64. doi: 10.1007/s00702-017-1717-8
41. Tsuboi Y, Uchikado H, Dickson DW. Neuropathology of Parkinson's disease dementia and dementia with Lewy bodies with reference to striatal pathology. *Parkinsonism Relat Disord.* (2007) 13:S221–4. doi: 10.1016/S1353-8020(08)70005-1
42. Castellano G, Bonilha L, Li LM, Cendes F. Texture analysis of medical images. *Clin Radiol.* (2004) 59:1061–9. doi: 10.1016/j.crad.2004.07.008
43. Nougaret S, Vargas HA, Lakhman Y, Sudre R, Do RK, Bibeau F, et al. Intravoxel incoherent motion-derived histogram metrics for assessment of response after combined chemotherapy and radiation therapy in rectal cancer: initial experience and comparison between single-section and volumetric analyses. *Radiology.* (2016) 280:446–54. doi: 10.1148/radiol.2016 150702
44. Basset O, Buquet B, Abouelkaram S, Delachartre P, Culioli J. Application of texture image analysis for the classification of bovine meat. *Food Chem.* (2000) 69:437–45. doi: 10.1016/S0308-8146(00)00057-1
45. Li G, Zhai G, Zhao X, An H, Spincemaille P, Gillen KM, et al. 3D texture analyses within the substantia nigra of Parkinson's disease patients on quantitative susceptibility maps and R2(*) maps. *Neuroimage.* (2019) 188:465–72. doi: 10.1016/j.neuroimage.2018.12.041
46. Baessler B, Mannil M, Oebel S, Maintz D, Alkadhi H, Manka R. Subacute and chronic left ventricular myocardial scar: accuracy of texture analysis on nonenhanced cine MR images. *Radiology.* (2017) 286:103–12. doi: 10.1148/radiol.2017170213
47. Valdes Hernandez MDC, Gonzalez-Castro V, Chappell FM, Sakka E, Makin S, Armitage PA, et al. Application of texture analysis to study small vessel disease and blood-brain barrier integrity. *Front Neurol.* (2017) 8:327. doi: 10.3389/fneur.2017.00327

Conflict of Interest: The authors declare that the research was conducted in the absence of any commercial or financial relationships that could be construed as a potential conflict of interest.

frontiers in Neurology

ORIGINAL RESEARCH
published: 05 May 2020
doi: 10.3389/fneur.2020.00381

The Effect of Scan Length on the Assessment of BOLD Delay in Ischemic Stroke

*Ayse Ceren Tanrıtanır[1], Kersten Villringer[1], Ivana Galinovic[1], Ulrike Grittner[2,3], Evgeniya Kirilina[4,5], Jochen B. Fiebach[1], Arno Villringer[6,7] and Ahmed A. Khalil[1,3,6,7]**

[1] Center for Stroke Research, Charité - Universitätsmedizin Berlin, Berlin, Germany, [2] Institute of Biometry and Clinical Epidemiology, Charité – Universitätsmedizin Berlin, Berlin, Germany, [3] Berlin Institute of Health (BIH), Berlin, Germany, [4] Department of Neurophysics, Max Planck Institute for Human Cognitive and Brain Sciences, Leipzig, Germany, [5] Center for Cognitive Neuroscience Berlin, Free University, Berlin, Germany, [6] Berlin School of Mind and Brain, Humboldt Universität zu Berlin, Berlin, Germany„ [7] Department of Neurology, Max Planck Institute for Human Cognitive and Brain Sciences, Leipzig, Germany

Objectives: To evaluate the impact of resting-state functional MRI scan length on the diagnostic accuracy, image quality and lesion volume estimation of BOLD delay maps used for brain perfusion assessment in acute ischemic stroke.

Methods: Sixty-three acute ischemic stroke patients received a 340 s resting-state functional MRI within 24 h of stroke symptom onset. BOLD delay maps were calculated from the full scan and four shortened versions (68 s, 136 s, 204 s, 272 s). The BOLD delay lesions on these maps were compared in terms of spatial overlap and volumetric agreement with the lesions derived from the full scans and with time-to-maximum (Tmax) lesions derived from DSC-MRI in a subset of patients ($n = 10$). In addition, the interpretability and quality of these maps were compared across different scan lengths using mixed models.

Results: Shortened BOLD delay scans showed a small volumetric bias (ranging from 0.05 to 5.3 mL; between a 0.13% volumetric underestimation and a 7.7% overestimation relative to the mean of the volumes, depending on scan length) compared to the full scan. Decreased scan length was associated with decreased spatial overlap with both the BOLD delay lesions derived from the full scans and with Tmax lesions. Only the two shortest scan lengths (68 and 136 s) were associated with substantially decreased interpretability, decreased structure clarity, and increased noisiness of BOLD delay maps.

Conclusions: BOLD delay maps derived from resting-state fMRI scans lasting 272 and 204 s provide sufficient diagnostic quality and adequate assessment of perfusion lesion volumes. Such shortened scans may be helpful in situations where quick clinical decisions need to be made.

Keywords: perfusion, acute stroke, BOLD delay, scan length, MRI

OPEN ACCESS

Edited by:
Peter Sörös,
University of Oldenburg, Germany

Reviewed by:
Bradley J. MacIntosh,
Sunnybrook Research Institute (SRI), Canada
Seena Dehkharghani,
New York University, United States

****Correspondence:***
Ahmed A. Khalil
ahmed-abdelrahim.khalil@charite.de

Specialty section:
This article was submitted to Applied Neuroimaging, a section of the journal Frontiers in Neurology

Received: *05 December 2019*
Accepted: *15 April 2020*
Published: *05 May 2020*

Citation:
Tanrıtanır AC, Villringer K, Galinovic I, Grittner U, Kirilina E, Fiebach JB, Villringer A and Khalil AA (2020) The Effect of Scan Length on the Assessment of BOLD Delay in Ischemic Stroke. Front. Neurol. 11:381. doi: 10.3389/fneur.2020.00381

INTRODUCTION

The assessment of brain perfusion in acute ischemic stroke can be used to guide clinical decision-making, particularly when considering the use of intravenous thrombolysis or mechanical thrombectomy in patients otherwise ineligible for these treatments (1–3). Dynamic susceptibility contrast MRI (DSC-MRI) is most commonly used for this purpose in routine clinical practice.

However, it requires the use of exogenous contrast agents, which have potentially severe side effects (4). Even in people with normal kidney function, the gadolinium-based contrast agents used for DSC-MRI accumulate in the brain with repeated administration (5, 6), which has led the European Medicines Agency to recommend restricting their use (7).

As part of the ongoing search for alternative perfusion imaging methods, many studies have recently shown that the temporal properties of the blood-oxygenation-level-dependent (BOLD) signal reflect aspects of perfusion. This is because the BOLD signal, while usually used to probe the hemodynamic response to neural activity, reflects an amalgam of different physiological processes. These include fluctuations originating from outside the brain that travel through the vasculature in a manner closely resembling blood flow (8–11). These non-neuronal oscillations, referred to as systemic low-frequency oscillations (sLFOs), exist in the low-frequency range of the signal (0.01–0.15 Hz). Studies have shown changes in the amplitude, frequency, and phase of sLFOs in areas of low blood flow (12–15). Currently, one of the most well-studied temporal properties of the BOLD signal in relation to perfusion is BOLD delay (also known as hemodynamic lag)–the delay in arrival of sLFOs to a certain voxel compared to a reference region (14).

Evidence for the relationship between BOLD delay and perfusion comes from several sources. Firstly, regions of BOLD delay have been detected in cerebrovascular disorders including stroke (14, 16–21), transient ischemic attack (22), and Moyamoya disease (23). Such regions are also observed in other conditions associated with more subtle changes in cerebral perfusion such as Alzheimer's disease (24), epilepsy (25), and sickle cell disease (26). Secondly, direct comparisons between perfusion modalities have shown that BOLD delay correlates with measures of perfusion derived from DSC-MRI (14, 16, 18–21, 27) and arterial spin labeling (17, 22, 23). In addition, we have recently shown that increased BOLD delay in acute stroke due to large vessel occlusion is reversible following vessel recanalization, and that this reversibility mirrors reperfusion detected using DSC-MRI (19). Thirdly, manipulation of the circulatory system through respiratory challenges affects sLFOs in a manner consistent with changes in cerebrovascular reactivity (28–34). Finally, the physiological basis for BOLD delay seems to lie in axial variations in the concentration of deoxyhemoglobin within arteries and veins caused by vasomotion or changes in oxygen saturation (35). These variations act as a "virtual tracer"—a contrast agent intrinsic to the blood (35).

All this evidence suggests that the use of BOLD delay for assessing perfusion is a promising alternative to DSC-MRI. However, the clinical applicability of BOLD delay is still limited due to its relatively long acquisition time, which particularly hampers its use in clinical situations where decisions have to be made extremely quickly, such as in acute stroke. Studies utilizing BOLD delay for brain perfusion assessment have varied widely in scan length, between 3.5 and 30 min (see **Table 1** for an overview), markedly longer than typical DSC-MRI scans (∼2 min). In this study, we evaluated the impact of scan length on the diagnostic accuracy, image quality and lesion volume estimation of BOLD delay maps used for brain perfusion assessment in acute ischemic stroke.

TABLE 1 | Overview of resting-state functional MRI scan lengths used in previous studies on BOLD delay for the assessment of brain perfusion.

Study	Investigated population	Scan length (min:s)
Lv et al. (14)	Acute stroke	5:50
Amemiya et al. (16)	Acute stroke and chronic hypoperfusion	10:00
Qian et al. (36)	Acute stroke	10:00
Christen et al. (23)	Moyamoya disease	3:36
Cologner et al. (26)	Sickle cell disease	6:00
Siegel et al. (17)	Subacute stroke	30:00[a]
Qian et al. (37)	Healthy individuals	6:40
Khalil et al. (18)	Acute stroke	5:50
Ni et al. (20)	Subacute stroke	8:00
Wu et al. (38)	Chronic hypoperfusion and moyamoya disease	5:00[b]
Tong et al. (27)	Healthy individuals	6:00
Chen et al. (21)	Acute stroke	8:00
Yang et al. (39)	Healthy individuals	10:00
Lv et al. (22)	Transient ischemic attack	8:00
Yan et al. (24)	Alzheimer's disease, mild cognitive impairment, and healthy individuals	6:40
Khalil et al. (19)	Acute stroke	5:50
Zhao et al. (40)	Chronic stroke	6:15
Nishida et al. (32)	Chronic hypoperfusion and moyamoya disease	7:20
Jahanian et al. (41)	Moyamoya disease and healthy individuals	4:00 to 6:00

[a]Minimum of 5 min of resting-state functional MRI data after motion scrubbing required.
[b]Total resting-state functional MRI data acquired was 20 min, but data was divided into pre- and post-acetazolamide administration (5 min each) for processing.

MATERIALS AND METHODS

Study Design

Patients with a confirmed clinical and radiological diagnosis of ischemic stroke who received a resting-state functional MRI scan together with a standard stroke protocol were recruited as part of the Longitudinal MRI Examinations of Patients With Brain Ischemia and Blood-Brain Barrier Permeability [LOBI-BBB] study clinicaltrials.gov NCT02077582 from June 2016 to December 2017. The LOBI-BBB study is a single-center, prospective cohort study of patients with acute ischemic stroke. A subset of patients received a follow-up (day 1) scan within 24 h of the first scan session (day 0 scan). This study was approved by the local institutional review board (EA1/200/13) and only patients who gave written informed consent were included. No exclusion criteria based on head motion were used, because we aimed at achieving a representative clinical population in our sample.

Imaging Protocol

A standard stroke MRI protocol was performed on a Siemens (Erlangen, Germany) Tim Trio 3 Tesla MRI scanner. The imaging protocol included a T2*-weighted image

(TR/TE=669/20 ms, matrix = 320 × 320, field of view = 220 mm, slice thickness = 5 mm, acquisition time = 1 min 21 s), a diffusion-weighted image (TR/TE = 8900/93 ms, matrix = 192 × 192, field of view = 229 mm, slice thickness = 2.5 mm, acquisition time = 2 min 21 s), a FLAIR image (TR/TE = 8000/96 ms, matrix = 232 × 256, field of view = 199*220 mm, slice thickness = 5 mm, acquisition time = 1 min 21 s) and a time-of-flight MR angiography (TR/TE = 21/3.4 ms, matrix = 218 × 384, field of view = 162 × 199 mm, slice thickness = 0.5 mm, acquisition time = 3 min 2 s). In addition, a resting-state functional MRI was performed using a multiband EPI scan (University of Minnesota sequence cmrr_mbep2d_bold R008) (42, 43): [850 (resting state) time points, TR/TE = 400/30 ms, flip angle 43°, matrix = 64 × 64, 192 × 192 mm field of view (FOV), multiband factor = 6, thirty 4.0 mm thick slices, acquisition time: 340 s]. During the scan, patients were requested to relax, lie still, and close their eyes. In a subset of patients, DSC-MRI data were acquired following the injection of a bolus of 5 mL Gadovist 1 mol/L and a saline flush at a flow rate of 5 mL/s with the following scanning parameters: TR/TE = 1390/29 ms, flip angle = 60, matrix = 128 × 128, 21 slices, slice thickness = 5 mm, acquisition time = 1 min 58 s.

Image Processing

Preprocessing

As a first step, the first 25 volumes (10 s) were removed from the full 340 s resting-state scan to allow for magnetization equilibrium. Then, four shortened sets of data of various lengths were produced from the resulting full 330 s resting state scan (68 s, 136 s, 204 s, 272 s), and are referred to in this paper as 0.2, 0.4, 0.6, 0.8 scan segments, respectively.

Preprocessing was performed on the resting-state data of differing lengths using FSL (https://fsl.fmrib.ox.ac.uk/fsl) and AFNI (https://afni.nimh.nih.gov/afni). This comprised volume realignment to the first volume, regression of the effect of three rigid body translations and three rotations, spatial smoothing with 6-mm Gaussian kernel, and band pass filtering (0.01–0.15 Hz). The mean framewise displacement across the scan segments (FD) was calculated (44) and rescaled (multiplied by 10) to increase the comparability of this variable with the rest of the coefficients in the mixed effects models. In addition, to assess the signal change related to head motion, DVARS was calculated, defined as the frame-to-frame root mean square change in voxel intensities averaged across the entire brain (44).

Time Shift Analysis

A template was used to extract the reference time series by averaging the BOLD signal across all voxels in the major venous sinuses. This template was created from the post-gadolinium high-resolution T1-weighted scans of eight subjects, as described in the Supplemental Material of (18). Briefly, segmented gray matter, white matter, and CSF tissue masks were combined and subtracted from the brain-extracted T1 image, leaving an image containing only the vessels. This was registered to MNI space, binarized, summed up across subjects, manually edited to remove voxels outside the major venous sinuses, and spatially smoothed.

The venous sinus was preferred over the whole brain signal because BOLD delay calculated using the venous sinus reference correlated more strongly with DSC-MRI-based perfusion maps in both chronic cerebrovascular disease (23) and acute stroke (18). The venous sinus reference also avoids the contamination of the BOLD delay assessment procedure by hypoperfused voxels because it extracts time courses from voxels outside the brain parenchyma.

BOLD delay maps were generated by assigning each voxel the value of the time shift that achieves maximum cross-correlation between the reference time series and the voxel's time series. For this purpose, we used *rapidtide*, which is a set of Python tools for finding time-lagged correlations (https://github.com/bbfrederick/rapidtide). Significance thresholds for the cross-correlation were set by *rapidtide* using a shuffling procedure (10,000 times) to calculate the distribution of null correlation values. To determine the offset associated with the highest correlation coefficient with the reference signal, we shifted the time course from −20 to +20 s. This long tracking range was necessary because delays in acute stroke patients have been shown to be very long (18, 19).

BOLD delay maps generated from the data of each scan segment were registered to an echo-planar imaging (EPI) template derived from a similar cohort of stroke patients (18, 19). A multi-stage registration procedure (rigid → affine → deformable) was applied using the *antsRegistrationSyn* script

TABLE 2 | Demographics and clinical characteristics of the study sample.

Variable	Whole sample	Patients with hypoperfusion
N	63	43
Age in years (median, IQR)	75 (65–79)	78 (65–83)
Sex (M/F)	39/24	23/20
Follow-up (*n*)	38	17
mRS (median, IQR)		
Admission	3 (2–4)	4 (3–4)
Discharge	2 (1–3)	3 (1–4)
NIHSS (median, IQR)		
Admission	4 (1–8)	7 (3–11)
Discharge	2 (0–3)	3 (1–5)
Previous stroke (*n*)	22	16
Time (in hours) from symptom onset to MRI (median, IQR)	9 (3–16)	8 (1–14)
Vessel occlusion on MRA (n)	26	24
Therapy (*n*)		
Thrombolysis	17	15
Mechanical thrombectomy	5	5
Stroke vascular territory (*n*)		
Anterior cerebral artery	1	0
Middle cerebral artery	29	19
Posterior cerebral artery	9	3
Multiple territories	24	21

MRS, Modified Rankin Scale; NIHSS, National Institutes of Health Stroke Scale.

from the ANTs software (http://stnava.github.io/ANTs/) (45). Lesions on the diffusion-weighted images (DWI) were manually delineated by a stroke researcher (A.C.T.) and checked by a senior stroke researcher and radiology resident (A.K.) The DWI and the delineated DWI lesions were registered to the template using ANTs. DWI lesions were masked during the registration process to improve registration (46). The results of all registrations were inspected visually for quality.

Quantitative Analysis

Patients with a visible perfusion lesion on their full-length BOLD delay maps (assessed by A.K., a stroke researcher and radiology resident with 7 years' experience with perfusion imaging in stroke) were eligible for quantitative analysis in this study. Perfusion lesions on the BOLD delay maps were automatically delineated using an in-house algorithm used in a previous study (19). This algorithm searches the vascular territory affected by the stroke (defined as the vascular territory where the acute DWI lesion is present) for areas of hypoperfusion on the BOLD delay maps. For this procedure, BOLD delay maps thresholded to >0 s, >2.3 s, and >4.6 s were analyzed separately, generating three perfusion lesion volume values for each dataset (one value per threshold). The potential influence of these thresholds on the outcomes of this study were accounted for in the models.

Spatial Comparison of BOLD Delay Lesions

The Dice similarity coefficient was used for spatially comparing perfusion lesions on BOLD delay maps from shorter scans with those from the full length scan. The Dice similarity coefficient is a statistic used for evaluating spatial overlap and ranges between +1 (perfect overlap) and 0 (no overlap) (47). The association between scan length and the Dice similarity coefficient value was investigated using a linear mixed model (two-level; random intercept), with head motion as a covariate (48).

Volumetric Comparison of BOLD Delay Lesions

BOLD delay lesion volumes were calculated and the following analyses were performed on them:

Bland-Altman analysis (49) was used for assessing the agreement between shorter scans and the full length scan on BOLD delay lesion volume.

A linear mixed effects model (two-level; random intercept and slope model) was used to investigate the association between scan length and BOLD delay lesion volume. Since the distribution of

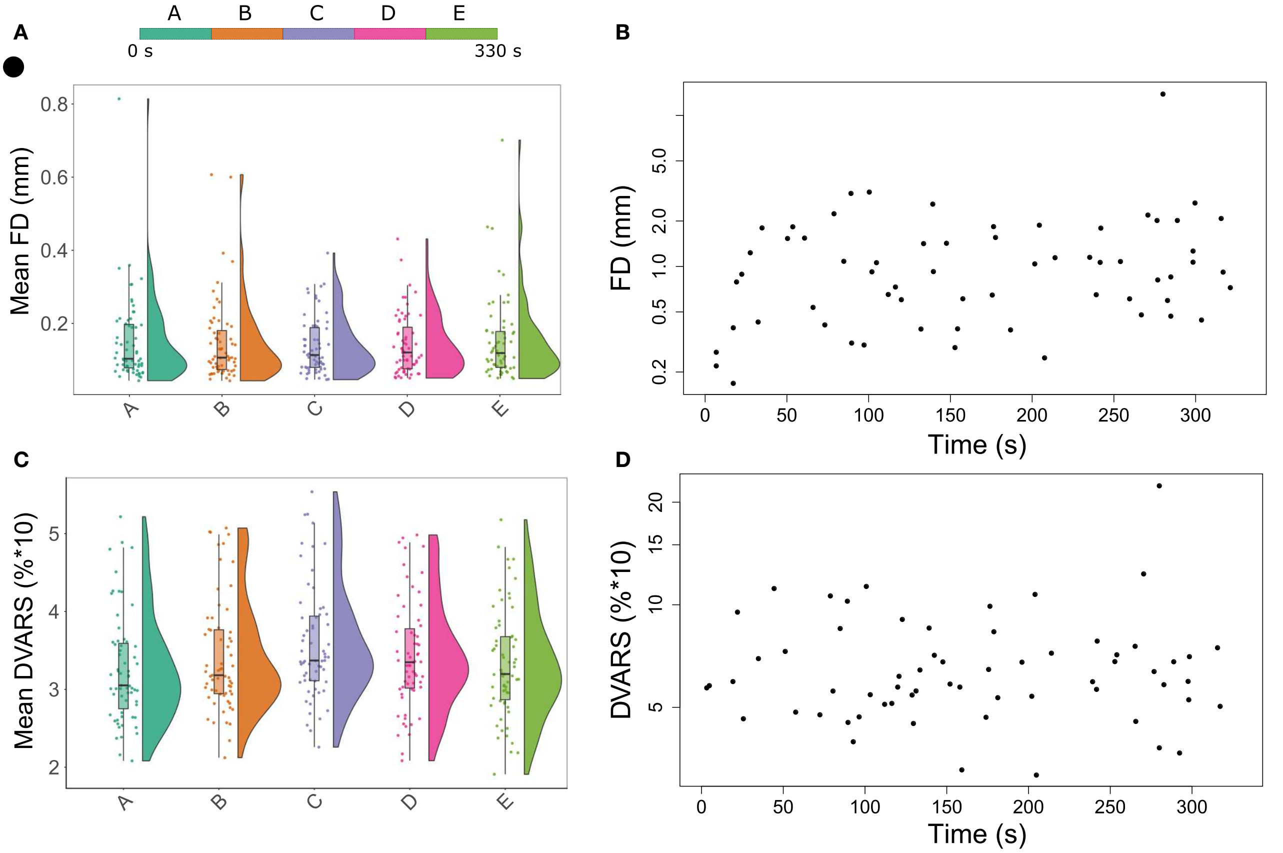

FIGURE 1 | Raincloud plots showing the distribution of mean head motion metrics (framewise displacement in **(A)** DVARS in **(C)** for each segment of the resting-state functional MRI scan. In **Figures 1B,D**, each point represents the maximum head motion value across the full scan (from one patient) measured using framewise displacement **(B)** and DVARS **(D)**, plotted against time.

BOLD delay lesion volumes was skewed, the volumes were log-transformed for this analysis. The BOLD delay thresholds (0 s, 2.3 s, 4.6 s; ref = 0 s) and the scan sessions (day 0 or day 1; ref = day 0) were accounted for in this model.

Spatial and Volumetric Comparison of a Subsample of Patients With DSC-MRI Data

In a subsample of the patients eligible for quantitative analysis (n = 10), DSC-MRI data was acquired during the same scanning session after the rsfMRI scan. DSC-MRI data were analyzed using Stroketool version 2.8 (2011 Digital Image Solutions—HJ Wittsack) by selecting an arterial input function of 5–10 voxels in the middle cerebral artery contralateral to the acute infarction (50). Time-to-maximum (Tmax) maps were calculated using block-circulant singular value decomposition deconvolution of the concentration-time curve (51).

In this subsample, the Tmax maps were delineated using the same automated procedure described above for the BOLD delay maps, after applying a Tmax threshold of >6 s (18, 52, 53). The Dice similarity coefficient was calculated between the perfusion lesions derived from each of the BOLD delay scans of different lengths and the Tmax maps. A Bland-Altman analysis was also performed to assess the agreement between Tmax perfusion lesion volumes and BOLD delay perfusion lesion volumes derived from the scans of different lengths.

Qualitative Analysis

Patients were included for qualitative analysis if they met the study's inclusion criteria, regardless of whether or not there was a visible perfusion lesion on their BOLD delay maps.

Two radiologists [K.V. [rater 1] and I.G. [rater 2]], both experienced in stroke perfusion imaging, visually assessed the BOLD delay maps of different scan lengths. The raters were blinded to all patient data and to the length of the scans from which the BOLD delay maps were generated, but had access to the DWI corresponding to each BOLD delay map. Prior to performing the readings, the raters were shown examples of the maps derived from an independent dataset (see **Supplementary Figure 2** for examples) and trained on how to fill in the data entry sheet.

Interpretability of Shortened BOLD Delay Maps

The raters assessed whether or not a perfusion lesion was visible on the BOLD delay maps, or if the BOLD delay map was uninterpretable. We calculated the agreement between the BOLD delay maps derived from each of the shortened scans and the BOLD delay maps derived from the full scan using unweighted Cohen's kappa. A binary logistic mixed model (48) (two level; random-intercept) was executed for comparing the interpretability of the BOLD delay maps (reference = "uninterpretable") derived from scans of different lengths while accounting for head motion and raters (ref = "rater 1").

Quality of BOLD Delay Maps

The raters assessed how noisy the BOLD delay maps were (on a scale of 1 to 3, with 3 indicating the highest level of noise) and how clear certain structures such as the ventricles were on the map (on a scale of 1 to 3, with 3 indicating the highest structure clarity). Examples of maps of various noisiness and structure clarity are shown in **Supplementary Figure 2**.

We used the quadratic-weighted Cohen's kappa (54) to assess the agreement between raters on the interpretability, noisiness, and structure clarity of the BOLD delay maps derived from each scan length.

Ordinal mixed models (55) were used to investigate the association between scan length and noise as well as structure clarity of the maps (two-level; random intercept models).

Note that in all statistical models used in this paper, subjects were level two units such that intra-individual correlation among the measures collected on a particular individual was taken into account and scan session identification (reference = "day 0") was included as a covariate in the models. All models in the qualitative analysis also accounted for the influence of the raters (reference = "rater 1").

Statistical Analysis

All statistical analyses were performed using *R* Statistical Software (56). The data and the code used for statistical analysis and data visualization in this study are publicly available at https://github.com/ahmedaak/BD_scan-shortening. Bland-Altman analysis was performed using the R package "blandr" (57), metrics of inter-rater agreement were calculated using the R package "irr" (58), linear mixed models using the "lmer" and "glmer" functions from the R package "lme4" (48), and ordinal mixed models using the "clmm" function from the R package "ordinal" (55). The distribution of continuous variables

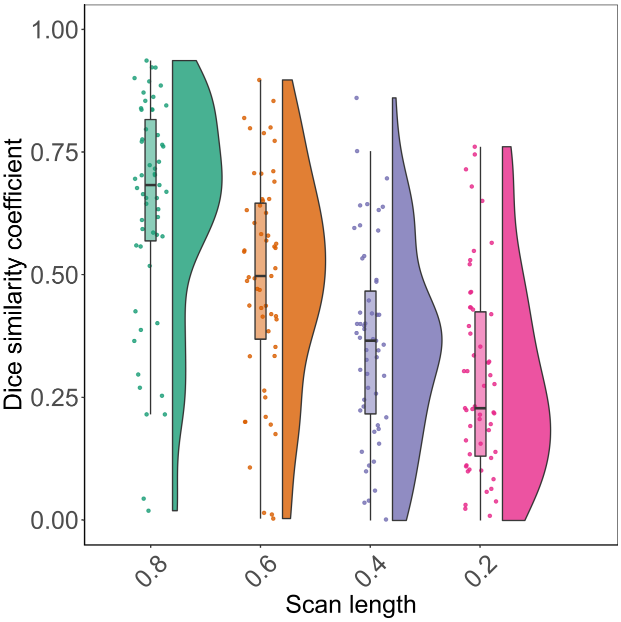

FIGURE 2 | Raincloud plots showing the distribution of Dice similarity coefficients (y axis) representing the degree of spatial overlap between BOLD delay lesions derived from resting-state functional MRI scans of different lengths (x axis) and the BOLD delay lesions derived from the full scan.

in different groups is visualized in this paper using raincloud plots, which combine dot plots, box plots, and violin plots (59). The distribution of categorical variables in different groups is visualized using spine plots (60).

RESULTS

Sixty-three patients who underwent an MRI scan within 24 h of stroke symptom onset were eligible for qualitative analysis. Forty-three of these patients had perfusion lesions on their BOLD delay maps and were selected for quantitative analysis. The characteristics of the two study groups for quantitative and qualitative analysis are presented separately in **Table 2**. The amount of head motion in each part of the rsfMRI scan is depicted for all patients in **Figure 1**.

The characteristics of the subsample who received a DSC-MRI scan are as follows: median age = 77.5 years (IQR = 63.5–80.3 years), median mRS at admission = 4 (IQR = 4–5), median mRS at discharge = 3 (IQR = 1–4), median NIHSS at admission = 11 (IQR = 7–16), median NIHSS at discharge = 4 (IQR = 2–8), median time from symptom onset to imaging = 1.5 h (IQR = 1–6.5 h). In this subsample, 7/10 patients were female, 3/10 had a follow-up MRI the next day, 4/10 had a previous stroke, 8/10 had a vessel occlusion on the TOF-MRA, 7/10 received intravenous thrombolysis, 4/10 received mechanical thrombectomy, 9/10 had an infarct in the MCA territory, and 1/10 had an infarct in the PCA territory. Data processing took a mean of 122 s (0.2 scan), 193 s (0.4 scan), 273 s (0.6 scan), 368 s (0.8 scan), and 411 s (full scan) per patient on an Intel® Xeon® X5570 CPU (2.93 GHz, 4 cores) with 64 GB of RAM. Note that a single thread was used for the processing.

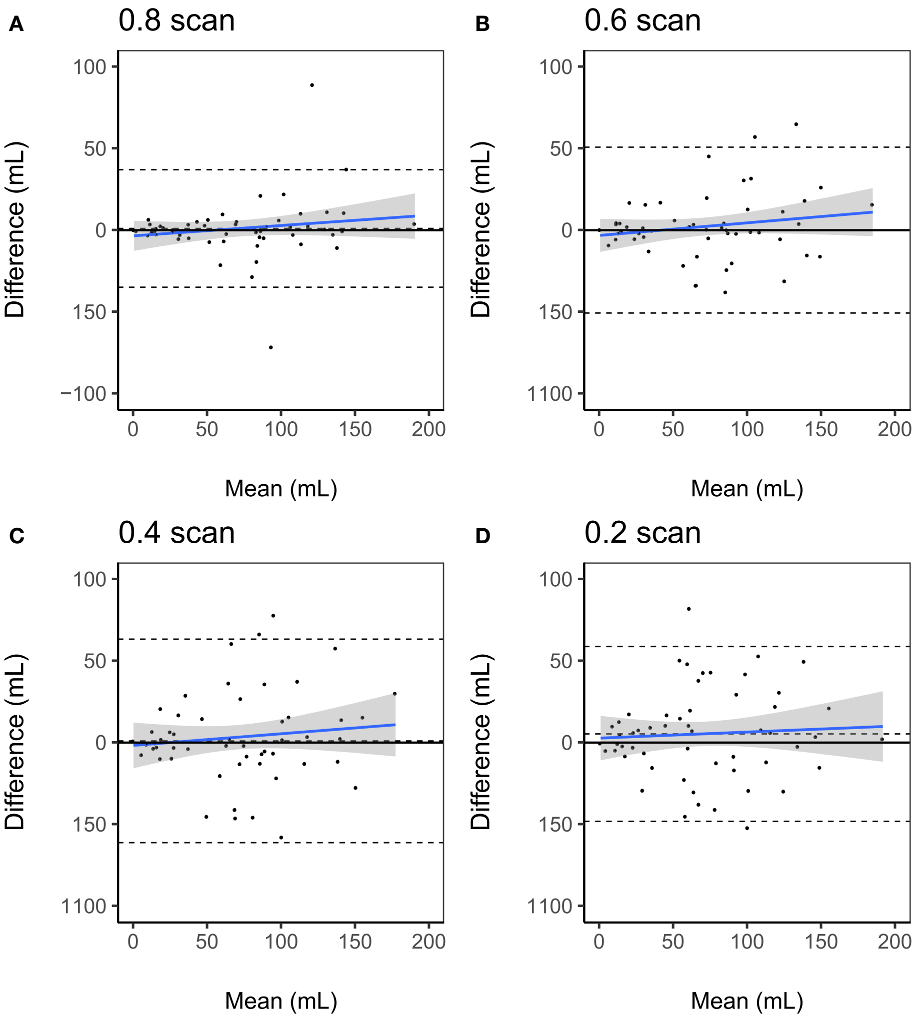

FIGURE 3 | Bland-Altman plots of volumetric agreement between BOLD delay lesion volumes derived from resting-state functional MRI scans of different lengths **(A)** 0.8 scan, **(B)** 0.6 scan, **(C)** 0.4 scan, **(D)** 0.2 scan and BOLD delay lesion volumes derived from the full scans. The upper and lower dashed lines represent the 95% limits of agreement and the middle dashed lines represent the bias (mean difference). The blue solid line and shaded gray region represent the regression lines and 95% confidence interval of the regression lines, respectively.

Quantitative Analysis

The DWIs and BOLD delay maps of all the patients in the quantitative analysis sample can be found here: https://doi.org/10.6084/m9.figshare.12022728.

Spatial Comparison of BOLD Delay Lesions

Figure 2 shows the distribution of spatial overlap metrics (Dice similarity coefficients) between BOLD delay lesions from each shortened scan and BOLD delay lesions from the full scan. The highest spatial overlap was between the 0.8 scan and the full scan (median = 0.68; IQR=0.56–0.81) and it decreased with decreasing scan length. The median Dice similarity coefficients between perfusion lesions from each BOLD delay scan length and Tmax perfusion lesions (for the subsample who also received DSC-MRI) were as follows: full scan = 0.29 (IQR = 0.02–0.33), 0.8 scan = 0.26 (IQR = 0.03–0.40), 0.6 scan = 0.17 (IQR = 0.03–0.39), 0.4 scan = 0.1 (IQR = 0.02–0.29), 0.2 scan = 0.16 (IQR = 0.02–0.32).

The results of the linear mixed model of the association between scan length and spatial overlap showed that a 1% decrease in scan length was associated with a 0.006 reduction on average in the Dice coefficient between the BOLD delay lesions derived from the shortened scan and the full scan (beta = 0.006, SE = 0.0004, $t = 13.6$, $p < 0.0001$).

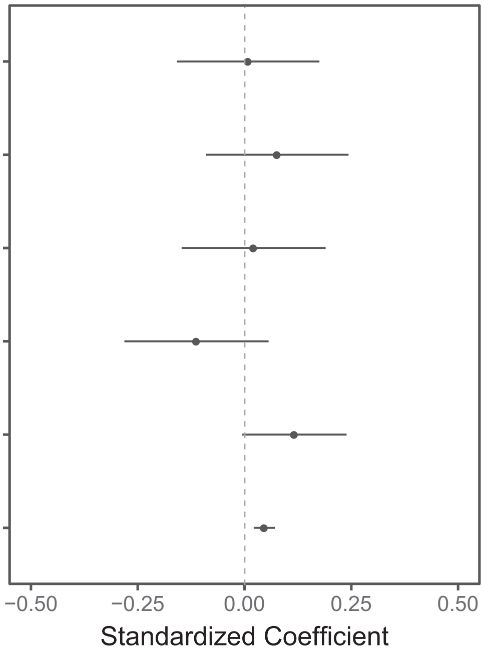

FIGURE 4 | Visualization of the results of the linear mixed model of the association between several predictors and BOLD delay lesion volumes. The points represent the standardized (beta) coefficients and the lines represent the 95% confidence intervals of the coefficients for each predictor. FD: framewise displacement. The scan lengths are shown as 0.8, 0.6, 0.4, and 0.2 with the full scan used as the reference category. This plot shows that the head motion metrics (mean FD and mean DVARS) are significantly associated with larger BOLD delay lesion volumes. There is no statistically significant difference between BOLD delay lesion volumes derived from the shorter resting-state functional MRI scans and the full scan. Note that only a subset of the predictors in this model are shown here—the numerical results of this linear mixed model, including the rest of the predictors, are shown in **Supplementary Table 1**.

Volumetric Comparison of BOLD Delay Lesions

The results of the Bland-Altman analysis are presented in **Figure 3** and the distribution of lesion volumes for each scan length is shown in **Supplementary Figure 1**. Compared to the BOLD delay lesion volumes derived from the full scan, the biases of the lesion volumes derived from the shortened scans were as follows: the 0.2 scan = 5.3 mL (a 7.7% overestimation relative to the mean of both scans, limits of agreement = −48.1–58.7 mL), 0.4 scan = 1.04 mL (a 4.5% overestimation relative to the mean of both methods, limits of agreement = −61.1–63.2), 0.6 scan = 0.05 mL (a 0.13% underestimation relative to the mean of both methods, limits of agreement = −50.6–50.7 mL), and 0.8 scan = 1.06 mL (a 1.4% overestimation relative to the mean of both methods, limits of agreement = −34.8–36.9 mL).

The results of the Bland-Altman analysis for the subsample who also received a DSC-MRI scan are shown in **Supplementary Figure 3**. Compared to the Tmax perfusion lesion volumes, the biases of the BOLD delay lesion volumes were as follows: the 0.2 scan = −14.5 mL (a 68.1% underestimation relative to the mean of both methods [BOLD delay and Tmax], limits of agreement = −80.6–51.5 mL), 0.4 scan = −8.2 mL (a 36.7% underestimation relative to the mean of both methods, limits of agreement = −68.0–51.7 mL), 0.6 scan = −18.3 mL (a 43.7% underestimation relative to the mean of both methods, limits of agreement = −80.2–43.5 mL), 0.8 scan = −17.2 (a 56.3% underestimation relative to the mean of both methods, limits of agreement = −65.7 to 31.3 mL), full scan = −12.9 mL (a 58.6% underestimation relative to the mean of both methods, limits of agreement = −58.6–32.6 mL).

The linear mixed model showed that there was no systematic impact of scan length on lesion volumes (**Figure 4** and **Supplementary Table 1**). Head motion measured using mean DVARS was associated with larger BOLD delay lesion volumes (beta = 0.05, 95% CI = 0.02–0.07, $t = 3.64$, $p = 0.0003$).

Qualitative Analysis

Diagnostic Accuracy

The interpretability of the BOLD delay maps derived from different scan lengths is shown in **Figure 5** for each of the raters. Agreement on map interpretability between BOLD delay maps derived from different scan lengths and those derived from the full scan are shown for each rater in **Supplementary Table 2**. The binary logistic mixed model revealed that scan lengths 0.2 (odds ratio = 0.21, 95% CI = 0.12–0.37, $p < 0.0001$) and 0.4 (odds ratio = 0.37, 95% CI = 0.21–0.64, $p = 0.0004$) were associated with decreased interpretability of the BOLD delay maps. Longer scans (0.8 and 0.6) showed no substantial association with interpretability of the BOLD delay maps (**Supplementary Table 3**).

Inter-Rater Agreement

Table 3 shows the inter-rater agreement on the interpretation, noisiness, and structure clarity of the BOLD delay maps derived

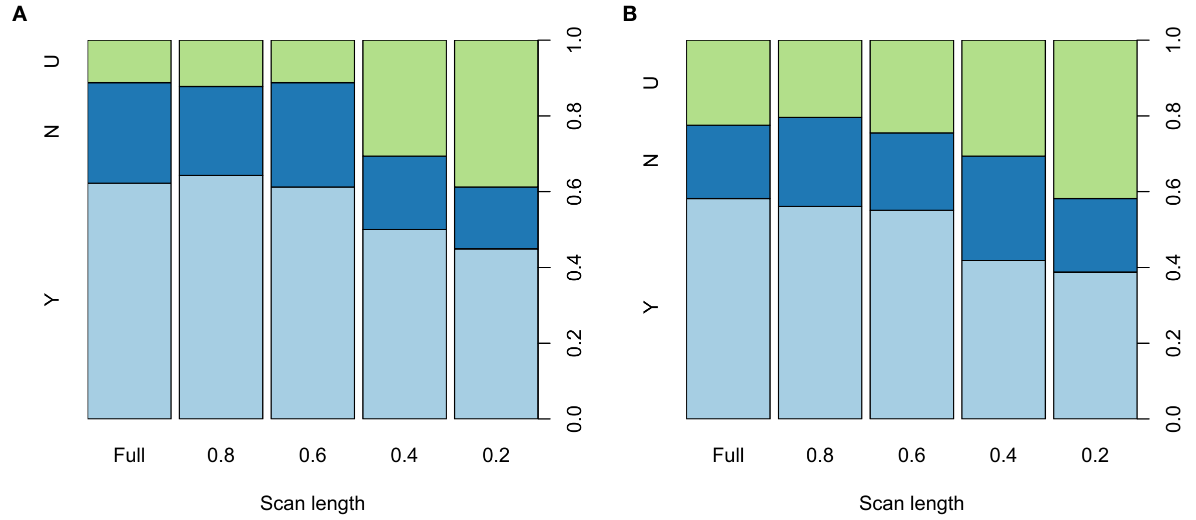

FIGURE 5 | Spine plots showing the distribution of the qualitative ratings of the BOLD delay maps derived from different resting-state functional MRI scan lengths made by rater 1 **(A)** and 2 **(B)** The maps were rated as either showing a perfusion lesion (Y, light blue), not showing a perfusion lesion (N, blue), or being uninterpretable (U, green). Statistically significant differences in interpretability are seen between the full scan and the 0.4 and 0.2 shortened scans. The quantitative results of the binary logistic mixed model investigating the effects of scan length on the interpretability of the BOLD delay maps are shown in **Supplementary Table 3**.

from different scan lengths. The raters' agreement on the interpretation of the BOLD delay maps was good across scan lengths (Cohen's kappa 0.64–0.82). Agreement on noisiness and structure clarity was markedly higher in the BOLD delay maps derived from the shorter scans than in those derived from the longer scans.

Quality of BOLD Delay Maps

The results of the qualitative assessment of scan noisiness and structure clarity by the two raters are shown in **Supplementary Figure 4**. The ordinal mixed models showed that scan lengths of 0.2 and 0.4, as well as head motion measured using mean framewise displacement and mean DVARS, were associated with more noise and less structure clarity on the BOLD delay maps (**Figure 6**). The quantitative results of the mixed models for noise and structure clarity are shown in **Supplementary Tables 4**, **5**, respectively.

DISCUSSION

In this study, the effects of scan length on the assessment of brain perfusion using BOLD delay maps in patients with ischemic stroke were systematically investigated. Our results show that scan length can be reduced from 5 min and 40 s to 3 min and 24 s without a significant loss of diagnostic accuracy and image quality of the BOLD delay maps.

A reduction of scan length by nearly two-and-a-half minutes is especially important in acute stroke, where patients are critically ill and decisions have to be made extremely quickly. The standard MRI protocol in our institution takes about 10 min (without perfusion imaging). Because time-to-treatment is a critical factor influencing stroke outcome, prolonging this by anything more than a few minutes is undesirable.

TABLE 3 | Inter-rater agreement (quadratic-weighted Cohen's kappa) on BOLD delay maps derived from different scan lengths.

Scan length	Interpretation[a]	Noise[b]	Structure clarity[b]
Full	0.64	0.22	0.40
0.8	0.71	0.29	0.15
0.6	0.82	0.25	0.26
0.4	0.75	0.67	0.40
0.2	0.67	0.72	0.48

[a] *Refers to whether the rater judged the map as showing aperfusion lesion, not showing a perfusion lesion, or being uninterpretable.*

[b] *Judged as high, medium or low.*

Our findings are overall in accordance with two previous studies. Lv et al. investigated the similarity between areas of BOLD signal delay and areas of hypoperfusion identified by DSC-MRI in acute stroke patients (61). The acquisition time was 5 min 50 s and the scan length was gradually decreased in increments of 10 volumes. They found that BOLD delay maps acquired in 3 min and 4 s provided qualitatively similar information to that of the full length scan in terms of overlap with the mean transit time (MTT; a parameter map derived from DSC-MRI) lesion of the subject. Christen et al., on the other hand, found that BOLD delay maps derived from resting-state functional MRI scans lasting 3 min and 36 s correlated highly with Tmax in Moyamoya patients (23). However, the impact of scan shortening on the diagnostic quality and clinical interpretability of BOLD delay maps was not systematically investigated in these studies.

In this study, agreement between raters on the evaluation of hypoperfusion presence at different scan lengths was good (weighted Cohen's kappa = 0.64 to 0.82). Data on the inter-rater

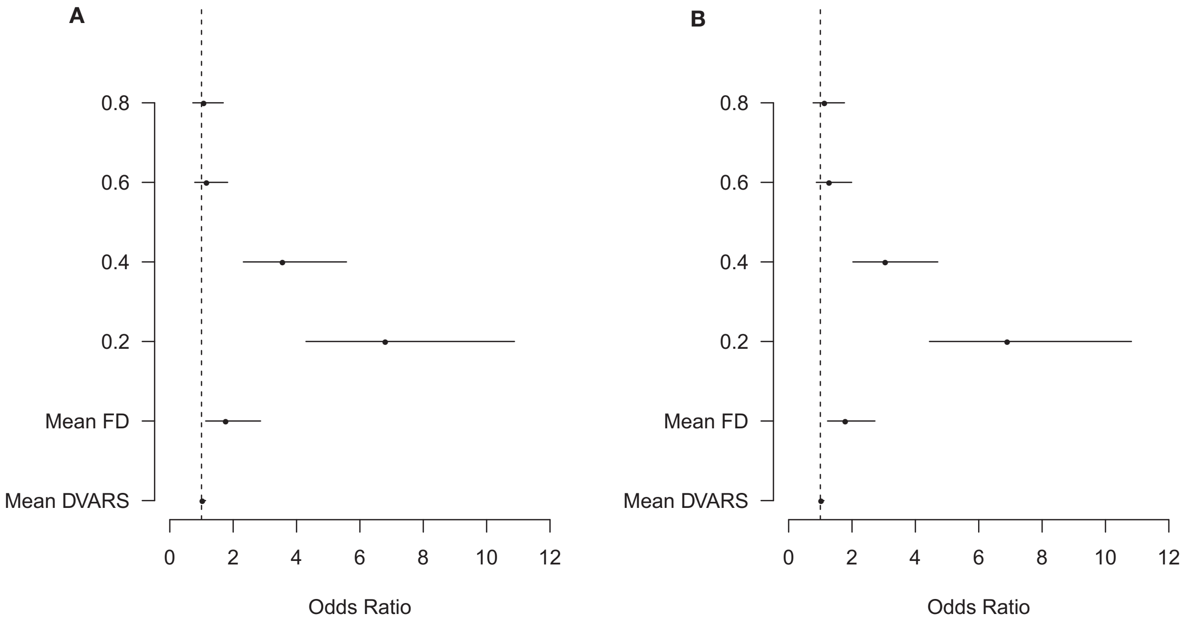

FIGURE 6 | Visualization of the results of the ordinal mixed models of the association between several predictors and BOLD delay map noisiness **(A)** and structure clarity **(B)**. The points represent the odds ratios and the lines represent the 95% confidence intervals of the odds ratios for each predictor. The vertical dashed line represents an odds ratio of 1. FD, framewise displacement. The scan lengths are shown as 0.8, 0.6, 0.4, and 0.2 with the full scan used as the reference category. The plot shows that head motion (mean FD and mean DVARS) as well as the shortened 0.4 and 0.2 scans are associated with a significantly higher odds of more noise and less structure clarity than full scans. Note that only a subset of the predictors in this model are shown here—the numerical results of this ordinal mixed model, including the rest of the predictors, are shown in **Supplementary Table 4** (noisiness) and 5 (structure clarity).

agreement of this relatively new perfusion imaging method has thus far been unavailable. In a study of 105 acute stroke patients, a similar level of inter-rater agreement on detecting perfusion deficits was found for DSC-MRI and ASL, with weighted Cohen's kappa values of 0.64 and 0.6, respectively (62). In our study, agreement on interpretability, structure clarity, and noisiness of the BOLD delay maps was higher for shorter scans than longer scans. This may be explained by the relative ease with which poor quality maps were judged by the raters. Overall, we found that the inter-rater agreement of this relatively new perfusion imaging method is similar to that observed when using more established perfusion imaging methods.

Several factors potentially interact with scan length to influence the diagnostic quality of BOLD delay maps. The temporal resolution of the resting-state functional MRI sequence is one such factor. Although the BOLD oscillations driving the calculation of BOLD delay are likely slow (<0.15 Hz), scanning with high temporal resolution, as done in this study using multiband EPI (42, 43), has the advantage of allowing high-frequency cardiac and respiratory activity to be filtered out of the data.

Head motion, on the other hand, causes undesired changes in the BOLD signal (44, 63) that adversely affect the cross-correlation underlying BOLD delay calculation. In a recent pilot study, we found that the intra-subject reproducibility of BOLD delay values in stroke patients was adversely influenced by head motion (64). In the current study, we therefore accounted for subject head motion in our analysis of the relationship between scan length and BOLD delay map quality and found that head motion significantly and adversely affected the level of noise, the structure clarity, and the volume of BOLD delay lesions, independent of scan length.

Considering that head motion is one of the main drawbacks hindering BOLD delay's use for brain perfusion assessment (14), exploring appropriate and reliable ways of reducing motion and its effects on the BOLD signal is crucial. Retrospective motion correction techniques such as scrubbing, which effectively removes volumes with high motion, have shown promise in functional connectivity studies (44). However, such techniques require that a sufficient amount of low-motion data remain after the removal of high-motion volumes (46). For this to be applicable, we need to know the minimum amount of data needed to generate adequate results. In functional connectivity studies, 10 to 15 min of data generally provide the best test-retest reliability (65). Our results suggest that much less data is required to provide diagnostically acceptable BOLD delay maps. With this knowledge, real-time motion monitoring approaches can allow us to continue scanning until a sufficient amount of low-motion data is acquired (66). This would reduce waste by reducing overscanning and, more importantly, allows scans to be tailored to the urgency of specific clinical situations.

Our study has a few limitations. We were unable to acquire DSC-MRI data in the entire sample in order to directly compare the shortened BOLD delay maps with a reference standard.

This was primarily due to the fact that we no longer routinely perform DSC-MRI at our stroke center due to the European Medicines Agency's recent recommendation to restrict the use of gadolinium-based contrast agents (7). However, the relationship between BOLD delay and perfusion measured using DSC-MRI has been established in several independent studies (14, 16, 18–21, 27). In this study, we chose to retrospectively break up longer scans into smaller parts, which is not the same as acquiring several scans of varying lengths. We chose this strategy for practical reasons, as acquiring several scans of different lengths would have greatly prolonged the scanning protocol and would have been infeasible in the context of acute stroke. However, this choice potentially limits how generalizable are results are to real-life situations where shortened scans are independently acquired. In addition, it should be kept in mind that several other potential factors may interact with scan length to influence BOLD delay map quality, including sequence parameters and field strength. Investigating the influence of these factors is beyond the scope of this study, and is currently the focus of ongoing work by our group (64). Finally, whether scan times longer than the full scan implemented in the current study (5 min 40 s) provide even better BOLD delay map quality is yet to be investigated. Such scans would not, however, be suitable in situations where urgent decision-making is required, such as acute stroke.

In conclusion, we show that BOLD delay maps derived from resting-state fMRI scans lasting 3 min 24 s provide sufficient diagnostic quality and adequate assessment of perfusion lesion volumes. This implies that scans can be shortened beyond currently usual scan times, which may be helpful for reducing the effect of patient motion or in situations where quick clinical decisions need to be made. Our results represent an important step toward implementing BOLD delay for contrast-agent-free assessment of brain perfusion in acute stroke patients in routine clinical practice.

DATA AVAILABILITY STATEMENT

The data and the code used for statistical analysis and data visualization in this study are publicly available at https://github.com/ahmedaak/BD_scan-shortening.

ETHICS STATEMENT

The studies involving human participants were reviewed and approved by Charité institutional review board EA1/200/13. The patients/participants provided their written informed consent to participate in this study.

AUTHOR CONTRIBUTIONS

AT, AK, JF, and AV: Conception or design of the work. JF, KV, IG, EK, and AK: Data collection. UG, IG, KV, AK, and AT: Data analysis and interpretation. AT and AK: Drafting the article. AT, KV, IG, UG, EK, JF, AV, and AK: Critical revision of the article and final approval of the version to be published.

ACKNOWLEDGMENTS

The authors thank the University of Minnesota Center for Magnetic Resonance Research for providing the multiband EPI sequence used in this study. Dr. Ahmed Khalil is a participant in the BIH-Charité Junior Clinician Scientist Program funded by the Charité –Universitätsmedizin Berlin and the Berlin Institute of Health.

SUPPLEMENTARY MATERIAL

The Supplementary Material for this article can be found online at: https://www.frontiersin.org/articles/10.3389/fneur.2020.00381/full#supplementary-material

REFERENCES

1. Fisher M, Albers GW. Advanced imaging to extend the therapeutic time window of acute ischemic stroke. *Ann Neurol.* (2013) 73:4–9. doi: 10.1002/ana.23744
2. Luby M, Warach SJ, Albers GW, Baron J-C, Cognard C, Dávalos A, et al. Identification of imaging selection patterns in acute ischemic stroke patients and the influence on treatment and clinical trial enrollment decision making. *Int J Stroke*. (2016) 11:180–90. doi: 10.1177/1747493015616634
3. Albers GW, Marks MP, Kemp S, Christensen S, Tsai JP, Ortega-Gutierrez S, et al. Thrombectomy for stroke at 6 to 16 hours with selection by perfusion imaging. *N Engl J Med.* (2018) 378:708–18. doi: 10.1056/NEJMoa1713973
4. Kuo PH, Kanal E, Abu-Alfa AK, Cowper SE. Gadolinium-based MR contrast agents and nephrogenic systemic fibrosis. *Radiology*. (2007) 242:647–9. doi: 10.1148/radiol.2423061640
5. McDonald RJ, McDonald JS, Kallmes DF, Jentoft ME, Murray DL, Thielen KR, et al. Intracranial Gadolinium Deposition after Contrast-enhanced MR Imaging. *Radiology*. (2015) 275:772–82. doi: 10.1148/radiol.15150025
6. Gulani V, Calamante F, Shellock FG, Kanal E, Reeder SB. Gadolinium deposition in the brain: summary of evidence and recommendations. *Lancet Neurol.* (2017) 16:564–70. doi: 10.1016/S1474-4422(17)30158-8
7. European Medicines Agency. *Gadolinium-Containing Contrast Agents*. (2018) Available Online at: https://www.ema.europa.eu/; https://www.ema.europa.eu/en/medicines/human/referrals/gadolinium-containing-contrast-agents [Accessed November 7, 2019].
8. Tong Y, Hocke LM, Licata SC, Frederick BD. Low-frequency oscillations measured in the periphery with near-infrared spectroscopy are strongly correlated with blood oxygen level-dependent functional magnetic resonance imaging signals. *J Biomed Opt.* (2012) 17:106004. doi: 10.1117/1.JBO.17.10.106004
9. Tong Y, Hocke LM, Lindsey KP, Erdogan SB, Vitaliano G, Caine CE, et al. Systemic low-frequency oscillations in BOLD signal vary with tissue type. *Front Neurosci.* (2016) 10:313. doi: 10.3389/fnins.2016.00313
10. Tong Y, Yao J. (fiona), Chen JJ, Frederick B, de B. The resting-state fMRI arterial signal predicts differential blood transit time through the brain. *J Cereb Blood Flow Metab*. (2018) 39:1148–60. doi: 10.1177/0271678X17753329
11. Tong Y, Hocke LM, Frederick BB. Low frequency systemic hemodynamic "noise" in resting state BOLD fMRI: characteristics, causes, implications,

mitigation strategies, and applications. *Front Neurosci.* (2019) 13:787. doi: 10.3389/fnins.2019.00787

12. Liu Y, D'Arceuil H, He J, Duggan M, Gonzalez G, Pryor J, et al. MRI of spontaneous fluctuations after acute cerebral ischemia in nonhuman primates. *J Magn Reson Imaging.* (2007) 26:1112–6. doi: 10.1002/jmri.21131
13. Qun-li Y, Zhang HY, Nie BB, Fang F, Jiao Y, Teng GJ. MRI assessment of amplitude of low-frequency fluctuation in rat brains with acute cerebral ischemic stroke. *Neurosci Lett.* (2012) 509:22–6. doi: 10.1016/j.neulet.2011.12.036
14. Lv Y, Margulies DS, Cameron Craddock R, Long X, Winter B, Gierhake D, et al. Identifying the perfusion deficit in acute stroke with resting-state functional magnetic resonance imaging. *Ann Neurol.* (2013) 73:136–9. doi: 10.1002/ana.23763
15. Tsai Y-H, Yuan R, Huang Y-C, Weng H-H, Yeh M-Y, Lin C-P, et al. Altered resting-state FMRI signals in acute stroke patients with ischemic penumbra. *PLoS ONE.* (2014) 9:e105117. doi: 10.1371/journal.pone.0105117
16. Amemiya S, Kunimatsu A, Saito N, Ohtomo K. Cerebral hemodynamic impairment: assessment with resting-state functional MR imaging. *Radiology.* (2014) 270:548–55. doi: 10.1148/radiol.13130982
17. Siegel JS, Snyder AZ, Ramsey L, Shulman GL, Corbetta M. The effects of hemodynamic lag on functional connectivity and behavior after stroke. *J Cereb Blood Flow Metab.* (2016) 36:2162–76. doi: 10.1177/0271678X15614846
18. Khalil AA, Ostwaldt AC, Nierhaus T, Ganeshan R, Audebert HJ, Villringer K, et al. Relationship between changes in the temporal dynamics of the blood-oxygen-level-dependent signal and hypoperfusion in acute ischemic stroke. *Stroke.* (2017) 48:925–31. doi: 10.1161/STROKEAHA.116.015566
19. Khalil AA, Villringer K, Filleböck V, Hu JY, Rocco A, Fiebach JB, et al. Non-invasive monitoring of longitudinal changes in cerebral hemodynamics in acute ischemic stroke using BOLD signal delay. *J Cereb Blood Flow Metab.* (2018) 40:23–34. doi: 10.1177/0271678X18803951
20. Ni L, Li J, Li W, Zhou F, Wang F, Schwarz CG, et al. The value of resting-state functional MRI in subacute ischemic stroke: comparison with dynamic susceptibility contrast-enhanced perfusion MRI. *Sci Rep.* (2017) 7:41586. doi: 10.1038/srep41586
21. Chen Q, Zhou J, Zhang H, Chen Y, Mao C, Chen X, et al. One-step analysis of brain perfusion and function for acute stroke patients after reperfusion: A resting-state fMRI study. *J. Magn. Reson. Imaging.* (2018) 50:221–9. doi: 10.1002/jmri.26571
22. Lv Y, Wei W, Song Y, Han Y, Zhou C, Zhou D, et al. Non-invasive evaluation of cerebral perfusion in patients with transient ischemic attack: an fMRI study. *J Neurol.* (2018) 266:157–64. doi: 10.1007/s00415-018-9113-3
23. Christen T, Jahanian H, Ni WW, Qiu D, Moseley ME, Zaharchuk G. Noncontrast mapping of arterial delay and functional connectivity using resting-state functional MRI: a study in Moyamoya patients. *J Magn Reson Imaging.* (2015) 41:424–30. doi: 10.1002/jmri.24558
24. Yan S, Qi Z, An Y, Zhang M, Qian T, Lu J. Detecting perfusion deficit in Alzheimer's disease and mild cognitive impairment patients by resting-state fMRI. *J Magn Reson Imaging.* (2018) 49:1099–104. doi: 10.1002/jmri.26283
25. Shah MN, Mitra A, Goyal MS, Snyder AZ, Zhang J, Shimony JS, et al. Resting state signal latency predicts laterality in pediatric medically refractory temporal lobe epilepsy. *Childs Nerv Syst.* (2018) 34:901–10. doi: 10.1007/s00381-018-3770-5
26. Coloigner J, Vu C, Bush A, Borzage M, Rajagopalan V, Lepore N, et al. BOLD delay times using group delay in sickle cell disease. In: Styner MA, and Angelini ED, editors. *SPIE Medical Imaging.* San Diego, CA: International Society for Optics and Photonics (2016). p. 97843M. doi: 10.1117/12.2217263
27. Tong Y, Lindsey KP, Hocke LM, Vitaliano G, Mintzopoulos D, Frederick BD. Perfusion information extracted from resting state functional magnetic resonance imaging. *J Cereb Blood Flow Metab.* (2017) 37:564–76. doi: 10.1177/0271678X16631755
28. Mandell DM, Han JS, Poublanc J, Crawley AP, Stainsby JA, Fisher JA, et al. Mapping cerebrovascular reactivity using blood oxygen level-dependent MRI in patients with arterial steno-occlusive disease: comparison with arterial spin labeling MRI. *Stroke.* (2008) 39:2021–8. doi: 10.1161/STROKEAHA.107.506709
29. Golestani AM, Wei LL, Chen JJ. Quantitative mapping of cerebrovascular reactivity using resting-state BOLD fMRI: validation in healthy adults. *Neuroimage.* (2016) 138:147–63. doi: 10.1016/j.neuroimage.2016.05.025
30. Smeeing DPJ, Hendrikse J, Petersen ET, Donahue MJ, de Vis JB. Arterial spin labeling and blood oxygen level-dependent MRI cerebrovascular reactivity in cerebrovascular disease: a systematic review and meta-analysis. *Cerebrovasc Dis.* (2016) 42:288–307. doi: 10.1159/000446081
31. Fierstra J, Van Niftrik C, Warnock G, Wegener S, Piccirelli M, Pangalu A, et al. Staging hemodynamic failure with blood oxygen-level-dependent functional magnetic resonance imaging cerebrovascular reactivity a comparison versus gold standard (15O-)H2O-positron emission tomography. *Stroke.* (2018) 49:621–9. doi: 10.1161/STROKEAHA.117.020010
32. Nishida S, Aso T, Takaya S, Takahashi Y, Kikuchi T, Funaki T, et al. Resting-state functional magnetic resonance imaging identifies cerebrovascular reactivity impairment in patients with arterial occlusive diseases: a pilot study. *Neurosurgery.* (2018). 85:680–8. doi: 10.1093/neuros/nyy434
33. Venkatraghavan L, Poublanc J, Han JS, Sobczyk O, Rozen C, Sam K, et al. Measurement of cerebrovascular reactivity as blood oxygen level-dependent magnetic resonance imaging signal response to a hypercapnic stimulus in mechanically ventilated patients. *J Stroke Cerebrovasc Dis.* (2018) 27:301–8. doi: 10.1016/j.jstrokecerebrovasdis.2017.08.035
34. Prokopiou PC, Pattinson KTS, Wise RG, Mitsis GD. Modeling of dynamic cerebrovascular reactivity to spontaneous and externally induced CO2 fluctuations in the human brain using BOLD-fMRI. *Neuroimage.* (2019) 186:533–48. doi: 10.1016/j.neuroimage.2018.10.084
35. Aso T, Urayama S, Fukuyama H, Murai T. Axial variation of deoxyhemoglobin density as a source of the low-frequency time lag structure in blood oxygenation level-dependent signals. *PLoS ONE.* (2019) 14:e0222787. doi: 10.1371/journal.pone.0222787
36. Qian T, Wang ZAPG. Measuring the timing information of blood flow in acute stroke with the background. *Proc. Intl. Soc. Mag. Reson. Med.* (2015) 23:2195.
37. Qian T, Zanchi D, Rodriguez C, Ackermann M, Giannakopoulos P, Haller S. Detecting perfusion pattern based on the background low-frequency fluctuation in resting-state functional MRI data and its influence on resting-state networks: an iterative post-processing approach. *Brain Connect.* (2017) 7:627–34. doi: 10.1089/brain.2017.0545
38. Wu J, Dehkharghani S, Nahab F, Allen J, Qiu D. The effects of acetazolamide on the evaluation of cerebral hemodynamics and functional connectivity using blood oxygen level-dependent MR imaging in patients with chronic steno-occlusive disease of the anterior circulation. *Am J Neuroradiol.* (2017) 38:139–45. doi: 10.3174/ajnr.A4973
39. Yang H-CS, Liang Z, Yao JF, Shen X, Frederick BD, Tong Y. Vascular effects of caffeine found in BOLD fMRI. *J Neurosci Res.* (2018) 97:456–66. doi: 10.1002/jnr.24360
40. Zhao Y, Lambon Ralph MA, Halai AD. Relating resting-state hemodynamic changes to the variable language profiles in post-stroke aphasia. *NeuroImage.* (2018) 20:611–9. doi: 10.1016/j.nicl.2018.08.022
41. Jahanian H, Christen T, Moseley ME, Zaharchuk G. Erroneous resting-state fMRI connectivity maps due to prolonged arterial arrival time and how to fix them. *Brain Connect.* (2018) 8:362–70. doi: 10.1089/brain.2018.0610
42. Feinberg DA, Moeller S, Smith SM, Auerbach E, Ramanna S, Matt F, et al. Multiplexed echo planar imaging for sub-second whole brain FMRI and fast diffusion imaging. *PLoS ONE.* (2010) 5:e15710. doi: 10.1371/journal.pone.0015710
43. Xu J, Moeller S, Auerbach EJ, Strupp J, Smith SM, Feinberg DA, et al. Evaluation of slice accelerations using multiband echo planar imaging at 3 T. *Neuroimage.* (2013) 83:991–1001. doi: 10.1016/j.neuroimage.2013.07.055
44. Power JD, Barnes KA, Snyder AZ, Schlaggar BL, Petersen SE. Spurious but systematic correlations in functional connectivity MRI networks arise from subject motion. *Neuroimage.* (2012) 59:2142–54. doi: 10.1016/j.neuroimage.2011.10.018
45. Tustison NJ, Avants BB. Explicit B-spline regularization in diffeomorphic image registration. *Front Neuroinform.* (2013) 7:39. doi: 10.3389/fninf.2013.00039
46. Siegel JS, Shulman GL, Corbetta M. Measuring functional connectivity in stroke: approaches and considerations. *J Cereb Blood Flow Metab.* (2017) 37:2665–78. doi: 10.1177/0271678X17709198
47. Dice LR. Measures of the amount of ecologic association between species. *Ecology.* (1945) 26:297–302. doi: 10.2307/1932409
48. Bates D, Mächler M, Bolker B, Walker S. Fitting linear mixed-effects models using lme4. *J Stat Softw.* (2014) 67:1–48. doi: 10.18637/jss.v067.i01

49. Martin Bland J, Altman D. Statistical methods for assessing agreement between two methods of clinical measurement. *Lancet*. (1986) 327:307–10. doi: 10.1016/S0140-6736(86)90837-8
50. Ebinger M, Brunecker P, Jungehülsing GJ, Malzahn U, Kunze C, Endres M, et al. Reliable perfusion maps in stroke MRI using arterial input functions derived from distal middle cerebral artery branches. *Stroke*. (2010) 41:95–101. doi: 10.1161/STROKEAHA.109.559807
51. Wu O, Østergaard L, Weisskoff RM, Benner T, Rosen BR, Sorensen AG. Tracer arrival timing-insensitive technique for estimating flow in MR perfusion-weighted imaging using singular value decomposition with a block-circulant deconvolution matrix. *Magn Reson Med.* (2003) 50:164–74. doi: 10.1002/mrm.10522
52. Olivot JM, Mlynash M, Thijs VN, Kemp S, Lansberg MG, Wechsler L, et al. Optimal tmax threshold for predicting penumbral tissue in acute stroke. *Stroke*. (2009) 40:469–75. doi: 10.1161/STROKEAHA.108.526954
53. Zaro-Weber O, Moeller-Hartmann W, Heiss WD, Sobesky J. Maps of time to maximum and time to peak for mismatch definition in clinical stroke studies validated with positron emission tomography. *Stroke*. (2010) 41:2817–21. doi: 10.1161/STROKEAHA.110.594432
54. Cohen J. A coefficient of agreement for nominal scales. *Educ Psychol Meas.* (1960) 20:37–46. doi: 10.1177/001316446002000104
55. Christensen RHB. *Regression Models for Ordinal Data*. R package version 2019. (2019) 4–25. Available online at: http://www.cran.r-project.org/package=ordinal/
56. R Core Team. (2013). *R: A Language and Environment for Statistical Computing*. Available Online at: http://www.R-project.org/. (accessed March 19, 2020).
57. Datta D. blandr: a bland-altman method comparison package for R. (2017) 10. doi: 10.5281/zenodo.824514
58. Gamer M, Lemon J, and Puspendra Singh IF. (2019). irr: various coefficients of interrater reliability and agreement. Available at: https://CRAN.R-project.org/package=irr. (accessed January 8, 2020).
59. Allen M, Poggiali D, Whitaker K, Marshall TR, Kievit RA. Raincloud plots: a multi-platform tool for robust data visualization. *Wellcome Open Res*. (2019) 4:63. doi: 10.12688/wellcomeopenres.15191.1
60. Meyer D, Zeileis A, Hornik K. Visualizing Contingency Tables. In: Chen C-H, Härdle W, and Unwin A, editors. *Handbook of Data Visualization*. Springer Berlin Heidelberg (2008). p. 589–616. doi: 10.1007/978-3-540-33037-0_23
61. Lv Y. *Application of Resting-State fMRI Methods to Acute Ischemic Stroke Dissertation*. (2013).
62. Bokkers RPH, Hernandez DA, Merino JG, Mirasol RV, Van Osch MJ, Hendrikse J, et al. Whole-brain arterial spin labeling perfusion MRI in patients with acute stroke. *Stroke*. (2012) 43:1290–4. doi: 10.1161/STROKEAHA.110.589234
63. Van Dijk KRA, Sabuncu MR, Buckner RL. The influence of head motion on intrinsic functional connectivity MRI. *Neuroimage*. (2012) 59:431–8. doi: 10.1016/j.neuroimage.2011.07.044
64. Khalil AA, Tanritanir AC, Grittner U, Villringer A, Fiebach J, Mekle R. Reproducibility of BOLD delay perfusion measurements in acute stroke patients. In: *Proceedings of the International Society for Magnetic Resonance in Medicine*. (2018). Available Online at: http://archive.ismrm.org/2018/4823.html [Accessed November 7, 2019].
65. Birn RM, Molloy EK, Patriat R, Parker T, Meier TB, Kirk GR, et al. The effect of scan length on the reliability of resting-state fMRI connectivity estimates. *Neuroimage*. (2013) 83:550–8. doi: 10.1016/j.neuroimage.2013.05.099
66. Dosenbach NUF, Koller JM, Earl EA, Miranda-Dominguez O, Klein RL, Van AN, et al. Real-time motion analytics during brain MRI improve data quality and reduce costs. *Neuroimage*. (2017) 161:80–93. doi: 10.1016/j.neuroimage.2017.08.025

Conflict of Interest: KV and JF were funded by the German Federal Ministry of Education and Research (01EO0801, 01EO01301). JF has received consulting, lecture, advisory board fees from BioClinica, Cerevast, Artemida, Brainomix. AK, KV, and JF were co-inventors of a patent application relating to a method for automated, user-independent delineation of perfusion lesions, used in this manuscript.

The remaining authors declare that the research was conducted in the absence of any commercial or financial relationships that could be construed as a potential conflict of interest.

frontiers in Neurology

ORIGINAL RESEARCH
published: 05 June 2020
doi: 10.3389/fneur.2020.00418

The Clinical Value of ^{18}F-FDG-PET in Autoimmune Encephalitis Associated With LGI1 Antibody

Xiao Liu[1†], Wei Shan[1,2,3†], Xiaobin Zhao[3,4], Jiechuan Ren[1,3], Guoping Ren[1,3], Chao Chen[1,3], Weixiong Shi[1,3], Ruijuan Lv[1,3], Zhimei Li[1,3], Yaou Liu[3,5], Lin Ai[3,4] and Qun Wang[1,2,3*]*

[1] Department of Neurology, Beijing Tiantan Hospital, Capital Medical University, Beijing, China, [2] Beijing Institute for Brain Disorders, Beijing, China, [3] China National Clinical Research Center for Neurological Diseases, Beijing, China, [4] Department of Nuclear Medicine, Beijing Tiantan Hospital, Capital Medical University, Beijing, China, [5] Department of Radiology, Beijing Tiantan Hospital, Capital Medical University, Beijing, China

Edited by:
Freimut Dankwart Juengling,
Universität Bern, Switzerland

Reviewed by:
Valentina Garibotto,
Geneva University Hospitals (HUG), Switzerland
Tino Prell,
University Hospital Jena, Germany

***Correspondence:**
Lin Ai
ailin@bjtth.org
Qun Wang
wangq@ccmu.edu.cn

†These authors have contributed equally to this work

Specialty section:
This article was submitted to Applied Neuroimaging, a section of the journal Frontiers in Neurology

Received: *25 September 2019*
Accepted: *21 April 2020*
Published: *05 June 2020*

Citation:
Liu X, Shan W, Zhao X, Ren J, Ren G, Chen C, Shi W, Lv R, Li Z, Liu Y, Ai L and Wang Q (2020) The Clinical Value of ^{18}F-FDG-PET in Autoimmune Encephalitis Associated With LGI1 Antibody. Front. Neurol. 11:418. doi: 10.3389/fneur.2020.00418

Purpose: The metabolic patterns of ^{18}F-fluoro-2-deoxy-*d*-glucose positron emission tomography (^{18}F-FDG-PET) in autoimmune encephalitis associated with leucine-rich glioma-inactivated 1 antibody (LGI1 AE) are still unclear. We performed a cohort study to investigate the clinical metabolic characteristics and diagnostic value based on ^{18}F-FDG-PET in patients with LGI1 AE.

Materials and Methods: A total of 34 patients including 18 patients (53%) in the acute phase and 16 patients (47%) in the chronic phase who were diagnosed with LGI1 AE were retrospectively analyzed from October 2014 to June 2018 at the Department of Neurology in Beijing Tiantan Hospital, the Capital Medical University. The clinical data were collected by searching through electronic medical records.

Results: The initial ^{18}F-FDG-PET scan indicated a significant abnormal metabolic pattern in 31 LGI1 AE patients (91%), whereas only 20 patients (59%) showed an abnormal MRI signal ($P < 0.05$). The ^{18}F-FDG-PET metabolic pattern was reversible after treatment; most of the patients showed an almost normal uptake of ^{18}F-FDG-PET after discharge. Regarding the spatial distribution, the abnormal metabolic pattern in LGI1 AE subjects exhibiting hypermetabolism was specifically located in the basal ganglia (BG) and medial temporal lobe (MTL). BG hypermetabolism was observed in 28 subjects (82%), and 68% of patients showed MTL hypermetabolism. A total of 17 patients (50%) exhibited faciobrachial dystonic seizures (FBDS), and the remaining subjects showed non-FBDS symptoms (50 and 50%). BG-only hypermetabolism was detected in seven subjects in the FBDS subgroup (7/16) but in only one subject in the non-FBDS subgroup (1/15) (44 vs. 7%, $P < 0.05$).

Conclusion: ^{18}F-FDG-PET imaging was more sensitive than MRI in the diagnosis of LGI1 AE. Isolated BG hypermetabolism was more frequently observed in subjects with FBDS, suggesting the potential involvement of the BG.

Keywords: LGI1, ^{18}F-FDG-PET, FBDS, basal ganglia, medial temporal lobe

INTRODUCTION

Autoimmune encephalitis (AE) associated with leucine-rich glioma-inactivated 1 (LGI1) antibody, described a decade ago, is a potentially treatable and recidivistic subtype of AE (1). It has been characterized as a subacute or rapidly progressive cognitive impairment accompanied by seizures, faciobrachial dystonic seizures (FBDS), and neuropsychiatric symptoms but rarely cancer (2). FBDS are highly specific and often appear as an initial symptom of LGI1 AE (3), which mainly presents with very frequent (medially 50 times per day) and brief involuntary movements of the ipsilateral face and limbs (usually <3 s for every episode) (4). However, whether FBDS should be treated as epileptic seizures is still controversial (5). Only certain studies have classified FBDS as epileptic-origin tonic seizures based on a detectable generalized electrodecremental event during the episode on ictal electroencephalogram (EEG) (6). However, other studies of LGI1 AE patients with FBDS have detected BG abnormalities on magnetic resonance imaging (MRI) that were not detected in subjects without FBDS, suggesting that FBDS might be a form of movement disorder (7). Hence, it is still difficult to confirm the origin or nature of FBDS.

For LGI1 AE patients, early diagnosis and treatment can prevent the development of the disease syndrome (8, 9). MRI is a preferred radiological modality in the early diagnosis of LGI1 AE, especially when antibody testing is negative or not available (10). Nevertheless, individual patients with LGI1 AE have been shown to exhibit negligible MRI findings, notably during the development of FBDS (4, 11, 12). Thus, it is necessary to find a novel or distinctive imaging pattern to expedite the early diagnosis of LGI1 AE (13). ^{18}F-Fluoro-2-deoxy-*d*-glucose positron emission tomography (^{18}F-FDG-PET) is a functional imaging modality for *in vivo* evaluation of the pathophysiology of the brain via application of ^{18}F-FDG; it has been reported to reveal abnormal metabolism patterns in AE subjects, such as typical medial temporal lobe (MTL) hypermetabolism, especially in AE patients with a negative MRI, thus implying that ^{18}F-FDG-PET has higher sensitivity than MRI in the diagnosis of AE subjects (14, 15). However, the ^{18}F-FDG-PET pattern of patients with LGI1 AE is not well characterized or established. Regional basal ganglia (BG) or MTL hypermetabolism on ^{18}F-FDG-PET has been observed in LGI1 AE patients (16–18). To date, only a limited number of isolated cases have been studied in subjects with LGI1 AE using ^{18}F-FDG-PET.

Thus, we conducted a retrospective study and reviewed the ^{18}F-FDG-PET data of 34 patients with a definite diagnosis of LGI1 AE based on symptoms, EEG, and LGI1 antibody testing. We evaluated the diagnostic value of ^{18}F-FDG-PET in LGI1 AE subjects, especially those with unremarkable MRI alterations, and we also aimed to interpret the localization of FBDS by showing different metabolic abnormalities of ^{18}F-FDG-PET in LGI1 AE patients with or without FBDS.

MATERIALS AND METHODS

Standard Protocol, Approvals, and Patients' Consents

The study was approved by the Ethics Committee of the Beijing Tiantan Hospital, which was affiliated with the Capital Medical University of the People's Republic of China. The study was conducted in accordance with the Declaration of Helsinki, and all patients and controls provided informed consent for the use of their medical records.

Study Participants

A total of 34 patients with LGI1 AE were retrospectively identified between October 2014 and June 2018 at the Department of Neurology in the Beijing Tiantan Hospital of the Capital Medical University. The inclusion criteria were based on representative clinical symptoms of LGI1 AE and the presence of positive LGI1 antibodies in the serum or cerebrospinal fluid (CSF). All included patients had undergone MRI and ^{18}F-FDG-PET scans for neurological assessment during clinical evaluation. The demographic, clinical presentation, laboratory testing, EEG, and neuroimaging data were reviewed by searching the electronic medical records.

The 34 patients included 18 patients (53%) in the acute phase and 16 patients (47%) in the chronic phase when they take PET examination based on the previous definition of the acute phase (within 3 months) and chronic phase (over 3 months) in the diagnosis of AE (10).

The patients were divided into two subgroups based on the presence of FBDS, namely, FBDS and non-FBDS. We compared the ^{18}F-FDG-PET findings in these two subgroups, analyzed the ^{18}F-FDG-PET hypermetabolic states in the BG of the subjects, and then inferred the possible etiology or nature of FBDS.

In this study, we randomly selected additional 20 age- and gender-matched controls (14 men and 6 women; median age 62.5 years; range, 25–83 years) for the quantitative analysis of FDG-PET based on volume of interest (VOI). The inclusion criteria are the following: (1) no brain diseases, (2) no mental disorders reported in the medical records, (3) no other diseases that indicated the brain function had been affected, (4) no abnormalities reported by the neuroradiologist, (5) adjustment for gender and age and random pickup of the control subjects.

Laboratory Detection

All patients underwent serum and CSF antibody detection, including *N*-methyl-D-aspartate receptor (NMDAR), LGI1, contactin-associated protein-2 (CASPR2), α-amino-3-hydroxy-5-methyl-4-isoxazolepropionic acid receptor (AMPAR), and γ-aminobutyric acid type B (GABAB). Serum and CSF samples were tested for the presence of LGI1 antibodies, using both cell-based assays (Euroimmun, Lübeck, Germany)

Abbreviations: ^{18}F-FDG-PET, ^{18}F-Fluoro-2-deoxy-*d*-glucose positron emission tomography; AE, autoimmune encephalitis; AMPAR, α-amino-3-hydroxy-5-methyl-4-isoxazolepropionic acid receptor; BG, basal ganglia; CASPR2, contactin-associated protein-2; CSF, cerebrospinal fluid; CT, computed tomography; EEG, electroencephalogram; FBDS, faciobrachial dystonic seizures; GABAB, γ-aminobutyric acid type B; LGI1, leucine-rich glioma-inactivated 1; MTL, medial temporal lobe; MRI, magnetic resonance imaging; NMDAR, *N*-methyl-D-aspartate receptor; SPM, statistical parametric mapping; SUVmax, standardized uptake max value.

and immunohistochemical analyses in the neuroimmunology laboratory of the Peking Union Medical College Hospital.

^{18}F-FDG-PET Acquisition

^{18}F-FDG-PET images were acquired using a PET/computed tomography (CT) scanner (Elite Discovery, GE HealthCare, Fairfield, Connecticut, USA). All patients (with a median age of 61 years, ranging from 31 to 78 years) fasted for at least 6 h, and blood glucose levels could not exceed 8 mmol/L. No patients received neuroleptic drugs to undergo FDG-PET. ^{18}F-FDG was intravenously injected at a dose of 3.7–5.0 MBq/kg within 1 min, and subsequent uptakes required that patients be in a quiet resting status for 1 h prior to scanning in a dedicated room after ^{18}F-FDG injection. First, a low-dose CT scan was performed, and the CT parameters for attenuation correction were 120 kV, pitch 0.984, automated tube current 60–180 mA, and slice thickness 3.75 mm. The PET scan was subsequently performed in 3D-TOF mode; for the LGI1 patients, a whole-body (including the brain region) FDG-PET scanning was acquired for approximately 30–35 min. The brain imaging data were reconstructed into trans-axial slices with a matrix size of 128 × 128 and a slice thickness of 3.3 mm, using an OSEM (ordered subset expectation maximization) algorithm.

Voxel-Based Analysis of Statistical Parametric Mapping

For statistical parametric mapping (SPM) analysis, 22 age-matched, healthy volunteers served as control subjects. PET data were analyzed by SPM8 software (Wellcome Department of Cognitive Neurology, University College, London, UK) running on Matlab 2014b (MathWorks Inc., Sherborn, MA, USA). First, PET images were co-registered with the SPM template T1-weighted MR. Co-registered PET images were then spatially normalized into a common Montreal Neurological Institute (MNI) atlas anatomical space following a 12-parameter affine transformation and non-linear transformations, yielding images composed of 2 mm × 2 mm × 2 mm voxels. Third, normalized images were smoothed using an isotropic Gaussian kernel to increase the signal-to-noise ratio. Subsequently, preprocessed PET image values were corrected to a mean value of 50 ml/dl/min by "proportional scaling" to reduce individual variation. A two-sample *t*-test, based on the specified 22 age- and gender-matched controls, was applied between included patient PET data and the control group and to best reduce the impact of age and gender. The regions were considered significant at a corrected level of $P < 0.01$ for a minimum cluster size of 100 contiguous voxels (8 mm^3 per voxel size). We purposefully chose a low threshold to detect any regions in which V_T/f_P was more significant in patients.

Data Analysis Based on VOI of Standardized Uptake Max Value

For these reported data, the region of interest (ROI) refers to the structure in 2D space (e.g., on a slice), and VOI refers to the structure in 3D space (i.e., a combination of ROIs of adjacent slices in two dimensions was labeled as a VOI). The value for radioactivity in each structure for each participant is the maximum of all pixels in all ROIs assayed for that structure, yielding a VOI. In our study, we selected three consecutive axial sections to define a certain volume (parameters included length, width, and height) to obtain the SUVmax (AW work station, GE HealthCare, USA). We calculated the SUVmax in three VOIs on FDG-PET based on the visual analysis, including the frontal cortex, BG, and MTL. The size of VOIs we selected was fixed, the center coordinate referred to the central location of VOIs, and they were individualized. One of the representative parameters of the individual was as follows: For the frontal cortex, the size of the volume was 25 * 20 * 9.9 mm, and the center coordinate of the volume was 72, 135, 30. For the BG, it was 40 * 30 * 9.9 mm, and the center coordinate was 109, 110, 23. For the MTL, the size of volume was 40 * 25 * 9.9 mm, and the center coordinate of volume was 112, 103, 18 (**Supplementary Figure 1**). The steps of quantitative comparison were as follows. (1) In the brain, the cubic VOIs were placed manually in the lesion. The SUVmax in the BG, MTL, and the frontal cortex was measured by three experienced neuroradiologists and nuclear imaging specialists (Lin Ai, Xiaobin Zhao, and Yaou Liu). All three specialists were blinded from clinical information of the conditions of either patients or controls, and in case of obvious discordance in their initial evaluations, an informed consensus statement was reached. The kappa coefficient of the three specialists was 0.88. (2) For normalization of SUVmax in the BG and MTL, the respective uptake values were divided by the values measured in the frontal VOI, which was chosen as the internal reference, as it was not expected to be altered in activity in LGI1 AE. Finally, we made a statistical comparison between 20 age- and gender-matched controls and 34 patients. (3) Receiver operating characteristic (ROC) curve analyses of normalized SUVmax in the BG and MTL for controls and patients were performed, and accordingly, optimal threshold values were set to 1.8 for BG and 1.3 for MTL.

Literature Review

An extensive literature search was performed for the terms "positron emission tomography" and "encephalitis" from January 2007 to October 2018. The reported results were reviewed and summarized. The primary search identified 112 publications on PubMed, and any studies and case reports that showed abnormal metabolism on brain PET in patients with AE were included. The subtypes of AE included NMDAR, LGI1, CASPR2, and GABAB. Ultimately, 19 studies and case series were reviewed (**Table 4**).

Statistical Analysis

Continuous variables with a normal distribution are presented as the mean ± standard deviation, and non-normal variables are expressed as the median (interquartile range, IQR). Continuous variables were compared using the *t*-test or non-parametric Mann–Whitney *U*-test. Categorical variables were compared and analyzed by Fisher's exact test. A two-tailed $P < 0.05$ was considered statistically significant. SPSS Statistics 23.0 software package for Windows (IBM Corp., Armonk, NY) was used for statistical analyses.

RESULTS

Clinical Characteristics

A total of 34 patients (24 men; a median age of 61 years, IQR 54–65 years old; age range, 31–78 years) with LGI1 AE were identified, and their clinical characteristics were reviewed (**Table 1**). A total of 33 patients (97%) exhibited epileptic seizures, and the remaining one subject presented only with FBDS. Complex partial seizures (CPS) and generalized tonic–clonic seizures (GTCS) were the two main patterns of epileptic seizures. A total of 17 patients (50%) presented with distinctive FBDS, which involved both the arm and ipsilateral face (71%), and only 24% of patients experienced disturbances of awareness. Other symptoms were memory loss (88%), psychiatric disorders (depression, 9%; hallucinations, 26%, disorder of behavior, 24%), somnipathy (50%), and hallucinations (26%). Only one patient (3%) exhibited colorectal adenoma, and the remaining 33 patients did not present with a tumor after a median follow-up of 1.55 years (range, 0.3–4 years).

TABLE 1 | Summary of the clinical characteristics of patients with LGI1 AE ($n = 34$).

Characteristics	Values
Age, year, median (IQR, range)	61 (54–65, 31–78)
Sex, male, *n* (%)	24 (71)
Clinical symptoms, *n* (%)	
FBDS	17 (50)
Seizures (except FBDS)	33 (97)
Memory loss	30 (88)
Psychiatric symptoms	20 (59)
Depression	3 (9)
Hallucinations	9 (26)
Disorder of behavior	8 (24)
Somnipathy	17 (50)
Hyponatremia, *n* (%)[a]	22 (65)
Tumors, *n* (%)	1 (3)
LGI1 antibody positive, *n* (%)	34 (100)
Only in serum	2 (6%)
Only in CSF	2 (6%)
Both in serum and CSF	30 (88%)
CSF abnormalities, *n* (%)[b]	10 (29)
EEG abnormalities, *n* (%)	
Total[c]	25 (74)
Ictal (FBDS)[d]	0 (0)
MRI abnormalities, *n* (%)	
Total	20 (59)
Only MTL lesion	18 (53)
Only BG lesion	1 (3)
Both BG and MTL lesions	1 (3)
^{18}F-FDG-PET abnormalities, *n* (%)	
Total	31 (91)
Only MTL lesion	3 (9)
Only BG lesion	8 (23)
Both BG and MTL lesions	20 (59)
Immunotherapy, *n* (%)	34 (100)
Relapse, *n* (%)	8 (24)

LGI1, leucine-rich glioma-inactivated 1; AE, autoimmune encephalitis; IQR, interquartile range; FBDS, faciobrachial dystonic seizures; CSF, cerebrospinal fluid; EEG, electroencephalogram; MRI, magnetic resonance imaging; MTL, medial temporal lobe; BG, basal ganglia; ^{18}F-FDG-PET, ^{18}F-fluoro-2-deoxy-d-glucose positron emission tomography.

[a] *Normal range 135–145 mmol/L.*

[b] *CSF leukocyte count of >5/μl or protein levels of >45 mg/dl were considered abnormal.*

[c] *Temporal area slow waves or epileptiform discharges were considered abnormal.*

[d] *Relevant discharges on video EEG during the ictal phase of FBDS were considered abnormal.*

Laboratory Testing

All 34 patients (100%) were positive for antibodies against the LGI1 protein (**Table 1**). LGI1 antibodies were commonly detectable in serum (94%) and CSF (94%), although two patients (6%) had positive LGI1 antibodies only in the CSF and in the serum (one patient each). Hyponatremia was reported for 22 patients (65%) (**Table 1**). A total of 10 out of 34 patients (29%) exhibited CSF pleocytosis (median, 7 white blood cells/μl; range, 6–16) and an increased protein concentration (median, 65 mg/dl; range, 49–73 mg/dl).

Brain Image Review of LGI1 AE Patients

A total of 20 patients (59%) exhibited T2-weighted image (T2WI) or fluid-attenuated inversion recovery (FLAIR) hyperintensity on MRI. No subjects exhibited abnormal signals on T1-weighted image (T1WI). Increased signals were noted only in the MTL for 18 out of 34 patients (53%). A single subject (3%) showed isolated BG hyperintensity, and the remaining one (3%) had hyperintensity in both the MTL and BG.

A total of 31 patients (91%) showed an abnormal metabolism as determined by ^{18}F-FDG-PET, and all of them (100%) presented with pure hypermetabolism. MTL and BG were two distinct metabolic targets in LGI1 AE patients (**Figures 2A,C**). Three patients (9%) exhibited increased glucose metabolism only in the MTL, whereas eight patients (23%) demonstrated BG-only hypermetabolism. The remaining 20 patients (59%) had increased metabolism in both the MTL and BG brain regions. Therefore, BG hypermetabolism was observed in 28 subjects (82%), and 68% of patients showed MTL hypermetabolism.

Concerning the diagnosis of LGI1 AE, a comparison was made between the MRI and ^{18}F-FDG-PET methods (**Figure 1**). Our diagnostic tracking showed that the sensitivity of ^{18}F-FDG-PET was apparently superior to that of MRI (91 vs. 59%, $P < 0.05$), but no significant difference was noted between the two imaging modalities in regard to the median time from onset to the initial scan (82.5 vs. 75 days, $P > 0.05$). ^{18}F-FDG-PET exhibited 100% metabolic changes when the MRI scans were positive; 11 out of 14 patients (79%) had altered glucose metabolism as demonstrated by ^{18}F-FDG-PET in the presence of normal or unremarkable MRI scans (**Figure 2B**), and seven of them (64%) had isolated BG hypermetabolism.

A total of 12 subjects (35%) received a follow-up by ^{18}F-FDG-PET, and all of them showed markedly decreased or normal uptake of ^{18}F-FDG compared with the initial degree of metabolism; follow-ups occurred 68 ± 10 days following clinical treatment (**Figure 2D**).

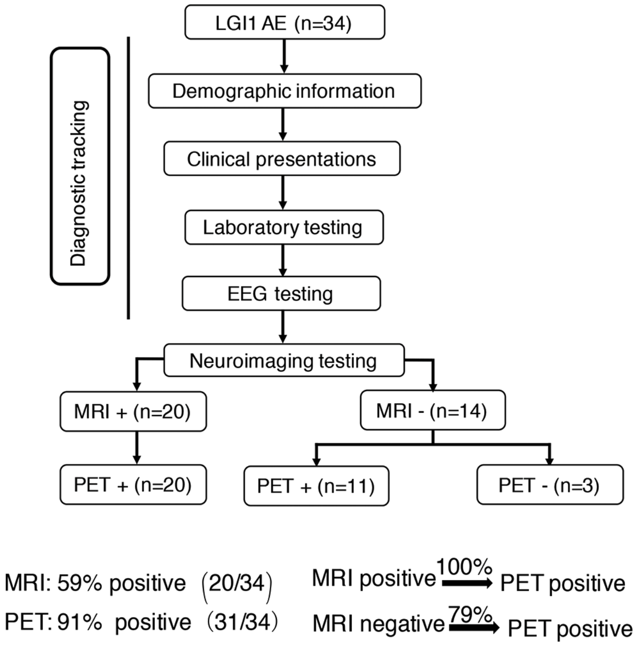

FIGURE 1 | Neuroimaging testing in the diagnostic tracking of LGI1 AE. Neuroimaging testing plays an essential role in the diagnosis of LGI1 AE. The sensitivity of ^{18}F-FDG-PET was higher than that of MRI; the ^{18}F-FDG-PET scan was always positive when the MRI was positive, but when the MRI scan was negative for the diagnosis of LGI1 AE, 79% of the patients were still positive on the ^{18}F-FDG-PET scan. LGI1, leucine-rich glioma-inactivated 1; AE, autoimmune encephalitis; EEG, electroencephalogram; MRI, magnetic resonance imaging; PET, ^{18}F-fluoro-2-deoxy-*d*-glucose positron emission tomography; +, positive; –, negative.

^{18}F-FDG-PET Pattern Among Subtypes of LGI1 AE Patients

The patients were divided into two subgroups as follows: FBDS ($n = 17$) and non-FBDS ($n = 17$). The imaging data are summarized in **Tables 2**, **3**. In the FBDS subgroup, ^{18}F-FDG-PET was more sensitive than MRI (94 vs. 53%, $P < 0.05$). A similar result was noted in the non-FBDS subgroup, although this did not reach statistical significance (88 vs. 65%, $P = 0.12$). For the analysis of the MRI-negative patients, the sensitivity of ^{18}F-FDG-PET in the FBDS subgroup was significantly higher than that of the subjects in the non-FBDS subgroup (50 vs. 29%, $P < 0.05$; **Figure 3A**).

A total of 31 patients (FBDS = 16, non-FBDS = 15) demonstrated increased metabolic changes as demonstrated by ^{18}F-FDG-PET analysis. We classified the metabolic pattern of the patients into three types (BG only, MTL only, and BG + MTL) based on the location of the lesions in every subgroup (**Figures 3B–D**). BG-only hypermetabolism was detected in 7 out of 16 subjects (44%) with FBDS, but this pattern was detected in only one patient with non-FBDS (1/15) (44 vs. 7%, $P < 0.05$; **Figure 3C**). In the subgroup of BG only, a total of seven patients (88%) presented with FBDS, and one subject manifested with non-FBDS ($P < 0.05$; **Figure 3D**). No significant differences were noted between the two subgroups regarding the time from onset to initial ^{18}F-FDG-PET scan (70.5 vs. 72 days, $P = 0.53$).

Literature Review on ^{18}F-FDG-PET Findings in Subtypes of AE

A total of 124 subjects with AE and PET scans were reviewed as shown in **Table 4**. For anti-NMDAR encephalitis, ^{18}F-FDG-PET mainly presented with hypometabolism in the occipital (63%) and parietal (42%) areas, in the BG (33%) and the temporal lobe (29%) (14, 19–27). Patients with CASPR2 and GABAB showed no specific metabolic pattern due to the limitations regarding the number of cases (19, 30–32). However, abnormal metabolism in the BG and temporal lobe was observed in 77 and 62%, respectively, of subjects with LGI1 AE, and this pattern was relatively specific compared to the results in other subtypes of AE (4, 11, 17–19, 21, 28, 29).

Semiquantitative Analysis Based on the ^{18}F-FDG-PET Normalized SUVmax Value

To support the SPM voxel-based analysis results ($P < 0.01$) shown in our figures, we also performed a VOI standardized uptake max value (SUVmax) data analysis. We showed different raw metabolism patterns in different cases, such as normal, BG only, MTL only, and BG + MTL (**Figure 4A**), and quantified the normalized SUVmax value (**Figure 4B**). For the BG threshold, the ROC statistical results showed that the area under the curve (AUC) value was 0.973, that sensitivity was 91.2%, that specificity was 100%, and that the best cutoff value was 1.8. For the MTL threshold, the ROC analysis showed that the AUC value was 0.938, that sensitivity was 82.4%, that specificity was 95%, and that the best cutoff value was 1.3. Our semiquantitative analysis results showed that the normalized SUVmax value in the BG and MTL was higher than that in controls, which suggested that the metabolism of BG and MTL was indeed increased and further supported our SPM data.

^{18}F-FDG-PET Characteristics of LGI1 AE Patients in Different Clinical Phases

Eighteen patients (53%) were in the acute phase, and 16 patients (47%) were in the chronic phase at the time of PET. In the acute phase, patients with LGI1 AE on FDG-PET mainly presented with hypermetabolism in the BG (median normalized SUVmax = 2.5, IQR 2.2–3.4) and MTL (median normalized SUVmax = 1.5, IQR 1.3–3.2) compared with 20 normal subjects. BG (median normalized SUVmax = 2.3, IQR 2.1–3.1) and MTL (median normalized SUVmax = 1.4, IQR 1.3–2.1) on FDG-PET showed still a hypermetabolism in the chronic phase. FDG-PET hypermetabolism was specifically located in the BG and MTL, whether it was in the acute phase or chronic phase ($P < 0.001$). However, there was no statistical metabolic change between acute and chronic phases for BG and MTL (**Figure 5**).

EEG Features

The EEG characteristics of all subjects during the ictal and interictal phases were reviewed. A total of 25 patients (74%) experienced EEG abnormalities, which mainly included ictal or interictal EEG with slow wave activities and epileptic discharge in the temporal and frontal regions. However, no rhythmic

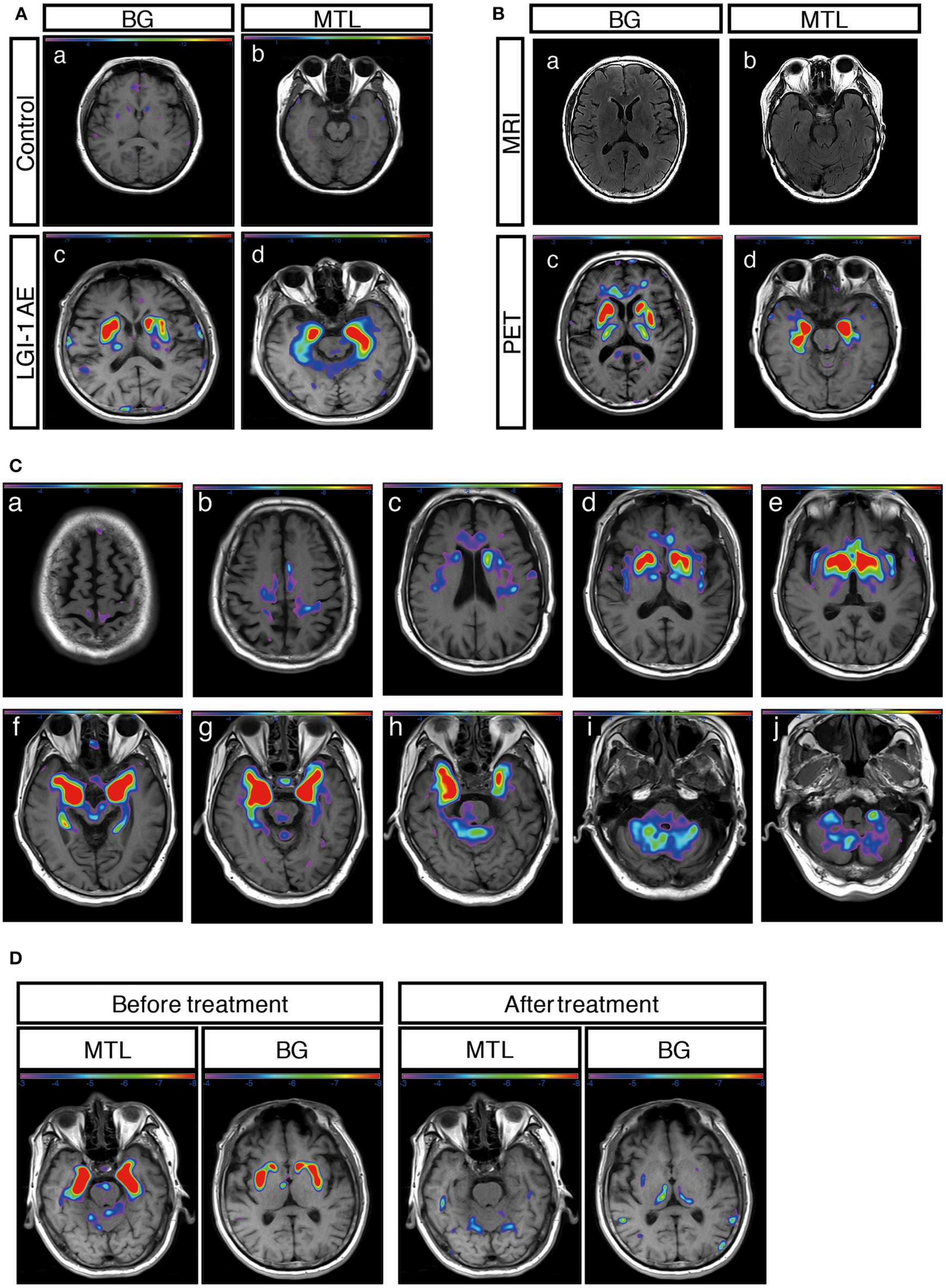

FIGURE 2 | ^{18}F-FDG-PET metabolic pattern in patients with LGI1 AE. **(A)** Typical BG and MTL hypermetabolism based on ^{18}F-FDG-PET in patients with LGI1 AE. Age-matched control patients with colorectal cancer in the absence of central nervous system lesions indicating healthy metabolism in the BG (a) and MTL (b). Representative increased metabolism in the BG (c) and MTL (d) in a patient with LGI1 AE. **(B)** MRI-negative and PET-positive metabolic patterns in LGI1 AE subjects. The axial fluid-attenuated inversion recovery image indicates a normal signal in the BG (a) and MTL (b), whereas ^{18}F-FDG-PET reveals hypermetabolism in the identical location from the same patient with LGI1 AE (c,d). **(C)** The brain sequences in ^{18}F-FDG-PET with LGI1 AE patients. Total brain ^{18}F-FDG-PET mapping indicates the

(Continued)

FIGURE 2 | BG and MTL as two distinctive targets in LGI1 AE patients (d–h). **(D)** The reversible metabolic pattern in LGI1 AE. ^{18}F-FDG-PET indicates increased ^{18}F-FDG uptake in the BG and MTL. Furthermore, the ^{18}F-FDG PET scan shows markedly decreased ^{18}F-FDG uptake in the BG and MTL during the 3-month follow-up period. LGI1, leucine-rich glioma-inactivated 1; AE, autoimmune encephalitis; MRI, magnetic resonance imaging; PET, ^{18}F-fluoro-2-deoxy-*d*-glucose positron emission tomography; MTL, medial temporal lobe; BG, basal ganglia.

TABLE 2 | ^{18}F-FDG-PET characteristics of LGI1 AE patients with FBDS ($n = 17$).

Patient	FBDS			Time from onset to MRI (day)	MRI	Time from onset to ^{18}F-FDG-PET (day)	^{18}F-FDG-PET before treatment		Follow-up ^{18}F-FDG-PET	
	Involvement	Loss of awareness	Ictal EEG		T2WI/FLAIR hyperintensity		Hypermetabolism	Hypometabolism	Time from treatment to follow-up (day)	Metabolic changes
1	Arm, Face	No	–	425	MTL	143	BG, MTL	–	45	Decreased
2	Arm, Face	No	Normal	75	Normal	80	BG, MTL	–	–	–
3	Arm	No	–	130	Normal	13	Normal	–	–	–
4	Arm, Face, Leg	Yes	Normal	174	MTL	188	MTL	–	112	Decreased
5	Face	No	–	92	MTL	98	BG, MTL	–	–	–
6	Arm, Face	Yes	Normal	214	MTL	91	BG, MTL	–	142	Decreased
7	Arm, Face, Leg	Yes	–	100	Normal	50	BG	–	82	Decreased
8	Arm, Leg	No	–	14	BG	25	BG	–	–	–
9	Arm, face	No	Normal	28	MTL	21	BG, MTL	–	–	–
10	Arm, Face	No	Normal	305	Normal	302	BG	–	–	–
11	Arm, Face	Yes	Normal	34	BG, MTL	35	BG, MTL	–	98	Decreased
12	Arm, Face	No	–	95	Normal	332	BG	–	–	–
13	Arm, Face	No	Normal	297	Normal	45	BG	–	27	Decreased
14	Arm, Face	No	–	257	Normal	276	BG	–	–	–
15	Arm, Face	No	Normal	17	Normal	94	BG	–	–	–
16	Arm, Face	No	–	45	MTL	127	BG, MTL	–	53	Decreased
17	Arm, Face	No	–	12	MTL	17	BG, MTL	–	–	–

^{18}F-FDG-PET, ^{18}F-fluoro-2-deoxy-d-glucose positron emission tomography; LGI1, leucine-rich glioma-inactivated 1; AE, autoimmune encephalitis; FBDS, faciobrachial dystonic seizures; EEG, electroencephalogram; MRI, magnetic resonance imaging; MTL, medial temporal lobe; BG, basal ganglia.

TABLE 3 | ^{18}F-FDG-PET features of LGI1 AE patients with non-FBDS ($n = 17$).

Patient	EEG		Time from onset to MRI (day)	T2WI/FLAIR hyperintensity	Time from onset to ^{18}F-FDG-PET (day)	^{18}F-FDG-PET before treatment		Follow-up ^{18}F-FDG-PET	
	Ictal	Interictal				Hypermetabolism	Hypometabolism	Time from treatment to follow-up (day)	Metabolic changes
1	–	TAD	12	MTL	11	MTL	–	–	–
2	Normal	Normal	190	MTL	372	BG, MTL	–	56	Decreased
3	TAD, FAD	TAD, FAD	798	MTL	797	BG, MTL	–	42	Decreased
4	Normal	Normal	34	MTL	50	BG, MTL	–	78	Decreased
5	–	Normal	75	MTL	92	MTL	–	–	–
6	Normal	FAD	94	Normal	91	BG, MTL	–	–	–
7	–	Normal	33	Normal	32	BG, MTL	–	–	–
8	TAD	TAD	4	Normal	43	Normal	–	–	–
9	TAD	Normal	87	MTL	130	BG, MTL	–	–	–
10	FAD	FAD, TAD	51	MTL	32	BG, MTL	–	–	–
11	–	Normal	12	MTL	19	BG, MTL	–	61	Decreased
12	–	FAD, TAD	148	MTL	185	BG, MTL	–	–	–
13	–	Normal	71	Normal	85	Normal	–	–	–
14	FAD, TAD	Normal	7	MTL	371	BG, MTL	–	25	Decreased
15	TAD	TAD	96	MTL	77	BG, MTL	–	–	–
16	TAD	TAD	67	Normal	64	BG, MTL	–	–	–
17	–	FAD, TAD	50	Normal	67	BG	–	–	–

^{18}F-FDG-PET, ^{18}F-fluoro-2-deoxy-d-glucose positron emission tomography; LGI1, leucine-rich glioma inactivated-1; AE, autoimmune encephalitis; FBDS, faciobrachial dystonic seizures; EEG, electroencephalogram; MRI, magnetic resonance imaging; TAD, temporal area slow waves or epileptiform discharges; FAD, frontal area slow waves or epileptiform discharges; MTL, medial temporal lobe; BG, basal ganglia.

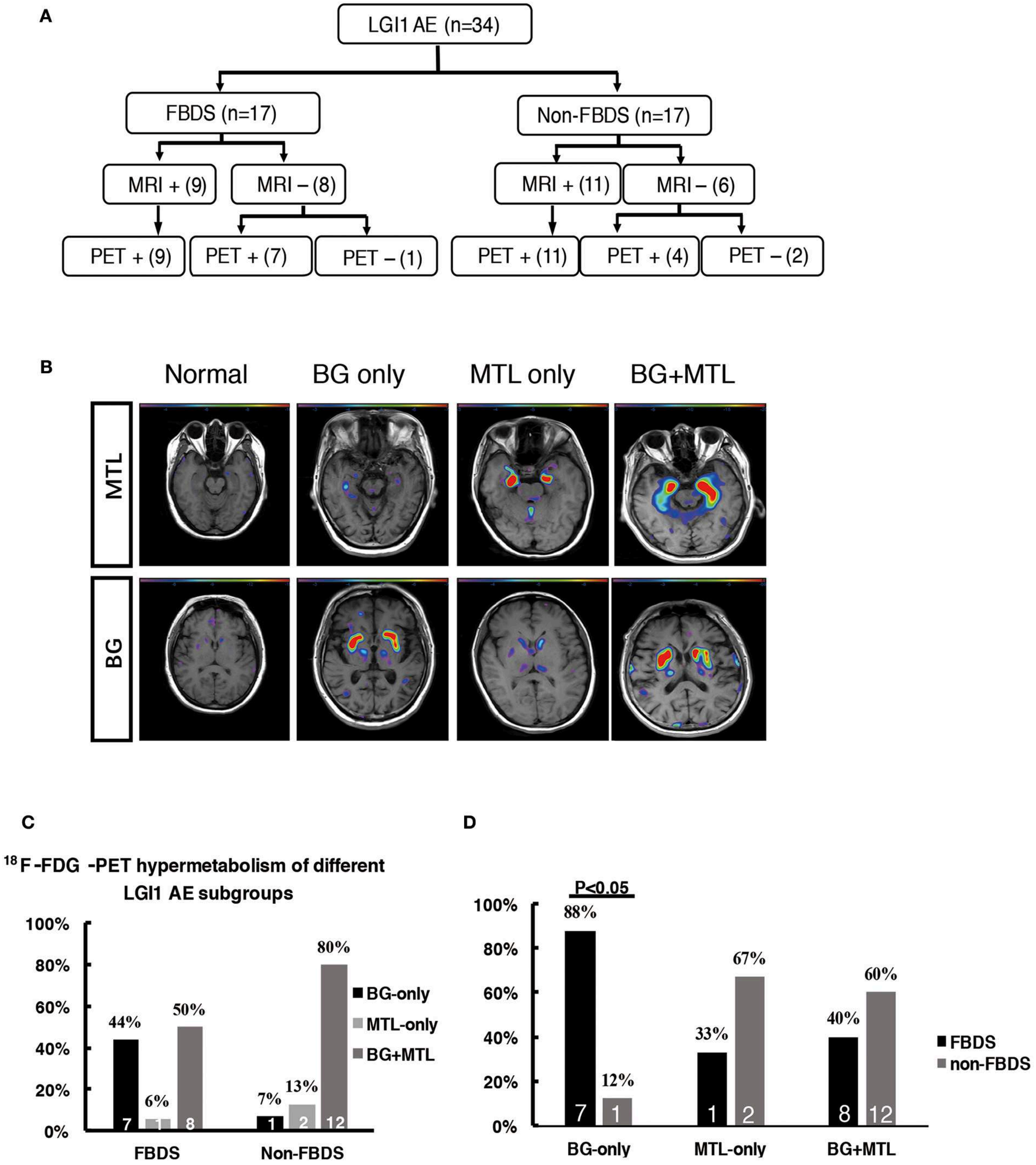

FIGURE 3 | ^{18}F-FDG-PET hypermetabolism in LGI1 AE patients with FBDS. **(A)** Neuroimaging comparison of the subgroups of LGI1 AE. **(B)** Representative ^{18}F-FDG-PET hypermetabolism among different subgroups after SPM ($P < 0.01$) analysis. **(C)** The comparison of the ^{18}F-FDG-PET hypermetabolic pattern between FBDS and non-FBDS. In the FBDS group, the abnormal PET signal more often appeared in the BG-only group and the BG + MTL group. However, in the non-FBDS group, the abnormal PET signal significantly appeared in the BG + MTL group. **(D)** A comparison of the ^{18}F-FDG-PET hypermetabolic pattern in FBDS and non-FBDS. In the BG-only group, the frequency of FBDS was higher than that of non-FBDS ($P < 0.001$). LGI1, leucine-rich glioma-inactivated 1; AE, autoimmune encephalitis; FBDS, faciobrachial dystonic seizures; MRI, magnetic resonance imaging; PET, ^{18}F-fluoro-2-deoxy-*d*-glucose positron emission tomography; MTL, medial temporal lobe; BG, basal ganglia. +, positive; –, negative.

discharges related to FBDS were noted except for artifacts of movements that were observed at the onset of dystonic seizures in eight patients with FBDS during the ictal phase. One subject with FBDS showed questionable low voltages in the right central and parietal areas around 5 s from onset (**Figure 6A**), and postictal EEG demonstrated rhythmic slow wave activity in the

TABLE 4 | Literature review of ^{18}F-FDG-PET pattern in subtypes of AE.

AE subtypes	References	Patient cases	^{18}F-FDG-PET findings	
			Hypermetabolism (*N*)	**Hypometabolism (*N*)**
NMDAR	(19)	3	BG (1)	Thalamus (2)
NMDAR	(20)	6	Temporal (6), Cerebellum (3), Frontal (6)	Occipital (3)
NMDAR	(21)	6	Temporal (5)	Parietal (6), Cingulate gyrus (1)
NMDAR	(22)	6	BG (4), Frontal (1), Temporal (1)	BG (1), Frontal (5), Temporal (4), Parietal (3), Occipital (6)
NMDAR	(23)	8	BG (6), Frontal (4), Temporal (2)	Occipital (7)
NMDAR	(14)	4	BG (2), Cerebellum (2)	Temporal (1), Parietal (1), Occipital (2)
NMDAR	(24)	1	BG (1)	–
NMDAR	(25)	1	–	Parietal (1), Occipital (1)
NMDAR	(26)	8	BG (2), Cerebellum (2), Occipital (1)	BG (2), Frontal (4), Temporal (3), Parietal (5), Occipital (6)
NMDAR	(27)	5	–	Frontal (3), Temporal (2), Parietal (4), Occipital (5)
LGI1	(4)	8	BG (4), Temporal (4)	BG (2), Temporal (2)
LGI1	(19)	1	Temporal (1)	–
LGI1	(21)	4	BG (3), Cerebellum (3), Occipital (2)	Cingulate gyrus (4)
LGI1	(28)	1	BG (1)	–
LGI1	(29)	5	BG (5), Temporal (3), Frontal (5)	–
LGI1	(17)	1	BG (1), Temporal (1)	–
LGI1	(18)	1	BG (1), Temporal (1)	–
LGI1	(11)	10	BG (7), Temporal (7)	–
LGI1	This study	34	BG (28), Temporal (23), Cerebellum (1)	–
CASPR2	(19)	2	BG (1)	–
CASPR2	(30)	3	BG (1), Thalamus (1)	Temporal (1), Occipital (1)
GABAB	(31)	5	Temporal (2)	The whole cerebral cortex (1)
GABAB	(32)	1	Temporal (1)	–

^{18}F-FDG-PET, ^{18}F-fluoro-2-deoxy-d-glucose positron emission tomography; AE, autoimmune encephalitis; NMDAR, N-methyl-d-aspartate receptor; LGI1, leucine-rich glioma inactivated-1; CASPR2, contactin-associated protein-2; GABAB, γ-aminobutyric acid type B; BG, basal ganglia.

left temporal region after the termination of FBDS, which was accompanied by hand automatism (**Figure 6B**).

Treatment and Follow-Up

All 34 patients (100%) were treated with first-line immunotherapy, including IV immunoglobulin (IVIG), IV methylprednisolone (IVMP), and oral steroids (for at least 6 months). A total of 26 patients (76%) were administered IVIG in combination with IVMP, whereas three patients (9%) used isolated IVIG and five patients (15%) received IVMP alone. Only one patient was administered azathioprine and mycophenolate mofetil (MMF) owing to the progression of the disease. Modified Rankin scores (mRS) were applied to evaluate the treatment response. Most patient conditions were improved following immunomodulatory therapies (mRS $\leq$ 2).

However, eight patients (24%) had a recurrence after a median follow-up of 1.55 years (range, 0.3–4 years). The distribution of metabolic patterns in the eight patients who relapsed is shown in **Figure 4C**. In the group with BG-only hypermetabolism, only one subject (12%) had a recurrence, and the remaining seven patients did not experience a relapse ($P < 0.05$). One patient (33%) who demonstrated MTL-only hypermetabolism experienced recurrence after a follow-up of 1 year. Six patients (30%) experienced a relapse, and 14 subjects did not relapse in the group with hypermetabolism in both the BG and MTL ($P < 0.05$). This showed that patients presenting with BG-only or BG + MTL hypermetabolism had a lower rate of relapse ($P < 0.05$).

DISCUSSION

In this study, we demonstrated that MRI plays a significant role in the diagnosis of anti-LGI1 encephalitis, whose main features are MTL or BG hyperintensities on T2WI/FLAIR. MRI was abnormal in 59% of subjects with LGI1 AE. We also described a specific metabolic pattern of ^{18}F-FDG-PET among a cohort of subjects with anti-LGI1 encephalitis and further compared functional PET imaging with structural MRI regarding the diagnosis of LGI1 AE. The rate of abnormal brain metabolism based on ^{18}F-FDG-PET imaging was 91%, and ^{18}F-FDG-PET imaging was diagnostically more sensitive than MRI in patients with LGI1 AE, with 79% of subjects exhibiting altered glucose metabolism on ^{18}F-FDG-PET in the absence of any abnormal MRI findings. The associated locations of the abnormal metabolism mainly included the BG and MTL, and the rate of abnormal findings in the BG and MTL was 82 and 68%, respectively. Our results suggest that ^{18}F-FDG-PET abnormalities may support the evidence for a clinical diagnosis of subjects with anti-LGI1 encephalitis. In addition, this study introduces a novel ^{18}F-FDG-PET pattern consisting of isolated striatal hypermetabolism in subjects with LGI1-mediated FBDS.

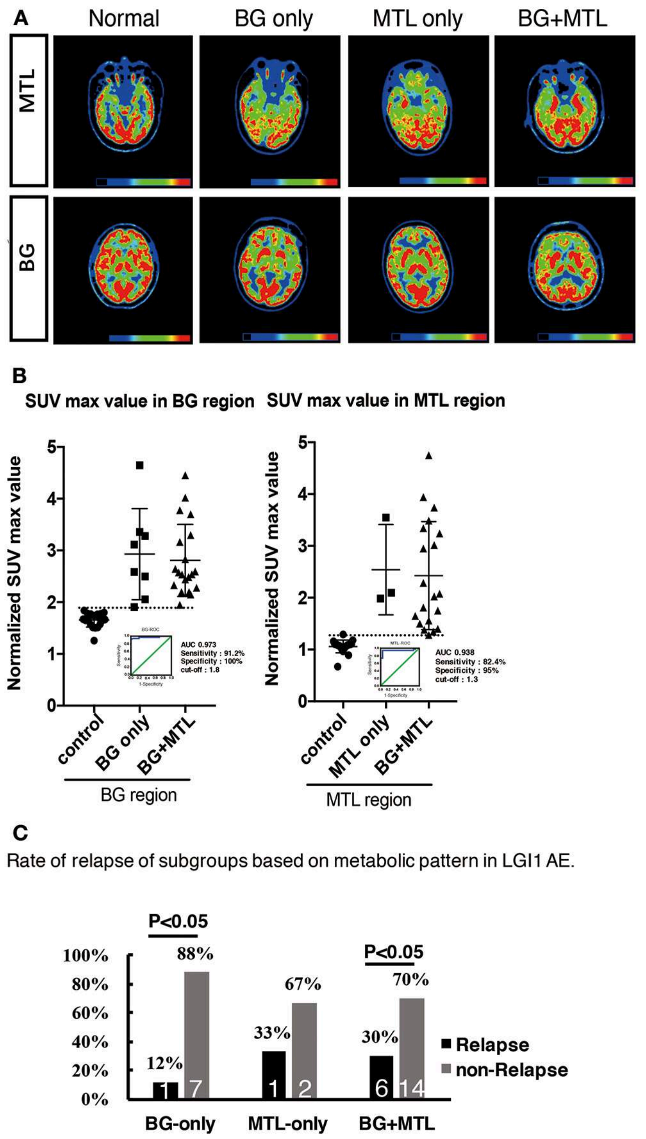

FIGURE 4 | ^{18}F-FDG-PET hypermetabolism in eight patients with LGI1 AE recurrence. **(A)** Representations of the distribution of metabolic patterns without SPM analysis. **(B)** Normalized SUVmax value in different brain regions and the threshold of BG and MTL based on ROC. **(C)** The rate of relapse of the subgroups based on the metabolic pattern. The findings showed that patients presenting with BG-only or BG + MTL hypermetabolism had a lower rate of relapse ($P < 0.05$). LGI1, leucine-rich glioma-inactivated 1; AE, autoimmune encephalitis; ^{18}F-FDG-PET, ^{18}F-fluoro-2-deoxy-*d*-glucose positron emission tomography; BG, basal ganglia; MTL, medial temporal lobe.

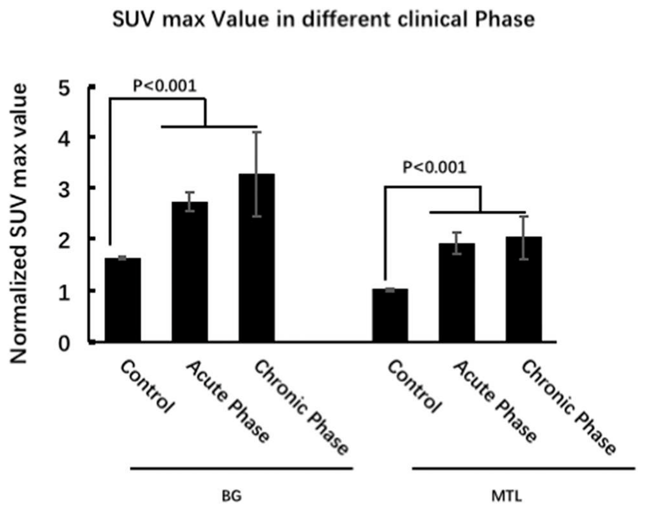

FIGURE 5 | ^{18}F-FDG-PET characteristics of LGI1 AE patients in different clinical phases. FDG-PET hypermetabolism was specifically located in the BG and MTL, whether it was in the acute phase or chronic phase, and there is no statistical metabolic change between acute and chronic phases for BG and MTL. LGI1, leucine-rich glioma-inactivated 1; AE, autoimmune encephalitis; ^{18}F-FDG-PET, ^{18}F-fluoro-2-deoxy-*d*-glucose positron emission tomography; BG, basal ganglia; MTL, medial temporal lobe.

Isolated striatal hypermetabolism was detected in 44% of subjects with FBDS but only in 7% of patients without FBDS. As a subject without FBDS exhibited isolated striatal hypermetabolism, we concluded that the BG might also be involved in the development of FBDS to a certain extent.

Brain glucose metabolism is closely associated with neuronal activity. Regional hypermetabolism may reflect exuberant neuronal activities induced by the inflammatory lesions of encephalitis. Furthermore, abnormalities in brain metabolic dysfunction usually change dynamically and currently precede structural changes. Our results primarily showed hypermetabolism or a healthy metabolism based on ^{18}F-FDG-PET scans in LGI1 AE subjects at first hospitalization, which was potentially consistent with prior studies (4, 11). In addition, similar to previous studies (16, 17), ^{18}F-FDG-PET indicated a reversible metabolic pattern in 12 patients who received follow-up. This observation supported the finding that ^{18}F-FDG-PET exhibited an optimal correlation with disease severity and the hypothesis that it might be used to evaluate treatment response in LGI1 AE patients.

Our results mainly showed an abnormal metabolic pattern among LGI1 AE subjects in the BG and MTL. However, we also found abnormal hypermetabolism in the striatal, cerebellar, and cortex areas in some individual cases (data not shown) (21, 29). Furthermore, prior reports showed that BG and MTL hypermetabolism was also found in some individual cases in other subtypes of AE (20, 21). However, this observation was not specific to the metabolic pattern of anti-LGI1 encephalitis; our study reviewed ^{18}F-FDG-PET patterns in AE and found that the BG and MTL were two distinctive targets in subjects with LGI1 AE compared to other subtypes of AE. Therefore, we may need more prospective studies to illustrate the metabolic pattern of other AE subtypes and to further evaluate the clinical value of striatal hypermetabolism for LGI1 AE subjects.

The origin of FBDS has been extensively debated, but no definite conclusions have been reached to date. Ictal EEG and neuroimaging examinations are the two main methods in current clinical use for explaining the etiology or localization of FBDS. On the one hand, ictal EEG mainly suggests an epileptic origin for FBDS, showing slow waves or epileptiform discharges in the temporal area during FBDS (4, 6, 33). On the other hand, neuroimaging examinations primarily suggest

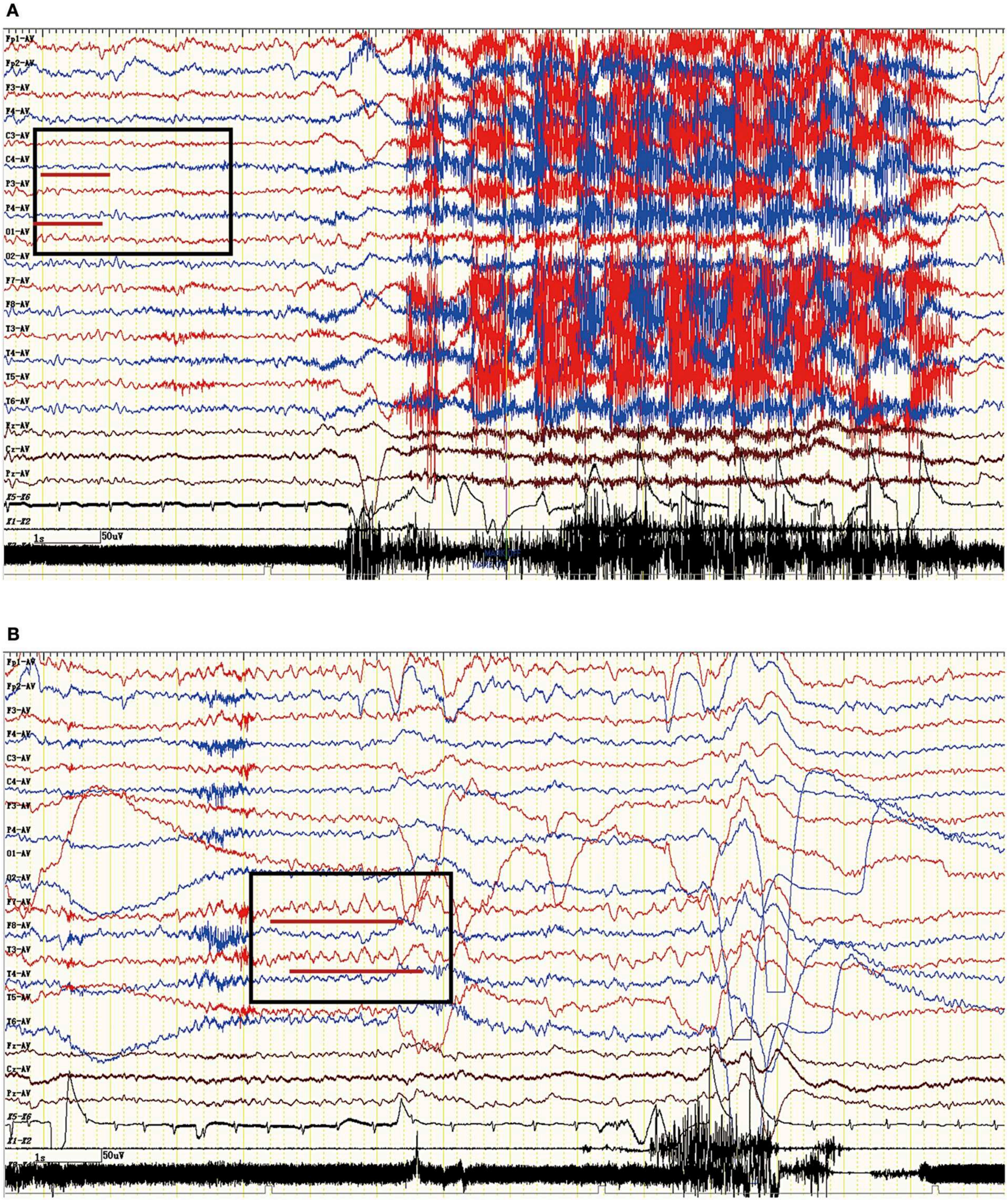

FIGURE 6 | Ictal EEG pattern in an LGI1 AE patient with FBDS. **(A)** The ictal EEG of a 50-year-old woman with FBDS. No significant rhythm changes were noted except for artifacts of movements that were observed at the onset of the dystonic seizures. However, the EEG indicated low voltage in the right central and parietal areas before 5 s from onset (square frame). **(B)** The postictal EEG of the patient with FBDS. The EEG demonstrated rhythmic slow wave activity in the left temporal region (square frame) after the termination of FBDS, which was accompanied by hand automatism. LGI1, leucine-rich glioma-inactivated 1; AE, autoimmune encephalitis; FBDS, faciobrachial dystonic seizures; EEG, electroencephalogram.

a BG localization, based on the evidence that the structural and functional changes in the striatum are easily detected in subjects with LGI1-associated FBDS (7, 18). Our study showed that pure BG hypermetabolism accounted for a higher proportion of FBDS, and it rarely appeared in subjects without FBDS in terms of functional ^{18}F-FDG-PET. Furthermore, ictal EEG simultaneously indicated no rhythmic epileptic discharges during the ictal phase of FBDS. Hence, this study suggests that abnormalities of the BG might be involved in the etiology of FBDS and further supports the hypothesis that LGI1-associated FBDS is more likely a form of movement disorder rather than an epileptic disease in nature. However, some authors also hypothesize that FBDS might originate from a network dysfunction between the cortical and subcortical areas (28). Thus, future studies are crucial to provide more evidence to settle this controversy by correlating quantitative FDG metabolic uptake values in the BG with the severity of FBDS and further evaluating the existence of lateralized correlations between striatal metabolic changes and the physical aspects of FBDS.

The main limitations of this study are as follows. (1) The study is retrospective in nature: as not all subjects diagnosed with LGI1 AE during the observation period consented to performing an ^{18}F-FDG-PET examination, a potential selection bias due to the small sample size may have been introduced. (2) Not all subtypes of AE were represented to be evaluated for an FDG pattern. (3) At the time point of the study, the diagnosis of LGI1 AE was mainly based on detection of antibodies, which might not necessarily match the final definite diagnosis in the further course of the disease. Therefore, our study was exploratory, and confirmatory tests should be taken with caution. Extensive prospective studies are required to verify the metabolism patterns of LGI1 AE, and a standardized ^{18}F-FDG-PET protocol is also needed to meet the requirements for diagnosing LGI1-associated AE.

CONCLUSION

^{18}F-FDG-PET imaging was more sensitive than MRI in the diagnosis of anti-LGI1 encephalitis, and BG and MTL hypermetabolism are two distinctive targets for LGI1 AE compared to other subtypes of AE. Isolated BG hypermetabolism was more frequently observed in subjects with FBDS and potentially suggests the involvement of BG.

DATA AVAILABILITY STATEMENT

The datasets generated for this study are available on request to the corresponding author.

ETHICS STATEMENT

The studies involving human participants were reviewed and approved by this study was approved by the Ethics committee of the Beijing Tiantan hospital that was affiliated to the Capital Medical University of the People's Republic of China. The patients/participants provided their written informed consent to participate in this study.

AUTHOR CONTRIBUTIONS

XL, WSha, and QW recruited, diagnosed, and assessed patients. XL, WSha, QW, XZ, JR, GR, CC, WShi, RL, ZL, and YL worked on the establishment of the separate databases. XL and WSha drafted a significant portion of the manuscript or figures. LA and QW reanalyzed and interpreted all final data. All authors contributed to the current version of the paper regarding conception or design, data analysis or editing, and read and approved the final manuscript.

FUNDING

This study was supported by the National Key R&D Program of China 2017YFC1307500, Beijing-Tianjin-Hebei Cooperative Basic Research Program H2018206435, Capital Healthy Development Research Funding 2016-1-2011, the National Natural Science Foundation of China (Grant Nos. 81801280 and 81601126), Beijing Postdoctoral Research Foundation (ZZ 2019-09), and China Postdoctoral Science Foundation (No. 2019M660719).

ACKNOWLEDGMENTS

The authors also thank the patients for their participation, all referring physicians, and Yanxue Zhao and Wei Zhang for technical assistance.

SUPPLEMENTARY MATERIAL

The Supplementary Material for this article can be found online at: https://www.frontiersin.org/articles/10.3389/fneur.2020.00418/full#supplementary-material

Supplementary Figure 1 | The volume of quantitative ^{18}F-FDG-PET based on VOI in one representative subject. For the frontal cortex, the size of the volume was 25 * 20 * 9.9mm, and the center coordinate of the volume was 72, 135, 30. For the MTL, the size of the volume was 40 * 25 * 9.9mm, and the center coordinate of the volume was 112, 103, 18. For the BG, it was 40 * 30 * 9.9mm, and the center coordinate was 109, 110, 23. ^{18}F-FDG-PET, ^{18}F-fluoro-2-deoxy-d-glucose positron emission tomography; VOI, volume of interest; MTL, medial temporal lobe; BG, basal ganglia.

REFERENCES

1. Lai M, Huijbers MGM, Lancaster E, Graus F, Bataller L, Balice-Gordon R, et al. Investigation of LGI1 as the antigen in limbic encephalitis previously attributed to potassium channels: a case series. *Lancet Neurol.* (2010) 9:776–85. doi: 10.1016/s1474-4422(10)70137-x
2. van Sonderen A, Thijs RD, Coenders EC, Jiskoot LC, Sanchez E, de Bruijn MA, et al. Anti-LGI1 encephalitis: clinical syndrome and long-term follow-up. *Neurology*. (2016) 87:1449–56. doi: 10.1212/WNL.0000000000003173
3. Simabukuro MM, Nobrega PR, Pitombeira M, Cavalcante WCP, Grativvol RS, Pinto LF, et al. The importance of recognizing faciobrachial dystonic seizures in rapidly progressive dementias. *Dement Neuropsychol.* (2016) 10:351–7. doi: 10.1590/s1980-5764-2016dn1004016

4. Irani SR, Michell AW, Lang B, Pettingill P, Waters P, Johnson MR, et al. Faciobrachial dystonic seizures precede LGI1 antibody limbic encephalitis. *Ann Neurol*. (2011) 69:892–900. doi: 10.1002/ana.22307
5. Striano P. Faciobrachial dystonic attacks: seizures or movement disorder? *Ann Neurol*. (2011) 70:179–80. doi: 10.1002/ana.22470
6. Andrade DM, Tai P, Dalmau J, Wennberg R. Tonic seizures: a diagnostic clue of anti-Lgi1 encephalitis? *Neurology*. (2011) 76:1355–7. doi: 10.1212/WNL.0b013e3182152808
7. Flanagan EP, Kotsenas AL, Britton JW, McKeon A, Watson RE, Klein CJ, et al. Basal ganglia T1 hyperintensity in LGI1-autoantibody faciobrachial dystonic seizures. *Neurol Neuroimmunol Neuroinflamm*. (2015) 2:e161. doi: 10.1212/NXI.0000000000000161
8. Thompson J, Bi M, Murchison AG, Makuch M, Bien CG, Chu K, et al. The importance of early immunotherapy in patients with faciobrachial dystonic seizures. *Brain*. (2018) 141:348–56. doi: 10.1093/brain/awx323
9. Irani SR, Stagg CJ, Schott JM, Rosenthal CR, Schneider SA, Pettingill P, et al. Faciobrachial dystonic seizures: the influence of immunotherapy on seizure control and prevention of cognitive impairment in a broadening phenotype. *Brain*. (2013) 136(Pt 10):3151–62. doi: 10.1093/brain/awt212
10. Graus F, Titulaer MJ, Balu R, Benseler S, Bien CG, Cellucci T, et al. A clinical approach to diagnosis of autoimmune encephalitis. *Lancet Neurol*. (2016) 15:391–404. doi: 10.1016/S1474-4422(15)00401-9
11. Shin YW, Lee ST, Shin JW, Moon J, Lim JA, Byun JI, et al. VGKC-complex/LGI1-antibody encephalitis: clinical manifestations and response to immunotherapy. *J Neuroimmunol*. (2013) 265:75–81. doi: 10.1016/j.jneuroim.2013.10.005
12. Heine J, Pruss H, Bartsch T, Ploner CJ, Paul F, Finke C. Imaging of autoimmune encephalitis–relevance for clinical practice and hippocampal function. *Neuroscience*. (2015) 309:68–83. doi: 10.1016/j.neuroscience.2015.05.037
13. Morbelli S, Arbizu J, Booij J, Chen MK, Chetelat G, Cross DJ, et al. The need of standardization and of large clinical studies in an emerging indication of [(18)F]FDG PET: the autoimmune encephalitis. *Eur J Nucl Med Mol Imaging*. (2017) 44:353–7. doi: 10.1007/s00259-016-3589-9
14. Probasco JC, Solnes L, Nalluri A, Cohen J, Jones KM, Zan E, et al. Abnormal brain metabolism on FDG-PET/CT is a common early finding in autoimmune encephalitis. *Neurol Neuroimmunol Neuroinflamm*. (2017) 4:e352. doi: 10.1212/NXI.0000000000000352
15. Morbelli S, Djekidel M, Hesse S, Pagani M, Barthel H. Role of 18F-FDG-PET imaging in the diagnosis of autoimmune encephalitis. *Lancet Neuro*. (2016) 15:1009–10. doi: 10.1016/s1474-4422(16)30140-5
16. Park S, Choi H, Cheon GJ, Wook Kang K, Lee DS. 18F-FDG PET/CT in anti-LGI1 encephalitis: initial and follow-up findings. *Clin Nucl Med*. (2015) 40:156–8. doi: 10.1097/RLU.0000000000000546
17. Kunze A, Drescher R, Kaiser K, Freesmeyer M, Witte OW, Axer H. Serial FDG PET/CT in autoimmune encephalitis with faciobrachial dystonic seizures. *Clin Nucl Med*. (2014) 39:e436–8. doi: 10.1097/RLU.0000000000000372
18. Lopez Chiriboga AS, Siegel JL, Tatum WO, Shih JJ, Flanagan EP. Striking basal ganglia imaging abnormalities in LGI1 ab faciobrachial dystonic seizures. *Neurol Neuroimmunol Neuroinflamm*. (2017) 4:e336. doi: 10.1212/NXI.0000000000000336
19. Baumgartner A, Rauer S, Mader I, Meyer PT. Cerebral FDG-PET and MRI findings in autoimmune limbic encephalitis: correlation with autoantibody types. *J Neurol*. (2013) 260:2744–53. doi: 10.1007/s00415-013-7048-2
20. Leypoldt F, Buchert R, Kleiter I, Marienhagen J, Gelderblom M, Magnus T, et al. Fluorodeoxyglucose positron emission tomography in anti-N-methyl-D-aspartate receptor encephalitis: distinct pattern of disease. *J Neurol Neurosurg Psychiatry*. (2012) 83:681–6. doi: 10.1136/jnnp-2011-301969
21. Wegner F, Wilke F, Raab P, Tayeb SB, Boeck AL, Haense C, et al. Anti-leucine rich glioma inactivated 1 protein and anti-N-methyl-D-aspartate receptor encephalitis show distinct patterns of brain glucose metabolism in 18F-fluoro-2-deoxy-d-glucose positron emission tomography. *BMC Neurol*. (2014) 14:136. doi: 10.1186/1471-2377-14-136s
22. Lagarde S, Lepine A, Caietta E, Pelletier F, Boucraut J, Chabrol B, et al. Cerebral (18)FluoroDeoxy-glucose positron emission tomography in paediatric anti N-methyl-D-aspartate receptor encephalitis: a case series. *Brain Dev*. (2016) 38:461–70. doi: 10.1016/j.braindev.2015.10.013
23. Yuan J, Guan H, Zhou X, Niu N, Li F, Cui L, et al. Changing brain metabolism patterns in patients with ANMDARE: serial 18F-FDG PET/CT findings. *Clin Nucl Med*. (2016) 41:366–70. doi: 10.1097/RLU.0000000000001164
24. Maeder-Ingvar M, Prior JO, Irani SR, Rey V, Vincent A, Rossetti AO. FDG-PET hyperactivity in basal ganglia correlating with clinical course in anti-NDMA-R antibodies encephalitis. *J Neurol Neurosurg Psychiatry*. (2011) 82:235–6. doi: 10.1136/jnnp.2009.198697
25. Moubtakir A, Dejust S, Godard F, Messaoud L, Morland D. 18F-FDG PET/CT in Anti-NMDA receptor encephalitis: typical pattern and follow-up. *Clin Nucl Med*. (2018) 43:520–1. doi: 10.1097/RLU.0000000000002098
26. Probasco JC, Solnes L, Nalluri A, Cohen J, Jones KM, Zan E, et al. Decreased occipital lobe metabolism by FDG-PET/CT: an anti-NMDA receptor encephalitis biomarker. *Neurol Neuroimmunol Neuroinflamm*. (2018) 5:e413. doi: 10.1212/NXI.0000000000000413
27. Solnes LB, Jones KM, Rowe SP, Pattanayak P, Nalluri A, Venkatesan A, et al. Diagnostic value of (18)F-FDG PET/CT versus MRI in the setting of antibody-specific autoimmune encephalitis. *J Nucl Med*. (2017) 58:1307–13. doi: 10.2967/jnumed.116.184333
28. Boesebeck F, Schwarz O, Dohmen B, Graef U, Vestring T, Kramme C, et al. Faciobrachial dystonic seizures arise from cortico-subcortical abnormal brain areas. *J Neurol*. (2013) 260:1684–6. doi: 10.1007/s00415-013-6946-7
29. Navarro V, Kas A, Apartis E, Chami L, Rogemond V, Levy P, et al. Motor cortex and hippocampus are the two main cortical targets in LGI1-antibody encephalitis. *Brain*. (2016) 139(Pt 4):1079–93. doi: 10.1093/brain/aww012
30. Chen Y, Xing XW, Zhang JT, Wang RX, Zhao W, Tan QC, et al. Autoimmune encephalitis mimicking sporadic creutzfeldt-jakob disease: a retrospective study. *J Neuroimmunol*. (2016) 295–296:1–8. doi: 10.1016/j.jneuroim.2016.03.012
31. Kim TJ, Lee ST, Shin JW, Moon J, Lim JA, Byun JI, et al. Clinical manifestations and outcomes of the treatment of patients with GABAB encephalitis. *J Neuroimmunol*. (2014) 270:45–50. doi: 10.1016/j.jneuroim.2014.02.011
32. Su M, Xu D, Tian R. (18)F-FDG PET/CT and MRI findings in a patient with anti-GABA(B) receptor encephalitis. *Clin Nucl Med*. (2015) 40:515–7. doi: 10.1097/RLU.0000000000000676
33. Chen C, Wang X, Zhang C, Cui T, Shi WX, Guan HZ, et al. Seizure semiology in leucine-rich glioma-inactivated protein 1 antibody-associated limbic encephalitis. *Epilepsy Behav*. (2017) 77:90–5. doi: 10.1016/j.yebeh.2017.08.011

Conflict of Interest: The authors declare that the research was conducted in the absence of any commercial or financial relationships that could be construed as a potential conflict of interest.

frontiers
in Neurology

PERSPECTIVE
published: 30 June 2020
doi: 10.3389/fneur.2020.00549

On the Origins of Diffusion MRI Signal Changes in Stroke

Stephen J. Blackband[1,2,3,4]*, **Jeremy J. Flint**[1,2], **Brian Hansen**[5], **Timothy M. Shepherd**[6], **Choong H. Lee**[6], **Wolfgang J. Streit**[1] **and John R. Forder**[2,4,7,8]

[1] Department of Neuroscience, University of Florida, Gainesville, FL, United States, [2] McKnight Brain Institute, University of Florida, Gainesville, FL, United States, [3] Center for Structural Biology, University of Florida, Gainesville, FL, United States, [4] National High Magnetic Field Laboratory, Tallahassee, FL, United States, [5] Center of Functionally Integrative Neuroscience, Aarhus University, Aarhus, Denmark, [6] Department of Radiology, New York University School of Medicine, New York, NY, United States, [7] Department of Biomedical Engineering, University of Florida, Gainesville, FL, United States, [8] Department of Radiology, University of Florida, Gainesville, FL, United States

Magnetic resonance imaging (MRI) is a leading diagnostic technique especially for neurological studies. However, the physical origin of the hyperintense signal seen in MR images of stroke immediately after ischemic onset in the brain has been a matter of debate since it was first demonstrated in 1990. In this article, we hypothesize and provide evidence that changes in the glial cells, comprising roughly one-half of the brain's cells and therefore a significant share of its volume, accompanying ischemia, are the root cause of the MRI signal change. Indeed, a primary function of the glial cells is osmoregulation in order to maintain homeostasis in the neurons and nerve fibers for accurate and consistent function. This realization also impacts our understanding of signal changes in other tissues following ischemia. We anticipate that this paradigm shift will facilitate new and improved models of MRI signals in tissues, which will, in turn, impact clinical utility.

Keywords: stroke, diffusion, glial cells, magnetic resonance (MR) imaging, magnetic resonance (MR) microscopy

Edited by:
Achim Gass,
University Medical Center
Mannheim, Germany

Reviewed by:
Kersten Villringer,
Charité–Universitätsmedizin
Berlin, Germany
Mark S. Bolding,
University of Alabama at Birmingham,
United States

****Correspondence:***
Stephen J. Blackband
sblackba@ufl.edu

Specialty section:
This article was submitted to
Applied Neuroimaging,
a section of the journal
Frontiers in Neurology

Received: *06 December 2019*
Accepted: *15 May 2020*
Published: *30 June 2020*

Citation:
Blackband SJ, Flint JJ, Hansen B, Shepherd TM, Lee CH, Streit WJ and Forder JR (2020) On the Origins of Diffusion MRI Signal Changes in Stroke. Front. Neurol. 11:549.
doi: 10.3389/fneur.2020.00549

INTRODUCTION

Magnetic resonance imaging (MRI) is now a leading human imaging modality, which has revolutionized our study and understanding of the brain, in sickness and in health. Of its many capabilities in the diagnosis of human disease, MRI has proven crucial for the early detection of stroke and for guiding effective treatments (1). In particular, diffusion-weighted imaging (DWI) detects the tissue affected by stroke almost immediately after the infarct. This ischemic region, first demonstrated by Moseley et al. (2), appears as a hyperintensity on the DW image that represents a decrease in the overall apparent diffusion coefficient (ADC) of water in the affected tissue. This ischemic region develops over time as the stroke progresses and, at later times, also results in a change in the transverse relaxation time, T_2 (3). In this article, we will be concerned with the initial diffusion changes and propose that glial cells drive the observed signal increase in acute stroke.

Currently, the origin of the observed diffusion signal increase in the infarct is still a matter of debate. Candidate mechanisms include changes in water exchange rates, membrane permeability, restricted diffusion effects, intra/extracellular compartmentation changes, and/or tortuosity effects potentially coupled with relaxation time differences between compartments—for a full discussion see Vestergaard-Poulson et al. (4), Hansen et al. (5). Neurite beading has also been suggested as a mechanism to explain the signal changes in the brain (6).

In order to uncover the likely mechanism(s) of these signal changes, MR microscopy was employed as a means for determining the origins of MR signals at the cellular level, albeit on very large cells initially (7). Since its inception three decades ago (7, 8), MR microscopy has continually improved, next being able to image the large L7 neuron from the sea slug *Aplysia californica* (9) and more recently applied to the study of isolated mammalian tissues at the single-cell level (10, 11).

This powerful methodology can be used to evaluate a hypothesis of the origin of the signal increase in DW images observed in stroke recently proposed by Le Bihan (12). He asserted that there is a restricted water pool near the cell membrane and that this slowly diffusing water pool would increase its volume as cells swell after an ischemic event. Curiously, the model involves only diffusion restriction on the inside of the cell membrane and not the outside. Moreover, if similar effects were to be applied externally, this would approximately double the volume of restricted water and change his conclusions significantly. Aside from that, MR microscopy studies of frog ova (6), *Aplysia californica* neurons (7), fixed animal (10), and human (11) neurons, and most recently live rat neurons (13) using MR microscopy methods, do not support this mechanism based upon membrane-bound water. If water diffusion was restricted at the cell membrane to the extent needed to affect the observed clinical signal changes seen in stroke, then DW images of these cells should include a relatively thick bright rim around the cell membranes where the restriction allegedly occurs. A bright rim of a size necessary to cause significant changes in volume fractions is not observed in any of the aforementioned cellular studies. Studies of erythrocyte ghosts also do not support this membrane-bound water hypothesis (14).

Alternatively, an intra/extracellular exchange mechanism was implied by Hsu et al. (15), following perfusion and tonicity studies performed in isolated *Aplysia californica* L7 neurons. In that work, following a 20% hypotonic perturbation, water diffusion in the cell cytoplasm remained constant, while T_2 increased, indicating the cell was behaving as a perfect osmometer. This observation suggested that, after an ischemic event, the cells swell by absorbing water from the extracellular space. Since the ADC stays constant, and the ADC inside the cell was presumed slower than outside the cell, the resulting volume average of signals would result in an overall reduction of the ADC as observed on DW images of infracted areas in stroke.

However, recent microimaging of single neurons in fixed and live tissue contradicts this idea since the neurons are hypointense in DW images, and ADC maps clearly show that ADC in the cell body is larger than that outside the cell body (10, 11). This being the case, one would then expect the reverse to happen—i.e., the DW image of stroke tissue would show a *hypointense* signal at the lesion as neurons swell.

This issue is further highlighted by data from our laboratory on excised, superfused brain slices. Diffusion signals obtained in segmented regions of the hippocampus correlated strongly with overall density of perikarya (16, 17) as observed in corresponding histology. Data from Shepherd et al. (17) is reproduced in modified form in **Figure 1** and clearly shows regions rich in neuronal cell bodies to display faster signal decay than regions less densely populated by perikarya. Therefore, if the neuronal volume fraction was increasing, one would expect the ADC to increase, not decrease. In addition, one would expect perikarya-rich tissue like the stratum pyramidale in the hippocampus's *Cornu Ammonis* (CA1, 2, 3) regions would be hyperintense in the DW images when, in fact, they are hypointense (18), indicating again that the cell bodies have a faster ADC than the surrounding neuropil.

We are thus left with a conundrum. What is the origin of the hyperintensity in DW images in ischemic areas? Here, we present evidence for an alternative mechanism for the observed signal changes in stroke. In this perspective piece, we hypothesize and evidence that glial cells may be an important contributor to the observed signal changes.

DISCUSSION

The number of glial cells in the brain is still a subject of debate, with estimates ranging from 10 times that of the neurons to a number equivalent to that of neurons (19, 20). Given the brain's complexity and the large variation in the ratio of glia to neurons found in different subregions, calculation of these ratios and the volume contributions across the entire brain is a difficult and controversial issue (21). However, whatever the true volume, it is certain that the glial cells comprise a significant fraction of the total brain volume. A primary role of the glial cells is to maintain homeostasis—neurons and nerves thus maintain their water content for accurate and efficient operation.

We hypothesize that the DW image changes observed at stroke onset are due to changes in the glial volume as these cells absorb water from the extracellular space and swell to maintain homeostasis of neurons. The resulting decrease in the ADC could then be explained provided that the diffusivity in the glial cells is lower than that of the neurons. A study by Lee et al. (22) on *Aplysia californica* neurons provides supporting evidence for this conjecture. In previous studies, the L7 neuron was stripped of surrounding tissue and cells by collagenase treatment; however, in Lee et al. (22), no collagenase was used, and the cell was extracted with the region containing satellite cells, mainly glia (23), intact. **Figure 2** from that publication (22) shows that in a DW image, the signal from the region containing satellite cells is hyperintense compared to the neuron, itself, indicating that the ADC in the glia is lower than that in the neuron. These glial cells provide the necessary homeostasis for the neurons. Thus, after an infarct, the glia swell, and assuming the ADC within them also does not change with an osmotic perturbation, as implied by Hsu et al. (15), then the average ADC from the tissue will decrease as observed *in vivo*. This is because the glial volume increases with respect to the neuronal and extracellular volume. Glia swelling in stroke is supported by literature, and neuronal shrinkage has been observed to occur alongside glial swelling. In the study by Liu et al. (24), astrocytes were seen to have swelling after 90 min of ischemia, whereas in the same regions,

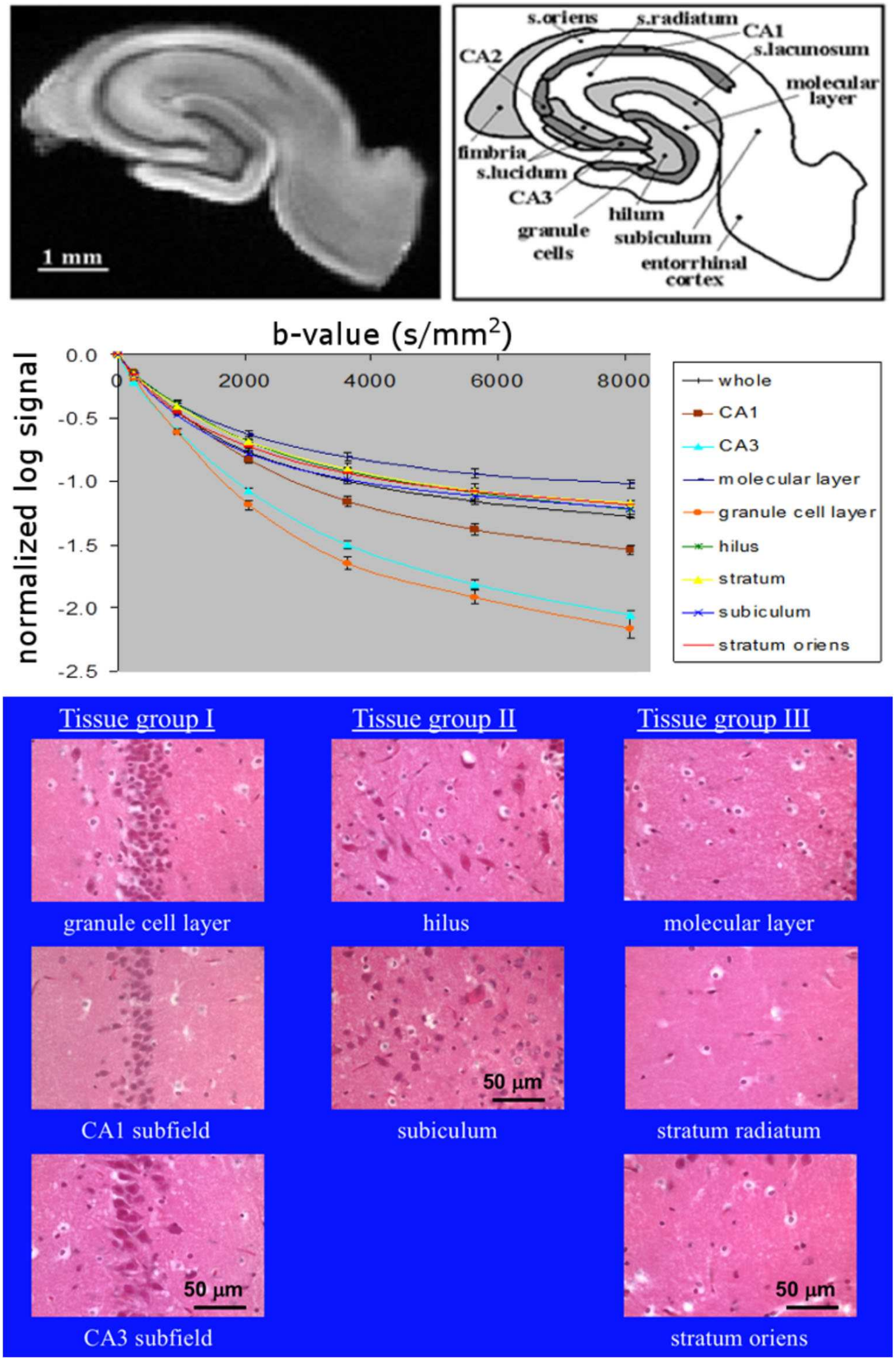

FIGURE 1 | Top: MR microimage of a hippocampal brain slice (left) with a schematic of the anatomy (right) (reproduced with permission from (17) (Creative Commons license https://creativecommons.org/licenses/by/4.0/, the two elements unaltered but placed side by side), with experimental details in that publication). **Middle**: diffusion curves from anatomical regions (16). **Bottom**: grouped histological regions by neuronal density going from left to right (16).

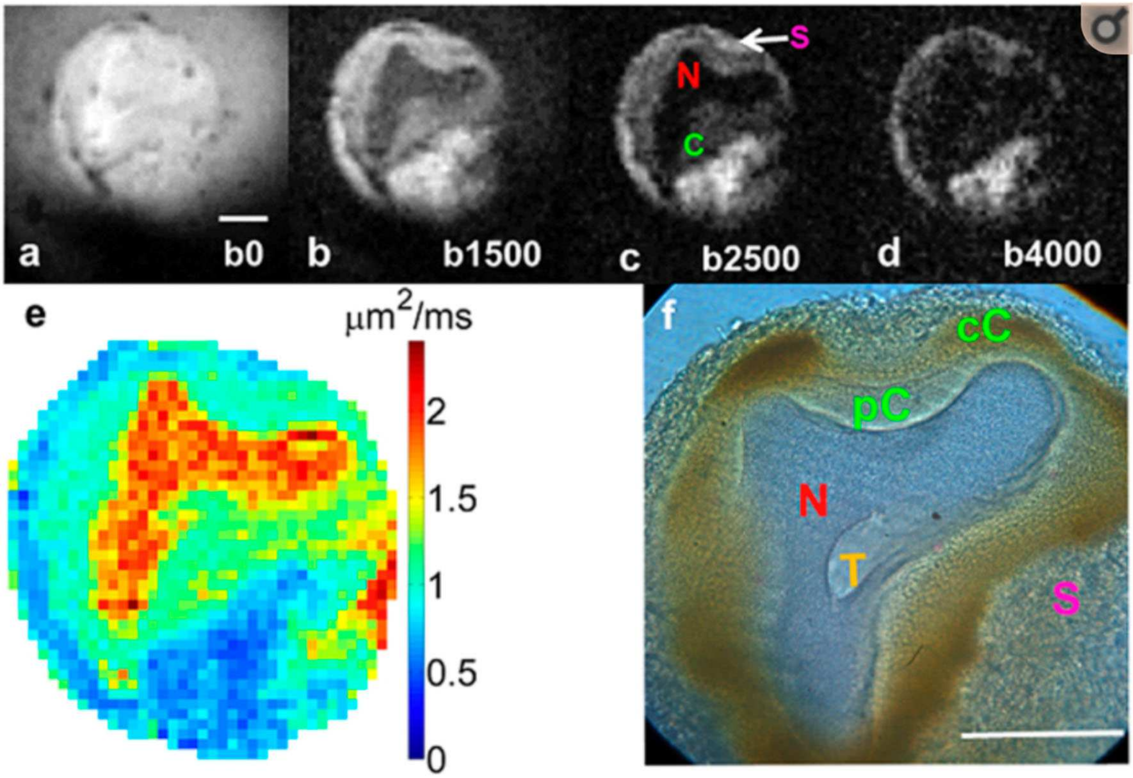

FIGURE 2 | Diffusion-weighted images of an *Aplysia californica* L7 neuron at 4 b-values **(a–d)**. Notice that the labeled satellite cells (S) are hyperintense compared to the neuron. **(e)** Calculated diffusion map and **(f)** corresponding histology. Data reproduced with permission from Lee et al. (22)—experimental details are in that publication.

the majority of neurons were shrunken by up to 25%. At 24 h post stroke, Garcia et al. (25) also observed swelling of astrocytes and shrinkage of neurons accompanied by initial axonal swelling and large hemispheric swelling (26). We, therefore, think it reasonable to assume that both neurons and extracellular water compartment contribute water to glial cells during ischemic events. We note here that these studies were not performed at the acute stage we are considering in this work, where we contend that the glia cells will be able to maintain the neuronal cell volume.

Since glial cells are ubiquitous in the nervous system, it would follow that the same mechanism will be evident in both gray and white matter. The axons of the white matter are myelinated making them much less permeable to water than the cell membrane. However the myelinated segments are interspersed with nodes of Ranvier that are approximately 1-μm length of unmyelinated axon membrane segments where ion and water exchange may occur. The length of the myelinated axolemma sections is dependent on the axon diameter (27). Further, there is evidence for water channels in the myelin sheath, itself (28). Whatever the mechanisms are, osmoregulation in axons is critical to ensure accurate and stable action potentials, whose conduction velocity is greatly accelerated by saltatory conduction (29). Again, osmoregulation in axon-rich brain tissue is affected by the glial cells. Thus, DW images should exhibit hyperintense signals during infarcts in both gray and white matter. At some point, the glial cells' capability for osmoregulation will be overwhelmed. This is supported by late-stage observations in rat brains exposed to sub-arachnoid hemorrhage (SAH): here, astrocyte volume was higher in SAH than in sham animals (30). We believe that at this point, vasogenic edema occurs, leading to measurable changes in T_1 and T_2 in the infarct. This potential causality between these events is the subject of future investigation.

We stress, here, that our discussion, thus far, has focused on the early stages of ischemia when the cells swell, and there is seen a hyperintensity in DW images, but no changes in T_2. It is in this early stage that we will first develop and test the glial hypothesis in future studies. The signal changes following the acute phase will be time dependent and also dependent on other factors such as age, location of the stroke, size of the stroke, etc. (31). Later studies will also test the effectiveness of our biological models for assessing treatment, such as reperfusion, etc. (31), that are used in the clinic.

Although our data provide evidence for our hypothesis regarding glial cell osmoregulation and its effects upon diffusion MRI, direct confirmation is required in mammalian tissues. It is not yet possible to image glial cells with MR microscopy as they are too small. However, future studies may involve diffusion measurements on cultured mammalian glial cells assuming that the compartmental averaging issues can be addressed. Future studies and modeling of these systems at the single-cell level will also have to take account of the age of the specimens as demonstrated in maturation studies of *Aplysia californica* L7 neurons (32).

In addition to this glial hypothesis, Le Bihan (33) also published data showing that functional changes in brain tissue could be detected using DWI data acquired in humans. To our knowledge, other groups have not been able to reproduce this result, leading to speculation that Le Bihan et al. may be actually observing an artifact from the BOLD-fMRI contrast mechanism (34). However, it is important to note that studies in isolated buffer-superfused brain slices (35) devoid of blood do support possible changes in DW image signal associated with neuronal activity, as do studies on optic nerves (36) and spinal cord white matter (37). Specifically, if the glial hypothesis was correct, then we suggest that it is also changes in glial volumes that lead to the reduced ADC with neuronal activation in both buffer-perfused and blood-perfused preparation. We note here that Stanisz (38) included a glial compartment in his modeling approach to the issue of diffusion changes in the brain, recognizing that it would impact his results. However his estimate of the glial volume was too low at 17%, and he had no direct evidence on the diffusion in the glia relative to the neurons, nor perturbation studies at the cellular level, so could not come to the conclusion that we have in this work.

How then do we explain DW image changes associated with ischemia in non-neural tissues, which do not contain glial cells? MR microscopy studies of isolated perfused hearts with MR microscopy exposed to an ischemic event show an immediate decrease in the ADC (39) and T_2 (40) after the ischemic insult. Without the osmoregulatory glial cells, the myocytes, themselves, will swell, leading to a change in the ADC and T_2 with cell swelling in a straightforward intra/extracellular tissue model of water exchange. We suspect this will be the case in other non-neuronal tissues, and this will be a subject for future investigations. Cardiac studies were not performed at microscopic resolution because of the relatively large sample sizes (whole, excised rabbit hearts). However, microscopic resolution will be feasible on isolated heart slices (41) in the same manner in which brain slices have been imaged (**Figure 1** in this paper). In this study on heart slices (41), the resolution was relaxed for SNR reasons to study multicomponent diffusion; however, since the sample size and equipment used is the same as that used for our **Figure 1**, MR microscopy will be feasible on the heart slices as well.

We note here that our discussion does hinge on using data from invertebrates to interpret rodent and clinical data. *Aplysia* is, indeed, an exceptionally well-used model for cells since theirs are large and accessible, so much so that the NIH funds an *Aplysia* facility in Miami to breed them for scientists. So far, studies of frog ova, *Aplysia* neurons, and mammalian tissues have produced broadly agreeing results with respect to intracellular water, i.e., reduced diffusion in the intracellular space compared to free water. In this work, it is assumed that the even slower diffusion in regions enriched with many glial cells, as observed in the satellite cells on the L7 neuron from *Aplysia californica*, will translate to mammalian tissues. Indeed, the very testing of the hypothesis presented here will be addressing this issue in future studies.

Caution is needed when trying to integrate results from cellular-level MR microscopy studies and preclinical MRI in animal models with the aim to interpret clinical data. Not only are the model systems employed in MR microscopy (frog eggs, isolated L7 neurons, acute brain slices, spinal cord, etc.) not directly comparable to the human brain but also the experimental details underlying the data are not comparable to clinical imaging. Extremely high SNR is required to achieve the image resolution needed to resolve individual cells. To achieve this, a combination of strong magnetic fields and minute (micro-)coils for radio frequency transmission and reception is typically used for MR microscopy on very small samples (7). Such setups are quite removed from clinical radiology. However, a more determining difference is related to the scanner gradient systems wherein MR microscopy and preclinical MRI gradients are typically strong (allowing short pulses), whereas for clinical DWI, diffusion gradient durations are typically an order of magnitude larger (on the order of TE/2). This is a problem because a lot of our current modeling assumes the short pulse approximation, which is rarely justified for clinical data. Furthermore, for longer diffusion times, water exchange likely cannot be ignored but largely is. The combined effects of diffusion time dependence, restriction sizes, exchange, etc., are difficult to untangle and likely quite different in MR microscopy and clinical MRI. Admittedly, this produces a situation where the comparison of MR microscopy to clinical MRI is complex. However, we point out that this is an issue common to all the microscopies (optical, confocal, X-ray, electron, atomic force, etc.), which interrogate small samples with specialized equipment not appropriate for direct clinical use. Care must be taken extending the results for clinical interpretation; for example, consider the sample preparation techniques required for electron microscopy (42). Still, we see MR microscopy as an essential tool to aid in understanding of clinical data, especially since the samples can be maintained as living tissue samples, allowing meaningful and informative perturbation studies to test models. We also point out that even if we can improve MRI to achieve true microscopic resolutions in the clinic, we will always be able to do much better on smaller samples with specialized equipment.

We end this perspective piece with a hefty dose of speculation or "what ifs." Maintaining a stable tonicity in axons is essential for accurate and reproducible action potentials and, thus, fidelity of communication in the brain. What if for some reason the glial cells are compromised? What if they become hypo- or hypertonic? This may lead to tonicity changes in the axons, changing the velocity of the action potential. We appreciate that this is a complex issue—changes in tonicity also change axonal diameter, which also impacts conduction velocity (43). An increase in conduction velocity may be a factor in movement disorders where astrocytes have been linked with neuroinflammation and neurodegeneration (44), for example, in Parkinson's disease. A decrease in conduction velocity may be a factor in poor memory formation, again involving astrocytes (44), for example, in Alzheimer's. What if variations in glial tonicity lead to mood disorders, where glial cells have already been implicated to play a role (45, 46)? These ideas are very speculative, and we are not suggesting that glial cell dysfunction is a panacea for brain diseases. However, speculation along these lines may lead to fruitful avenues of research and potential clinical application in which MRI may play a major role. Replenishing the glial cells in some way may prove a potential treatment and seems feasible now that it has been demonstrated that they migrate when injected into the brain (47).

In conclusion, we have proposed and provide experimental support for the hypothesis that it is changes in glial cell volume that cause the ADC changes in ischemic brain tissue after stroke onset in both gray and white matter. Echoing a well-known statement on the relationship between mass and space, water tells glial cells how to change, and the glial cells tell water how to move, potentially solving a nearly 30-year-old mystery on the origin of the diffusion signal changes in stroke. With this in mind, new and accurate models of the tissue signals and how they evolve become possible. Other mechanisms will likely be involved in the resulting tissue changes to varying degrees; perturbation studies on model systems, both fixed and live, will facilitate the elucidation of these effects. It is our belief that this understanding will help improve the sensitivity and specificity of MRI for the diagnosis and monitoring of stroke, in particular, for distinguishing between reversible and irreversible ischemia and guiding the most effective course of personalized therapy. This understanding will also impact our interpretation of MR signals in both normal tissue and pathological tissues.

DATA AVAILABILITY STATEMENT

Publicly available datasets were analyzed in this study. This data can be found here: https://www.ncbi.nlm.nih.gov/pubmed/14663342, https://www.ncbi.nlm.nih.gov/pubmed/26059695.

AUTHOR CONTRIBUTIONS

JJF, TS, and CL performed the MR microscopy experiments described and processed image data and subsequent analysis. BH performed data processing and modeling. WS advised on glial cell biology. JRF advised on perfusion issues. SB originated the glial cell hypothesis and its consequences and was the PI and supervisor of studies from which results were reproduced, and wrote this manuscript. All authors contributed to the article and approved the submitted version.

FUNDING

Funding was provided by the NIH and NSF over the decades (see publications for grant numbers). MR imaging studies were performed in the McKnight Brain Institute at the National High Magnetic Field Laboratory's AMRIS Facility, which is supported by the National Science Foundation Cooperative Agreement Nos. DMR-1157490 and DMR-1644779. This NSF grant also funded SB for the generation of this manuscript. Many thanks to Dr. Peter Basser for his edits of an early version of this manuscript.

REFERENCES

1. Kamalian S, Lev MH. Stroke imaging. *Radiol Clin North Am.* (2019) 57:717–32. doi: 10.1016/j.rcl.2019.02.001
2. Moseley ME, Cohen Y, Mintorovitch J. Early detection of regional cerebral ischemic injury in cats: evaluation of diffusion and T2-weighted MRI and spectroscopy. *Magn Reson Med*. (1990) 14:330–46. doi: 10.1002/mrm.1910140218
3. Siemonsen S, Lobel U, Sedlacik J, Forkert ND, Mouridsen K, Ostergaard L, et al. Elevated T2-values in MRI of stroke patients shortly after symptom onset do not predict irreversible tissue infarction. *Brain*. (2012) 135(Pt 6):1981–9. doi: 10.1093/brain/aws079
4. Vestergaard-Poulson P, Hansen B, Ostergaard L, Jakobsen R. Microstructural changes in ischemic cortical grey matter predicted by a model of diffusion-weighted MRI. *J Magn Res Imag.* (2007) 26:529–40. doi: 10.1002/jmri.21030
5. Hansen B, Vestergaard-Poulson P. Mapping the parameter space of a T2-dependant model of water diffusion MR in brain tissue. *MagnReson Imaging*. (2006) 24:1031–8. doi: 10.1016/j.mri.2006.04.012
6. Budde MD, Frank JA. Neurite beading is sufficient to decrease the apparent diffusion coefficient after ischemic stroke. *Proc Natl Acad Sci.* (2010) 107:14472–7. doi: 10.1073/pnas.1004841107
7. Callaghan PT. *Principles of Nuclear Magnetic Resonance Microscopy*. Oxford: Clarendon Press (1991).
8. Aguayo JB, Blackband SJ, Schoeniger J, Mattingly MA, Hintermann M. NMR imaging of a single cell: the NMR microscope. *Nature*. (1986) 322:190–1. doi: 10.1038/322190a0
9. Schoeniger JS, Aiken N, Hsu E, Blackband SJ. Relaxation-time and diffusion NMR microscopy of single neurons. *JMagnResonB*. (1994) 103:261–73. doi: 10.1006/jmrb.1994.1039
10. Flint JJ, Lee CH, Hansen B, Fey M, Schmidig D, Bui JD, et al. Magnetic resonance microscopy of mammalian neurons. *NeuroImage.* (2009) 46:1037–40. doi: 10.1016/j.neuroimage.2009.03.009
11. Flint JJ, Hansen B, Portnoy S, Lee CH, King MA, Fey M, et al. Magnetic resonance microscopy of human and porcine neurons and cellular processes. *Neuroimage*. (2012) 60:1404–11. doi: 10.1016/j.neuroimage.2012.01.050
12. Le Bihan D. The 'wet mind': water and functional neuroimaging. *Phys Med Biol.* (2007) 52:R57–90. doi: 10.1088/0031-9155/52/7/R02
13. Flint JJ, Menon K, Hansen B, Forder J, Blackband SJ. Visualization of live mammalian neurons during rest and kainite-induced activation using magnetic resonance microscopy. *Neuroimage.* (2020) doi: 10.1016/j.neuroimage.2020.116997. [Epub ahead of print].
14. Thelwall P, Grant SC, Stanisz GJ, Blackband SJ. Human Erythrocyte Ghosts: exploring the origins of multiexponential water diffusion in a model biological tissue with magnetic resonance. *Magn Reson Med.* (2002) 48:649–57. doi: 10.1002/mrm.10270
15. Hsu EW, Aiken NR, Blackband SJ. NMR microscopy of single neurons under hypotonic perturbation. *Am J Physiol.* (1996) 271:C1895–C900. doi: 10.1152/ajpcell.1996.271.6.C1895
16. Shepherd TM. *Diffusion Magnetic Resonance Imaging In A Rat Hippocampal Slice Model Of Acute Brain Injury*. Ph.D. thesis, University of Florida, Gainesville, FL, United States. (2003).
17. Shepherd TM, Thelwall PE, Blackband SJ, Pike BR, Hayes RL, Wirth ED 3rd. Diffusion magnetic resonance imaging study of a rat hippocampal slice model of acute brain injury. *J Cereb Blood Flow Metab.* (2003) 23:1461–70. doi: 10.1097/01.WCB.0000100852.67976.C2
18. Portnoy S, Flint JJ, Blackband SJ, Stanisz GJ. Oscillating and pulsed gradient diffusion magnetic resonance microscopy over an extended b-value range: implications for the characterization of tissue microstructure. *MagnReson Med.* (2013) 69:1131–45. doi: 10.1002/mrm.24325
19. von Bartheld CS, Bahney J, Herculano-Houzel S. The search for the true numbers of neurons and glial cells in the human brain: A review of 1250 years of cell counting. *J Comp Neurol.* (2016) 524:3865–95. doi: 10.1002/cne.24040
20. Azevedo FA, Carvalho LR, Grinberg LT, Farfel JM, Ferretti RE, Leite RE, et al. Equal numbers of neuronal and non-neuronal cells make the human brain

an isometrically scaled-up primate brain. *J Comp Neuro*. (2009) 513:532–41. doi: 10.1002/cne.21974

21. Herculano-Houzel S, Collins CE, Wong P, Kaas JH. Cellular scaling rules for primate brains. *PNAS*. (2007) 104:3562–67. doi: 10.1073/pnas.0611396104
22. Lee CH, Flint JJ, Hansen B, Blackband SJ. Investigation of the subcellular architecture of L7 neurons of Aplysia californica using magnetic resonance microscopy (MRM) at 7.8 microns. *Sci Rep*. (2015) 5:11147. doi: 10.1038/srep11147
23. Colonnier M, Tremblay JP, McLennan H. Synaptic contacts on glial cells in the abdominal ganglion of Aplysia californica. *J Comp Neurol*. (1979) 188:391–400. doi: 10.1002/cne.901880304
24. Liu KF, Li F, Tatlisumak T, Garcia JH, Sotak CH, Fisher M, et al. Regional Variations in the Apparent Diffusion Coefficient and the Intracellular Distribution of Water in Rat Brain During Acute Focal Ischemia. *Stroke*. (2001) 32:1897–905. doi: 10.1161/01.STR.32.8.1897
25. Garcia JH, Yoshida Y, Chen H, Li Y, Zhang ZG, Lian J, et al. Progression from ischemic injury to infarct following middle cerebral artery occlusion in the rat. *Am J Pathol*. (1993) 142:623–35.
26. Garcia JH, Kamijyo Y. Cerebral infarction. Evolution of histopathological changes after occlusion of a middle cerebral artery in primates. *J Neuropathol Exp Neurol*. (1974) 33:408–21. doi: 10.1097/00005072-197407000-00007
27. Rushton WA. A theory of the effects of fibre size in medullated nerve. *J Physiol*. (1951) 115:101–22. doi: 10.1113/jphysiol.1951.sp004655
28. Rash J. Molecular disruptions of the panglial syncytium block potassium siphoning and axonal saltatory conduction: pertinence to neuromyelitis optica and other demyelinating diseases of the central nervous system. *Neuroscience*. (2010) 168:982–1008. doi: 10.1016/j.neuroscience.2009.10.028
29. Tasaki I. The electro-saltatory transmission of the nerve impulse and the effect of narcosis upon the nerve fiber. *Am J Phys*. (1939) 127:211–27. doi: 10.1152/ajplegacy.1939.127.2.211
30. Anzabi M, Ardalan M, Iversen NK, Rafati AH, Hansen B, Ostergaard L. Hippocampal atrophy following subarachnoid hemorrhage correlates with disruption of astrocyte morphology and capillary coverage by AQP4. *Cell Neurosci*. (2018) 12:19. doi: 10.3389/fncel.2018.00019
31. Fiehler J, Fiebach JB, Gass A, Hoehn M, Kucinski T, Neumann-Haefelin T, et al. Diffusion-weighted imaging in acute stroke - a tool of uncertain value? *Review Cerebrovasc Dis*. (2002) 14:187–96. doi: 10.1159/000065675
32. Aiken N, Hsu E, Horsman A, Blackband SJ. Maturation effects on the NMR microimaging characteristics of single neurons. *Am J Physiol*. (1996) 271:C1295–C302. doi: 10.1152/ajpcell.1996.271.4.C1295
33. Le Bihan D. Diffusion, confusion and functional MRI. *NeuroImage*. (2012) 62:1131–6. doi: 10.1016/j.neuroimage.2011.09.058
34. Miller KL, Bulte DP, Devlin H, Robson MD, Wise RG, Woolrich MW, et al. Evidence for a vascular contribution to diffusion FMRI at high *b* value. *Proc Natl Acad Sci USA*. (2007) 104:20967–72. doi: 10.1073/pnas.0707257105
35. Flint J, Hansen B, Vestergaard-Poulsen P, Blackband SJ. Diffusion weighted magnetic resonance imaging of neuronal activity in the hippocampal slice model. *NeuroImage*. (2009) 46:411–8. doi: 10.1016/j.neuroimage.2009.02.003
36. Spees WM, Lin T, Song S. White matter diffusion fMRI of mouse optic nerve. *NeuroImage*. (2013) 65:209–15. doi: 10.1016/j.neuroimage.2012.10.021
37. Tirosh N, Nevo U. Neuronal activity significantly reduces water displacement: DWI of a vital rat spinal cord with no hemodynamic effect. *NeuroImage*. (2013) 76:98–107. doi: 10.1016/j.neuroimage.2013.02.065
38. Stanisz GJ. Diffusion MR in biological systems: tissue compartments and exchange. *Israel J Chem*. (2003) 43:33–44. doi: 10.1560/E0WU-7FFH-31M6-VLYT
39. Hsu EW, Xue R, Holmes A, Forder JR. Delayed reduction of tissue water diffusion after myocardial ischemia. *Am J Physiol*. (1998) 275 (Heart Circ Physiol 44):H697–H702. doi: 10.1152/ajpheart.1998.275.2.H697
40. Chatham JC, Ackerman S, Blackband SJ. High resolution 1H NMR imaging of regional ischemia in the isolated perfused rabbit heart at 4.7T. *Magn Reson Med*. (1991) 21:144–150. doi: 10.1002/mrm.1910210118
41. Forder JR, Bui JD, Buckley DL, Blackband SJ. MR imaging measurement of compartmental water diffusion in perfused heart slices. *Am J Physiol Heart Circ Physiol*. (2001) 281:H1280–5. doi: 10.1152/ajpheart.2001.281.3.H1280
42. Nguyen JNT, Harbison AM. Scanning electron microscopy sample preparation and imaging. *Methods Mol Biol*. (2017) 1606:71–84. doi: 10.1007/978-1-4939-6990-6_5
43. Krarup C, Moldovan M. Nerve conduction and excitability studies in peripheral nerve disorders. *CurrOpin Neurol*. (2009) 22:460–6. doi: 10.1097/WCO.0b013e3283304c9d
44. Neal M, Richardson JR. Epigenetic regulation of astrocyte function in neuroinflammation and neurodegeneration. *BiochimBiophys Acta Mol Basis Dis*. (2018) 1864:432–43. doi: 10.1016/j.bbadis.2017.11.004
45. Haroon E, Miller AH, Sanacora G. Inflammation, glutamate and glia: a trio of trouble in mood disorders. *Neuropsychopharmacology*. (2017) 42:193–215. doi: 10.1038/npp.2016.199
46. Öngür D, Bechtholt AJ, Carlezon WA Jr, Cohen BM. Glial abnormalities in mood disorders. *Harv Rev Psychiatry*. (2014) 22:334–7. doi: 10.1097/HRP.0000000000000060
47. Streit WJ, Rabchevsky AG. Grafting of cultured microglial cells into the lesioned spinal cord of adult rats enhances neurite outgrowth. *J Neurosci Res*. (1997) 47:34–48. doi: 10.1002/(SICI)1097-4547(19970101)47:1<34::AID-JNR4>3.0.CO;2-G

Conflict of Interest: The authors declare that the research was conducted in the absence of any commercial or financial relationships that could be construed as a potential conflict of interest.

frontiers in Neurology

METHODS
published: 11 August 2020
doi: 10.3389/fneur.2020.00847

Ontario Neurodegenerative Disease Research Initiative (ONDRI): Structural MRI Methods and Outcome Measures

Joel Ramirez[1]*, **Melissa F. Holmes**[1], **Christopher J. M. Scott**[1], **Miracle Ozzoude**[1], **Sabrina Adamo**[1], **Gregory M. Szilagyi**[1], **Maged Goubran**[1,2], **Fuqiang Gao**[1], **Stephen R. Arnott**[3], **Jane M. Lawrence-Dewar**[4], **Derek Beaton**[3], **Stephen C. Strother**[2,3], **Douglas P. Munoz**[5], **Mario Masellis**[1,6], **Richard H. Swartz**[1,6], **Robert Bartha**[7], **Sean Symons**[8], **Sandra E. Black**[1,6] **and the ONDRI Investigators**

[1] Hurvitz Brain Sciences Program, Sunnybrook Research Institute, University of Toronto, Toronto, ON, Canada, [2] Department of Medical Biophysics, University of Toronto, Toronto, ON, Canada, [3] Rotman Research Institute, Baycrest, Toronto, ON, Canada, [4] Thunder Bay Regional Health Research Institute, Thunder Bay, ON, Canada, [5] Centre for Neuroscience Studies, Queen's University, Kingston, ON, Canada, [6] Department of Medicine (Neurology), Sunnybrook Health Sciences Centre and University of Toronto, Toronto, ON, Canada, [7] Department of Medical Biophysics, Centre for Functional and Metabolic Mapping, Robarts Research Institute, University of Western Ontario, London, ON, Canada, [8] Department of Medical Imaging, University of Toronto, Sunnybrook Health Sciences Centre, Toronto, ON, Canada

Edited by:
Christian Gaser,
Friedrich Schiller University Jena, Germany

Reviewed by:
Jeffrey L. Gunter,
Mayo Clinic, United States
Shannon Risacher,
Indiana University Bloomington,
United States

***Correspondence:**
Joel Ramirez
joel.ramirez1@sunnybrook.ca

Specialty section:
This article was submitted to Applied Neuroimaging, a section of the journal Frontiers in Neurology

Received: 06 January 2020
Accepted: 07 July 2020
Published: 11 August 2020

Citation:
Ramirez J, Holmes MF, Scott CJM, Ozzoude M, Adamo S, Szilagyi GM, Goubran M, Gao F, Arnott SR, Lawrence-Dewar JM, Beaton D, Strother SC, Munoz DP, Masellis M, Swartz RH, Bartha R, Symons S, Black SE and the ONDRI Investigators (2020) Ontario Neurodegenerative Disease Research Initiative (ONDRI): Structural MRI Methods and Outcome Measures. Front. Neurol. 11:847. doi: 10.3389/fneur.2020.00847

The Ontario Neurodegenerative Research Initiative (ONDRI) is a 3 years multi-site prospective cohort study that has acquired comprehensive multiple assessment platform data, including 3T structural MRI, from neurodegenerative patients with Alzheimer's disease, mild cognitive impairment, Parkinson's disease, amyotrophic lateral sclerosis, frontotemporal dementia, and cerebrovascular disease. This heterogeneous cross-section of patients with complex neurodegenerative and neurovascular pathologies pose significant challenges for standard neuroimaging tools. To effectively quantify regional measures of normal and pathological brain tissue volumes, the ONDRI neuroimaging platform implemented a semi-automated MRI processing pipeline that was able to address many of the challenges resulting from this heterogeneity. The purpose of this paper is to serve as a reference and conceptual overview of the comprehensive neuroimaging pipeline used to generate regional brain tissue volumes and neurovascular marker data that will be made publicly available online.

Keywords: MRI, Alzheimer, Parkinson, amyotrophic lateral sclerosis, frontotemporal dementia, cerebrovascular disease, stroke, cerebral small vessel disease

INTRODUCTION

The Ontario Neurodegenerative Research Initiative (ONDRI) is a multi-site prospective cohort study following patients with neurodegenerative diseases including Alzheimer's disease (AD), mild cognitive impairment (MCI), Parkinson's disease (PD), amyotrophic lateral sclerosis (ALS), frontotemporal dementia (FTD), and cerebrovascular disease (CVD). Over the course of 3 years, multiple assessment platforms acquired comprehensive data from the 520 patients including: neuroimaging (1–3), clinical and demographic assessments (4), neuropsychology (5), genetic variations (6, 7), eye tracking and pupillometry, retinal layer analyses using spectral-domain optical coherence tomography (8), gait and balance performance (9), and neuropathology. The multi-modal data collected from ONDRI will be used to explore earlier detection, guide development of novel therapy, and improve patient care. ONDRI's mission is to bring new diagnostic biomarkers and prognostic tools into clinical practice in order track disease progression and potential response to future symptomatic and disease-modifying therapies targeting dementia/cognitive impairment.

This paper describes the methods implemented to extract normal and pathological brain tissue volumetric information from the structural Magnetic Resonance Imaging (MRI) provided by the ONDRI neuroimaging platform. It includes a comprehensive methodological overview of the structural neuroimaging pipeline's previously published and validated components, with numerous figures to provide a visual description of how the measures were obtained from the MRI, some recommendations for reporting and data analysis, and a brief section providing some basic descriptive statistics to illustrate the whole brain volumetrics that can be obtained from the ONDRI patient cohorts.

Structural MRI processing for volumetrics was performed by the neuroimaging group in the L.C. Campbell Cognitive Neurology Research Unit, within the Hurvitz Brain Sciences Research Program, at the Sunnybrook Research Institute, in Toronto, Canada. The image processing pipeline (**Figure 1**) has been optimized for an aging population, with a particular emphasis on accounting for chronic stroke and post stroke cortical and subcortical lesions, numerous imaging markers of cerebral small vessel disease, as well as, the focal and global brain atrophy observed in neurodegenerative patient populations such as AD and FTD.

The main goal of this paper is to highlight the overall features of the neuroimaging pipeline that would be of interest to a neurologist, clinician, or non-imaging researcher seeking to utilize the ONDRI data that will be made publicly available through an application process on October, 2020. For more information on the ONDRI project, please visit: http://ondri.ca/.

METHODS

Study Participants

Ethics approval was obtained from all participating institutions. Participants were recruited at 14 health centers across six cities in Ontario, Canada: Hamilton General Hospital and McMaster Medical Centre in Hamilton; Hotel Dieu Hospital and Providence Care Hospital in Kingston; London Health Science Centre and Parkwood Institute in London; Elizabeth Bruyère Hospital and The Ottawa Hospital in Ottawa; Thunder Bay Regional Health Sciences Centre in Thunder Bay; and Baycrest Health Sciences (Baycrest), Centre for Addiction and Mental Health (CAMH), St. Michael's Hospital (SMH), Sunnybrook Health Sciences Centre (Sunnybrook), and Toronto Western Hospital—University Health Network (UHN) in Toronto.

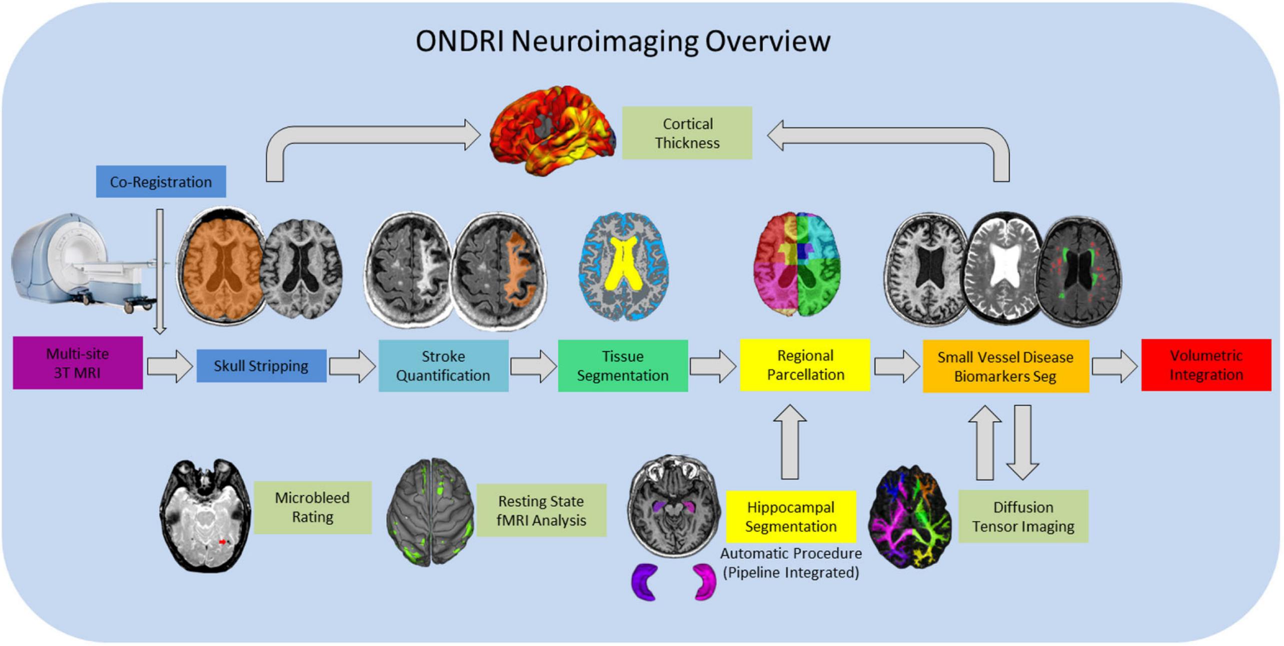

FIGURE 1 | ONDRI MRI processing pipeline overview. General workflow moves from left to right for final volumetric output resulting in a comprehensive spreadsheet in the form of a .csv file. Hippocampal volumes are segmented using the SBHV method (10) which was fully integrated into the pipeline and are included in the final volumetric spreadsheet. Microbleed Rating, Resting State fMRI Analysis, and Diffusion Tensor Imaging (DTI) analyses are processed separately, however, the DTI and Cortical Thickness pipelines are dependent on some components of the primary pipeline, thus, results from these processes are provided in separate spreadsheets.

Full study participant details are previously described (4). Briefly, AD/MCI patients met National Institute on Aging Alzheimer's Association criteria for probable or possible AD, or MCI (11, 12); PD patients met criteria for idiopathic PD defined by the United Kingdom's Parkinson's Disease Society Brain Bank clinical diagnostic criteria (13); ALS patients met El Escorial World Federation of Neurology diagnostic criteria for possible, probable, or definite familial or sporadic ALS (14); FTD patients included possible or probable behavioral variants of frontotemporal degeneration (15), agrammatic/non-fluent and semantic variants of primary progressive aphasia (16), and possible or probable progressive supranuclear palsy (17); CVD patients experienced a mild to moderate ischemic stroke event, verified on neuroimaging, 3 or more months prior to enrollment in compliance with the National Institute of Neurological Disorders and Stroke-Canadian Stroke Network vascular cognitive impairment harmonization standards (18).

For illustrative purposes of the neuroimaging pipeline outputs, baseline MRI data are included for the following ONDRI patient cohorts: 126 AD/MCI, 140 PD, 40 ALS, 53 FTD, and 161 CVD.

MRI Acquisition

Neuroimaging was acquired at the following sites using each site's respective 3T MRI system: a General Electric (GE, Milwaukee, WI) Discovery 750 was used at Sunnybrook, McMaster University/Hamilton General Hospital, and CAMH; a GE Signa HDxt at UHN; a Philips Medical Systems (Philips, Best, Netherlands) Achieva system at Thunder Bay Regional Health Sciences Centre; a Siemens Health Care (Siemens, Erlangen, Germany) Prisma at Sunnybrook and London Health Sciences Centre/Parkwood Hospital; a Siemens TrioTim at Ottawa Hospital/Élisabeth Bruyère Hospital, Hotel Dieu Hospital/Providence Care Hospital and Baycrest; and a Siemens Skyra at SMH.

Harmonized with the Canadian Dementia Imaging Protocol (19), the National Institute of Neurological Disorders and Stroke–Canadian Stroke Network Vascular Cognitive Impairment Harmonization Standards (18), full MRI acquisition protocol details for each imaging site are provided on **Supplementary Table 1**. In brief, the following structural MRI sequences were obtained for each study participant: 3D T1-weighted (T1), T2-weighted fluid attenuated inversion recovery (FLAIR), interleaved T2-weighted and proton density (T2/PD), and T2*gradient recalled echo (GRE). It should be noted that additional imaging protocol included a 30/32 direction diffusion tensor imaging (DTI), resting state functional MRI, and arterial spin labeling (acquired only at one site), but are beyond the scope of this paper and will be presented elsewhere (1). Prior to image processing for volumetric quantification, MRI were fully evaluated by a neuroradiologist (SS) for incidental findings and for imaging quality by a medical biophysics scientist (RB).

Structural Image Processing Methods: Overview

The structural neuroimaging pipeline used in ONDRI is a component based algorithm commonly referred to as SABRE-Lesion Explorer (SABRE-LE) (20–23). This is a semi-automated personalized approach to imaging-based quantification, as it can provide a comprehensive volumetric profile at the individual patient level. While it may take longer to process each individual relative to fully automatic methods, this careful patient-focused approach is more robust to the large variability in stroke and neurodegenerative patient population. This method has been previously validated (23–25) and implemented in other Canadian studies (26–29). The following sections describe the SABRE-LE comprehensive pipeline method and the volumetric data that is extracted in greater detail. Data visualization was performed using RStudio version 1.2.1335 (RStudio, Inc., Boston, MA) and ITKSnap (30).

Brain Regions of Interest: SABRE

The neuroimaging pipeline integrates a brain region parcellation process called Semi-Automatic Brain Region Extraction (SABRE) (20). This method separates the brain into 26 regions of interest (ROIs: 13 per hemisphere) derived from anatomical landmarks manually identified per hemisphere on each individual patient (**Figure 2** and **Table 1**). Each imaging analyst was required to achieve an intraclass correlation coefficient (ICC) > 0.90 in order to work on ONDRI patient imaging analysis. The automatic SunnyBrook Hippocampal Volumetry (SBHV) tool (10) was subsequently integrated into the SABRE pipeline (**Figure 3**), resulting in a total of 28 ROIs (left + right hippocampus) (see following section). The SABRE brain maps are personalized maps that are unique to each individual patient and was developed from the Talairach grid system (31). Relative to many brain mapping methods that implement non-linear (i.e., "warping") techniques to register an individual

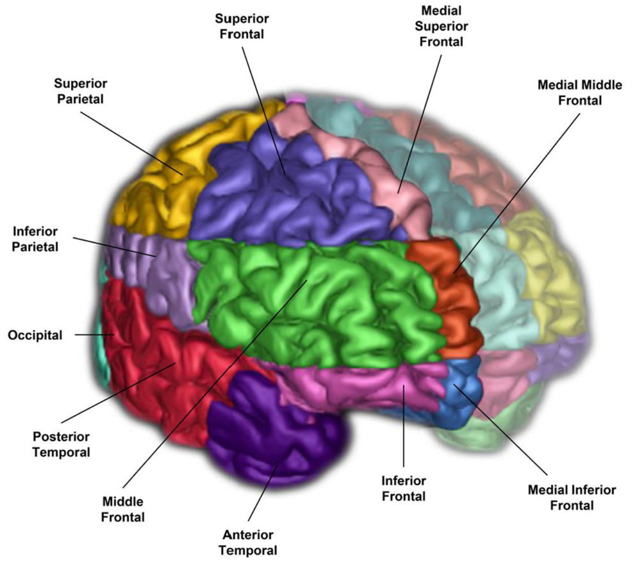

FIGURE 2 | A 3-D surface volume rendering of T1-weighted MRI showing right hemisphere SABRE regions in different colours. Left hemisphere regions were made translucent for illustrative purposes, however, SABRE regions are separately parcellated for each hemisphere and delineated using individualized anatomical landmarks for both left and right sides.

TABLE 1 | SABRE-LE neuroimaging pipeline brain tissue and lesion codes (top), and detailed SABRE brain region codes (bottom).

Imaging descripton	**Code**	
Supratentorial total intracranial volume	ST_TIV	
Normal appearing gray matter	NAGM	
Normal appearing white matter	NAWM	
Sulcal cerebrospinal fluid	CSF	
Ventricular cerebropsinal fluid	CSF	
Periventricular white matter hyperintensities	Pwmh	
Deep white matter hyperintensities	dWMH	
Periventricular lacunes	pLACN	
Deep lacunes	dLACN	
Enlarged perivascular spaces	PVS	
Chronic stroke lesions	Stroke	
SABRE brain region name	**Code**	**Lobe**
Superior frontal	SF	Frontal
Middle frontal	MF	Frontal
Inferior frontal	IF	Frontal
Medial inferior frontal	MIF	Frontal
Medial superior frontal	MSF	Frontal
Medial middle frontal	MMF	Frontal
Superior parietal	SP	Parietal
Inferior parietal	IP	Parietal
Occipital	O	Occipital
Anterior temporal	AT	Temporal
Posterior temporal	PT	Temporal
Anterior basal ganglia/thalamus	ABGT	Basal ganglia/thalamus
Posterior basal ganglia/thalamus	PBGT	Basal ganglia/thalamus
Hippocampus	HP	Medial temporal

Note that each regional code will be preceded by an "L" or "R" indicating the left or right hemisphere.

patient's MRI to a standardized template, such as the Montreal Neurological Institute brain (MNI152) (32), the SABRE approach is essentially reversed, by mapping a brain template onto the individual patient's MRI. This method accounts for natural individual differences in anatomy but more importantly, it is a method that can compensate for significant focal and global brain atrophy that is found in stroke, dementia, and neurodegenerative patients.

Hippocampus

The hippocampus is an important part of the limbic system that has been studied extensively in dementia, given its significant role in memory functions (33, 34). The ONDRI pipeline incorporates the multi-atlas based Sunnybrook Hippocampal Volumetric (SBHV) segmentation tool (**Figure 3**) that was developed and validated using the Sunnybrook Dementia Study and the Alzheimer's Disease Neuroimaging Initiative (ADNI1) (10).

For ONDRI, the SBHV segmentation has been fully integrated into the SABRE-LE pipeline, and includes left and right hippocampal sub-classifications for parenchyma, hypointensities, and stroke volumes (when present). Currently, there is some controversy over the pathophysiological origin and relevance of small cavities commonly observed in the hippocampus (35–38), which are particularly relevant in the ONDRI CVD patients. Additionally, large cortico-subcortical strokes can extend from the cortex into the hippocampus. Given these vascular issues potentially affecting the overall hippocampal volume, ONDRI provides sub-classifications for parenchyma, hypointensities, and stroke volumes based on the neuroimaging characteristics (i.e., intensity) using the voxel segmentation classifications and takes a neutral stance on the pathophysiological origin of small cavities observed in this region.

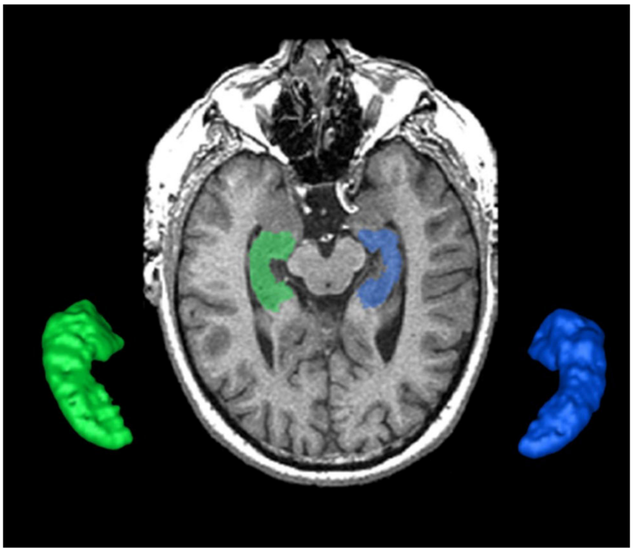

FIGURE 3 | The SunnyBrook Hippocampal Volumetric (SBHV) segmentation showing left (BLUE) and right (GREEN) hippocampi overlayed on an axial T1 MRI and extracted as 3-D surface volume renderings. Note images are in radiological convention.

Total Intracranial Volume

The supratentorial total intracranial volume (ST-TIV) is a measure of all brain matter that is located below the dura mater. It is referred to as *supratentorial* because the SABRE-LE method removes all tissue below the tentorium, including the cerebellum and portions of the brain stem (20, 22). Although the removal of infratentorial structures was necessary for technical segmentation reasons, researchers particularly interested in the cerebellum, and brainstem can apply additional imaging tools [e.g., (39)] to obtain these structures from the original acquisitions upon special request.

In addition to sex-related differences, there are also normal variations in head size. In order to account for these differences, most neuroimaging studies implement some form of head-size correction. This is also particularly important when assessing brain atrophy in cross-sectional studies, as a true measure of

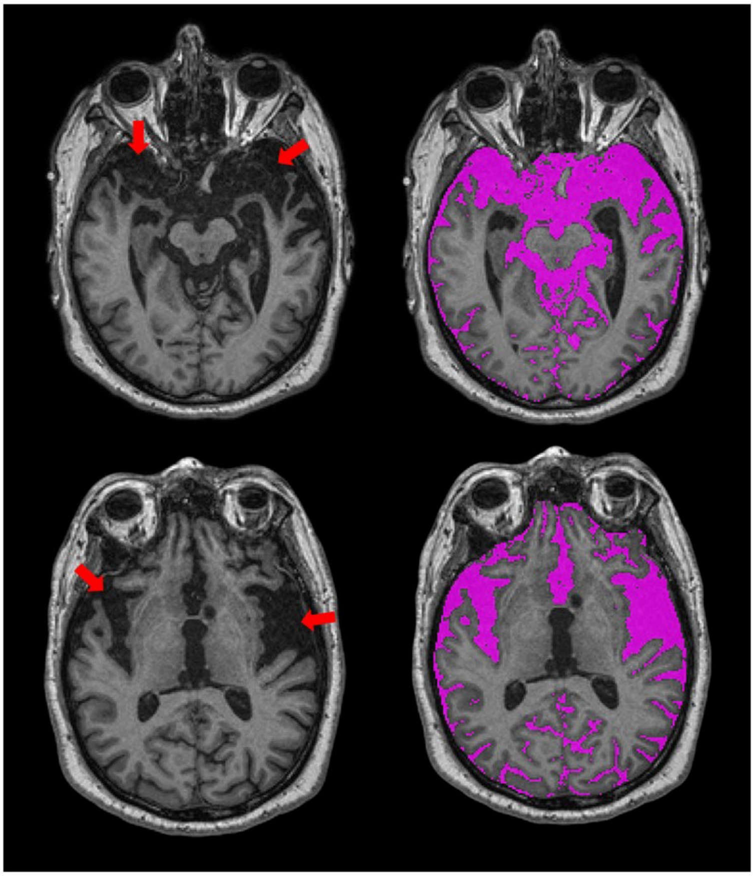

FIGURE 4 | Axial views of T1-weighted MRI from an ONDRI FTD patient. Red arrows point to regions with significant focal brain atrophy. The SABRE-LE processing pipeline accounts for this focal atrophy since it includes a measure of everything below the dura mater, including sub-arachnoid and sulcal cerebrospinal fluid (CSF), shown in purple.

the total intracranial capacity will provide an indication of where "there used to be brain and now there is cerebrospinal fluid (CSF)." The presence of focal atrophy due to stroke and neurodegenerative processes tends to result in over and under erosion errors with many fully automated T1-based skull stripping techniques, due to the similarity in intensity between background and sulcal CSF. The SABRE-LE method accounts for the presence of focal atrophy since it includes a measure of everything below the dura mater, including sub-arachnoid CSF, thus, providing a more accurate measure of head-size in neurodegenerative patient populations (**Figure 4**).

It is important to note that there are numerous acceptable head-size correction methods reported in the literature (40). A simple method involves dividing each volume of interest by the total head size to obtain a proportional volume (41). ONDRI provides raw volumes and head size volumes (i.e., ST-TIV) for each individual patient.

Brain Tissue Segmentation

A robust T1 intensity-based brain tissue segmentation, optimized for aging and dementia, is performed after skull stripping and removal of non-brain tissue (24). This automatic segmentation method deals with scanner inhomogeneities by fitting localized histograms to Gaussians to allocate voxels into gray matter (GM), white matter (WM), and cerebrospinal fluid (CSF) tissue classes. After manual ventricular CSF (vCSF) relabelling, there are four brain tissue types that are segmented for volumetrics using SABRE-LE (**Table 2**):

- Normal appearing gray matter (NAGM)
- Normal appearing white matter (NAWM)
- Sulcal cerebrospinal Fluid (sCSF)
- Ventricular CSF (vCSF).

The T1-based tissue segmentation is further corrected for misclassified volumes using a PD-T2/FLAIR-based lesion segmentation algorithm to account for the voxels appearing as GM or CSF on T1 (42) due to WM changes from stroke and cerebral small vessel disease. For this reason, the GM and WM volumes are denoted as "normal appearing" (NAGM, NAWM) to signify that these volumes have been re-labeled as normal appearing after having been corrected with an additional multi-modal MRI segmentation approach (**Figure 5**). Additional

TABLE 2 | Data is shown as mean (standard deviation) unless otherwise specified. Raw values are presented for transparency purposes.

Demographics	AD/MCI	ALS	FTD	PD	CVD
Number of participants	126	40	52	140	155
Age, years	71.0 (8.2)	62.0 (8.7)	67.8 (7.1)	67.9 (6.3)	69.3 (7.4)
Sex, *n* (%) female	57 (45.2)	16 (40.0)	19 (36.5)	31 (22.1)	48 (31.0)
ST-TIV, cc	1235.6 (144.6)	1203.6 (162.8)	1245.8 (129.6)	1316.6 (127.0)	1224.5 (133.2)
NAWM, cc	395.4 (344.5)	425.0 (78.8)	295.1 (59.4)	446.1 (61.2)	387.4 (54.4)
NAGM, cc	533.3 (51.4)	556.2 (65.7)	252.5 (56.0)	574.7 (47.1)	535.7 (52.3)
sCSF, cc	256.3 (62.1)	195.9 (52.9)	277.0 (57.8)	252.3 (53.3)	242.6 (59.3)
vCSF, cc	45.7 (28.4)	23.8 (11.1)	43.7 (16.6)	38.2 (19.4)	41.3 (23.0)
pWMH*, mm^3	2564.5 (2811.2)	1040.0 (1252.5)	2736.0 (1623.8)	2563.5 (2708.0)	4054.0 (7468.0)
dWMH*, mm^3	289.5 (424.7)	208.0 (386.5)	138.5 (379.3)	259.5 (225.7)	555.0 (584.0)
LACN*, mm^3	15.5 (66.0)	14.5 (12.2)	9.5 (55.5)	17.5 (70.0)	92.0 (291.0)
PVS*, mm^3	45.5 (35.5)	17.5 (9.5)	32.5 (36.3)	34.0 (30.0)	44.0 (33.0)
Stroke*, mm^3	–	90.0[a]	393.0 (294.0)[b]	531.5 (1269.0)[c]	4644.5 (12963.0)[d]

**Data is shown as median (interquartile range). [a]Available in 1/40 participants. [b]Available in 6/52 participants. [c]Available in 4/140 participants. [d]Available in 88/155 participants AD/MCI, Alzheimer's Disease and Mild Cognitive Impairment; ALS, Amyotrophic Lateral Sclerosis; FTD, Frontotemporal Dementia; PD, Parkinson's Disease; VCI, Vascular Cognitive Impairment; ST-TIV, supratentorial total intracranial volume; NAWM, normal appearing white matter; NAGM, normal appearing gray matter; sCSF, sulcal cerebrospinal fluid; vCSF, ventricular cerebrospinal fluid; pWMH, periventricular white matter hyperintensities; dWMH, deep white matter hyperintensities; LACN, lacunes; PVS, perivascular spaces.*

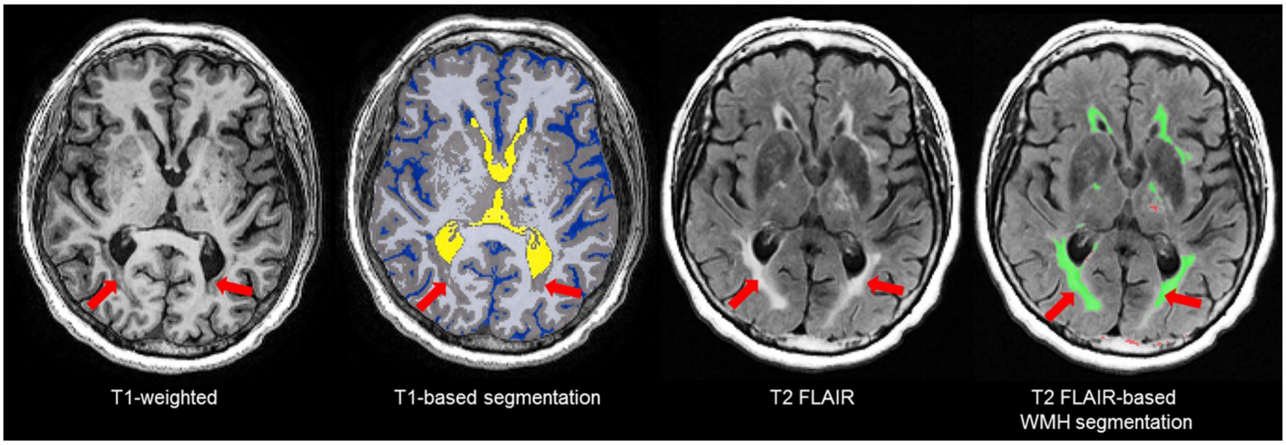

FIGURE 5 | Due to relative intensities on different MRI sequences, WMH (red arrows) on T2 FLAIR are not hyperintense (bright) on T1-weighted images and tend to appear as GM (gray) or CSF (blue) intensity on T1. Thus, T1-based segmentations tend to inflate the GM and CSF volumes in patients with stroke and cerebral small vessel disease. To account for this, ONDRI's imaging pipeline integrates an additional T2/FLAIR-based WMH segmentation to correct for this misclassification error (42) to produce a normal appearing WM/GM (NAWM/NAGM) volumes.

brain tissue volumes for stroke lesions and cerebral small vessel disease markers are discussed in the following sections.

The NAGM and NAWM volumes can be summed to obtain a measure of parenchymal volume or reported individually for head-size corrected measures to assess potential atrophy. Additionally, a segmentation mask is generated which is used for diffusion tensor imaging (DTI) analyses, where diffusion metrics of the "normal appearing" WM tracts can be separately analyzed from the diffusion within the various types of white matter lesions including WMH, lacunar infarcts, and cortical-subcortical stroke lesions. Details of ONDRI DTI analysis pipeline are discussed elsewhere (1).

The SABRE-LE method segments sCSF and vCSF into separate compartments. The initial T1-based segmentation automatically labels hypointense voxels into a CSF class, and then the ventricles are manually relabelled to a vCSF class by neuroimaging analysts following a standardized procedure. Note that although some vCSF segmentation tools based on standardized templates use smoothing algorithms that reclassify all voxels within the ventricular compartment as ventricles, the SABRE-LE method does not. With the SABRE-LE method, choroid plexus are not arbitrarily removed or re-classified as CSF and thus remain as part of the overall tissue segmentation. Ventricular volumes are often used as a simple indicator of overall brain atrophy, and have the potential for use as a differential indicator of disease and dementia severity (**Figure 6**) (43–45).

White Matter Hyperintensities of Presumed Vascular Origin (WMH)

Also referred to as leukoaraiosis, white matter lesions, subcortical hyperintensities, and even, unidentified bright objects, WMH are radiological anomalies commonly associated with cerebral small vessel disease. Recently, the STandards for ReportIng Vascular changes on nEuroimaging (STRIVE) (46) have established a set of criteria that recommends the use of the term *white matter hyperintensities of presumed vascular origin* (WMH), as the standard terminology to refer to these regions of hyperintense (bright) signal found on particular MRI. It is important to note that as previously mentioned, WMH do not appear hyperintense on all types of MRIs and often appear isointense to GM on T1 (**Figure 7**). Additionally, despite the naming convention, it is important to note that WMH are not limited to the white matter regions of the brain, as they are also commonly observed in subcortical GM structures such as the basal ganglia and thalamus. However, to avoid confusion between studies, ONDRI recommends the use of the more popular term "white matter hyperintensities."

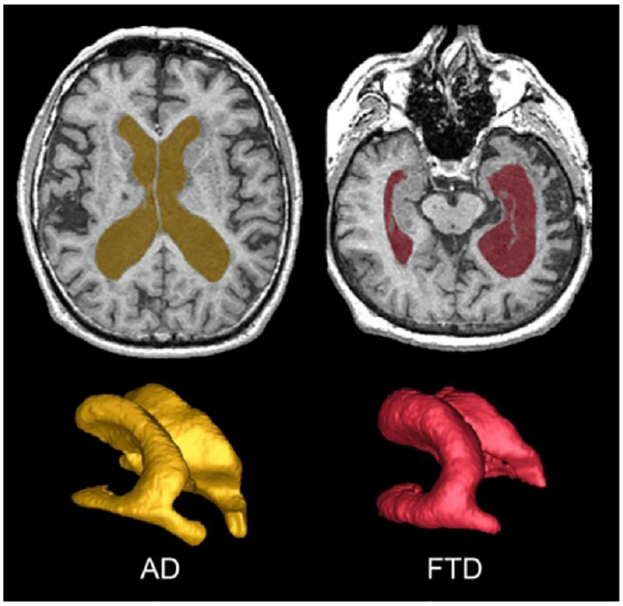

FIGURE 6 | Top row shows axial view of vCSF segmentation overlayed on T1 MRI for patients with AD (left) and FTD (right). Bottom row shows 3D surface volume renderings of the vCSF segmentation. Note the differences in ventricle size and the hemispheric differences between the two neurodegenerative diseases.

Periventricular (pWMH) and Deep White (dWMH) Hyperintensities

Although WMH can be subdivided using SABRE ROIs, the most common regional delineation of WMH is the separation between periventricular (pWMH) and deep white (dWMH). Historically controversial (47, 48), this concept is based on several theories and research findings which suggest that WMH in close proximity to the ventricles (hence the term "periventricular") have a different pathological etiology (49, 50) and are differentially correlated with cognitive/behavior deficits in comparison to the more distal dWMH (despite the confusing fact that pWMH are technically found in deeper white matter than dWMH). Additionally, recent imaging-pathology correlations suggest that a common substrate of pWMH relates to vasogenic edema due to leakage and increased vascular resistance caused by venous collagenosis, a small vessel venular disease of the deep medullary venules (as opposed to the arterial side of the cerebral vasculature) (51–53). It is also interesting to note that there is no standard consensus in the literature on how to define pWMH vs. dWMH, with some papers using a proportional distance to the dura mater (54), some using an arbitrary cut-off (typically 13 mm from the ventricles) (55), and others using a 3D connectivity

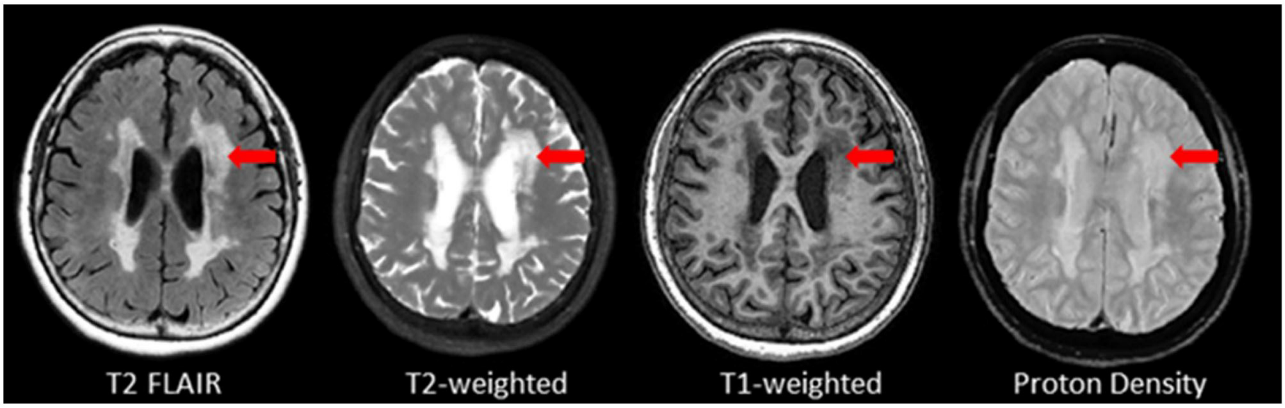

FIGURE 7 | Axial view of various coregistered structural MRI sequences showing the relative intensity differences of WMH. Note that white matter hyperintensities are not hyperintense (i.e., bright) on T1-weighted MRI.

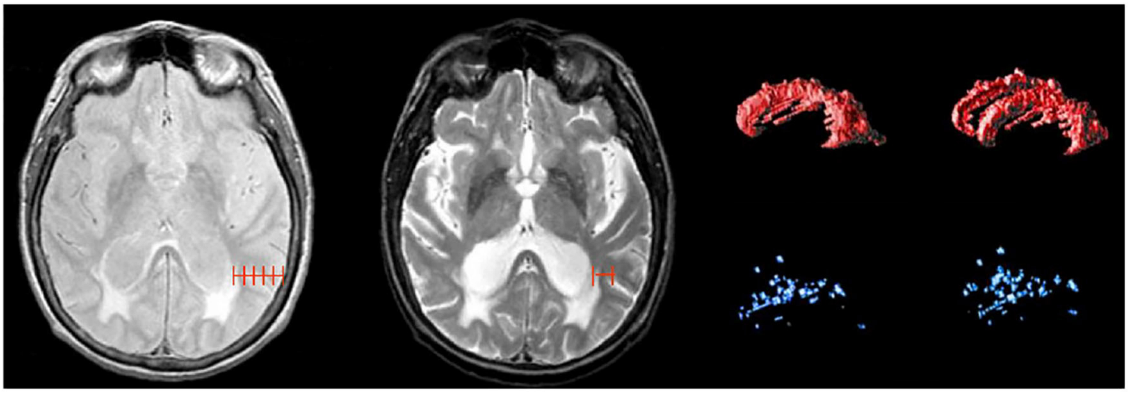

FIGURE 8 | Shows different methods for segmenting periventricular and deep WMH. Left image shows a proportional distance from the ventricular lining to the dura mater; middle image shows an arbitrary distance of 13 mm from ventricles, right image shows 3D connectivity algorithm supported by ONDRI, displayed as 3D volume renderings of pWMH (red) and dWMH (blue) shown in sagittal and slightly tilted anterior views.

algorithm (23, 56)—the method that is currently supported by ONDRI (see **Figure 8**).

Lacunes

Lacunes of presumed vascular origin are cystic fluid-filled cavities in the subcortical brain regions (57, 58). They appear hypointense (dark) on T1, hyperintense (bright) on PD and T2, and can appear as a lesion with a hypointense central core surrounded by a hyperintense rim/halo on FLAIR MRI (**Figure 9**, bottom row). The recent STRIVE criteria (46) provides some consensus-based guidelines regarding their definition, however, previous studies have used various terms (e.g., "*white matter lesions*," "*lacunar infarcts*," "*covert strokes*") and radiological descriptions to classify these lesions (59). Often difficult to differentiate from MRI-visible perivascular spaces (PVS) (next section), lacunes tend to be larger and less linear than PVS. They are associated with increased risk of stroke, dementia, and gait disturbances (60). It is important to note that due to the poor sensitivity of FLAIR in thalamic regions (61) (**Figure 9**, top row), the ONDRI imaging pipeline integrates an additional T2-based segmentation in order to capture any potential lesions in this subcortical region that may not appear on FLAIR.

MRI-Visible (Enlarged) Perivascular Spaces (PVS)

Recent studies suggest that the brain utilizes the glymphatic system (62, 63) to clear fluid and metabolic waste, using a complex series of perivascular channels surrounding the brain's veins and arteries. It has been suggested that when the perivascular channels are compromised due to aging, disease, or trauma, the perivascular space becomes enlarged and consequently, visible on structural MRI (64–67). MRI-visible (enlarged) perivascular spaces (PVS) on T2 appear as small (<3 mm diameter), linear, hyperintensities following the course of the vasculature (**Figure 10**). Additionally, PVS appear hypointense (dark) on T1, isointense to GM on PD (vs. lacunes which are bright on PD), and are very difficult to visualize on 2D FLAIR, particularly in the basal ganglia region. Current research suggests that PVS found in the white matter regions may indicate Cerebral Amyloid Angiopathy (CAA), while PVS in the basal ganglia may be more indicative of hypertensive arteriopathy (68–71). Moreover, recent basic science research and limited clinical evidence supports the theory that clearance of amyloid and other metabolites occurs primarily during deep sleep (72, 73).

Previously referred to as dilated Virchow-Robin spaces, measurement of PVS burden is typically accomplished using visual rating scales under this old naming convention (74, 75). However, the novel quantitative method supported by ONDRI provides a volumetric measure of PVS. This method has been previously validated with common PVS visual scales and has been used to study AD, normal elderly, and stroke and cerebrovascular disease patients being assessed with sleep polysomnography (72, 76). Although both lacunes and PVS volumes are segmented automatically using the SABRE-LE pipeline, false positive minimization procedures are manually performed to remove incorrect segmentations and to reallocate PVS to lacunes or vice versa depending on strict intensity and shape-based criteria. Only highly trained neuroimaging analysts achieving ICCs and DICE Similarity Indices (SI) > 0.90 are allowed to perform this procedure. Moreover, a research neuroradiologist (FG) was consulted when faced with complex radiological anomalies that were commonly observed in the CVD patient cohort.

Cerebral Microbleeds

Although the SABRE-LE structural pipeline method used by ONDRI does not support a cerebral microbleed (CMB) segmentation algorithm, this brief section has been included to describe this important measure of cerebral small vessel disease burden. In ONDRI, CMB, and superficial siderosis burden are being assessed visually by a highly qualified neuroradiologist (SS). Cerebral microbleeds (CMB) have been shown to reflect perivascular leakage of red blood cells that can be visualized as low signal intensities (hypointense/dark spots) on T2*-weighted

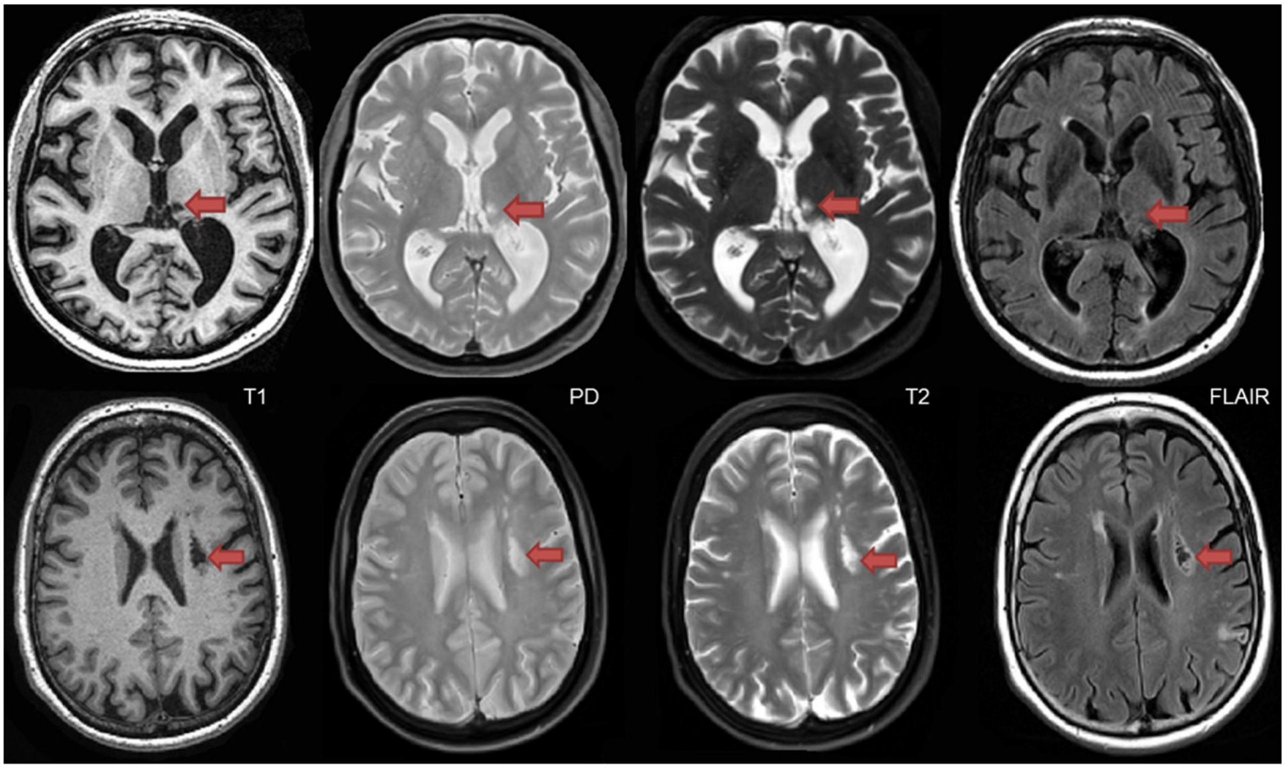

FIGURE 9 | Top row shows a thalamic lacune as it appears on different coregistered MRI, hypointense (dark) on T1, hyperintense on PD-T2, and difficult to detect on FLAIR. In contrast, the bottom row shows a subcortical lacunar infarct that presents with the classic central CSF-like hypointensity with a surrounding hyperintense halo/rim on FLAIR.

gradient-recalled echo (GRE) (**Figure 11**) and susceptibility weighted imaging (SWI) (77). There are two commonly used methods of assessing CMB burden, the Microbleed Anatomical Rating Scale (MARS) (78) and the Brain Observer MicroBleed Scale (BOMBS) (79) visual rating scales. Previous studies have shown that CMB are associated with an increased risk of stroke, intracerebral hemorrhage, cognitive decline, and dementia (80–84). Differences in anatomical distribution suggest that CMB found in deep centrencephalic brain regions (basal ganglia, thalamus, and brain stem) are more closely related to hypertensive arteriopathy (85), while lobar CMB are more closely associated with CAA and AD pathology (86–89), leading to the development of the Boston criteria for the diagnosis of possible/probable CAA (90, 91).

Chronic Stroke

According to recent estimates, stroke is the 2nd most common cause of death worldwide (92) and the second leading cause of dementia (93). In a 2013 global report, there were ∼25.7 million stroke survivors, and 7.5 million deaths from ischemic and hemorrhagic stroke (94). In Canada, ∼62,000 people are treated for stroke and transient ischemic attack. In a series of publications, the Heart and Stroke Foundation Canadian Best Practice Committees have been developing various evidence-based recommendations to address issues regarding: telestroke technologies (95); managing transitions of care following stroke (96); mood, cognition, and fatigue following stroke (97); hyperacute stroke care (98); secondary prevention of stroke (99); and stroke during pregnancy (100, 101).

Although the term "stroke" may encompass a wide range of clinical criteria (102), the Vascular Cognitive Impairment (VCI) (18) inclusion-exclusion criteria for ONDRI CVD patients was limited to mild-moderate ischemic stroke patients, defined by a Modified Rankin Scale (MRS) (103) score of 0–3. It is important to note that although there are a number of imaging techniques used to measure acute stroke in the early stages (within a couple of hours of stroke), the MRI methods applied to ONDRI CVD patients are measures of post-stroke lesions, often referred to as *chronic stroke*, with structural MRI acquired > 3 months post ischemic stroke event.

As there are currently no reliable automatic ways to quantify the range of cortico-subcortical stroke lesions, ONDRI neuroimaging analysts manually delineate the stroke under the direct supervision of a highly experienced research neuroradiologist (FG). This manual delineation is strictly limited to cortical strokes appearing as hyperintense (bright) on FLAIR and hypointense (dark) on T1, although the entire stroke volume often extended into the subcortical regions of the brain (**Figure 12**). Although this total volume does not separate the hypointense necrotic stroke core from the surrounding partially

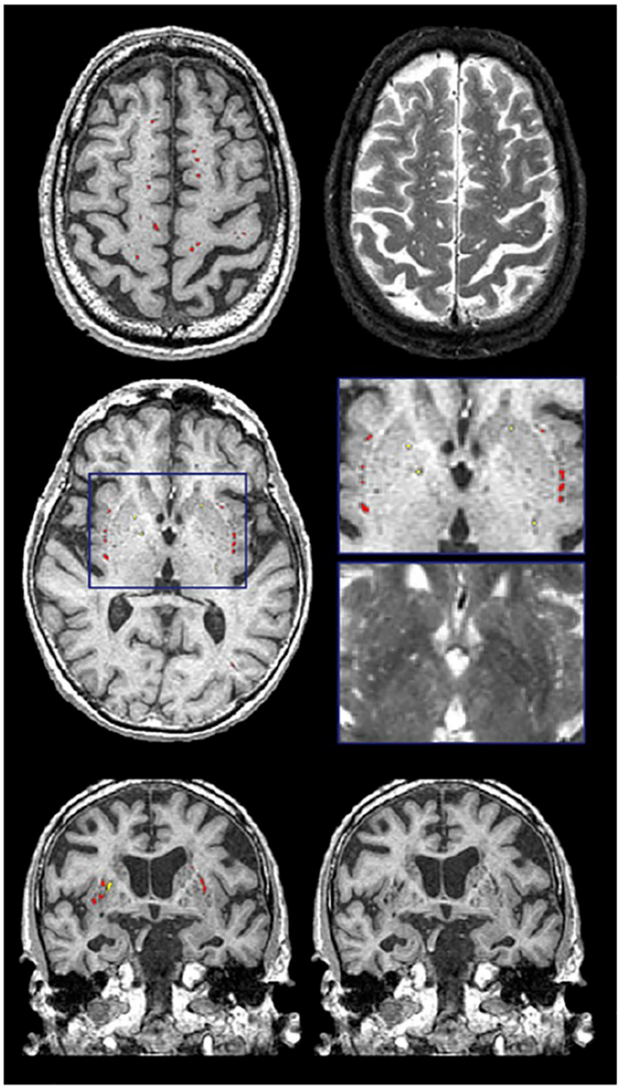

FIGURE 10 | Examples of the PVS segmentation (red and yellow) over-layed onto structural MRI in axial (top 2 rows) and coronal views (bottom row).

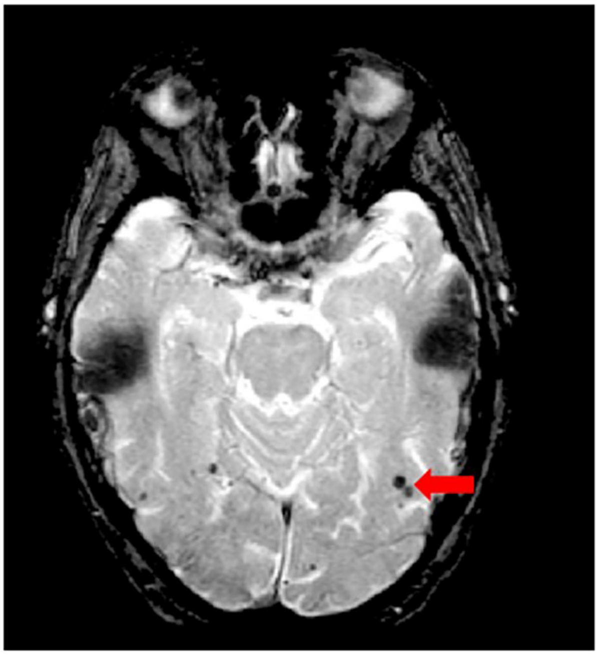

FIGURE 11 | Axial view of iron-sensitive T2* gradient echo (GRE) with red arrow pointing to cerebral microbleeds visualized as hypointensities (dark).

infarcted hyperintense region indicating varying degrees of gliosis and encephalomalacia, future automatic segmentation techniques are currently being tested in ONDRI to include this sub-segmentation.

RECOMMENDATIONS FOR REPORTING AND ANALYSIS

Here we provide some general guidelines for reporting and analysis that can be useful for researchers wishing to use ONDRI data.

First and foremost, when reporting data for characterization of the sample being analyzed, we recommend that the original raw volumes are reported in tables for transparency and between-study comparisons; however, statistical analyses should generally be performed on head-size corrected volumes. Head size correction accounts for individual variations in intracranial capacity and sex-related differences in head size (104). Additionally, depending on the research question, the volume of interest (i.e., NAWM, NAGM, CSF, or WMH) could also be reported as a proportion of the total volume within each SABRE region, or they can be reported as a proportion of the total head-size (ST-TIV) for age-independent normalization/correction. The version or date of the data release should also be reported.

There are several ways that WMH can be analyzed and it depends on the research question in mind. The simplest approach is to sum the dWMH and pWMH, which results in a whole brain measure of small vessel disease burden. Regional analyses of WMH can also be performed to assess WMH burden within a SABRE ROI. Additionally, WMH within different ROIs can be combined by simply summing the volumes from different SABRE regions to generate a larger ROI (e.g., sum all pWMH and dWMH volumes within all frontal SABRE brain region parcellations using the Frontal Lobe Codes shown on **Table 1**).

It is important to note that many measures of cerebral small vessel disease, such as pWMH and dWMH, are typically non-normally distributed (105), often inter-correlated (54), are known to be age-related (106), and commonly associated with vascular risk factors such as hypertension (107). Thus, careful attention to these factors and previous research findings highlight ONDRI's recommendation to consider these additional factors when analyzing imaging-based markers of cerebral small vessel

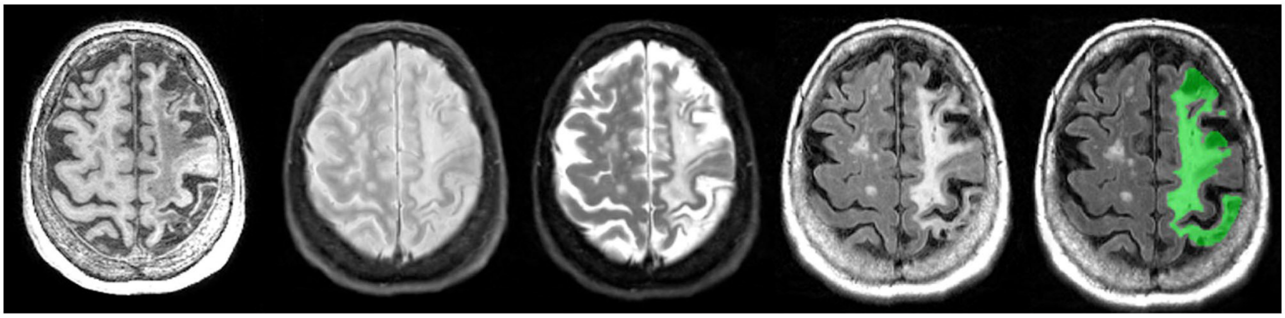

FIGURE 12 | Axial view of coregistered structural MRI sequences (left to right): T1, PD, T2, and FLAIR. Images illustrate relative intensity differences of a large cortico-subcortical stroke lesion across various types of MRI. The last pane shows ONDRI's manual segmentation of the entire stroke core and surrounding hyperintense partially infarcted tissue volume in green.

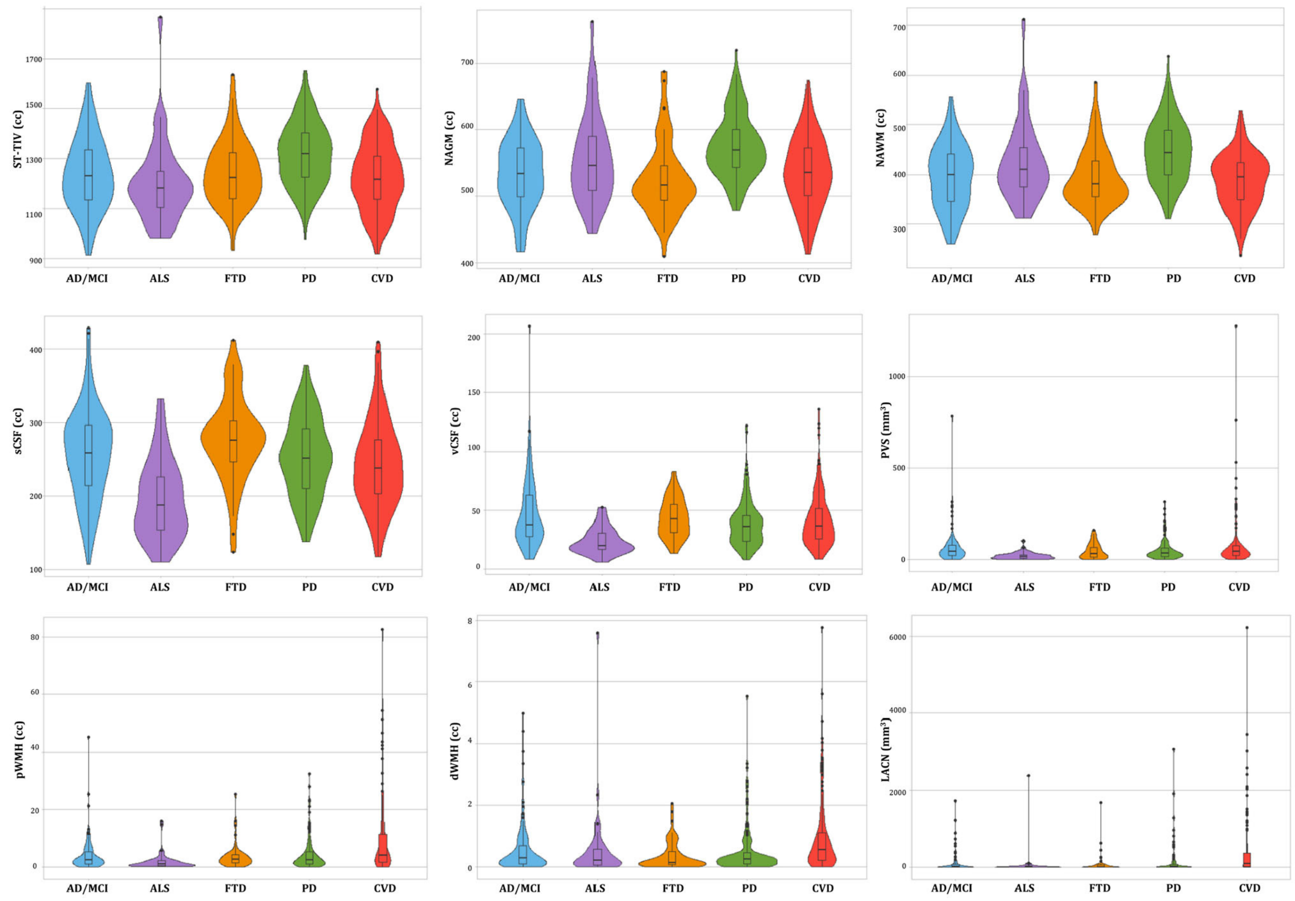

FIGURE 13 | Descriptive violin plots of the ONDRI disease cohorts showing median and interquartile range volumetrics for whole brain supratentorial total intracranial volume (ST-TIV), normal appearing gray matter (NAGM), normal appearing white matter (NAWM), sulcal cerebrospinal fluid (sCSF), ventricular CSF (vCSF), MRI-visible enlarged perivascular space (PVS) volumes, periventricular white matter hyperintensities (pWMH), deep WMH (dWMH), and lacunes (LACN).

disease. Given the skewed, non-normal distribution of WMH (even after head-size correction), WMH volumes are typically transformed (e.g., log) prior to standard parametric analyses. For this reason, approaches designed to deal with complex distributions should be considered (108).

Since the pipeline automatically segments lesions in the periventricular region from the deep white regions, the lacunar volumes are also provided in this manner. While some future studies may argue a pathophysiological difference between these two locations of lacunar presentation, there are currently limited studies to suggest this anatomical delineation. Given this, we recommend that the two volumes be summed together prior to analysis. Interestingly, lacunes and PVS volumes are not typically head-size corrected in the clinical/scientific literature, however, age, sex, WMH, and a measure of brain atrophy (e.g., BPF or vCSF), and proper accounting of vascular risk are recommended covariates when analyzing lacunes and PVS (109, 110). Note that in many publications, lacunes, and PVS are reported as counts (i.e., number of), because they are often measured using visual rating methods that require the user to count the number of lacunes or PVS observed on an MRI—often leading to wide variations in definitions and conflicting findings in the literature (59, 111). Since the lacunes and PVS in ONDRI are quantified using segmentation based imaging analyses, PVS and lacunar volumes are provided rather than counts.

Finally, any analyses using ONDRI's CVD cohort should consider the common comorbidities of depression, obstructive sleep apnea, and cognitive impairment (112), as well the subcortical silent brain infarcts/lacunes, WMH, and potentially, CMB, which have recently been acknowledged as playing an important role in primary stroke prevention (113).

RESULTS AND CONCLUSION

Of the $n = 520$ patients with MRI acquired, the ONDRI neuroimaging pipeline was unable to process $n = 1$ FTD patient due to extreme motion artifact (despite 2 baseline attempts on 2 separate occasions), and $n = 6$ CVD patients due to poor imaging quality ($n = 3$ FLAIR not usable, $n = 2$ T1 not usable, $n = 1$ PD/T2 not acquired). To illustrate whole brain data extraction volumetric results from this pipeline, neuroimaging summary statistics for each ONDRI disease cohort are summarized on **Table 2**, and descriptive violin plots showing median and interquartile ranges are provided for whole brain ST-TIV, NAGM, NAWM, sCSF, vCSF, pWMH, and dWMH PVS, and LACN are displayed on **Figure 13**. Stroke volumes were not graphed due to the limited number of ONDRI patients with cortico-subcortical stroke lesions.

It is important to note that the details in this manuscript focus on ONDRI's baseline data that will be released in October 2020, the longitudinal follow-up data will be forthcoming.

Additionally, a cohort of cognitively normal older adults recruited from the Brain-Eye Amyloid Memory (BEAM) study (clinicaltrials.gov—NCT02524405) with harmonized neuroimaging, neuropsychology, and data acquisition protocol, will be included in ONDRI for comparative analyses. Participants in BEAM were recruited from five sites (Sunnybrook, Baycrest, CAMH, SMH, and UHN) that also participated in ONDRI.

ONDRI is the first multi-site, multiple assessment platform study examining several neurodegenerative and neurovascular diseases using a harmonized protocol that includes standardized structural neuroimaging. The wide range of complex, and often overlapping, brain pathologies represented in this cohort of neurodegenerative patients included a number of comorbid cerebral small vessel disease markers, cortico-subcortical stroke lesions, combined with focal and global atrophy, posing significant challenges to common imaging analysis tools. In this paper, we presented the neuroimaging pipeline methods implemented in ONDRI that were used to overcome many of these challenges.

To further ensure a high level of data quality, the volumetric data generated by the ONDRI structural neuroimaging team were further subjected to comprehensive quality control analysis pipelines including a novel multivariate outlier detection algorithm developed by the ONDRI neuroinformatics group for identification of anomalous observations (114, 115). Future work will include generating longitudinal measures that will also be made publicly available. As the neuroimaging data are combined with releases from ONDRI's clinical, neuropsychology, genomics, eye tracking, gait and balance, ocular, and neuropathology platforms, it becomes evident that ONDRI is a gold mine of data opening the door to an unprecedented broad range of cross-platform analyses resulting in numerous opportunities for discovery and advances in diagnosis, prognosis, outcomes, and care of neurodegenerative diseases.

DATA AVAILABILITY STATEMENT

The datasets generated for this study are available on request to info@ondri.ca.

ETHICS STATEMENT

The studies involving human participants were reviewed and approved by Ethics approval was obtained from all participating institutions. Participants were recruited at 14 health centers across six cities in Ontario, Canada: Hamilton General Hospital and McMaster Medical Centre in Hamilton; Hotel Dieu Hospital and Providence Care Hospital in Kingston; London Health Science Centre and Parkwood Institute in London; Elizabeth Bruyère Hospital and The Ottawa Hospital in Ottawa; Thunder Bay Regional Health Sciences Centre in Thunder Bay; and Baycrest Health Sciences, Centre for Addiction and Mental Health, St. Michael's Hospital, Sunnybrook Health Sciences Centre, and Toronto Western Hospital (University Health Network) in Toronto. The patients/participants provided their written informed consent to participate in this study.

AUTHOR CONTRIBUTIONS

JR: conceptualization, data curation, formal analysis, investigation, methodology, software, validation, visualization, writing (draft, review, and editing), and supervision. MH: data curation, formal analysis, investigation, methodology, software, validation, visualization, and writing (draft, review, and editing). CS: conceptualization, data curation, formal analysis, investigation, methodology, software, validation, visualization, writing (review and editing), and supervision. MO: data curation, methodology, software, visualization, and writing (review and editing). SA: data curation, software, validation, visualization, and writing (review and editing). GS: conceptualization, data curation, methodology, and

software. MG: data curation, investigation, methodology, software, validation, and writing (draft, review, and editing). FG: conceptualization, data curation, investigation, validation, visualization, writing (review and editing), and supervision. SA and DB: data curation, formal analysis, investigation, validation, and writing (review and editing). JL-D: investigation, resources, validation, writing (draft, review, and editing), and funding acquisition. SCS: conceptualization, investigation, writing (draft, review, and editing), supervision, and funding acquisition. DM, MM, and RS: conceptualization, resources, investigation, writing (review and editing), supervision, and funding acquisition. RB: conceptualization, data curation, resources, investigation, writing (review and editing), and supervision. SS: data curation, resources, investigation, writing (review and editing), and supervision. SB: conceptualization, resources, investigation, methodology, visualization, writing (review and editing), supervision, and funding acquisition. All authors contributed to the article and approved the submitted version.

FUNDING

This work was funded by the Ontario Neurodegenerative Disease Research Initiative, through the Ontario Brain Institute, an independent non-profit corporation, funded partially by the government of Ontario. The opinions, results, and conclusions are those of the authors and no endorsement by the Ontario Brain Institute is intended or should be inferred. Matching funds were provided by participant hospital and research foundations, including the Baycrest Foundation, Bruyere Research Institute, Centre for Addiction and Mental Health Foundation, London Health Sciences Foundation, McMaster University Faculty of Health Sciences, Ottawa Brain and Mind Research Institute, Queen's University Faculty of Health Sciences, the Thunder Bay Regional Health Sciences Centre, the University of Ottawa Faculty of Medicine, and the Windsor/Essex County ALS Association. The Temerty Family Foundation provided the major infrastructure matching funds.

ACKNOWLEDGMENTS

We would like to thank the ONDRI participants for the time, consent, and participation in our study. Thank you to the L.C. Campbell Foundation, and the analysts and software developers in the LC Campbell Cognitive Neurology research team who have contributed to the ONDRI imaging analysis, including Edward Ntiri, Hassan Akhavein, Parisa Mojiri, Kirstin Walker, Rita Meena, Pugaliya Puveendrakumaran, Courtney Berezuk, and Alicia McNeely. This paper is available in preprint version online: https://doi.org/10.1101/2019.12.13.875823.

ONDRI INVESTIGATORS

Michael Strong, Peter Kleinstiver, Natalie Rashkovan, Susan Bronskill, Sandra E. Black, Michael Borrie, Elizabeth Finger, Corinne Fischer, Andrew Frank, Morris Freedman, Sanjeev Kumar, Stephen Pasternak, Bruce Pollock, Tarek Rajji, Dallas Seitz, David Tang-Wai, Carmela Tartaglia, Brenda Varriano, Agessandro Abrahao, Marvin Chum, Christen Shoesmith, John Turnbull, Lorne Zinman, Jane Lawrence-Dewar, Donna Kwan, Brian Tan, Julia Fraser, Bill McIlroy, Ben Cornish, Karen Van Ooteghem, Frederico Faria, Manuel Montero-Odasso, Yanina Sarquis-Adamson, Alanna Black, Barry Greenberg, Wendy Hatch, Chris Hudson, Elena Leontieva, Ed Margolin, Efrem Mandelcorn, Faryan Tayyari, Sherif Defrawy, Don Brien, Ying Chen, Brian Coe, Doug Munoz, Alisia Bonnick, Leanne Casaubon, Dar Dowlatshahi, Ayman Hassan, Jennifer Mandzia, Demetrios Sahlas, Gustavo Saposnik, Richard H. Swartz, David Breen, David Grimes, Mandar Jog, Anthony Lang, Connie Marras, Mario Masellis, Tom Steeves, Dennis Bulman, Allison Ann Dilliott, Mahdi Ghani, Rob Hegele, John Robinson, Ekaterina Rogaeva, Sali Farhan, Rob Bartha, Hassan Haddad, Nuwan Nanayakkara, Joel Ramirez, Christopher Scott, Sean Symons, Courtney Berezuk, Melissa Holmes, Sabrina Adamo, Miracle Ozzoude, Mojdeh Zamyadi, Stephen Arnott, Derek Beaton, Malcolm Binns, Wendy Lou, Pradeep Raamana, Stephen Strother, Kelly Sunderland, Athena Theyers, Abiramy Uthirakumaran, Guangyong (GY) Zou, Sujeevini Sujanthan, Mojdeh Zamyadi, David Munoz, Roger A. Dixon, John Woulfe, Brian Levine, Paula McLaughlin, JB Orange, Alicia Peltsch, Angela Roberts, Angela Troyer.

SUPPLEMENTARY MATERIAL

The Supplementary Material for this article can be found online at: https://www.frontiersin.org/articles/10.3389/fneur.2020.00847/full#supplementary-material

REFERENCES

1. Haddad SMH, Scott CJM, Ozzoude M, Holmes M, Arnott SR, Nanayakkara ND, et al. Comparison of quality control methods for automated diffusion tensor imaging analysis pipelines. *PLoS ONE.* (2020) 14:e0226715. doi: 10.1371/journal.pone.0226715
2. Kapoor A, Bartha R, Black SE, Borrie M, Freedman M, Gao F, et al. Structural brain magnetic resonance imaging to rule out comorbid pathology in the assessment of Alzheimer's disease dementia: findings from the Ontario Neurodegenerative Disease Research Initiative (ONDRI) study and clinical trials over the past 10 years. *J Alzheimer's Dis.* (2020) 74:747–57. doi: 10.3233/JAD-191097
3. Scott CJM, Arnott SR, Chemparathy A, Dong F, Solovey I, Gee T, et al. An overview of the quality assurance and quality control of magnetic resonance imaging data for the Ontario Neurodegenerative Disease Research Initiative (ONDRI): pipeline development and neuroinformatics. *bioRxiv.* (2020). doi: 10.1101/2020.01.10.896415
4. Farhan SMK, Bartha R, Black SE, Corbett D, Finger E, Freedman M, et al. The Ontario Neurodegenerative Disease Research Initiative (ONDRI). *Can J Neurol Sci.* (2017) 44:196–202. doi: 10.1017/cjn.2016.415
5. McLaughlin PM, Sunderland KM, Beaton D, Binns MA, Kwan D, Levine B, et al. The quality assurance and quality control protocol

for neuropsychological data collection and curation in the Ontario Neurodegenerative Disease Research Initiative (ONDRI) study. *Assessment.* (2020). doi: 10.1177/1073191120913933. [Epub ahead of print].

6. Dilliott AA, Evans EC, Farhan SMK, Ghani M, Sato C, Zhang M, et al. Genetic variation in the ontario neurodegenerative disease research initiative. *Can J Neurol Sci*. (2019) 46:491–8. doi: 10.1017/cjn.2019.228
7. Farhan SMK, Dilliott AA, Ghani M, Sato C, Liang E, Zhang M, et al. The ONDRISeq panel: custom-designed next-generation sequencing of genes related to neurodegeneration. *NPJ Genomic Med*. (2016) 1:16032. doi: 10.1038/npjgenmed.2016.32
8. Wong BM, Cheng RW, Mandelcorn ED, Margolin E, El-Defrawy S, Yan P, et al. Validation of optical coherence tomography retinal segmentation in neurodegenerative disease. *Transl Vis Sci Technol*. (2019) 8:6. doi: 10.1167/tvst.8.5.6
9. Montero-Odasso M, Pieruccini-Faria F, Bartha R, Black SE, Finger E, Freedman M, et al. Motor phenotype in neurodegenerative disorders: gait and balance platform study design protocol for the Ontario Neurodegenerative Research Initiative (ONDRI). *J Alzheimer's Dis*. (2017) 59:707–21. doi: 10.3233/JAD-170149
10. Nestor SM, Gibson E, Gao F-Q, Kiss A, Black SE. A direct morphometric comparison of five labeling protocols for multi-atlas driven automatic segmentation of the hippocampus in Alzheimer's disease. *Neuroimage.* (2013) 66:50–70. doi: 10.1016/j.neuroimage.2012.10.081
11. Albert MS, DeKosky ST, Dickson D, Dubois B, Feldman HH, Fox NC, et al. The diagnosis of mild cognitive impairment due to Alzheimer's disease: recommendations from the National Institute on Aging-Alzheimer's Association workgroups on diagnostic guidelines for Alzheimer's disease. *Alzheimers Dement*. (2011) 7:270–9. doi: 10.1016/j.jalz.2011.03.008
12. McKhann GM, Knopman DS, Chertkow H, Hyman BT, Jack CR, Kawas CH, et al. The diagnosis of dementia due to Alzheimer's disease: recommendations from the National Institute on Aging-Alzheimer's Association workgroups on diagnostic guidelines for Alzheimer's disease. *Alzheimers Dement*. (2011) 7:263–9. doi: 10.1016/j.jalz.2011.03.005
13. Gibb WR, Lees AJ. The relevance of the Lewy body to the pathogenesis of idiopathic Parkinson's disease. *J Neurol Neurosurg Psychiatry*. (1988) 51:745–52. doi: 10.1136/jnnp.51.6.745
14. Brooks BR. El Escorial World Federation of Neurology criteria for the diagnosis of amyotrophic lateral sclerosis. Subcommittee on motor neuron diseases/amyotrophic lateral sclerosis of the world federation of neurology research group on neuromuscular diseases and the El Escorial. *J Neurol Sci*. (1994) 124(Suppl.):96–107. doi: 10.1016/0022-510X(94)90191-0
15. Rascovsky K, Hodges JR, Knopman D, Mendez MF, Kramer JH, Neuhaus J, et al. Sensitivity of revised diagnostic criteria for the behavioural variant of frontotemporal dementia. *Brain*. (2011) 134:2456–77. doi: 10.1093/brain/awr179
16. Gorno-Tempini ML, Hillis AE, Weintraub S, Kertesz A, Mendez M, Cappa SF, et al. Classification of primary progressive aphasia and its variants. *Neurology*. (2011) 76:1006–14. doi: 10.1212/WNL.0b013e31821103e6
17. Höglinger GU, Respondek G, Stamelou M, Kurz C, Josephs KA, Lang AE, et al. Clinical diagnosis of progressive supranuclear palsy: the movement disorder society criteria. *Mov Disord*. (2017) 32:853–64. doi: 10.1002/mds.26987
18. Hachinski V, Iadecola C, Petersen RC, Breteler MM, Nyenhuis DL, Black SE, et al. National Institute of Neurological Disorders and *Stroke*-Canadian Stroke Network vascular cognitive impairment harmonization standards. *Stroke.* (2006) 37:2220–41. doi: 10.1161/01.STR.0000237236.88823.47
19. Duchesne S, Chouinard I, Potvin O, Fonov VS, Khademi A, Bartha R, et al. The canadian dementia imaging protocol: harmonizing national cohorts. *J Magn Reson Imaging.* (2019) 49:456–65. doi: 10.1002/jmri.26197
20. Dade LA, Gao FQ, Kovacevic N, Roy P, Rockel C, O'Toole CM, et al. Semiautomatic brain region extraction: a method of parcellating brain regions from structural magnetic resonance images. *Neuroimage*. (2004) 22:1492–502. doi: 10.1016/j.neuroimage.2004.03.023
21. Gibson E, Gao F, Black SE, Lobaugh NJ. Automatic segmentation of white matter hyperintensities in the elderly using FLAIR images at 3T. *J Magn Reson*. (2010) 31:1311–22. doi: 10.1002/jmri.22004
22. Ramirez J, Scott C, McNeely A, Berezuk C, Gao F, Szilagyi G, et al. Lesion explorer: a video-guided, standardized protocol for accurate and reliable MRI-derived volumetrics in Alzheimer's disease and normal elderly. *J Vis Exp*. (2014) 10:887. doi: 10.3791/50887
23. Ramirez J, Gibson E, Quddus A, Lobaugh NJ, Feinstein A, Levine B, et al. Lesion Explorer: a comprehensive segmentation and parcellation package to obtain regional volumetrics for subcortical hyperintensities and intracranial tissue. *Neuroimage.* (2011) 54:963–73. doi: 10.1016/j.neuroimage.2010.09.013
24. Kovacevic N, Lobaugh NJ, Bronskill MJ, Levine B, Feinstein A, Black SE. A robust method for extraction and automatic segmentation of brain images. *Neuroimage.* (2002) 17:1087–100. doi: 10.1006/nimg.2002.1221
25. Ramirez J, Scott CJM, Black SE. A short-term scan-rescan reliability test measuring brain tissue and subcortical hyperintensity volumetrics obtained using the lesion explorer structural MRI processing pipeline. *Brain Topogr*. (2013) 26:35–8. doi: 10.1007/s10548-012-0228-z
26. Dey AK, Stamenova V, Bacopulos A, Jeyakumar N, Turner GR, Black SE, et al. Cognitive heterogeneity among community-dwelling older adults with cerebral small vessel disease. *Neurobiol Aging.* (2019) 77:183–93. doi: 10.1016/j.neurobiolaging.2018.12.011
27. Ramirez J, Singh N, Adamo S, Maged G, Thayalasuthan V, Zhang B, et al. Carotid atherosclerosis and cerebral small vessel disease: preliminary results from the canadian atherosclerosis imaging network project 1. *Atheroscler Suppl*. (2018) 32:156. doi: 10.1016/j.atherosclerosissup.2018.04.473
28. Sam K, Peltenburg B, Conklin J, Sobczyk O, Poublanc J, Crawley AP, et al. Cerebrovascular reactivity and white matter integrity. *Neurology*. (2016) 87:2333–9. doi: 10.1212/WNL.0000000000003373
29. Swardfager W, Cogo-Moreira H, Masellis M, Ramirez J, Herrmann N, Edwards JD, et al. The effect of white matter hyperintensities on verbal memory. *Neurology*. (2018) 90:e673–82. doi: 10.1212/WNL.0000000000004983
30. Yushkevich PA, Piven J, Hazlett HC, Smith RG, Ho S, Gee JC, et al. User-guided 3D active contour segmentation of anatomical structures: significantly improved efficiency and reliability. *Neuroimage*. (2006) 31:1116–28. doi: 10.1016/j.neuroimage.2006.01.015
31. Talairach J, Tournoux P. *Co-Planar Stereotaxic Atlas of the Human Brain 3-Dimensional Proportional Grid System: An Approach to Cerebral Imaging.* Stuttgart: Thieme Medical Publishers (1988).
32. Mazziotta JC, Toga AW, Evans A, Fox P, Lancaster J. A probabilistic atlas of the human brain: theory and rationale for its development. *Int Consortium Brain Mapping (ICBM) Neuroimage.* (1995) 2:89–101. doi: 10.1006/nimg.1995.1012
33. Frisoni GB, Jack CR. Harmonization of magnetic resonance-based manual hippocampal segmentation: a mandatory step for wide clinical use. *Alzheimers Dement*. (2011) 7:171–4. doi: 10.1016/j.jalz.2010.06.007
34. Moodley KK, Chan D. The hippocampus in neurodegenerative disease. *Front Neurol Neurosci*. (2014) 34:95–108. doi: 10.1159/000356430
35. Bastos-Leite AJ, Van Waesberghe JH, Oen AL, Van Der Flier WM, Scheltens P, Barkhof F. Hippocampal sulcus width and cavities: comparison between patients with Alzheimer disease and non-demented elderly subjects. *Am J Neuroradiol*. (2006) 27:2141–5. Available online at: http://www.ajnr.org/content/27/10/2141
36. Maller JJ, Réglade-Meslin C, Chan P, Daskalakis ZJ, Thomson RHS, Anstey KJ, et al. Hippocampal sulcal cavities: prevalence, risk factors and relationship to memory impairment. *Brain Res*. (2011) 1368:222–30. doi: 10.1016/j.brainres.2010.10.089
37. Van Veluw SJ, Wisse LEM, Kuijf HJ, Spliet WGM, Hendrikse J, Luijten PR, et al. Hippocampal T2 hyperintensities on 7 Tesla MRI. *NeuroImage Clin*. (2013) 3:196–201. doi: 10.1016/j.nicl.2013.08.003
38. Yao M, Zhu YC, Soumaré A, Dufouil C, Mazoyer B, Tzourio C, et al. Hippocampal perivascular spaces are related to aging and blood pressure but not to cognition. *Neurobiol Aging.* (2014) 35:2118–25. doi: 10.1016/j.neurobiolaging.2014.03.021
39. Park MTM, Pipitone J, Baer LH, Winterburn JL, Shah Y, Chavez S, et al. Derivation of high-resolution MRI atlases of the human cerebellum at 3T and segmentation using multiple automatically generated templates. *Neuroimage.* (2014) 95:217–31. doi: 10.1016/j.neuroimage.2014.03.037

40. Vågberg M, Granåsen G, Svenningsson A. Brain parenchymal fraction in healthy adults—a systematic review of the literature. *PLoS ONE*. (2017) 12:e0170018. doi: 10.1371/journal.pone.0170018
41. Rudick RA, Fisher E, Lee JC, Simon J, Jacobs L. Use of the brain parenchymal fraction to measure whole brain atrophy in relapsing-remitting MS. Multiple Sclerosis Collaborative Research Group. *Neurology*. (1999) 53:1698–704. doi: 10.1212/WNL.53.8.1698
42. Levy-Cooperman N, Ramirez J, Lobaugh NJ, Black SE. Misclassified tissue volumes in Alzheimer disease patients with white matter hyperintensities: importance of lesion segmentation procedures for volumetric analysis. *Stroke*. (2008) 39:1134–41. doi: 10.1161/STROKEAHA.107.498196
43. Nestor SM, Rupsingh R, Borrie M, Smith M, Accomazzi V, Wells JL, et al. Ventricular enlargement as a possible measure of Alzheimer's disease progression validated using the Alzheimer's disease neuroimaging initiative database. *Brain*. (2008) 131:2443–54. doi: 10.1093/brain/awn146
44. Sapkota S, Ramirez J, Stuss DT, Masellis M, Black SE. Clinical dementia severity associated with ventricular size is differentially moderated by cognitive reserve in men and women. *Alzheimers Res Ther*. (2018) 10:89. doi: 10.1186/s13195-018-0419-2
45. Tavares TP, Mitchell DGV, Coleman K, Shoesmith C, Bartha R, Cash DM, et al. Ventricular volume expansion in presymptomatic genetic frontotemporal dementia. *Neurology*. (2019) 93:e1699–706. doi: 10.1212/WNL.0000000000008386
46. Wardlaw JM, Smith EE, Biessels GJ, Cordonnier C, Fazekas F, Frayne R, et al. Neuroimaging standards for research into small vessel disease and its contribution to ageing and neurodegeneration. *Lancet Neurol*. (2013) 12:822–38. doi: 10.1016/S1474-4422(13)70124-8
47. Barkhof F, Scheltens P. Is the whole brain periventricular? *J Neurol Neurosurg Psychiatry*. (2006) 77:143–4. doi: 10.1136/jnnp.2005.075101
48. Sachdev P, Wen W. Should we distinguish between periventricular and deep white matter hyperintensities? *Stroke*. (2005) 36:2342–3. doi: 10.1161/01.STR.0000185694.52347.6e
49. Gouw AA, Seewann A, van der Flier WM, Barkhof F, Rozemuller AM, Scheltens P, et al. Heterogeneity of small vessel disease: a systematic review of MRI and histopathology correlations. *J Neurol Neurosurg Psychiatry*. (2011) 82:126–35. doi: 10.1136/jnnp.2009.204685
50. Simpson JE, Ince PG, Higham CE, Gelsthorpe CH, Fernando MS, Matthews F, et al. Microglial activation in white matter lesions and non-lesional white matter of ageing brains. *Neuropathol Appl Neurobiol*. (2007) 33:670–83. doi: 10.1111/j.1365-2990.2007.00890.x
51. Black SE, Gao FQ, Bilbao J. Understanding white matter disease: imaging-pathological correlations in vascular cognitive impairment. *Stroke*. (2009) 40:S48–52. doi: 10.1161/STROKEAHA.108.537704
52. Keith J, Gao F, Noor R, Kiss A, Balasubramaniam G, Au K, et al. Collagenosis of the deep medullary veins: an underrecognized pathologic correlate of white matter hyperintensities and periventricular infarction? *J Neuropathol Exp Neurol*. (2017) 76:299–312. doi: 10.1093/jnen/nlx009
53. Moody DM, Brown WR, Challa VR, Anderson RL. Periventricular venous collagenosis: association with leukoaraiosis. *Radiology*. (1995) 194:469–76. doi: 10.1148/radiology.194.2.7824728
54. Decarli C, Fletcher E, Ramey V, Harvey D, Jagust WJ. Anatomical mapping of white matter hyperintensities (WMH): exploring the relationships between periventricular WMH, deep WMH, and total WMH burden. *Stroke*. (2005) 36:50–5. doi: 10.1161/01.STR.0000150668.58689.f2
55. Sachdev P, Chen X, Wen W. White matter hyperintensities in mid-adult life. *Curr Opin Psychiatry*. (2008) 21:268–74. doi: 10.1097/YCO.0b013e3282f945d5
56. van den Heuvel DM, ten VD, de Craen AJ, dmiraal-Behloul F, Olofsen H, Bollen EL, et al. Increase in periventricular white matter hyperintensities parallels decline in mental processing speed in a non-demented elderly population. *J Neurol Neurosurg Psychiatry*. (2006) 77:149–53. doi: 10.1136/jnnp.2005.070193
57. Fisher CM. Lacunes: small, deep cerebral infarcts. *Neurology*. (1998) 50:841. doi: 10.1212/WNL.50.4.841-a
58. Roman GC. On the history of lacunes, etat crible, and the white matter lesions of vascular dementia. *Cerebrovasc Dis*. (2002) 13:1–6. doi: 10.1159/000049142
59. Potter GM, Marlborough FJ, Wardlaw JM. Wide variation in definition, detection, and description of lacunar lesions on imaging. *Stroke*. (2011) 42:359–66. doi: 10.1161/STROKEAHA.110.594754
60. Vermeer SE, Longstreth WTJr, Koudstaal PJ. Silent brain infarcts: a systematic review. *Lancet Neurol*. (2007) 6:611–9. doi: 10.1016/S1474-4422(07)70170-9
61. Bastos Leite AJ, van Straaten EC, Scheltens P, Lycklama G, Barkhof F. Thalamic lesions in vascular dementia: low sensitivity of fluid-attenuated inversion recovery (FLAIR) imaging. *Stroke*. (2004) 35:415–9. doi: 10.1161/01.STR.0000109226.67085.5A
62. Jessen NA, Munk ASF, Lundgaard I, Nedergaard M. The glymphatic system: a beginner's guide. *Neurochem Res*. (2015) 40:2583–99. doi: 10.1007/s11064-015-1581-6
63. Rasmussen MK, Mestre H, Nedergaard M. The glymphatic pathway in neurological disorders. *Lancet Neurol*. (2018) 17:1016–24. doi: 10.1016/S1474-4422(18)30318-1
64. Ballerini L, Lovreglio R, Valdés Hernández MDC, Ramirez J, MacIntosh BJ, Black SE, et al. Perivascular spaces segmentation in brain MRI using optimal 3D filtering. *Sci Rep*. (2018) 8:5. doi: 10.1038/s41598-018-19781-5
65. Ramirez J, Berezuk C, McNeely AA, Gao F, McLaurin J, Black SE. Imaging the perivascular space as a potential biomarker of neurovascular and neurodegenerative diseases. *Cell Mol Neurobiol*. (2016) 36:289–99. doi: 10.1007/s10571-016-0343-6
66. Tarasoff-Conway JM, Carare RO, Osorio RS, Glodzik L, Butler T, Fieremans E, et al. Clearance systems in the brain-implications for Alzheimer disease. *Nat Rev Neurol*. (2015) 11:457–70. doi: 10.1038/nrneurol.2015.119
67. Wardlaw JM, Benveniste H, Nedergaard M, Zlokovic BV, Mestre H, Lee H, et al. Perivascular spaces in the brain: anatomy, physiology and pathology. *Nat Rev Neurol*. (2020) 16:137–53. doi: 10.1038/s41582-020-0312-z
68. Banerjee G, Kim HJ, Fox Z, Jäger HR, Wilson D, Charidimou A, et al. MRI-visible perivascular space location is associated with Alzheimer's disease independently of amyloid burden. *Brain*. (2017) 140:1107–16. doi: 10.1093/brain/awx003
69. Charidimou A, Jaunmuktane Z, Baron JC, Burnell M, Varlet P, Peeters A, et al. White matter perivascular spaces: an MRI marker in pathology-proven cerebral amyloid angiopathy? *Neurology*. (2014) 82:57–62. doi: 10.1212/01.wnl.0000438225.02729.04
70. Charidimou A, Hong YT, Jager HR, Fox Z, Aigbirhio FI, Fryer TD, et al. White matter perivascular spaces on magnetic resonance imaging: marker of cerebrovascular amyloid burden? *Stroke*. (2015) 46:1707–9. doi: 10.1161/STROKEAHA.115.009090
71. Martinez-Ramirez S, Pontes-Neto OM, Dumas AP, Auriel E, Halpin A, Quimby M, et al. Topography of dilated perivascular spaces in subjects from a memory clinic cohort. *Neurology*. (2013) 80:1551–6. doi: 10.1212/WNL.0b013e31828f1876
72. Berezuk C, Ramirez J, Gao F, Scott CJM, Huroy M. Virchow-robin spaces : correlations with polysomnography-derived sleep parameters. *Sleep*. (2015) 38:853–8. doi: 10.5665/sleep.4726
73. Xie L, Kang H, Xu Q, Chen MJ, Liao Y, Thiyagarajan M, et al. Sleep drives metabolite clearance from the adult brain. *Science*. (2013) 342:373–7. doi: 10.1126/science.1241224
74. Adams HHH, Cavalieri M, Verhaaren BFJ, Bos D, Van Der Lugt A, Enzinger C, et al. Rating method for dilated virchow-robin spaces on magnetic resonance imaging. *Stroke*. (2013) 44:1732–5. doi: 10.1161/STROKEAHA.111.000620
75. Patankar TF, Mitra D, Varma A, Snowden J, Neary D, Jackson A. Dilatation of the Virchow-Robin space is a sensitive indicator of cerebral microvascular disease: study in elderly patients with dementia. *Am J Neuroradiol*. (2005) 26:1512–20. Available online at: http://www.ajnr.org/content/26/6/1512
76. Ramirez J, Berezuk C, McNeely AA, Scott CJM, Gao F, Black SE. Visible Virchow-Robin spaces on magnetic resonance imaging of Alzheimer's disease patients and normal elderly from the Sunnybrook dementia study. *J Alzheimer's Dis*. (2015) 43:415–24. doi: 10.3233/JAD-132528
77. Greenberg SM, Vernooij MW, Cordonnier C, Viswanathan A, Al-Shahi Salman R, Warach S, et al. Cerebral microbleeds: a guide to detection and interpretation. *Lancet Neurol*. (2009) 8:165–74. doi: 10.1016/S1474-4422(09)70013-4

78. Gregoire SM, Chaudhary UJ, Brown MM, Yousry TA, Kallis C, Jager HR, et al. The Microbleed Anatomical Rating Scale (MARS): reliability of a tool to map brain microbleeds. *Neurology.* (2009) 73:1759–66. doi: 10.1212/WNL.0b013e3181c34a7d
79. Cordonnier C, Potter GM, Jackson CA, Doubal F, Keir S, Sudlow CLM, et al. Improving interrater agreement about brain microbleeds: development of the Brain Observer MicroBleed Scale (BOMBS). *Stroke.* (2009) 40:94–9. doi: 10.1161/STROKEAHA.108.526996
80. Akoudad S, Wolters FJ, Viswanathan A, de Bruijn RF, van der Lugt A, Hofman A, et al. Association of cerebral microbleeds with cognitive decline and dementia. *JAMA Neurol.* (2016) 73:934–43. doi: 10.1001/jamaneurol.2016.1017
81. Boyle PA, Yu L, Nag S, Leurgans S, Wilson RS, Bennett DA, et al. Cerebral amyloid angiopathy and cognitive outcomes in community-based older persons. *Neurology.* (2015) 85:1930–6. doi: 10.1212/WNL.0000000000002175
82. Goos JD, Kester MI, Barkhof F, Klein M, Blankenstein MA, Scheltens P, et al. Patients with Alzheimer disease with multiple microbleeds: relation with cerebrospinal fluid biomarkers and cognition. *Stroke.* (2009) 40:3455–60. doi: 10.1161/STROKEAHA.109.558197
83. Poels MMF, Vernooij MW, Ikram MA, Hofman A, Krestin GP, Van Der Lugt A, et al. Prevalence and risk factors of cerebral microbleeds: an update of the rotterdam scan study. *Stroke.* (2010) 41:S103–6. doi: 10.1161/STROKEAHA.110.595181
84. Akoudad S, Portegies MLP, Koudstaal PJ, Hofman A, Van Der Lugt A, Ikram MA, et al. Cerebral microbleeds are associated with an increased risk of stroke: the rotterdam study. *Circulation.* (2015) 132:509–16. doi: 10.1161/CIRCULATIONAHA.115.016261
85. Charidimou A, Linn J, Vernooij MW, Opherk C, Akoudad S, Baron JC, et al. Cortical superficial siderosis: detection and clinical significance in cerebral amyloid angiopathy and related conditions. *Brain.* (2015) 138:2126–39. doi: 10.1093/brain/awv162
86. Cordonnier C, van der Flier WM. Brain microbleeds and Alzheimer's disease: innocent observation or key player? *Brain.* (2011) 134:335–44. doi: 10.1093/brain/awq321
87. Mesker DJ, Poels MMF, Ikram MA, Vernooij MW, Hofman A, Vrooman HA, et al. Lobar distribution of cerebral microbleeds. *Arch Neurol.* (2011) 68:93. doi: 10.1001/archneurol.2011.93
88. Pettersen J, Sathiyamoorthy G, Gao F, Szilagyi G, Nadkarni N, St George-Hyslop P, et al. Microbleed topography, leukoaraiosis, and cognition in probable Alzheimer disease from the sunnybrook dementia study. *Arch Neurol.* (2008) 65:790–5. doi: 10.1001/archneur.65.6.790
89. Martinez-Ramirez S, Romero JR, Shoamanesh A, McKee AC, Van Etten E, Pontes-Neto O, et al. Diagnostic value of lobar microbleeds in individuals without intracerebral hemorrhage. *Alzheimer's Dement.* (2015) 11:1480–8. doi: 10.1016/j.jalz.2015.04.009
90. Boulouis G, Charidimou A, Greenberg SM. Sporadic cerebral amyloid angiopathy: pathophysiology, neuroimaging features, and clinical implications. *Semin Neurol.* (2016) 36:233–43. doi: 10.1055/s-0036-1581993
91. Smith EE, Greenberg SM. Clinical diagnosis of cerebral amyloid angiopathy: validation of the Boston criteria. *Curr Atheroscler Rep.* (2003) 5:260–6. doi: 10.1007/s11883-003-0048-4
92. Feigin VL, Norrving B, Mensah GA. Global burden of stroke. *Circ Res.* (2017) 120:439–48. doi: 10.1161/CIRCRESAHA.116.308413
93. Gorelick PB, Scuteri A, Black SE, DeCarli C, Greenberg SM, Iadecola C, et al. Vascular contributions to cognitive impairment and dementia: a statement for healthcare professionals from the american heart association/american stroke association. *Stroke.* (2011) 42:2672–713. doi: 10.1161/STR.0b013e3182299496
94. Feigin VL, Krishnamurthi RV, Parmar P, Norrving B, Mensah GA, Bennett DA, et al. Update on the global burden of ischemic and hemorrhagic stroke in 1990–2013: the GBD 2013 study. *Neuroepidemiology.* (2015) 45:161–76. doi: 10.1159/000441085
95. Blacquiere D, Lindsay MP, Foley N, Taralson C, Alcock S, Balg C, et al. Canadian stroke best practice recommendations: telestroke best practice guidelines update 2017. *Int J Stroke.* (2017) 12:886–95. doi: 10.1177/1747493017706239
96. Cameron JI, OConnell C, Foley N, Salter K, Booth R, Boyle R, et al. Canadian stroke best practice recommendations: managing transitions of care following stroke, guidelines update 2016. *Int J Stroke.* (2016) 11:807–22. doi: 10.1177/1747493016660102
97. Lanctôt KL, Lindsay MP, Smith EE, Sahlas DJ, Foley N, Gubitz G, et al. Canadian stroke best practice recommendations: mood, cognition and fatigue following stroke, 6th edition update 2019. *Int J Stroke.* (2019). doi: 10.1177/1747493019847334. [Epub ahead of print].
98. Casaubon LK, Boulanger J-M, Glasser E, Blacquiere D, Boucher S, Brown K, et al. Canadian stroke best practice recommendations : acute inpatient stroke care guidelines, update 2015. *Int J Stroke.* (2016) 11:239–52. doi: 10.1177/1747493015622461
99. Wein T, Lindsay MP, Côté R, Foley N, Berlingieri J, Bhogal S, et al. Canadian stroke best practice recommendations: secondary prevention of stroke, sixth edition practice guidelines, update 2017. *Int J Stroke.* (2018) 13:420–43. doi: 10.1177/1747493017743062
100. Ladhani NNN, Swartz RH, Foley N, Nerenberg K, Smith EE, Gubitz G, et al. Canadian stroke best practice consensus statement: acute stroke management during pregnancy. *Int J Stroke.* (2018) 13:743–58. doi: 10.1177/1747493018786617
101. Swartz RH, Ladhani NNN, Foley N, Nerenberg K, Bal S, Barrett J, et al. Canadian stroke best practice consensus statement: secondary stroke prevention during pregnancy. *Int J Stroke.* (2018) 13:406–19. doi: 10.1177/1747493017743801
102. Sacco RL, Kasner SE, Broderick JP, Caplan LR, Connors JJ, Culebras A, et al. An updated definition of stroke for the twenty-first century: a statement for healthcare professionals from the American heart association/American stroke association. *Stroke.* (2013) 44:2064–89. doi: 10.1161/STR.0b013e318296aeca
103. van Swieten JC, Koudstaal PJ, Visser MC, Schouten HJ, van Gijn J. Interobserver agreement for the assessment of handicap in stroke patients. *Stroke.* (1988) 19:604–7. doi: 10.1161/01.STR.19.5.604
104. Decarli C, Massaro J, Harvey D, Hald J, Tullberg M, Au R, et al. Measures of brain morphology and infarction in the framingham heart study: establishing what is normal. *Neurobiol Aging.* (2005) 26:491–510. doi: 10.1016/j.neurobiolaging.2004.05.004
105. Carmichael O, Schwarz C, Drucker D, Fletcher E, Harvey D, Beckett L, et al. Longitudinal changes in white matter disease and cognition in the 1st year of the Alzheimer disease neuroimaging initiative. *Arch Neurol.* (2010) 67:1370–8. doi: 10.1001/archneurol.2010.284
106. Pantoni L. Cerebral small vessel disease: from pathogenesis and clinical characteristics to therapeutic challenges. *Lancet Neurol.* (2010) 9:689–701. doi: 10.1016/S1474-4422(10)70104-6
107. Basile AM, Pantoni L, Pracucci G, Asplund K, Chabriat H, Erkinjuntti T, et al. Age, hypertension, and lacunar stroke are the major determinants of the severity of age-related white matter changes. *LADIS.* (2006) 21:315–22. doi: 10.1159/000091536
108. Nguyen LH, Holmes S. Ten quick tips for effective dimensionality reduction. *PLoS Comput Biol.* (2019) 15:e1006907. doi: 10.1371/journal.pcbi.1006907
109. Zhu YC, Dufouil C, Mazoyer B, Soumare A, Ricolfi F, Tzourio C, et al. Frequency and location of dilated Virchow-Robin spaces in elderly people: a population-based 3D MR imaging study. *AJNR Am J Neuroradiol.* (2011) 32:709–13. doi: 10.3174/ajnr.A2366
110. Zhu YC, Tzourio C, Soumare A, Mazoyer B, Dufouil C, Chabriat H. Severity of dilated Virchow-Robin spaces is associated with age, blood pressure, and MRI markers of small vessel disease: a population-based study. *Stroke.* (2010) 41:2483–90. doi: 10.1161/STROKEAHA.110.591586
111. Francis F, Ballerini L, Wardlaw JM. Perivascular spaces and their associations with risk factors, clinical disorders and neuroimaging features: a systematic review and meta-analysis. *Int J Stroke.* (2019) 14:359–71. doi: 10.1177/1747493019830321
112. Swartz RH, Bayley M, Lanctôt KL, Murray BJ, Cayley ML, Lien K, et al. Post-stroke depression, obstructive sleep apnea, and cognitive impairment: rationale for, and barriers to, routine screening. *Int J Stroke.* (2016) 11:509–18. doi: 10.1177/1747493016641968
113. Smith EE, Saposnik G, Biessels GJ, Doubal FN, Fornage M, Gorelick PB, et al. Prevention of stroke in patients with silent

cerebrovascular disease: a scientific statement for healthcare professionals from the American Heart Association/American Stroke Association. *Stroke*. (2017) 48:e44–71. doi: 10.1161/STR.0000000000000116

114. Beaton D, Sunderland KM, Levine, B, Mandzia J, Masellis M, Swartz RH, et al. Generalization of the minimum covariance determinant algorithm for categorical and mixed data types. *bioRxiv*. (2019) 333005. doi: 10.1101/333005
115. Sunderland KM, Beaton D, Fraser J, Kwan D, McLaughlin PM, Montero-Odasso M, et al. The utility of multivariate outlier detection techniques for data quality evaluation in large studies: an application within the ONDRI project. *BMC Med Res Methodol*. (2019) 19:102. doi: 10.1186/s12874-019-0737-5

Conflict of Interest: The authors declare that the research was conducted in the absence of any commercial or financial relationships that could be construed as a potential conflict of interest.

frontiers in Neurology

ORIGINAL RESEARCH
published: 28 August 2020
doi: 10.3389/fneur.2020.00828

Signs of Intracranial Hypertension, Hypermobility, and Craniocervical Obstructions in Patients With Myalgic Encephalomyelitis/Chronic Fatigue Syndrome

Björn Bragée [1,2], Anastasios Michos [2], Brandon Drum [1,2], Mikael Fahlgren [2,3], Robert Szulkin [1] and Bo C. Bertilson [1,2,3]*

[1] Division of Family Medicine and Primary Care, Department of Neurobiology, Care Sciences and Society, Karolinska Institutet, Solna, Sweden, [2] ME-center, Bragée Clinics, Stockholm, Sweden, [3] Academic Primary Health Care Center, Stockholm Health Care Services, Region Stockholm, Stockholm, Sweden

OPEN ACCESS

Edited by:
Christian Gaser,
Friedrich Schiller University Jena, Germany

Reviewed by:
Lucinda Bateman,
Bateman Horne Center, United States
Vincent C. Lombardi,
University of Nevada, United States

***Correspondence:**
Björn Bragée
bjorn.bragee@ki.se

Specialty section:
This article was submitted to Applied Neuroimaging, a section of the journal Frontiers in Neurology

Received: *18 November 2019*
Accepted: *02 July 2020*
Published: *28 August 2020*

Citation:
Bragée B, Michos A, Drum B, Fahlgren M, Szulkin R and Bertilson BC (2020) Signs of Intracranial Hypertension, Hypermobility, and Craniocervical Obstructions in Patients With Myalgic Encephalomyelitis/Chronic Fatigue Syndrome. Front. Neurol. 11:828. doi: 10.3389/fneur.2020.00828

The pathophysiology of myalgic encephalomyelitis/chronic fatigue syndrome (ME/CFS) is unknown. In this study, we test the hypothesis that hypermobility, signs of intracranial hypertension (IH), and craniocervical obstructions may be overrepresented in patients with ME/CFS and thereby explain many of the symptoms. Our study is a retrospective, cross-sectional study, performed at a specialist clinic for referred patients with severe ME/CFS as defined by the Canada Consensus Criteria. The first 272 patients with ME/CFS were invited to participate, and 229 who provided prompt informed consent were included. Hypermobility was assessed using the Beighton Score. IH was assessed indirectly by the quotient of the optic nerve sheet diameter (ONSD)/eyeball transverse diameter on both sides as measured on magnetic resonance imaging (MRI) of the brain. We also included assessment of cerebellar tonsil position in relation to the McRae line, indicating foramen magnum. Craniocervical obstructions were assessed on MRI of the cervical spine. Allodynia was assessed by quantitative sensory testing (QST) for pain in the 18 areas indicative of fibromyalgia syndrome (FMS). A total of 190 women, mean age 45 years, and 39 males, mean age 44 years, were included. Hypermobility was identified in 115 (50%) participants. MRI of the brain was performed on 205 participants of whom 112 (55%) had an increased ONSD and 171 (83%) had signs of possible IH, including 65 (32%) who had values indicating more severe states of IH. Cerebellar tonsils protruding under the McRae line into the foramen magnum were identified in 115 (56%) of the participants. MRI of the cervical spine was performed on 125 participants of whom 100 (80%) had craniocervical obstructions. Pain at harmless pressure, allodynia, was found in 96% of the participants, and FMS was present in 173 participants or 76%. Compared to a general population, we found a large overrepresentation of hypermobility, signs of IH, and craniocervical obstructions. Our hypothesis was strengthened for future studies on the possible relation between ME/CFS symptoms and hypermobility, IH, and craniocervical obstructions in a portion of patients with ME/CFS. If our findings are confirmed, new diagnostic and therapeutic approaches to this widespread neurological syndrome should be considered.

Keywords: fatigue syndrome, chronic, pain, Ehlers Danlos syndrome, Arnold-Chiari malformation, magnetic resonance imaging, intracranial hypertension, pseudotumor cerebri, hypermobility, joint

INTRODUCTION

Myalgic encephalomyelitis/chronic fatigue syndrome (ME/CFS) is characterized by severe unmitigable fatigue, post-exertional malaise (PEM), pain, and neurological and immunological dysfunction as noted in the Canada Consensus Criteria (CCC) for ME/CFS from 2003 (1).

The true prevalence of ME/CFS is unknown although previous international studies provide estimates of 0.2 to 1.6% (2). ME/CFS is more common in women aged 30–39 years. The disorder results in large costs of treating and managing this syndrome, which are estimated to exceed $20 billion annually in United States alone (3). The pathophysiological origins of ME/CFS remain unclear. Since the 1960s, a multitude of hypotheses of causality have been proposed, most of which explain disease origins with an infection. A number of bacteria and viruses have been proposed as ME/CFS-causative although there remains no broad consensus (4). The World Health Organization now classifies ME/CFS as a neurological disease of postviral origin (G93.3) (5).

At the request of the Stockholm Region County Council, we started an ME/CFS specialty clinic in 2017 aimed at ME/CFS diagnosis, treatment, and research. Using an extensive neurological protocol, we found that patients frequently had clinical findings including hypermobility and central nervous system (CNS) pathologies, including magnetic resonance imaging (MRI) findings in the brain and the craniocervical region. Thus, we hypothesize that hypermobility and craniocervical obstruction are overrepresented in patients with ME/CFS and that a large portion of these patients may have a degree of intracranial hypertension (IH), which may explain many of the ME/CFS symptoms. To our knowledge, this is the first study of ME/CFS focusing on a possible mechanical pathophysiology.

METHODS

Study Design and Participants

This study is a retrospective cross-sectional study of consecutive patients referred to our open care specialty ME/CFS clinic. Ethical approval was granted by the Swedish Ethical Review Authority (nr. 2019-01566).

At the start of the study, 620 patients had been referred to our clinic, of whom 272 were diagnosed with ME according to the CCC (ICD G93.3). Each of these patients was asked via a letter to participate in the study, and 229 who provided informed consent to participate within 6 weeks were included. Data were extracted from patients' medical records.

Hypermobility and Neurological Assessment

Hypermobility was assessed using nine tests to create a Beighton Score (from 0 to 9) with five or more indicating hypermobility (6). General joint hypermobility according to cutoff values stated by Singh was identified (7). Neurological assessment was done using discomfort drawings and quantitative sensory testing (QST). Discomfort drawings were assessed for pattern of neuropathic pain and pattern of widespread pain (7). QST was performed using an electronic device, the Somedic® algometer, to establish the threshold for skin pressure pain. The pressure was gradually increased with a 1 cm^2 surface area probe at stipulated areas in all four body quadrants. The pain thresholds for pressure were measured at 18 locations according to the 1990 ACR protocol, and participants with 11 or more stipulated areas with pain threshold values under the normal 400 kPa/cm^2 met criteria for fibromyalgia syndrome (FMS) (8). The number of pain threshold measurements from 1 to 399 kPa/cm^2 and from 1 to 199 kPa/cm^2 were recorded. The criteria for FMS was evaluated for all participants and required tenderness on pressure (tender points) in at least 11 of 18 specified sites and the presence of widespread pain for more than 6 months for diagnosis. Widespread pain is defined as axial pain, left- and right-sided pain, and upper and lower segment pain.

MRI of the Brain

MRI scans of the brain were offered to all participants. MRIs were conducted in different labs and included T1- or T2-weighted scans with or without fluid-attenuated inversion recovery (FLAIR) with a section thickness of 3 mm. Scans were assessed by an experienced radiologist through the Regions MRI database, using Sectra® software, which offers built-in measurement tools. An interrater reliability (IRR) study of the MRI assessments was performed on 100 randomized participants for whom the radiologist assessments were compared to those made by a resident physician and a medical student.

The eyeball transverse diameter (ETD) was measured on axial sections of T2-weighted images. This was measured in the posterior chamber at the largest diameter of the retina's inner edges from left to right. The optic nerve sheath diameter (ONSD) was measured on the same axial T2 sections 3 mm from the midline of the optic nerve's inner limit to the posterior chamber along its axis. If the measurement did not allow a precision of 1/10 mm due to low resolution, the distance was appreciated to 1/10 mm from the external margins of the thick optic sheath layers covering the optic nerve (**Figure 1**). The range for normal ONSD is 4.8–5.8 mm, and a value of >5.8 mm corresponds to an elevated CSF pressure (>25 mm Hg) indicating IH (9). The

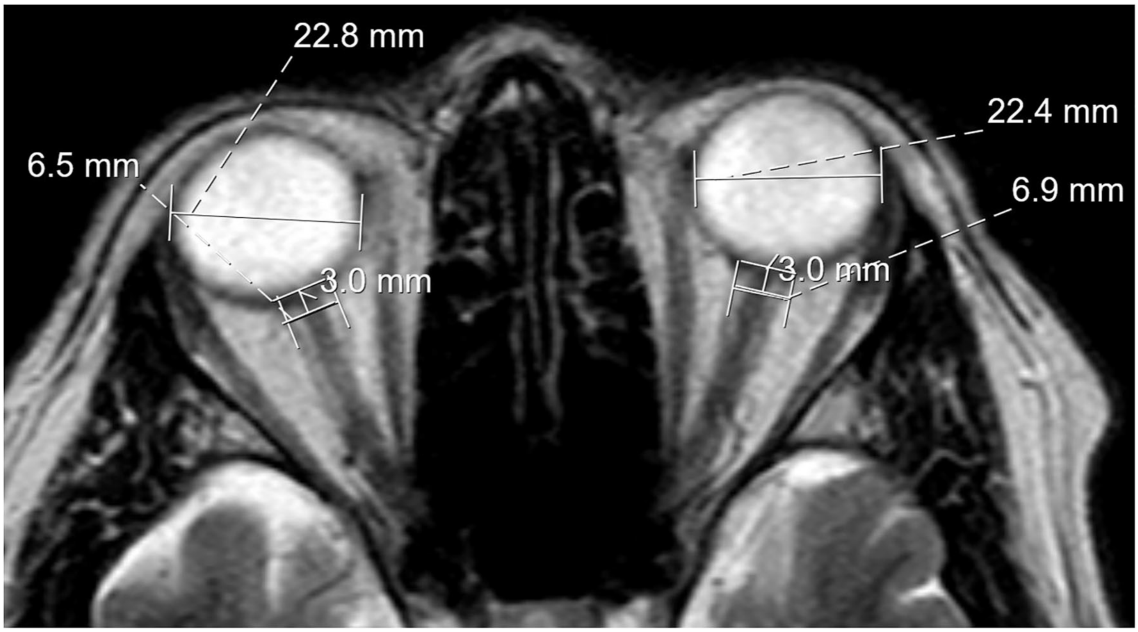

FIGURE 1 | MRI scan demonstrating eyeball transverse diameter and optic nerve sheath diameter measurements, which, in this case, indicates abnormal widening.

ONSD/ETD ratio has a normal value of 0.19 ± 0.02, and values > 0.25 are related to IH with severe symptoms (10, 11).

The foramen magnum was identified and measured on a midsagittal slice on T1-weighted scans. Distances were measured by the length of a line (McRae line) drawn on a sagittal skull radiograph joining the basion and opisthion as described by FW Smith (**Figure 2A**) (9). The position of the cerebellar tonsils and, if so, degree of herniation were measured as the distance from the McRae line to the most inferior point of the tonsil on frontal or sagittal projections on T1- or T2-weighted MRI scans (**Figure 2B**).

The clivo-axial angle (CXA) was measured on a midline sagittal slice on T1-weighted scans. A straight line was drawn along the caudal edge of the clivus bone, and a second was drawn by extending a straight line along the posterior axial line from the base of the axis to the dens. The angle at the intersection of these two lines was then measured. A CXA of <150° was considered abnormal as stated by Henderson et al., who in 2018 reported a growing recognition of the relationship between a kyphotic CXA and the risk of brainstem deformity and craniocervical instability (10).

All variables were recorded and rounded to the nearest millimeter except the CXA, which was measured in degrees.

MRI of the Cervical Spine

When clinical findings were suggestive of cervical spine pathology, an MRI from C1 to T2 was ordered in cases lacking recent imaging. MRI scans of the cervical spine were acquired and assessed using the same labs and machines as used for MRI of the brain. Spondylolisthesis (forward or backward slipping of a vertebral body), osteophytes (bone formations that may obstruct nerve and other soft tissue passages), spinal cysts, and syringomyelia were noted regardless of segment or severity. Spinal cord compression due to bulging or herniated discs or bones impinging upon the medulla spinalis was noted on axial and sagittal sections. The level of most prominent reduction of space in the spinal cord was noted as well as the degree of reduction. The area immediately above and below the most reduced area was compared to the area in which the most prominent reduction was located. All areas were measured in mm^2, and the difference was then calculated as a percentage of reduction compared with the closest normal segments. Correlation between the degree of joint hypermobility and the ONSD/ETD ratio as a marker for IH was calculated.

RESULTS

Characteristics of the Participants

There was a skewed sex distribution among the participants with 83% being women. The mean age of the 190 female participants was 45 years and, for the 39 men, 44 years (range 17–75 years). The mean body mass index (BMI) of participants was 25.1 for women and 24.9 for men. A BMI > 25 was noted in 101 (44%) participants, and a BMI > 30 was noted in 34 participants (15%).

The mean duration of ME-related symptoms was approximately 9 ± 8 years. We could assess earlier care contacts through our regional common medical record system for 198 participants. The mean number of contacts with the health care system during the last 5 years was 90. The mean number of diagnoses that participants had received over the last 5 years included 20 somatic diagnoses and three psychiatric diagnoses. A total of 150 (76%) participants had received at least

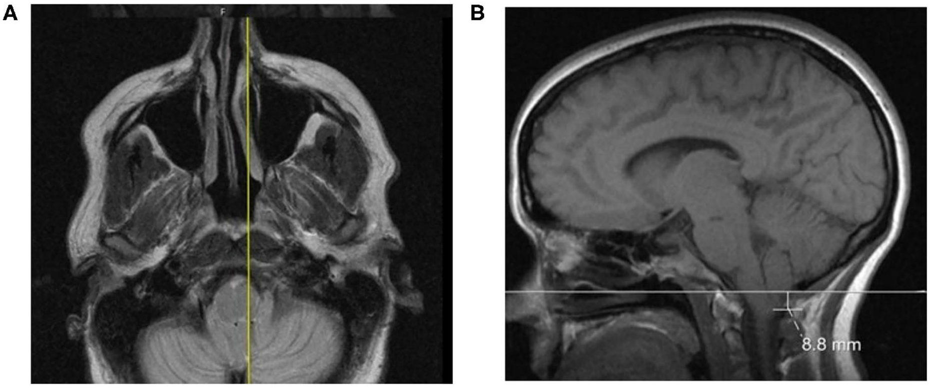

FIGURE 2 | (A) A case featuring a right-sided, low-lying cerebellar tonsil; **(B)** The axial projection position.

TABLE 1 | Prevalence of general hypermobility in different groups with cutoff values according to Singh (7).

Age	Sex	Cutoff value	Number of participants	Of whom with GJH	Prevalence (%)
14–19	Male	≥4	2	2	100%
	Female	≥5	2	1	50%
20–39	Male	≥4	10	5	50%
	Female	≥4	65	36	55%
40–59	Male	≥2	21	9	43%
	Female	≥4	103	54	52%
60–69	Male	≥1	6	2	33%
	Female	≥3	16	5	31%
70–101	Female	≥2	4	1	25%
Sum			229	115	50%

one psychiatric diagnosis. The diagnosis of FMS had been given to 31 participants (16%). There were 48 participants (25%) who had received an ME/CFS diagnosis before first admission to the clinic.

The prevalence of permanent sick leave was 39% and, together with other forms of social welfare, 57% of the participants had their income covered by social insurance, 10% had no income at all, and 25% still worked to some degree. The education level was high as 40% of participants had previous or actual work with an academic background, and 10% had blue-collar work.

Hypermobility and Neurological Assessments

General joint hypermobility was identified in 115 participants or 50% (**Table 1**). A total of 93 participants (41%) had Beighton scores of >4 points. A diagnosis of hEDS when criteria other than hypermobility are considered had been given earlier or after admission to 44 participants (20%).

Assessment of pain drawings could be made in all but four participants, and 192 or 85% marked pain in all four body quadrants—that is, widespread pain.

Allodynia criteria, defined as pain at harmless pressure, were met in 219 participants (96%) with 153 (67%) having >11 painful areas with a limit of 200 kpa/cm^2, that is, half the criteria limit for FMS. The criteria for FMS were met in 173 of our 229 participants, that is, in 76%.

MRI of the Brain

MRI exams of the brain were performed on 205 (90%) participants. Twenty-four participants did not undergo a brain MRI scan due to claustrophobia or other contraindications. The exams were performed within 6 months before or after the first visit to the clinic in 171 participants (84%). Examiner IRRs ranged between 0.77 and 0.88 for the assessment of ONSD, ETD, tonsil position, and craniocervical obstructions.

ONSD had a mean of 5.64 ± 0.67, and values >5.8 mm were found bilaterally in 61 participants and unilaterally in 51 participants, that is, all together in 55% of the participants. ETD had a mean value of 23.5 ± 1.1 mm bilaterally. The mean ONSD/ETD was 0.24 ± 0.03 and a value >0.22 on either side was found in 171 of our participants (83%). An ONSD/ETD larger than 0.25 was identified in 87 participants (42%).

The position of the cerebellar tonsils under the McRae line of the cerebellar tonsils had a mean value of 0.80 ± 2.95 mm. Negative values indicate a position above the McRae line, and positive values represent a position below the line (**Table 2**).

The mean CXA was 148° ± 10°, and 114 participants (56%) had a CXA of <150°.

MRI of the Cervical Spine

An MRI scan of the cervical spine was or had been performed in 125 participants (55%).

Spondylolisthesis was identified in eight (6%) and osteophytes in 11 (9%) participants. Spinal cysts or syrinxes were not identified in any scan. Obstructions of different varieties were present in 100 participants (80%). More than one segment of C1–T2 was obstructed in 80 participants (64%). Spinal cord compressions were most frequent at C5–C6 (53%) and C6–C7 (28%). The age distribution and findings of obstructions is presented in **Table 3**.

TABLE 2 | The position of the cerebellar tonsils in relation to the McRae line as measured on MRI scans of the brain in participants with ME/CFS ($n = 205$) and in the general population.

	Number of participants	Study prevalence (%)	Normal prevalence (%)	Comments (over representation)
A Both tonsils >2 mm above line	22	11	50	No obstruction (−5X)
B Both tonsils in line or 1–2 mm above line	68	33	25	No obstruction (=)
C Any tonsil under line	115	56	25	Obstruction (2X)
D Any tonsil 3–4 mm under line	51	25	8	Tonsillar ectopia (3X)
E Any tonsil 5 mm or more under line	27	13	3	Chiari 1 (4X)
F Both tonsils 5 mm or more under line	7	3	1	Chiari 1 (3X)

A participant could be included in two groups (C-E). Normal prevalence was determined by Smith (A–E) (12) Vernooij (F) (13).

TABLE 3 | Findings of obstructions in the cervical spine on MRI scan of the cervical spine. Number of participants.

Age	All participants	MRI exams	Obstr. findings	% of MRI exams
18–19	2	1	0	0
20-29	30	15	7	47
30–39	47	28	21	75
40–49	72	39	32	82
50–59	52	30	28	93
60–69	22	10	10	100
70–75	4	2	2	100
All	229	125	100	80

DISCUSSION

Our hypothesis that general joint hypermobility and craniocervical obstructions is overrepresented in patients with ME/CFS and that many of these patients may have a degree of IH was supported by our findings outlined above. Based on these findings, we propose that joint hypermobility and craniocervical obstructions may be one pathway to develop ME/CFS. ME/CFS as defined by the large CCC umbrella may include subgroups with infectious, immunological, traumatic, and craniocervical origins. The complexity of ME/CFS and the difficulty faced in diagnosing this syndrome is reflected by the numerous healthcare contacts with 90 visits in the last 5 years although the mean in the general population, including those with chronic diseases, is <30. The many diagnoses our participants had encountered prior to admission at our clinic is also conspicuous.

TABLE 4 | A comparison of our study population ($n = 205$) and a healthy reference population ($n = 314$) for optic nerve sheath diameter and eyeball transverse diameter as assessed by MRI scan of the brain.

	Bragée ME-center (±**SD**)	Reference population (±**SD**) (16)	*p*-value*
ONSD mm	5.64 ± 0.67	4.71 ± 0.31	<0.001
ETD mm	23.47 ± 1.05	21.24 ± 0.79	<0.001
ONSD/ETD ratio	0.24 ± 0.03	0.22 ± 0.01	<0.001

**Per two sample t-test using the published means from reference population. ONSD, Optic Nerve Sheath Diameter; ETD, Eyeball Transverse Diameter.*

Joint hypermobility was overrepresented in our study as 49% of the participants with ME/CFS had a Beighton score >4 compared to 3% in the general population (6). To discriminate between ME/CFS and Ehlers Danlos syndrome hypermobility type (hEDS), other features were also considered, including overly relaxed skin, a history of joint displacements, bruising, and a family history including or typical for hEDS. A Beighton score cutoff value for hEDS is 5 or more. The diagnosis of hEDS was made or confirmed by the physicians at the clinic, specialists who are experienced in pain medicine. Unfortunately, the genetic clinic in the region does not accept referrals for hEDS without suspicion of the vascular type of EDS, and there is no available specific biomarker to confirm the diagnosis of hEDS. A diagnosis of hEDS was present in 20% of our study population, and the prevalence in the general population is <1% (11). Such an overrepresentation of connective tissue disorders, such as hEDS, has, to the best of our knowledge, not been previously described in a large adult ME/CFS cohort. However, the comorbidity between hEDS and ME/CFS has been proposed in many reviews and shown in a cohort of 68 children and controls previously (14). Furthermore, numerous neurological and spinal manifestations of hEDS are known, giving symptoms similar to those in ME/CFS (15).

ONSD and the ONSD/ETD ratios are related to IH. Our results indicate that IH may contribute to ME/CFS symptoms (**Table 4**). ONSD ratios indicating IH were significantly more common in our study cohort compared to that of the healthy adult population as described in a study by Kim et al. of 314 individuals (16). ONSD values of >5.8 mm, indicating IH, were found in a majority of our participants. However, when we calculated ONSD/ETD ratios, which are considered a more adequate predictor of IH than ONSD as they eliminate body-size-related variability, 171 participants (83%) had ratios >0.22. ONSD/ETD ratios >0.22 has been found in 5% of the normal population (16). The ratio has a small variation as the normal value is 0.19 ± 0.02. In our population, 65 participants (32%) had an ONSD/ETD ratio >0.25, indicating a considerable and significant difference. In a study of 1,766 participants with either IH or intracranial hypotension, an ONSD/ETD ratio of 0.29 ± 0.04 was used as an indicator of significantly elevated intracranial pressure (17) although 0.25 was correlated to IH in a separate study of patients who underwent surgery for vascular infarctions (18). This suggests that a portion of patients with ME/CFS may have more harmful intracranial pressure.

Low cerebellar tonsils that protrude into the foramen magnum may obstruct the flow of CSF and indirectly cause IH. The limit for what is considered a low position of cerebellar tonsils varies between investigators, and most argue that a position >5 mm below the McRae line bilaterally should be considered a Chiari 1 malformation. That criteria was fulfilled by 3.4% of our participants as compared to prevalence in a normal population, which is estimated to be 0.3–1%, indicating at least a three-fold higher prevalence in our participants with ME/CFS (12). Others have used a definition for Chiari 1 malformation when the position of the tonsils are $\geq$3 mm below the McRae line, which occurred in 4% of patients referred for MRI for different diagnosis in a retrospective study of 2,480 MRI scans (19). Normal values vary with age and sex, and the position of the cerebellar tonsils rises with age due to general cerebral atrophy (12). Only a fraction (11%) of our participants with ME/CFS had a normal cerebellar tonsil position well above the McRae line. Symptom onset in our study population was greater in the 25–45 age range, when symptoms of Chiari syndrome usually also first present (20).

Interestingly, a high proportion of our participants with ME/CFS exhibited signs of IH, and the criteria for ME/CFS include many symptoms similar to those of IH, including cognitive dysfunction, headache, dizziness, and pain. We contend that IH symptoms should not exclude patients from being evaluated for and potentially diagnosed with ME/CFS. A connection between ME/CFS and IH has previously been suggested by Higgins 2017 (21). In Higgins' study, 5 out of 20 patients with ME/CFS also had increased CSF pressure, >20 cm H_2O.

Also interesting is that 173 or 76% of participants had concomitant FMS. The prevalence of allodynia was even higher at 96%. This finding, characteristic of widespread sensitization, is a strong argument for CNS engagement in ME/CFS. A shared pathophysiology between ME/CFS, IH, and FMS has also been hypothesized by Hulens (22). Other criteria for FMS are illness of more than 3 months and pain in all four body quadrants. As all participants had a pain duration of more than 6 months, which is a criterion for referral to the clinic, and the majority also fulfilled the criteria of pain distribution, FMS seems to be a very common comorbidity even if that diagnosis only had been given to 25% of the participants prior to admission.

The correlation between the degree of joint hypermobility and the ONSD/ETD ratio as a marker for IH was very weak. There might be unknown confounders, or both IH and joint hypermobility can contribute to ME/CFS symptomatology independently.

Craniocervical obstructions were frequent in our study sample. Most of these were disc bulges and hernias, which were found in 80% of participants who underwent MRI of the cervical spine. These kinds of obstructions are increasingly frequent with increased age and may be asymptomatic. However, our study population was relatively young with a mean age of 45 years. One of the surprisingly few studies on the normal prevalence of craniocervical obstructions is the still often cited work by Boden from 1990, in which 63 asymptomatic volunteers participated (23). Of the 40 participants with age <40 years, four participants or 10% had disc bulging or hernias; of the 23 participants with age >40 years, two participants or 9% had such findings. If we presume that all of our participants without a present MRI scan are free from findings of obstruction of this kind (which gives an underestimate of the true obstruction prevalence in our sample), we still find a significant overrepresentation compared with the groups in Boden's study. The prevalence of cervical hernias or disc bulging in our study with this presumption is 35% with such findings in 28 of altogether 79 participants <40 years of age. In the group >40 years of age, we find such obstructions in 48%, that is, in 72 of altogether 150 participants. Comparing these prevalence's with Boden's study using a Chi-square test shows a significant overrepresentation of craniocervical obstructions in our study, both in the age group <40 years ($p = 0.003$) and in those >40 years ($p = 0.004$).

In the Wakayama Spine Study, a more recent study on spine pathology from 2014, Teraguchi and others studied the prevalence of spine disc degeneration grade 3–4 in the whole spine of 975 Japanese volunteers from the general population (24). The findings in that study correspond well to the craniocervical obstructions we observe as disc bulging or disc hernia. The Wakayama cohort is interesting as also patients with different symptoms were recruited, for example, 25% reported neck pain. It should, therefore, reflect the general population rather than the healthy population. This Wakayama Spine Study makes it possible to also compare prevalence of craniocervical obstructions in both males and females. In ME/CFS, there is an overrepresentation of women, and the relatively small number of men in our study does not justify proper statistical evaluation of differences in prevalence. However, for females and the cohort as a whole, we found a significantly higher proportion of craniocervical obstructions, in particular, among females younger than 50 years of age ($p < 0.01$). In our cohort, 25 participants had no cervical obstructions and 100 had. In the Wakayama study, 367 participants had no cervical obstructions, and 608 had. The difference is significant with $p < 0.01$ using Fisher exact test. See **Table 5**.

Craniocervical obstructions causing changed CSF flow and neuronal dysfunction have been proposed as a possible vehicle to develop ME/CFS symptoms. In a recent study from Johns Hopkins University, three patients with cervical spinal stenosis and ME/CFS who underwent decompressive spine surgery were considerably improved and relieved from ME/CFS symptoms (25). Another common observation in patients with ME/CFS is that they find relief from nausea, vertigo, and pain symptoms in a supine position. This observation prompts the hypothesis that an upright position may alter CSF and blood flow in the craniocervical area due to the weight of the head compressing cervical segments and gravity pulling cerebellar tonsils caudally/into the foramen magnum. This hypothesis is supported by a pilot study by Freeman et al. on 1,200 patients with neck pain in which they found that both cervical spine obstructions and tonsil position were more prominent in MRI exams conducted in the upright position (9). Consequently, in

TABLE 5 | MRI findings of craniocervical obstructions with comparison to the Wakayama spine study by Teraguchi et al. (24).

	Female participants (number of)					Male participants (number of)				
	Our study		Wakayama study			Our study		Wakayama study		
Age	No obstr.	Obstr.	No obstr	Obstr.	*Stat.diff.	No obstr.	Obstr.	n:o	No obstr.	Stat. diff
<50	18	57	63	24	$p < 0.01$	5	3	28	10	n.s
50–59	1	24	59	57	$p < 0.01$	1	4	31	28	n.s
60–69	0	7	72	86	$P < 0.05$	0	3	22	43	n.s
70–79	0	2	48	124	n.s	0	0	17	72	n.s
>79	0	0	17	101	n.s.	0	0	10	63	n.s.
All	19	90	259	392	$p < 0.01$	6	10	108	216	n.s

Statistical difference between groups using Fischer exact test.

a future study, patients with ME/CFS should be examined with upright MRI of the craniocervical area and compared with the standard supine MRI.

Several limitations may be noted in our study. First, our patient cohort may differ from what is seen in other clinics as referral to our clinic requires that patients have severe symptoms indicating ME/CFS. Second, the CCC are inclusive and may not discriminate sufficiently between other disorders, such as idiopathic intracranial hypertension (26). Third, MRI assessments were done by a single radiologist and, thus, not confirmed. However, we made an IRR assessment between the radiologist, a resident physician, and a medical student, and we found good-to-excellent reliability for most assessments. Fourth, we did not perform a direct measurement of IH as this would have required the use of invasive methods. However, measuring ONSD is considered a reliable method for indirectly measuring IH and corresponds to directly measured intracranial pressure (17).

Neuroinflammation of the CNS is a proposed consequence of craniocervical obstructions and IH. This idea was recently raised by articles on ME/CFS and IH (24, 25). Other mechanisms that may cause neuroinflammation in the CNS are also possible. For instance, the "glymphatic system," a functional metabolic waste clearance system that engages the CNS, can contribute to IH, and obstructions or flow disturbances can compromise the glymphatic system (27). Komaroff recently expressed this view of ME/CFS pathophysiology (3). We have no ground to say that cervical obstructions cause neuroinflammation and ME/CFS; however, our observation that craniocervical obstructions were very frequent in our population of patients with ME/CFS prompts a question: Is there a substantial subgroup of patients, worldwide, with ME/CFS for whom findings of craniocervical obstructions are signs of undetected IH?

Findings and symptoms from the head and neck region, shoulder, and arms should not be seen only as common complaints among patients with ME/CFS. Rather, as relevant information for future studies to evaluate a possible correlation between craniocervical obstructions, IH, ME/CFS, and neuroinflammation of the CNS. Future studies may also consider a common pathological pathway between ME/CFS and FMS.

CONCLUSIONS

In this relatively large novel study on symptoms and signs of IH, hypermobility and craniocervical obstructions in patients with ME/CFS we found to have a significant overrepresentation in our cohort compared to the general population. These signs might explain some of the major clinical symptoms and signs of ME/CFS, such as brain fog, fatigue, orthostatic intolerance, PEM, preference for the supine position, widespread pain, CNS neuroinflammation, immunological reactivity, and autoimmunity mechanisms. If our findings are further validated, a paradigm shift in the diagnostic methods and treatments for patients with ME/CFS may occur.

DATA AVAILABILITY STATEMENT

The data from the study are available from the publication date in a de-identified form to other investigators whose proposed use of the data has been approved by an independent review committee and after proposal approval, but should not be spread or used for purposes beyond data confirmation.

ETHICS STATEMENT

The studies involving human participants were reviewed and approved by Swedish Ethical Review Authority (nr. 2019-01566). The patients/participants provided their written informed consent to participate in this study.

AUTHOR CONTRIBUTIONS

Conceptualization was made by BBr and BBe. Methodology was created by BBr, software usage by BBr, validation of results by AM, MF, and BD. Formal analyses were completed by BBr. and RS, investigations made by BBr, AM, MF, and BD, resources arranged by BBr Data curation was performed by BBr. The manuscript was written by BBr and reviewed and edited by BBe. Data were visualized by BD and BB. The project administrator was BBe and BBr was responsible for funding acquisition.

All authors contributed to the article and approved the submitted version.

FUNDING

This research had no external funding and was financed by Bragée Clinics.

ACKNOWLEDGMENTS

We are grateful to our research group PIAF (Pain, Inflammation and Fatigue) for their scientific support, to the Bragée Clinics for their financial support, and to all our Alma Mater, Karolinska Institutet, for their continued involvement. We would like to thank Editage (www.editage.com) for English language editing.

REFERENCES

1. Carruthers BM, Jain AK, De Meirleir KL, Peterson DL, Klimas NG, Lerner AM, et al. Myalgic encephalomyelitis/chronic fatigue syndrome. *J Chronic Fatigue Syndrome.* (2003) 11:7–115. doi: 10.1300/J092v11n01_02
2. Valdez AR, Hancock EE, Adebayo S, Kiernicki DJ, Proskauer D, Attewell JR, et al. Estimating prevalence, demographics, and costs of ME/CFS using large scale medical claims data and machine learning. *Front Pediatr.* (2018) 6:412. doi: 10.3389/fped.2018.00412
3. Komaroff AL. Advances in understanding the pathophysiology of chronic fatigue syndrome. *JAMA*. (2019) 322:499–500. doi: 10.1001/jama.2019.8312
4. Friedberg F, Bateman L, Bested AC, Friedman KJ, Gurwitt A, Jason LA, et al. *ME/CFS: A primer for Clinical Practioners*. New York, NY: International Association for CFS/ME (2014). p. 50.
5. Carruthers BM, van de Sande MI, De Meirleir KL, Klimas NG, Broderick G, Mitchell T, et al. Myalgic encephalomyelitis: international consensus criteria. *J Intern Med.* (2011) 270:327–38. doi: 10.1111/j.1365-2796.2011.02428.x
6. Kumar B, Lenert P. Joint hypermobility syndrome: recognizing a commonly overlooked cause of chronic pain. *Am J Med.* (2017) 130:640–7. doi: 10.1016/j.amjmed.2017.02.013
7. Singh H, McKay M, Baldwin J, Nicholson L, Chan C, Burns J, et al. Beighton scores and cut-offs across the lifespan: cross-sectional study of an Australian population. *Rheumatology.* (2017) 56:1857–64. doi: 10.1093/rheumatology/kex043
8. Wolfe F, Smythe HA, Yunus MB, Bennett RM, Bombardier C, Goldenberg DL, et al. The American College of Rheumatology (1990). Criteria for the classification of fibromyalgia. report of the multicenter criteria committee. *Arthritis Rheum.* (1990) 33:160–72. doi: 10.1007/978-3-642-86812-2_2
9. Freeman MD, Rosa S, Harshfield D, Smith F, Bennett R, Centeno CJ, et al. A case-control study of cerebellar tonsillar ectopia (Chiari) and head/neck trauma (whiplash). *Brain Inj.* (2010) 24:988–94. doi: 10.3109/02699052.2010.490512
10. Henderson FC Sr, Henderson FC Jr, Wilson WA, Mark AS, Koby M. et al. Utility of the clivo-axial angle in assessing brainstem deformity: pilot study and literature review. *Neurosurg Rev.* (2018) 41:149–63. doi: 10.1007/s10143-017-0830-3
11. Malfait F, Francomano C, Byers P, Belmont J, Berglund B, Black J, et al. The 2017 international classification of the Ehlers-Danlos syndromes. *Am J Med Genet C Semin Med Genet.* (2017) 175:8–26. doi: 10.1002/ajmg.c.31552
12. Smith BW, Strahle J, Bapuraj JR, Muraszko KM, Garton HJ, Maher CO. Distribution of cerebellar tonsil position: implications for understanding Chiari malformation. *J Neurosurg.* (2013) 119:812–9. doi: 10.3171/2013.5.JNS121825
13. Vernooij MW, Ikram MA, Tanghe HL, Vincent AJ, Hofman A, Krestin GP, et al. Incidental findings on brain MRI in the general population. *N Engl J Med.* (2007) 357:1821–8. doi: 10.1056/NEJMoa070972
14. Barron DF, Cohen BA, Geraghty MT, Violand R, Rowe PC. Joint hypermobility is more common in children with chronic fatigue syndrome than in healthy controls. *J Pediatr.* (2002) 141:421–5. doi: 10.1067/mpd.2002.127496
15. Henderson FC Sr, Austin C, Benzel E, Bolognese P, Ellenbogen R, Francomano CA et al. Neurological and spinal manifestations of the Ehlers-Danlos syndromes. *Am J Med Genet C Semin Med Genet.* (2017) 175:195–211. doi: 10.1002/ajmg.c.31549
16. Kim DH, Jun JS, Kim R. Measurement of the optic nerve sheath diameter with magnetic resonance imaging and its association with eyeball diameter in healthy adults. *J Clin Neurol.* (2018) 14:345–50. doi: 10.3988/jcn.2018.14.3.345
17. Bekerman I, Sigal T, Kimiagar I, Ben Ely A, Vaiman M. The quantitative evaluation of intracranial pressure by optic nerve sheath diameter/eye diameter CT measurement. *Am J Emerg Med.* (2016) 34:2336–42. doi: 10.1016/j.ajem.2016.08.045
18. Albert AF, Kirkman MA. Clinical and radiological predictors of malignant middle cerebral artery infarction development and outcomes. *J Stroke Cerebrovasc Dis.* (2017) 26:2671–9. doi: 10.1016/j.jstrokecerebrovasdis.2017.06.041
19. Öktem Hea. Prevalence of Chiari type I malformation on cervical magnetic resonance imaging: a retrospective study. *Anatomy*. (2016) 2016:40–5. doi: 10.2399/ana.15.039
20. Fernandez AA, Guerrero AI, Martinez MI, Vazquez ME, Fernandez JB, Chesa i Octavio E, et al. Malformations of the craniocervical junction (Chiari type I and syringomyelia: classification, diagnosis and treatment). *BMC Musculoskelet Disord.* (2009) 10 (Suppl. 1):S1. doi: 10.1186/1471-2474-10-S1-S1
21. Higgins JNP, Pickard JD, Lever AML. Chronic fatigue syndrome and idiopathic intracranial hypertension: different manifestations of the same disorder of intracranial pressure? *Med Hypotheses.* (2017) 105:6–9. doi: 10.1016/j.mehy.2017.06.014
22. Hulens M, Rasschaert R, Vansant G, Stalmans I, Bruyninckx F, Dankaerts W. The link between idiopathic intracranial hypertension, fibromyalgia, and chronic fatigue syndrome: exploration of a shared pathophysiology. *J Pain Res.* (2018) 11:3129–40. doi: 10.2147/JPR.S186878
23. Boden SD, McCowin PR, Davis DO, Dina TS, Mark AS, Wiesel S. Abnormal magnetic-resonance scans of the cervical spine in asymptomatic subjects. A prospective investigation. *J Bone Joint Surg Am.* (1990) 72:1178–84. doi: 10.2106/00004623-199072080-00008
24. Teraguchi M, Yoshimura N, Hashizume H, Muraki S, Yamada H, Minamide A, et al. Prevalence and distribution of intervertebral disc degeneration over the entire spine in a population-based cohort: the Wakayama Spine Study. *Osteoarthritis Cartilage.* (2014) 22:104–10. doi: 10.1016/j.joca.2013.10.019
25. Rowe PC, Marden CL, Heinlein S, Edwards CC, 2nd. Improvement of severe myalgic encephalomyelitis/chronic fatigue syndrome symptoms following surgical treatment of cervical spinal stenosis. *J Transl Med.* (2018). 16:21. doi: 10.1186/s12967-018-1397-7
26. Friedman DI, Liu GT, Digre KB. Revised diagnostic criteria for the pseudotumor cerebri syndrome in adults and children. *Neurology.* (2013) 81:1159–65. doi: 10.1212/WNL.0b013e3182a55f17
27. Bezerra MLS, Ferreira A, de Oliveira-Souza R. Pseudotumor cerebri and glymphatic dysfunction. *Front Neurol.* (2017) 8:734. doi: 10.3389/fneur.2017.00734

Conflict of Interest: The authors declare that the research was conducted in the absence of any commercial or financial relationships that could be construed as a potential conflict of interest.

ORIGINAL RESEARCH
published: 16 October 2020
doi: 10.3389/fneur.2020.503235

Long Longitudinal Tract Lesion Contributes to the Progression of Alzheimer's Disease

Caimei Luo [1,2,3,4], Mengchun Li [1,2,3,4], Ruomeng Qin [1,2,3,4], Haifeng Chen [1,2,3,4], Lili Huang [1,2,3,4], Dan Yang [1,2,3,4], Qing Ye [1,2,3,4], Renyuan Liu [1,2,3,4], Yun Xu [1,2,3,4], Hui Zhao [1,2,3,4] and Feng Bai [1,2,3,4]**

[1] The State Key Laboratory of Pharmaceutical Biotechnology, Department of Neurology, Affiliated Drum Tower Hospital of Medical School, Institute of Brain Science, Nanjing University, Nanjing, China, [2] Jiangsu Key Laboratory for Molecular Medicine, Medical School of Nanjing University, Nanjing, China, [3] Jiangsu Province Stroke Center for Diagnosis and Therapy, Nanjing, China, [4] Nanjing Neuropsychiatry Clinic Medical Center, Nanjing, China

Background: The degenerative pattern of white matter (WM) microstructures during Alzheimer's disease (AD) and its relationship with cognitive function have not yet been clarified. The present research aimed to explore the alterations of the WM microstructure and its impact on amnestic mild cognitive (aMCI) and AD patients. Mechanical learning methods were used to explore the validity of WM microstructure lesions on the classification in AD spectrum disease.

Methods: Neuropsychological data and diffusion tensor imaging (DTI) images were collected from 28 AD subjects, 31 aMCI subjects, and 27 normal controls (NC). Tract-based spatial statistics (TBSS) were used to extract diffusion parameters in WM tracts. We performed ANOVA analysis to compare diffusion parameters and clinical features among the three groups. Partial correlation analysis was used to explore the relationship between diffusion metrics and cognitive functions controlling for age, gender, and years of education. Additionally, we performed the support vector machine (SVM) classification to determine the discriminative ability of DTI metrics in the differentiation of aMCI and AD patients from controls.

Results: As compared to controls or aMCI patients, AD patients displayed widespread WM lesions, including in the inferior longitudinal fasciculus, inferior fronto-occipital fasciculi, and superior longitudinal fasciculus. Significant correlations between fractional anisotropy (FA), mean diffusivity (MD), and radial diffusion (RD) of the long longitudinal tract and memory deficits were found in aMCI and AD groups, respectively. Furthermore, through SVM classification, we found DTI indicators generated by FA and MD parameters can effectively distinguish AD patients from the control group with accuracy rates of up to 89 and 85%, respectively.

Conclusion: The WM microstructure is extensively disrupted in AD patients, and the WM integrity of the long longitudinal tract is closely related to memory, which would hold

Edited by:
Jennifer L. Whitwell,
Mayo Clinic, United States

Reviewed by:
Ying Han,
Capital Medical University, China
Xin Li,
Beijing Normal University, China

***Correspondence:**
Feng Bai
baifeng515@126.com
Hui Zhao
zhaohuigyc2002@163.com

Specialty section:
This article was submitted to Applied Neuroimaging, a section of the journal Frontiers in Neurology

Received: *07 October 2019*
Accepted: *13 August 2020*
Published: *16 October 2020*

Citation:
Luo C, Li M, Qin R, Chen H, Huang L, Yang D, Ye Q, Liu R, Xu Y, Zhao H and Bai F (2020) Long Longitudinal Tract Lesion Contributes to the Progression of Alzheimer's Disease. Front. Neurol. 11:503235. doi: 10.3389/fneur.2020.503235

potential value for monitoring the progression of AD. The method of classification based on SVM and WM damage features may be objectively helpful to the classification of AD diseases.

Keywords: Alzheimer's disease, white matter damage, cognitive impairment, diffusion tensor imaging, support vector machine

INTRODUCTION

Alzheimer's disease (AD) is a chronic neurodegenerative disease characterized by progressive cognitive decline in multiple domains, including memory, language, executive function, and attention. AD accounts for 60–70% of the ∼47.5 million dementia cases worldwide (1), exerting huge distress to patients and their families, as well as an extraordinary financial burden. Amnesic mild cognitive impairment (aMCI) is a prodromal stage of dementia, between normal aging and very early dementia, of which 10–15% progress to AD annually (2). Since there is no cure for AD, there is a great need for monitoring markers in the earlier phase of the disease.

The etiology and pathogenesis of AD are still unsolved. Gray matter neurodegeneration theory has attracted the most attention, particularly the decrease of hippocampal volume (3). Recently, however, there has been an increasing interest in the potential contributions of white matter (WM) integrity damage to the pathogenesis of AD (4, 5). Evidence from the autosomal-dominant AD revealed that WM hyperintensities were a core feature in the process of AD, which can impair cognition either directly, or indirectly by interacting with tau pathology (6, 7). Moreover, the tract-specific WM hyperintensities volume rate was negatively associated with the functional connection in the corresponding connected brain regions (8). The gradual loss of morphological and functional integrity of cortico-cortical pathways [e.g., corpus callosum (CC), inferior fronto-occipital fasciculi (IFOF), superior longitudinal fasciculi (SLF), and inferior longitudinal fasciculi (IFL)] and limbic pathways (e.g., fornix and cingulum) were dominant features accompanied with AD pathogenesis (9). To our knowledge, few studies have investigated the role of cortico-cortical WM integrity on memory processes in patients with aMCI or AD.

Diffusion tensor imaging (DTI) provides an indirect method of detecting a neuroanatomical structure on a microscopic level using water molecules' degree of anisotropy and structural orientation within a voxel (10), which is sensitive to the alterations in the WM structure such as myelin loss, axonal injury, cell death, and edema (11). The parameter of fractional anisotropy (FA) reflects the integrity of the axon. Decreased FA values indicate axonal damage. Mean diffusivity (MD) indicates the rate of molecular diffusion, which increases along with the WM injury (10, 12, 13). Axial diffusion (AxD) reflects the diffusion of water molecules parallel to the axon direction. The radial diffusion (RD) reflects the diffusion of water molecules perpendicular to the axon direction.

Region of interest (ROI) based analysis, voxel-based analysis (VBA), and tract-based spatial statistics (TBSS) are all methods widely used in DTI studies (10). ROI-based methods are highly subjective and only focuses on a certain fiber bundle or a few fiber bundles. Due to requiring a prior assumption, describing the intrinsic WM lesions with ROI-based methods are difficult and may result in poor repeatability. Meanwhile, the VBA method also exhibits some problems, such as registration irregularity and smooth kernel selection (14). Superior to ROI and VBA, TBSS analyzes WM lesions using standard registration algorithms, which do not require prior assumptions, smoothness, or data distribution (14, 15).

The support vector machine (SVM) approach represents a data-driven method for solving classification tasks (16). This approach for neuroimaging data has been widely applied to diagnose individual-level patients. Compared to classifiers based on other methods like decision trees and artificial neural networks, SVM has certain advantages such as high accuracy, avoids less overfitting, and direct geometric interpretation (16). Several studies have used the SVM to classify AD and healthy control based on the features screened from structural MRI (17, 18). The results have shown a high performance with accuracy of up to 92.48%. Until now, few studies have focused on the classification effect based on information from DTI data in the AD spectrum. Therefore, our study aimed to explore the pattern of WM microstructure changes in AD-spectrum patients using the TBSS method. Moreover, SVM was performed to determine the discriminative ability of these DTI metrics in separating aMCI and AD from controls.

MATERIALS AND METHODS

Participants

Overall, 78 right-handed subjects were recruited from the Neurological Department of Nanjing Drum Tower Hospital from September 2016 to December 2018. Among them, 20 subjects were AD patients, 31 subjects were aMCI patients, and 27 subjects were healthy elderly controls. The research protocol received approval from the ethics committees of the Affiliated Drum Tower Hospital of Nanjing University Medical School (clinical trials government identifier: NCT01364246), and each participant provided written informed consent before the experiment. A series of standardized clinical evaluations were arranged, including an interview to obtain medical records, a detailed neuropsychological test battery, a whole-brain 3.0T MRI scan, a general medical examination, and an integrated neurological examination which was implemented by an experienced neurologist (Dr. Zhao).

The clinical diagnosis of aMCI was based on the recommendations of previous studies (19–21), which were as follows: (1) chief complaint of memory impairment, corroborated by the subject and/or an informant; (2) objective impaired memory function documented by an auditory verbal learning test—Huashan 20-min delayed recall (AVLT-DR) score ≤ 1.5 *SD* of age and education adjusted norms; clinical dementia rating scale—sum of the boxes (CDR-SB) score = 0.5 (with a score of at least 0.5 on the memory domain); (3) normal general cognitive functions evaluated by a mini-mental state examination (MMSE) score ≥ 24; (4) preserved basic activities of daily living or minimal impairment in complex instrumental functions; (5) not diagnosed with dementia. Patients with AD met the National Institute of Neurological and Communicative Disorders and Stroke and the Alzheimer's Disease and Related Disorders Association (NINCDS-ADDRA) criteria for probable AD (22). The criteria for NC participants were as follows: (1) no concerns of cognitive impairment; (2) normal in the neurological examination and cerebral MRI scan; (3) MMSE scores ≥ 28, Montreal cognitive assessment (MoCA) scores ≥ 25, CDR scores = 0, and other scores of neuropsychological battery (as described in Part 2.2) within the normal range.

The exclusion criteria applied to all subjects were as follows: (1) vascular cognitive impairment (Hachinski Ischemic Scale score > 4 points), or other types of dementia; (2) depression or other mental disorders, or a history of drug or alcohol addiction; (3) other central nervous system diseases that impact cognitive decline (e.g., epilepsy, Parkinson's disease, or encephalitis) or systemic diseases that interfere with cognitive function (e.g., thyroid dysfunctions, vitamin b12 or folacin deficiency); (4) severe end-stage disease or severe diseases in acute stages; (5) visible WM hyperintensities higher than Fazekas I grade (23); (6) any contraindication for MRI or poor images quality; (7) <6 years of education.

Neuropsychological Evaluation

A standardized neuropsychological test battery was performed by a professional neuropsychologist who was blinded to the MR imaging results. The Chinese version of the MMSE, the Beijing version of MoCA (24), and CDR (25) scores were used for general cognitive screening. Depression was assessed by the Hamilton depression rating scale (HAMD). Daily life ability was assessed by the activities of daily living scale (ADL). Memory was assessed using the AVLT-DR test and auditory verbal learning test recognition (AVLT-R) (20). The animal fluency test (AFT) and Boston naming test (BNT) were used for language domain assessment. Executive function was evaluated using the trail making test B (TMT-B) and the Stroop-C test. Processing speed was assessed using the trail making test A (TMT-A) and the Stroop-B test. The raw scores of AFT, BNT, TMT-B, Stroop-C, TMT-A, and Stroop-B were transformed to a Z standardization value by the following rule: standardized language (Z-lang) = (Z-AFT+Z-BNT)/2; standardized executive function (Z-EF) = (Z-TMT-B+Z-Stroop-C)/2; standardized processing speed scores (Z-proc) = (Z-TMT-A+Z-Stroop-B)/2. Due to severe dementia, some patients in the AD group failed to complete the TMT test within 10 min, which resulted in missing data.

MRI Data Acquisition

Whole-brain MRI scanning was performed on a 3.0 T scanner (Achieva 3.0 T TX, Philips Medical Systems, the Netherlands, equipped with an 8-channel head coil). During scanning, cushions and headphones were used to immobilize the subject's head and reduce scanner noise. The conventional three-dimensional T1-weighted acquisition was performed for anatomical reference, using magnetization-prepared rapid gradient-echo sequence with the following parameters: repetition time (TR)/echo time (TE) = 9.8/4.6 Ms, flip angle (FA) = 8°, in-plane resolution = 1.0 mm^2, field of view (FOV) = 256 × 256 mm, matrix = 256 × 256, and 192 sagittal slices, slice thickness = 1 mm. Diffusion-weighted images were acquired using a spin-echo planar imaging (EPI) sequence (TR/TE = 9,154 /5 ms, FOV = 224 × 224 mm, matrix size 112 × 112, voxel size 2 × 2 × 2 mm^3, slice thickness = 2.5 mm) with both 32-directional diffusion encoding (b = 1,000 s/mm^2 for each direction) and no diffusion encoding (b = 0 s/mm^2). In addition, fluid-attenuated inversion recovery (FLAIR) sequence images were collected to exclude organic physical illness or WM hyperintensity lesions and were obtained with the following parameters: TR/TE = 4,500/344 ms, FA = 90°, matrix = 272 × 272, slice thickness = 1.0 mm, slice number = 200.

Image Preprocessing and TBSS

Before any pre-process procedures, visual inspection was conducted for all images' artifact, signal-noise ratio, and head motion for quality control. The imaging data were preprocessed using the FSL toolbox (http://fsl.fmrib.ox.ac.uk/fsl/fslwiki) (26, 27). Preprocessing steps comprised of the following: (1) NIFTI format images were converted from the DICOM format; (2) corrected for head motion and eddy current distortions using affine registration in Eddy Current Correction; (3) non-brain voxels were extracted using the Brain Extraction Tool (28) (included in the FSL package) with an extraction factor of 0.2 to generate a binary brain mask; (4) voxel-wise diffusion parameters, including FA, MD, RD, and AxD were then calculated using DTIFIT. All individual FA, MD, RD, and AxD images were performed using TBSS in the FMRIB software library (http://fsl.fmrib.ox.ac.uk/fsl/fslwiki/TBSS/UserGuider). Detailed methods were introduced in the article by Smith et al. (14). The main steps were as follows: (1) each individual original FA map was aligned to a target FMRIB58_ FA template in the MNI space using fully non-linear registrations; (2) all co-registered FA maps were averaged to produce a mean FA image and a mean FA skeleton which represents the centers of all tracts common to the group (using a threshold of mean FA at 0.2 to include non-skeleton voxels); (3) individually aligned FA images were projected onto the mean FA skeleton; (4) the resulting skeletonized FA images were used for voxel-wise cross-subject statistical analysis. Diffusivity maps for MD, RD, and AxD were generated by applying the same steps outlined above.

Support Vector Machine-Based Classification

SVM has been extensively applied in disease classification. Generally, the SVM procedure involves three stages: feature selection, classifier training, and predication. SVM starts with the feature selection as the basis for classification to form a high dimensional space. Then SVM conducts the classifier training to construct a hyperplane that optimally separates the classes. Lastly, the classifier is used to predict the class label when a new sample is added to the classifier. The validation testing and training dataset is completely independent. In this study, the SVM analysis was performed based on the

TABLE 1 | Demographic and clinical characteristics of all subjects.

	NC (*n* = 27)	aMCI (*n* = 31)	AD (*n* = 20)	*P*	*Power*
Age (years)	62.30 ± 6.46	66.70 ± 8.90	65.85 ± 9.47	0.113	0.65
Gender (*n*, %)				0.259	
Male	14 (51.9)	10 (32.3)	10 (50.0)		-
Female	13 (48.1)	21 (67.7)	10 (50.0)		-
Education (years)	11.74 ± 2.90	11.55 ± 3.00	9.55 ± 3.79^{a,b}	0.046	0.68
Hypertension	12 (44.4)	12 (38.7)	5 (25.0)	0.385	-
Hyperlipidemia	3 (11.1)	7 (22.6)	1 (5.0)	0.182	-
Diabetes	4 (14.8)	6 (19.4)	0 (0.0)	0.121	-
MMSE (M,IQR)	29 (2)	27 (1)	19.5 (11.25)^{a,b}	<0.001	-
MOCA (M,IQR)	26 (3)	22 (5)^{a}	14 (6.75)^{a,b}	<0.001	-
HAMD	5.67 ± 5.13	5.03 ± 3.97	4.50 ± 3.58	0.653	0.95
ADL (M, IQR)	8 (0)	8 (0)	10.5 (5.75)^{a,b}	<0.001	-
CDR (M, IQR)	0 (0)	0.5 (0)^{a}	1 (1)^{a,b}	<0.001	-
CDR = 0	27 (100)	0	0		-
CDR = 0.5	0	31 (100)	1 (5)		-
CDR = 1	0	0	10 (50)		-
CDR = 2	0	0	5 (25)		–
CDR = 3	0	0	4 (20)		-
AVLT-DR	6.32 ± 1.89	2.23 ± 1.65^{a}	0.65 ± 1.14^{a,b}	<0.001	0.97
AVLT-R	21.33 ± 1.96	17.52 ± 2.56^{a}	11.05 ± 5.78^{a,b}	<0.001	0.99
Z-Lang	0.45 ± 0.46	0.16± 0.76^{a}	−0.85 ± 0.67^{a,b}	<0.001	0.997
Z-Executive	0.7^{η} ± 0.85	0.6^{η} ± 0.76	/	0.271	-
Z-Processing speed	0.4^{η} ± 0.87	0.3^{η}± 0.82	/	0.846	-

Data are represented as mean ± SD or median (IQR) or n (%); a: vs. NC $P < 0.05$; b: vs. aMCI $P < 0.05$; η, data × 10^{-4} equal to original data; Z-Lang, Z standardized language ability; Z-EF, Z standardized executive function; Z-proc, Z standardized processing speed; MMSE, mini-mental state examination; MoCA, Montreal cognitive assessment; CDR, clinical dementia rating; AVLT-DR, auditory verbal learning test delayed recall; AVLT-R, auditory verbal learning test recognition; HAMD, Hamilton depression rating scale; ADL, activities of daily living scale. aMCI, amnestic mild cognitive; AD, Alzheimer's disease; NC, normal control.

TABLE 2 | Significant clusters of FA values among the three groups by TBSS analysis.

Anatomical extent of cluster$^{\#,\&}$	Cluster voxel	NC	aMCI	AD	*P*	*Power*
ATR-L	100	0.342 ± 0.038	0.332 ± 0.056	0.289 ± 0.031^{a,b}	<0.001***	0.994
ATR-R	128	0.348 ± 0.041	0.338 ± 0.043	0.298 ± 0.028^{a,b}	<0.001***	0.972
CST-L	67	0.475 ± 0.034	0.472 ± 0.041	0.433 ± 0.041^{a,b}	0.001***	0.986
CST-R	161	0.482 ± 0.037	0.5 ± 0.048	0.455 ± 0.041^{b}	0.002***	0.967
For ma	598	0.668 ± 0.02	0.661 ± 0.036	0.611 ± 0.025^{a,b}	<0.001***	1.0
For mi	1099	0.55 ± 0.031	0.541 ± 0.036	0.5 ± 0.026^{a,b}	<0.001***	1.0
IFOF-L	295	0.49 ± 0.023	0.486 ± 0.044	0.438 ± 0.022^{a,b}	<0.001***	1.0
IFOF-R	285	0.51 ± 0.03	0.505 ± 0.044	0.454 ± 0.035^{a,b}	<0.001***	1.0
ILF-L	88	0.539 ± 0.034	0.548 ± 0.066	0.481 ± 0.035^{a,b}	<0.001***	1.0
ILF-R	58	0.53 ± 0.037	0.528 ± 0.045	0.479 ± 0.044^{a,b}	<0.001***	0.997
SLF-R	20	0.481 ± 0.038	0.481 ± 0.06	0.448 ± 0.06	0.062	0.845
UF-L	18	0.375 ± 0.035	0.373 ± 0.037	0.346 ± 0.029	0.01	0.778
CC	3401	0.642 ± 0.029	0.629 ± 0.047	0.582 ± 0.039^{a,b}	<0.001***	1.0

$^{\&}$Significant clusters from TBSS results among three groups through a GLM (corrected by threshold-free cluster enhancement, $P < 0.01$); FA values are presented as means ± SD; $^{***}P < 0.05$ after Bonferroni correction. a: vs. NC $P < 0.05$ (Bonferroni correction); b: vs. aMCI $P < 0.05$ (Bonferroni correction); $^{\#}$Anatomical locations were defined from JHU ICBM-DTI-81 white-matter labels and JHU WM tractography atlas. ATR, anterior thalamic radiation; CST, corticospinal tract; For ma, forceps major; For mi, forceps minor; IFOF, inferior fronto-occipital fasciculus; ILF, inferior longitudinal fasciculus; SIF, superior longitudinal fasciculus; UF, uncinate fasciculus; CC, corpus callosum; L, left; R, right; aMCI, amnestic mild cognitive; AD, Alzheimer's disease. NC, normal control; FA, fractional anisotropy.

combined mean FA and mean MD values of clusters which showed significant group differences using the LIBSVM toolkit (https://www.csie.ntu.edu.tw/∼cjlin/libsvm/). Due to the small sample size, we used the leave one out cross-validation (LOOCV) test to evaluate the average discriminant accuracy among the three groups. This strategy provides an optimistic estimation of accuracy since only one subject is left out for testing while the others are used to train the classifier and get the optimal parameters, just as mentioned in Weikai et al.'s research (29, 30). The performance of a classifier can also be quantified using sensitivity, specificity, and the area under the receiver operating characteristic curve (ROC) according to the results of cross-validation.

Statistical Analysis

Voxel-wise statistical analysis of FA, MD, RD, and AxD maps was conducted using randomize (part of FSL toolbox), a non-parametric permutation program inference on statistic maps when the null distribution is ambiguous. A standard general linear model (GLM) design matrix was applied across all subjects to identify the significant regions among three groups with age, gender, and years of education controlled as possible confounding variables. Random permutations were 5000, $P < 0.01$, using threshold-free cluster enhancement (TFCE) for multiple comparison corrections. Mean FA, MD, RD, and AxD values of significant clusters on each tract (anatomical locations of the significant clusters were defined by ICBM-DTI-81 white-matter labels atlas and JHU white-matter tractography atlas) were extracted based on the fslstats command. The following WM tracts were discussed in our present research: anterior thalamic radiation (ATR); corticospinal tract (CST); cingulum of the cingulate gyrus (Ccing); cingulum of the hippocampus (Chippo); forceps major (for ma); forceps minor (for mi); IFOF; IFL; SLF; uncinate fasciculus (UF); superior longitudinal fasciculus-temporal part (SLFt); and CC. Mean FA, MD, RD, and AxD values of each significant cluster were analyzed using ANOVA and *post-hoc* analyses (using the Bonferroni correction).

Statistical analysis of demographic, clinical variables, and neuropsychological scores was all performed using SPSS version 20 (SPSS, Chicago, IL, U.S.A). Continuous variables were tested by one-way ANOVA (LSD for *post-hoc* analysis) or a Kruskal–Wallis test (non-normally distributed variables). Categorical variables were compared using the Chi-squared test or Fisher's exact test. Partial correlation analysis was performed to detect the relationship between diffusion metrics of a cluster which showed significant group differences and the neuropsychological scores in aMCI and AD groups, respectively, controlling for the effect of age, gender, and years of education. Power analysis

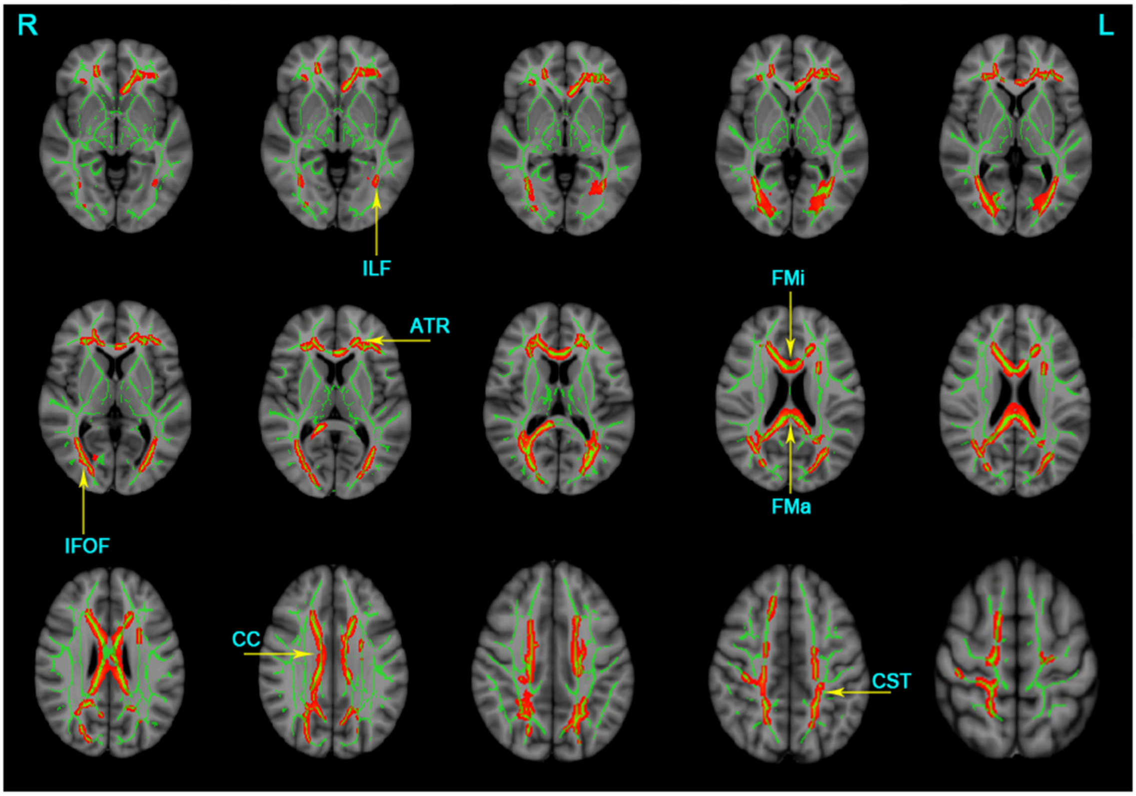

FIGURE 1 | Clusters with decreased FA in AD patients by TBSS analysis. Significant clusters (red, threshold-free cluster enhancement corrected and Bonferroni corrected) in axial views overlaid onto the group averaged FA skeleton (green) and the MNI152 T1 template; ATR, anterior thalamic radiation; CST, corticospinal tract; FMa, forceps major; FMi, forceps minor; IFOF, inferior fronto-occipital fasciculus; ILF, inferior longitudinal fasciculus; CC, corpus callosum; L, left; R, right. FA, fractional anisotropy.

TABLE 3 | Significant clusters of MD values among the three groups by TBSS analysis.

Cluster$^{\#,\&}$	Cluster voxel	NC	aMCI	AD	*P*	*Power*
ATR-L	628	0.819 ± 0.05	0.848 ± 0.085	0.964 ± 0.077^{a,b}	<0.001***	1.0
ATR-R	353	0.811 ± 0.058	0.823 ± 0.084	0.95 ± 0.067^{a,b}	<0.001***	1.0
CST-L	568	0.708 ± 0.02	0.717 ± 0.019	0.753 ± 0.03^{a,b}	<0.001***	1.0
CST-R	126	0.725 ± 0.019	0.736 ± 0.03	0.762 ± 0.038^{a,b}	<0.001***	0.99
Ccing-L	219	0.726 ± 0.023	0.729 ± 0.04	0.781 ± 0.039^{a,b}	<0.001***	1.0
Ccing-R	5	0.703 ± 0.032	0.712 ± 0.051	0.741 ± 0.048	0.014	0.96
For ma	333	0.772 ± 0.029	0.784 ± 0.039	0.83 ± 0.03^{a,b}	<0.001***	0.99
For mi	3358	0.75 ± 0.031	0.772 ± 0.048	0.817 ± 0.04^{a,b}	<0.001***	0.99
IFOF-L	691	0.745 ± 0.026	0.754 ± 0.041	0.8 ± 0.039^{a,b}	<0.001***	0.99
IFOF-R	462	0.731 ± 0.029	0.738 ± 0.039	0.784 ± 0.035^{a,b}	<0.001***	1.0
ILF-L	87	0.818 ± 0.035	0.811 ± 0.035	0.859 ± 0.04^{a,b}	<0.001***	0.995
SLF-L	1278	0.733 ± 0.026	0.732 ± 0.031	0.774 ± 0.027^{a,b}	<0.001***	1.0
SLF-L	428	0.729 ± 0.02	0.729 ± 0.032	0.764 ± 0.03^{a,b}	<0.001***	1.0
UF-L	142	0.737 ± 0.02	0.756 ± 0.032	0.784 ± 0.033^{a,b}	<0.001***	1.0
UF-R	8	0.714 ± 0.026	0.719 ± 0.04	0.75 ± 0.03^{a,b}	<0.001***	0.995
CC	5093	0.832 ± 0.03	0.859 ± 0.062	0.918 ± 0.046^{a,b}	0.001***	1.0

$^{\&}$Significant clusters from TBSS results among three groups through a GLM (corrected by threshold-free cluster enhancement, $P < 0.01$); MD data reflect the original values × 10^{-3} and are presented as means ± SD; $^{***}P < 0.05$ after Bonferroni correction. a: vs. NC $P < 0.05$ (Bonferroni correction); b: vs. aMCI $P < 0.05$ (after Bonferroni correction); $^{\#}$Anatomical locations were defined from JHU ICBM-DTI-81 white-matter labels and JHU WM tractography atlas. ATR, anterior thalamic radiation; CST, corticospinal tract; Ccing, cingulum (cingulate gyrus); For ma, forceps major; For mi, forceps minor; IFOF, inferior fronto-occipital fasciculus; ILF, inferior longitudinal fasciculus; SIF, superior longitudinal fasciculus; UF, uncinate fasciculus; CC: corpus callosum; L, left; R, right; aMCI, amnestic mild cognitive; AD, Alzheimer's disease. NC, normal control, MD, mean diffusivity.

was performed in the G power 3.1.9.2 version. $P < 0.05$ was statistically significant.

RESULTS

Demographics and Clinical Characterizations

No significant differences were found in gender, age, HAMD, hyperlipidemia ratio, hypertension ratio, or diabetes ratio among the three groups (**Table 1**). However, the individuals in the AD group had significantly lower years of education than those in the NC and aMCI groups ($P = 0.046$, **Table 1**). Significant differences in the MMSE, MoCA, ADL, CDR, AVLT-DR, AVLT-R, and Z-lang scores were found among the three groups (for details see **Table 1**). There was no difference in the scores of executive function and processing speed between the NC and aMCI groups.

TBSS Analyses Between Groups and *post-hoc* Analysis

The TBSS analyses revealed widespread WM microstructure changes among the three groups. For reduced FA, the anatomical locations and clusters voxel were listed in **Table 2**, including the bilateral ATR, CST, IFOF, ILF, and unilateral for ma, for mi, right SLF, left UF, and CC. For each subject, the mean FA values across all voxels in each significant cluster were computed for further *post-hoc* analysis. Compared to the NC and aMCI groups, the AD group presented decreased FA values in the bilateral ATR, IFOF, ILF, and unilateral left CST, for ma, for mi, and CC (Bonferroni correction, $P < 0.05$) (**Figure 1**). No significant differences in FA values were found between the NC and aMCI groups.

The significant clusters of MD values among the three groups were listed as follows: the bilateral ATR, CST, Ccing, IFOF, SLF, UF, and unilateral for ma, for mi, CC, and left ILF (**Table 3**). In contrast to the NC group, the AD group displayed increased MD in the bilateral ATR, CST, IFOF, SLF, UF, and unilateral for ma, for mi, CC, left ILF, and left Ccing (Bonferroni correction, $P < 0.05$) (**Figure 2**). No significant changes in MD values were found in aMCI and NC.

Multiple tracts were identified where elevated RD reached significant levels in AD patients, including the bilateral ATR, CST, IFOF, ILF, SLF, and for ma, for mi, and left Ccing (Bonferroni correction, $P < 0.05$). Compared with the NC group, significant elevated RD values were found (**Table 4**, **Figure 3**) in the tract of the right CST, right IFOF, right ILF, and for mi in the aMCI group. Likewise, significant elevated AxD values were identified (**Table 5**, **Figure 3**) in the bilateral ATR, ILF, SLF, and left CST, left IFOF, right UF, for ma, and for mi. As for AxD value, there was no difference between the aMCI and NC groups.

Correlation Between Cognitive Domains and Diffusion Metrics in the aMCI or AD Group

For the aMCI group, significant correlations were found between the mean FA value of ROI and AVLT-DR scores in the following tracts: left IFOF ($r = 0.42$, $P = 0.024$, **Figure 4A**), right IFOF ($r = 0.39$, $P = 0.035$, **Figure 4B**), and left ILF ($r = 0.45$, $P = 0.014$,

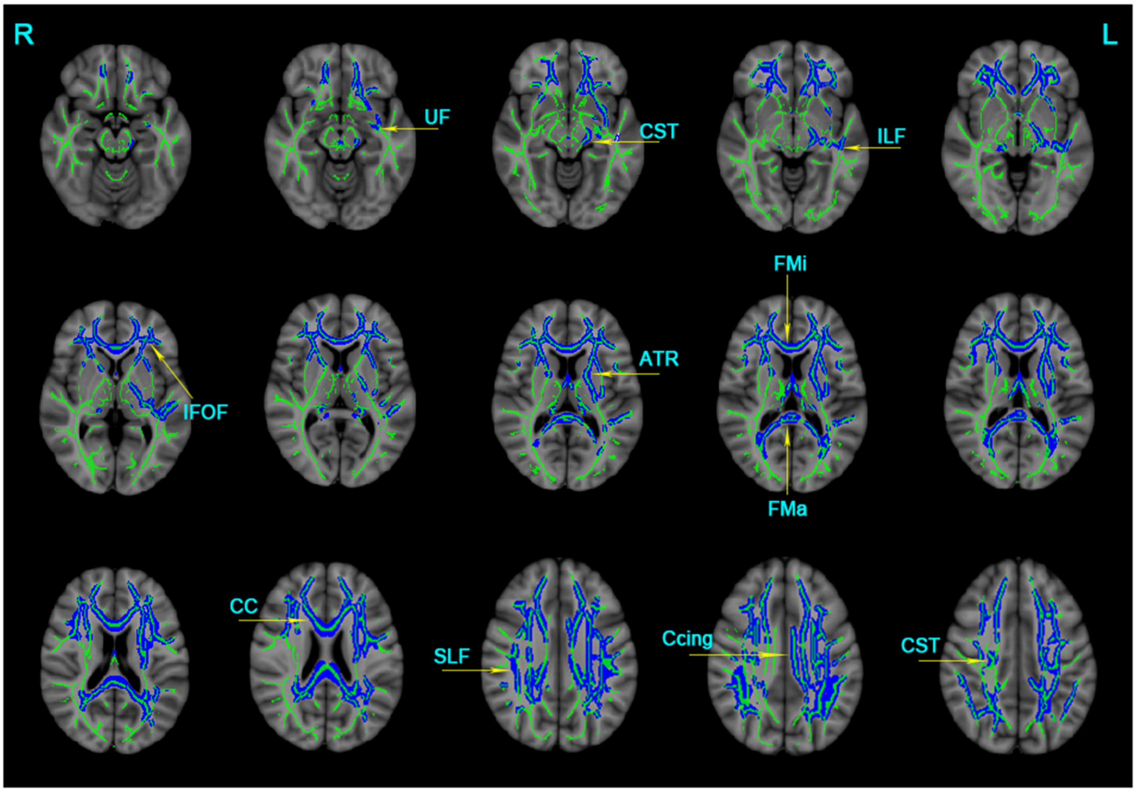

FIGURE 2 | Clusters with increased MD in AD patients by TBSS analysis. Significant clusters (blue, threshold-free cluster enhancement corrected and Bonferroni corrected) in axial views overlaid onto the averaged MD skeleton of all participants (green) and the MNI152 T1 template; ATR, anterior thalamic radiation; CST: corticospinal tract; Ccing: cingulum (cingulate gyrus); FMa: forceps major; FMi: forceps minor; IFOF, inferior fronto-occipital fasciculus; ILF, inferior longitudinal fasciculus; SIF, superior longitudinal fasciculus; UF, uncinate fasciculus; CC, corpus callosum; L: left; R: right; MD, mean diffusivity.

TABLE 4 | Significant clusters of RD values among three groups by TBSS analysis.

Cluster$^{\#,\&}$	Cluster voxel	NC	aMCI	AD	*P*	*Power*
ATR-L	523	0.649 ± 0.053	0.68 ± 0.093	0.802 ± 0.077^{a,b}	<0.001***	1.0
ATR-R	288	0.646 ± 0.066	0.668 ± 0.093	0.807 ± 0.068^{a,b}	<0.001***	1.0
CST-L	646	0.467 ± 0.025	0.476 ± 0.025^{a}	0.514 ± 0.035^{a,b}	<0.001***	1.0
CST-R	311	0.519 ± 0.027	0.525 ± 0.035	0.56 ± 0.036^{a,b}	<0.001***	0.999
Ccing-L	226	0.446 ± 0.034	0.452 ± 0.044	0.514 ± 0.054^{a,b}	<0.001***	1.0
Ccing-R	21	0.5 ± 0.039	0.518 ± 0.043	0.548 ± 0.064^{a,b}	0.005	0.965
For ma	621	0.413 ± 0.025	0.424 ± 0.045	0.481 ± 0.038^{a,b}	<0.001***	1.0
For mi	3254	0.512 ± 0.032	0.531 ± 0.049^{a}	0.579 ± 0.041^{a,b}	<0.001***	1.0
IFOF-L	705	0.545 ± 0.027	0.55 ± 0.047	0.604 ± 0.039^{a,b}	<0.001***	1.0
IFOF-R	664	0.544 ± 0.028	0.551 ± 0.044^{a}	0.602 ± 0.035^{a,b}	<0.001***	1.0
ILF-L	126	0.533 ± 0.03	0.527 ± 0.058	0.588 ± 0.05^{a,b}	<0.001***	1.0
ILF-R	44	0.511 ± 0.03	0.511 ± 0.042^{a}	0.552 ± 0.045^{a,b}	0.001***	0.998
SLF-L	653	0.547 ± 0.031	0.538 ± 0.031	0.58 ± 0.033^{a,b}	<0.001***	0.993
SLF-L	187	0.531 ± 0.031	0.53 ± 0.04	0.572 ± 0.039^{a,b}	<0.001***	0.997

$^{\&}$Significant clusters from TBSS results among three groups through a GLM (corrected by threshold-free cluster enhancement, $P < 0.01$); RD data equal to the original values × 10^3 and are presented as means ± SD; $^{***}P < 0.05$ after Bonferroni correction. a: vs. NC $P < 0.05$; b: vs. aMCI $P < 0.05$; $^{\#}$Anatomical locations were defined from the JHU WM tractography atlas. ATR, anterior thalamic radiation; CST, corticospinal tract; Ccing, cingulum (cingulate gyrus); For ma, forceps major; For mi, forceps minor; IFOF, inferior fronto-occipital fasciculus; ILF, inferior longitudinal fasciculus; SIF, superior longitudinal fasciculus; L, left; R, right; aMCI, amnestic mild cognitive; AD, Alzheimer's disease. NC, normal control, RD, radial diffusion.

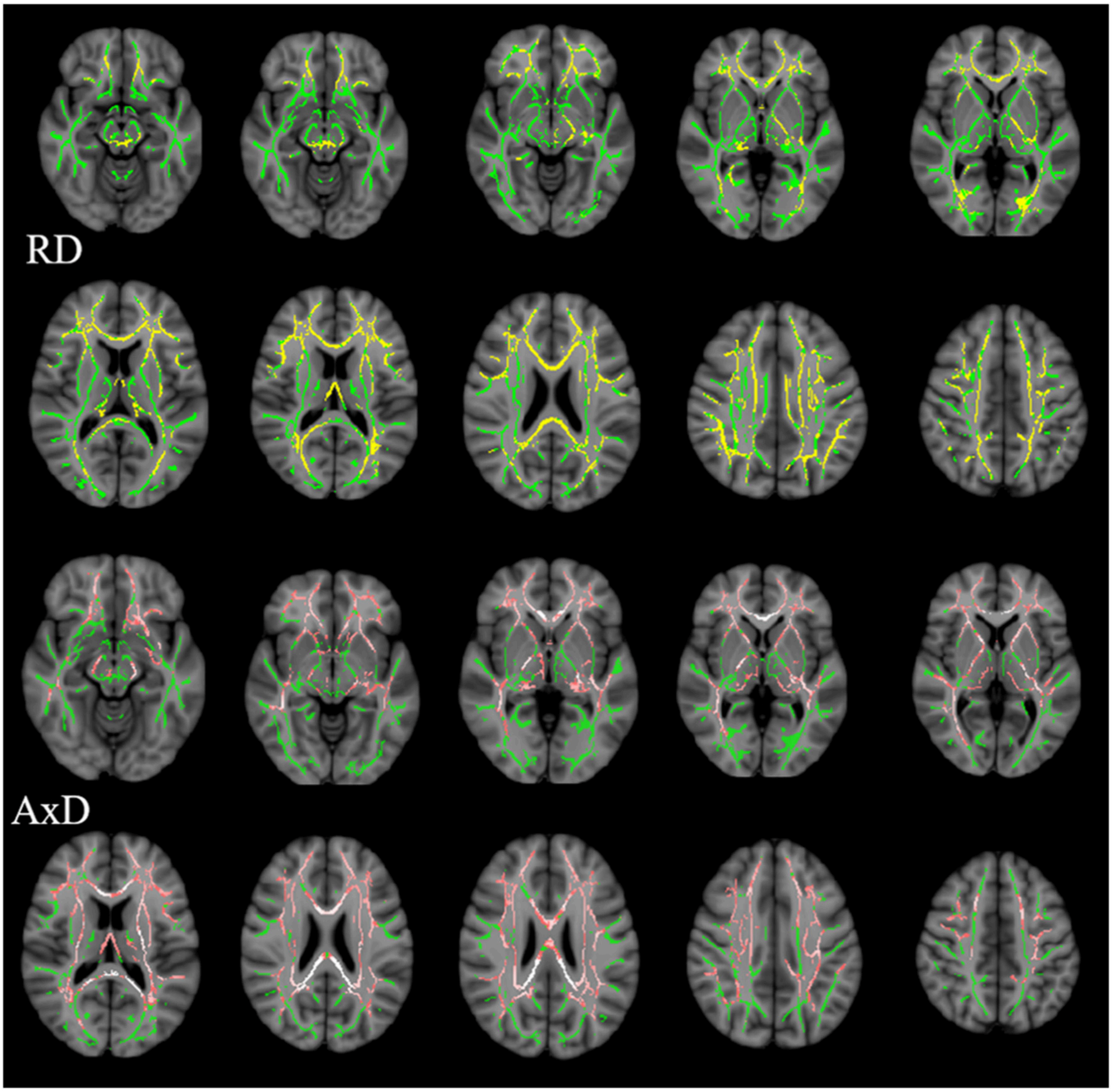

FIGURE 3 | Clusters with increased RD/AxD in AD patients in TBSS analysis. Significant clusters (significant RD clusters are in yellow, significant AxD clusters are in pink, threshold-free cluster enhancement corrected and Bonferroni corrected) in axial views overlaid onto the averaged FA skeleton of all participants (green) and the MNI152 T1 template; RD, radial diffusion; AxD, axial diffusion.

Figure 4C). The mean MD value of ROI in the right Ccing ($r = -0.48$, $P = 0.006$, **Figure 4E**) and right SLF ($r = -0.37$, $P = 0.039$, **Figure 4F**) was negatively associated with the AVLT-DR scores. The average RD value of ROI in the left ILF was negatively correlated with the AVLT-DR scores ($r = -0.438$, $P = 0.02$, **Figure 4D**) and language function ($r = -0.414$, $P = 0.028$ **Figure 4G**). Moreover, the left ILF FA value had a negative correlation with the AVLT-DR scores in the AD group ($r = -0.54$, $P = 0.0159$, **Figure 4H**). It is worth pointing out that the correlations all listed above were not able to survive Bonferroni correction. No significant correlations were observed between other cognitive domains and DTI metrics in both the aMCI and AD groups.

DTI Metrics Separate AD Patients From Other Participants by SVM Classification

The results of the SVM classification demonstrated the discriminative power of disrupted diffusion metrics in the differentiation of AD patients from the other two groups (**Figure 5**). The disrupted FA value exhibited an area under curve (AUC) of 0.94 (accuracy 89%, sensitivity 85%, specificity 93%, **Figure 5A**) for discriminating AD patients from controls, and an AUC of 0.77 (accuracy 69%, sensitivity 70%, specificity 68%, **Figure 5B**) for discrimination between AD and aMCI. The disrupted MD value showed an AUC of 0.94 (accuracy 85%, sensitivity 85%, specificity 85%, **Figure 5C**) for discrimination between AD and controls, and an AUC value of 0.78

TABLE 5 | Significant clusters of AxD values among three groups by TBSS analysis.

Anatomical extent of cluster$^{\#,\&}$	**Cluster voxel**	**NC**	**aMCI**	**AD**	***P***	***Power***
ATR-L	748	1.21 ± 0.058	1.236 ± 0.092	1.361 ± 0.075^{a,b}	<0.001***	1.0
ATR-R	498	1.202 ± 0.068	1.21 ± 0.101	1.346 ± 0.11^{a,b}	<0.001***	1.0
CST-L	398	1.199 ± 0.035	1.229 ± 0.058	1.287 ± 0.061^{a,b}	<0.001***	1.0
CST-R	362	1.185 ± 0.032	1.208 ± 0.06	1.213 ± 0.034^{a,b}	0.084	0.84
For ma	197	1.666 ± 0.066	1.686 ± 0.08	1.747 ± 0.073^{a,b}	0.001***	0.971
For mi	2430	1.243 ± 0.042	1.276 ± 0.057	1.325 ± 0.042^{a,b}	<0.001***	1.0
IFOF-L	646	1.141 ± 0.028	1.151 ± 0.048	1.206 ± 0.037^{a,b}	<0.001***	1.0
IFOF-R	781	1.238 ± 0.034	1.21 ± 0.056	1.207 ± 0.054^{a,b}	0.053	0.898
ILF-L	60	1.327 ± 0.046	1.309 ± 0.058	1.375 ± 0.056^{a,b}	<0.001***	0.996
ILF-R	64	1.384 ± 0.055	1.329 ± 0.091	1.296 ± 0.084^{a,b}	0.001***	0.999
SLF-R	1080	1.116 ± 0.037	1.138 ± 0.048	1.212 ± 0.037^{a,b}	<0.001***	1.0
SLF-L	551	1.122 ± 0.032	1.139 ± 0.054	1.195 ± 0.04^{a,b}	<0.001***	1.0
UF-L	172	1.2 ± 0.038	1.227 ± 0.042	1.27 ± 0.052^{a,b}	<0.001***	1.0

$^{\&}$Significant clusters from TBSS results among three groups through a GLM (corrected by threshold-free cluster enhancement, $P < 0.01$); AxD data equal to the original values × 10^3 and are presented as means ± SD; $^{***}P < 0.05$ after Bonferroni correction. a: vs. NC $P < 0.05$; b: vs. aMCI $P < 0.05$; $^{\#}$Anatomical locations were defined from the JHU WM tractography atlas. ATR, anterior thalamic radiation; CST, corticospinal tract; Ccing, cingulum (cingulate gyrus); For ma, forceps major; For mi, forceps minor; IFOF, inferior fronto-occipital fasciculus; ILF, inferior longitudinal fasciculus; SIF, superior longitudinal fasciculus; L, left; R, right; aMCI, amnestic mild cognitive; AD, Alzheimer's disease. NC, normal control, AxD, axial diffusion.

(accuracy 73%, sensitivity 65%, specificity 78%, **Figure 5D**) for discrimination between AD and aMCI. It should be noted that the identifying accuracy of aMCI from control participants was lower than 50% for both the FA and MD value.

DISCUSSION

This current study investigated the potential roles of DTI metrics in the discriminative ability of AD-spectrum patients. Using TBSS and SVM classification approaches, three observations were made: (i) limbic association tracts, cortico-cortical, interhemispheric, and corticospinal tracts were widely damaged in AD patients; (ii) the long longitudinal tracts (including IFOF, ILF, and SLF in our study) are closely related to memory function in aMCI or AD patients. (iii) DTI metrics of the WM microstructure allowed for the classification of these samples, indicating their potential role as "trait" neuroimaging markers for monitoring the progression of AD.

Relative to normal elderly adults, AD patients displayed decreased FA values and increased MD/RD/AxD values in widespread brain regions, including temporoparietal regions and the fronto-parietal cortex. The aMCI group showed a tendency topographic concordant with the AD group. Previous DTI studies have demonstrated that WM alterations in clinical AD spectrum disease were initially localized in the medial temporal limbic associated tracts, then prominently spread to the temporal and parietal, and to a lesser extent, the frontal lobes which was associated with WM as the disease progressed (31–33). The pattern of WM change is consistent with the pathology of AD which primarily involves the temporal lobe. In the present study, the WM integrity of AD patients decreased in the bilaterally limbic tracts (UF and Ccing), which were in line with previous literatures (34, 35). The UF is a WM tract connecting the anterior part of the temporal lobe with the frontal lobe which is associated with episodic memory. A 3-years follow-up research considered WM abnormality in UF as a potential indicator of the conversion from aMCI to AD (36). The cingulum occupying the central position of the papez circuit is assumed to be vital for normal memory functions (37). UF and cingulum tract damage would lead to memory decline. In addition, impaired CC was also observed in the dementia group. CC is the main connectivity pathway between hemispheres. Any neurodegenerative process involving the cerebral WM may have an impact on the diffusivity of CC (31). Our findings of destruction in the IFOF, ILF, and SLF in the aMCI and AD groups were consistent with previous ROI-based and voxel-based DTI studies, which showed damage of the WM regions outside the medial temporal lobe (MTL) network in AD patients (34). Our results supported the hypothesis that AD had a disconnection process (38).

There are many theories about the underlying pathophysiology of WM damage (39). Previous studies observed Wallerian degeneration secondary to neuronal damage in the AD brains postmortem (40). Pathological vascular deposition of amyloid protein β (Aβ) might play a role in the microvascular alterations and WM lesions in AD through neuroinflammation (39–41). A large body of literature on prior DTI work has shown neurodegenerative changes of brain WM in aMCI when compared to healthy controls (42–44), typically in the posterior cingulate gyrus and hippocampus (45, 46). In the present study, we failed to observe cingulate gyrus and hippocampus diffusion metric differences in the aMCI subjects. Nonetheless, the mean RD value in ROI of the for mi, right IFOF, and left ILF have shown significant differences in the aMCI group when compared with normal control. It might be due to the fact that the patients in our cohort are in the extremely early stage of aMCI, and the cognitive impairment was relatively slight.

When considering the relation between cognitive domains and DTI metrics, the scores of memory performance revealed significant correlations with the FA, MD, and RD index in certain specific fiber bundles in the present aMCI or AD group.

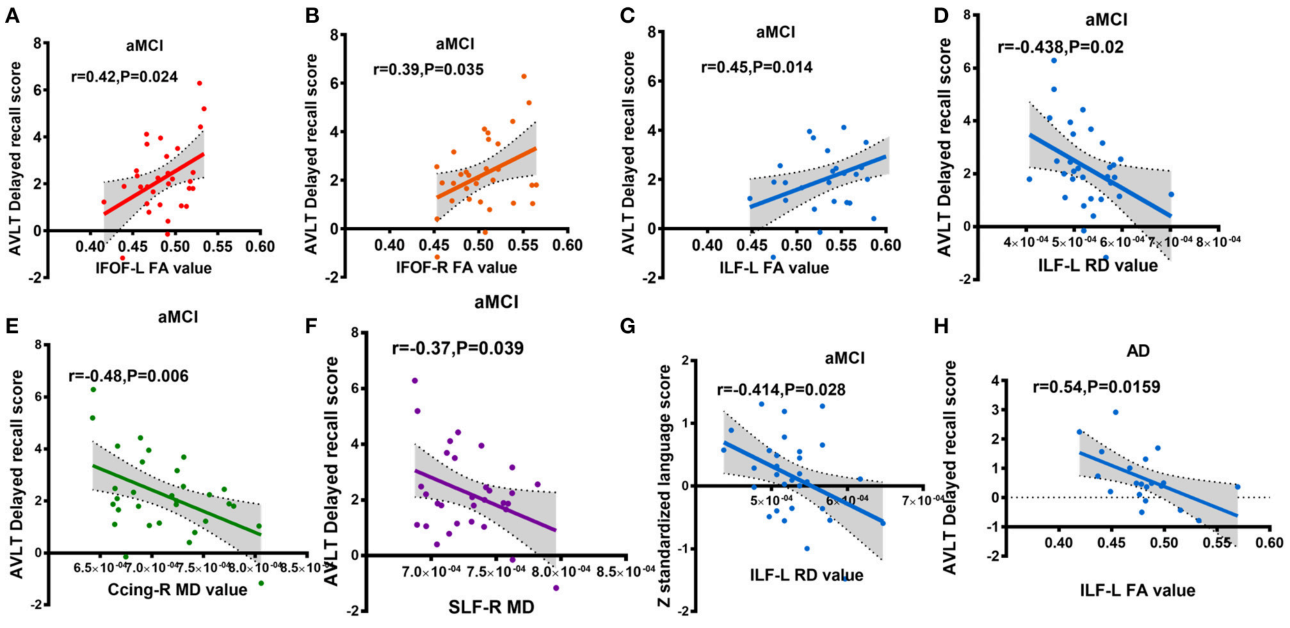

FIGURE 4 | Partial correlations between cognitive scores and altered diffusion value, adjusted for years of education, age, and gender (A-G: aMCI group; H: AD group); **(A)** correlation between IFOF-L FA value and AVLT delayed recall score; **(B)** correlation between IFOF-R FA value and AVLT delayed recall score; **(C)** correlation between ILF-L FA value and AVLT delayed recall score; **(D)** correlation between ILF-L RD value and AVLT delayed recall score; **(E)** correlation between Ccing-R MD value and AVLT delayed recall score; **(F)** correlation between SLF-R MD value and AVLT delayed recall score; **(G)** correlation between ILF-L RD value and z standardized language AVLT delayed recall score; **(H)** correlation between ILF-L FA value and AVLT delayed recall score. Ccing, cingulum (cingulategyrus); IFOF, inferior fronto-occipital fasciculus; ILF, inferior longitudinal fasciculus; SIF, superior longitudinal fasciculus; L, left; R, right. FA, fractional anisotropy; MD, mean diffusivity; RD, radial diffusion aMCI, amnestic mild cognitive; AD, Alzheimer's disease; AVLT-DR, auditory verbal learning test delayed recall. Different colors represent different fibers.

Recent research has shown that associations between the WM microstructure and memory or executive function were evident across widespread regions of the brain in a mixed sample of AD and healthy elderly subjects (47). However, no significant linear relationship between the degree of WM disruption and the level of cognitive function (memory and executive abilities) were found within either the AD or healthy older adult group (47). In our study within the aMCI group, AVLT-DR scores were positively related to the mean FA value of significant clusters in the bilateral IFOF and left ILF; and negatively related to the mean MD value of significant clusters in the right Ccing and right SLF. The IFOF served as a direct connection from the extra-striata occipital cortex to the anterior temporal lobe, playing an important role in visuospatial processing, object recognition, and memory (46). Previous tractography studies in aMCI and AD have shown diffusion abnormalities in the IFOF (34, 48). We further confirmed its close relationship to memory function in the preclinical phase of dementia. Meanwhile, the relationship between the IFOF, the cingulum tracts, and memory performance indicated that memory function depends on both the integrity of MTL structures and their connectivity with temporal, parietal, and frontal lobe regions. On the contrary, the FA value in the left ILF was negatively related to the AVLT-DR scores in the AD group. Namely, some subjects with higher FA values suffered from poorer memory function. It could be the results of dispersed WM impairment and gray matter atrophy in the AD group.

MTL substructures are the earliest regions affected by AD pathology, mainly amyloid deposition, and neurofibrillary tangle tau pathology. Anatomically, WM degeneration in AD follows the topographic progression of cortical AD pathology (49, 50). As mentioned above, AD pathological invasion was initially localized in MTL, and then gradually spread to the temporal, parietal, and frontal lobes. In the current study, the early stage of the aMCI group showed WM disruption in the right IFOF and left ILF as reflected by the RD property. While in the dementia stage, more extensive and severe white matter damage was observed. IFOF has complex intrinsic projections of the brain, including extensive cortical termination territories within the middle and superior frontal, middle and posterior temporal lobes, superior parietal, and angular gyri (51, 52). This means that the diffusion abnormalities of IFOF could influence the structural connectivity architecture among the MTL, the frontal lobe, and the parietal lobe (53). Besides, the ILF also has projections involving the MTL (54). Therefore, we speculated that in the early stages, long fibers pathway damage could indirectly affect the MTL connectivity, which can be used to explain early memory loss. The mediation role of long longitudinal tract alterations during the progression of AD needs to be investigated in more large-scale cohorts.

SVM provides great potential for future artificial intelligence aided diagnosis, and has been increasingly implemented in various classification problems (49). For instance, SVM successfully classified multiple sclerosis patients from healthy

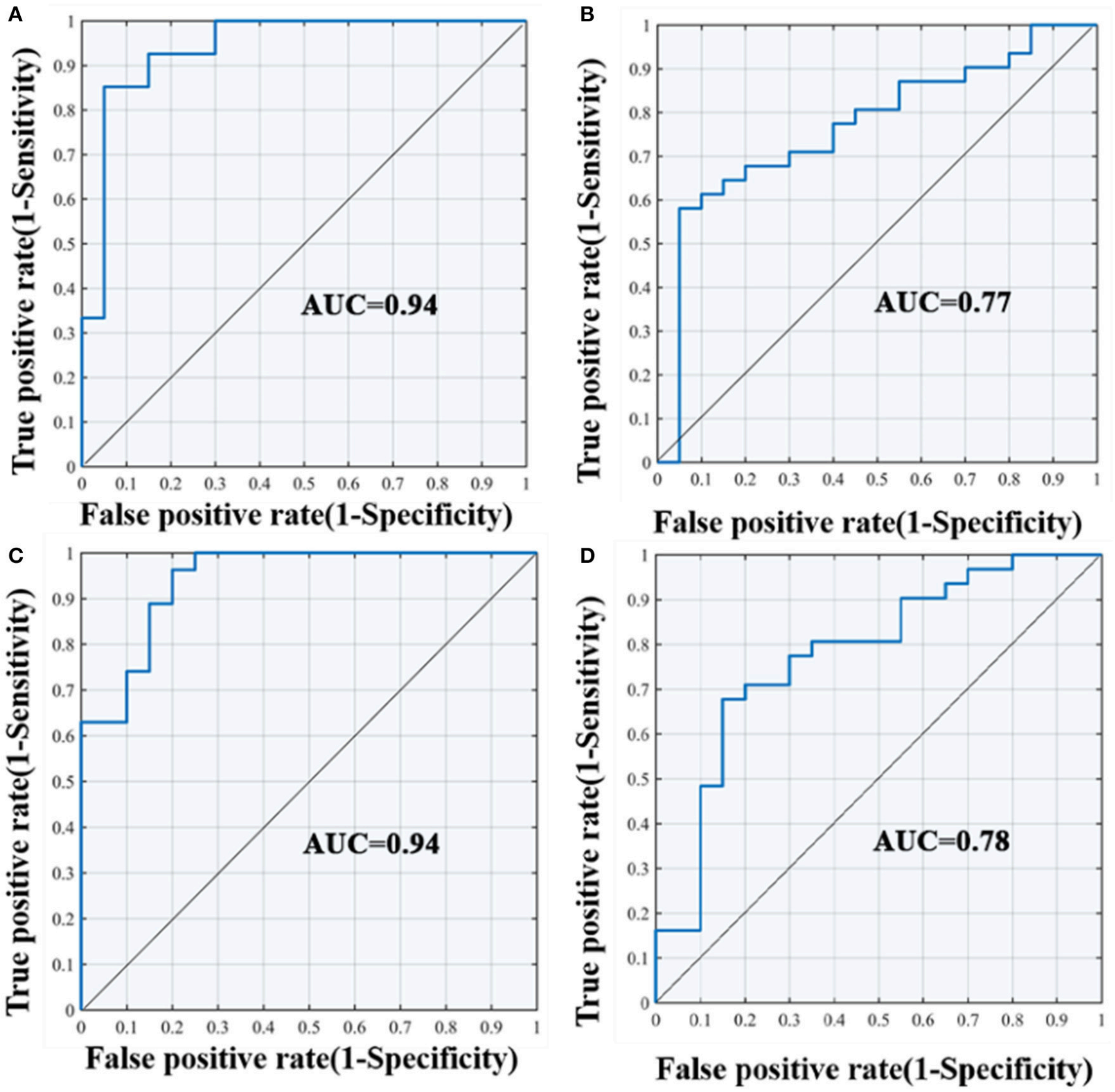

FIGURE 5 | ROC curves of the SVM classification between groups. **(A)** differentiate the AD and NC group according to FA value; **(B)** differentiate the AD and aMCI group according to FA value; **(C)** differentiate the AD and NC group according to MD value; **(D)** differentiate the AD and aMCI group according to MD value; AUC, area under curve; SVM, support vector machine; ROC, receiver operating characteristic curve.

controls with accuracies as high as 89% by combined DTI and functional data (50). Similarly, we revealed that combining disrupted diffusion metrics and SVM classification, the accuracy of classification was higher than 85% in distinguishing AD patients from controls, which shows promise comparable with previous brain microstructure studies to predict progression (55, 56). A moderate discernment was observed between the AD patients and aMCI with the accuracy of 69 and 73%. We did fail to distinguish with high accuracy (lower than 50%) between aMCI patients with the NC. This could be due to the little difference between cognitive levels between both groups. It may also be due to insufficient sample size which affects the classification efficiency. These findings shed light on the potential utility of brain WM microstructural-based markers combined with SVM classification for the individual prediction of disease progression, which may provide a novel avenue into the early diagnosis of AD.

Several limitations of the study should be considered. Firstly, our small sample may limit the statistical power of the differences of WM integrity between groups. Replication in an independent and larger cohort is necessary. Secondly, our diagnosis of aMCI was purely based on clinical symptoms. The sample would be less heterogeneous if biomarkers were added into the inclusion criteria. Thirdly, our research mainly focused on WM microstructure alteration. Future research should investigate the association between WM alterations, gray matter atrophy, metabolic function changes, and pathological indicators to offer a comprehensive insight into the pathologic basis of WM neurodegeneration.

The original intention of this study was to analyze the integrity of the whole brain WM in patients on the AD spectrum and hoped that the machine learning classification could suitably classify the disease according to the characteristics of WM damage. We initially explored the role of mechanical classification in assisting clinical diagnosis of AD diseases to make up for the drawbacks of subjectivity in assessment by the artificial cognition scale and to compensate for the shortcomings of being easily affected by education level and cultural background. This study found that consistent with previous reports, AD patients have extensive WM damage. Long connective fibers lesions are obviously associated with memory deficiency. The effect of mechanical classification in the early stage of the disease is not very satisfactory, but it is very favorable in the AD stage.

CONCLUSION

The WM microstructure is extensively disrupted in AD. An impaired long longitudinal tract (including IFOF, ILF, and SLF) is closely related to memory deficits. DTI metrics of the brain WM microstructure may hold potential value for the diagnosis of AD as an imaging biomarker. The classification effect of SVM in the early stages of AD disease needs to be further exploration.

DATA AVAILABILITY STATEMENT

The datasets generated for this study are available on request to the corresponding author.

ETHICS STATEMENT

The research protocol received approval from ethics committee of the Affiliated Drum Tower Hospital of Nanjing University Medical School (clinical trials government identifier: NCT01364246) and each participant provided written informed consent prior to any experimental procedures.

AUTHOR CONTRIBUTIONS

HZ and FB designed the study, collected the data, and edited the manuscript. YX designed the study and edited the manuscript. CL collected the data, wrote and edited the manuscript, and performed the statistics. RQ wrote and edited the manuscript. ML, DY, LH, and RL collected the data. HC and QY validated the statistics. All authors contributed to the article and approved the submitted version.

FUNDING

This work was supported partly by grants from the National Natural Science Foundation of China (No. 81822013; 81630028; 81671665), the Jiangsu Provincial Key Medical Talents (No. ZDRCA2016085), the Key Research and Development Program of Jiangsu Province of China (BE2016610), the National Key Research and Development Program of China (2016YFC1300500-504), and Jiangsu Province Key Medical Discipline (ZDXKA2016020).

REFERENCES

1. Burns A, Iliffe S. Alzheimer's disease. *BMJ.* (2009) 338:b158. doi: 10.1136/bmj.b158
2. DeCarli C. Mild cognitive impairment: prevalence, prognosis, aetiology, and treatment. *Lancet Neurol.* (2003) 2:15–21. doi: 10.1016/S1474-4422(03)00262-X
3. Cash DM, Rohrer JD, Ryan NS, Ourselin S, Fox NC. Imaging endpoints for clinical trials in Alzheimer's disease. *Alzheimer Res Ther.* (2014) 6:87. doi: 10.1186/s13195-014-0087-9
4. Phillips OR, Joshi SH, Piras F, Orfei MD, Iorio M, Narr KL, et al. The superficial white matter in Alzheimer's disease. *Hum Brain Mapp.* (2016) 37:1321–34. doi: 10.1002/hbm.23105
5. Sachdev PS, Zhuang L, Braidy N, Wen W. Is Alzheimer's a disease of the white matter? *Curr Opin Psychiatry.* (2013) 26:244–51. doi: 10.1097/YCO.0b013e32835ed6e8
6. Lee S, Viqar F, Zimmerman ME, Narkhede A, Tosto G, Benzinger TL, et al. White matter hyperintensities are a core feature of Alzheimer's disease: evidence from the dominantly inherited Alzheimer network. *Ann Neurol.* (2016) 79:929–39. doi: 10.1002/ana.24647
7. Tosto G, Zimmerman ME, Hamilton JL, Carmichael OT, Brickman AM. The effect of white matter hyperintensities on neurodegeneration in mild cognitive impairment. *Alzheimers Dement.* (2015) 11:1510–9. doi: 10.1016/j.jalz.2015.05.014
8. Taylor ANW, Kambeitz-Ilankovic L, Gesierich B, Simon-Vermot L, Franzmeier N, Araque Caballero MÁ, et al. Tract-specific white matter hyperintensities disrupt neural network function in Alzheimer's disease. *Alzheimer Dement.* (2017) 13:225–35. doi: 10.1016/j.jalz.2016.06.2358
9. Delbeuck X, van der Linden M, Collette F. Alzheimer's disease as a disconnection syndrome? *Neuropsychol Rev.* (2003) 13:79–92. doi: 10.1023/A:1023832305702
10. Ranzenberger LR, Snyder T. *Diffusion Tensor Imaging. StatPearls*. Treasure Island, FL: StatPearls Publishing (2019).
11. Franzino MA, Geren JJ, Meiman GL. Group discussion among the terminally ill. *Int J Group Psychother.* (1976) 26:43–8. doi: 10.1080/00207284.1976.11491315
12. Alves GS, Oertel Knöchel V, Knöchel C, Carvalho AF, Pantel J, Engelhardt E, et al. Integrating retrogenesis theory to Alzheimer's disease pathology: insight from DTI-TBSS investigation of the white matter microstructural integrity. *BioMed Res Int.* (2015) 2015:291658. doi: 10.1155/2015/291658
13. Filippi M, Agosta F. Diffusion tensor imaging and functional MRI. *Handb Clin Neurol.* (2016) 136:1065–87. doi: 10.1016/B978-0-444-53486-6.00056-9
14. Smith SM, Jenkinson M, Johansen-Berg H, Rueckert D, Nichols TE, Mackay CE, et al. Tract-based spatial statistics: voxelwise analysis of multi-subject diffusion data. *NeuroImage.* (2006) 31:1487–505. doi: 10.1016/j.neuroimage.2006.02.024
15. Acosta-Cabronero J, Nestor PJ. Diffusion tensor imaging in Alzheimer's disease: insights into the limbic-diencephalic network and methodological considerations. *Front Aging Neurosci.* (2014) 6:266. doi: 10.3389/fnagi.2014.00266
16. Yang ZR. Biological applications of support vector machines. *Brief Bioinform.* (2004) 5:328–38. doi: 10.1093/bib/5.4.328
17. Beheshti I, Demirel H, Farokhian F, Yang C, Matsuda H, Alzheimer's Disease Neuroimaging Initiative. Structural MRI-based detection of Alzheimer's disease using feature ranking and classification error. *Comput Methods Programs Biomed*. (2016) 137:177–93. doi: 10.1016/j.cmpb.2016.09.019
18. Beheshti I, Demirel H, Matsuda H, Alzheimer's Disease Neuroimaging Initiative. Classification of Alzheimer's disease and prediction of mild

cognitive impairment-to-Alzheimer's conversion from structural magnetic resource imaging using feature ranking and a genetic algorithm. *Comput Biol Med*. (2017) 83:109–19. doi: 10.1016/j.compbiomed.2017.02.011

19. Petersen RC. Mild cognitive impairment as a diagnostic entity. *J Intern Med.* (2004) 256:183–94. doi: 10.1111/j.1365-2796.2004.01388.x
20. Guo Q, Zhao Q, Chen M, Ding D, Hong Z. A comparison study of mild cognitive impairment with 3 memory tests among Chinese individuals. *Alzheimer Dis Assoc Disord.* (2009) 23:253–9. doi: 10.1097/WAD.0b013e3181999e92
21. Winblad B, Palmer K, Kivipelto M, Jelic V, Fratiglioni L, Wahlund LO, et al. Mild cognitive impairment–beyond controversies, towards a consensus: report of the International Working Group on Mild cognitive impairment. *J Intern Med.* (2004) 256:240–6. doi: 10.1111/j.1365-2796.2004.01380.x
22. McKhann G, Drachman D, Folstein M, Katzman R, Price D, Stadlan EM. Clinical diagnosis of Alzheimer's disease: report of the NINCDS-ADRDA Work Group under the auspices of department of health and human services Task Force on Alzheimer's disease. *Neurology.* (1984) 34:939–44. doi: 10.1212/WNL.34.7.939
23. Wahlund LO, Barkhof F, Fazekas F, Bronge L, Augustin M, Sjogren M, et al. A new rating scale for age-related white matter changes applicable to MRI and CT. *Stroke.* (2001) 32:1318–22. doi: 10.1161/01.STR.32.6.1318
24. Lu J, Li D, Li F, Zhou A, Wang F, Zuo X, et al. Montreal cognitive assessment in detecting cognitive impairment in Chinese elderly individuals: a population-based study. *J Geriatr Psychiatry Neurol.* (2011) 24:184–90. doi: 10.1177/0891988711422528
25. Morris JC. The Clinical Dementia Rating (CDR): current version and scoring rules. *Neurology.* (1993) 43:2412–4. doi: 10.1212/WNL.43.11.2412-a
26. Jenkinson M, Beckmann CF, Behrens TE, Woolrich MW, Smith SM. FSL. *NeuroImage.* (2012) 62:782–90. doi: 10.1016/j.neuroimage.2011.09.015
27. Smith SM, Jenkinson M, Woolrich MW, Beckmann CF, Behrens TE, Johansen-Berg H, et al. Advances in functional and structural MR image analysis and implementation as FSL. *NeuroImage.* (2004) 23(Suppl.1):S208–19. doi: 10.1016/j.neuroimage.2004.07.051
28. Smith SM. Fast robust automated brain extraction. *Hum Brain Mapp.* (2002) 17:143–55. doi: 10.1002/hbm.10062
29. Li W, Qiao L, Zhang L, Wang Z, Shen D. Functional brain network estimation with time series self-scrubbing. *IEEE J Biomed Health Inform.* (2019) 23:2494–504. doi: 10.1109/JBHI.2019.2893880
30. Li W, Wang Z, Zhang L, Qiao L, Shen D. Remodeling pearson's correlation for functional brain network estimation and autism spectrum disorder identification. *Front Neuroinform.* (2017) 11:55. doi: 10.3389/fninf.2017.00055
31. Kantarci K, Murray ME, Schwarz CG, Reid RI, Przybelski SA, Lesnick T, et al. White-matter integrity on DTI and the pathologic staging of Alzheimer's disease. *Neurobiol Aging.* (2017) 56:172–9. doi: 10.1016/j.neurobiolaging.2017.04.024
32. Kantarci K, Schwarz CG, Reid RI, Przybelski SA, Lesnick TG, Zuk SM, et al. White matter integrity determined with diffusion tensor imaging in older adults without dementia: influence of amyloid load and neurodegeneration. *JAMA Neurol.* (2014) 71:1547–54. doi: 10.1001/jamaneurol.2014.1482
33. Nowrangi MA, Lyketsos CG, Leoutsakos JM, Oishi K, Albert M, Mori S, et al. Longitudinal, region-specific course of diffusion tensor imaging measures in mild cognitive impairment and Alzheimer's disease. *Alzheimer Dement.* (2013) 9:519–28. doi: 10.1016/j.jalz.2012.05.2186
34. Pievani M, Agosta F, Pagani E, Canu E, Sala S, Absinta M, et al. Assessment of white matter tract damage in mild cognitive impairment and Alzheimer's disease. *Hum Brain Mapp.* (2010) 31:1862–75. doi: 10.1002/hbm.20978
35. Xie S, Xiao JX, Wang YH, Wu HK, Gong GL, Jiang XX. Evaluation of bilateral cingulum with tractography in patients with Alzheimer's disease. *Neuroreport.* (2005) 16:1275–8. doi: 10.1097/01.wnr.0000174061.41897.ee
36. Hiyoshi-Taniguchi K, Oishi N, Namiki C, Miyata J, Murai T, Cichocki A, et al. The uncinate fasciculus as a predictor of conversion from amnestic mild cognitive impairment to Alzheimer disease. *J Neuroimaging.* (2015) 25:748–53. doi: 10.1111/jon.12196
37. Bubb EJ, Metzler-Baddeley C, Aggleton JP. The cingulum bundle: anatomy, function, and dysfunction. *Neurosci Biobehav Rev.* (2018) 92:104–27. doi: 10.1016/j.neubiorev.2018.05.008
38. Contreras JA, Avena-Koenigsberger A, Risacher SL, West JD, Tallman E, McDonald BC, et al. Resting state network modularity along the prodromal late onset Alzheimer's disease continuum. *NeuroImage Clin.* (2019) 22:101687. doi: 10.1016/j.nicl.2019.101687
39. Caso F, Agosta F, Filippi M. Insights into white matter damage in Alzheimer's disease: from postmortem to *in vivo* diffusion tensor MRI studies. *Neurodegener Dis.* (2016) 16:26–33. doi: 10.1159/000441422
40. Brun A, Englund E. A white matter disorder in dementia of the Alzheimer type: a pathoanatomical study. *Ann Neurol.* (1986) 19:253–62. doi: 10.1002/ana.410190306
41. Tian J, Shi J, Bailey K, Mann DM. Relationships between arteriosclerosis, cerebral amyloid angiopathy and myelin loss from cerebral cortical white matter in Alzheimer's disease. *Neuropathol Appl Neurobiol.* (2004) 30:46–56. doi: 10.1046/j.0305-1846.2003.00510.x
42. Fellgiebel A, Muller MJ, Wille P, Dellani PR, Scheurich A, Schmidt LG, et al. Color-coded diffusion-tensor-imaging of posterior cingulate fiber tracts in mild cognitive impairment. *Neurobiol Aging.* (2005) 26:1193–8. doi: 10.1016/j.neurobiolaging.2004.11.006
43. Huang J, Friedland RP, Auchus AP. Diffusion tensor imaging of normal-appearing white matter in mild cognitive impairment and early Alzheimer disease: preliminary evidence of axonal degeneration in the temporal lobe. *AJNR Am J Neuroradiol.* (2007) 28:1943–8. doi: 10.3174/ajnr.A0700
44. Shu N, Wang Z, Qi Z, Li K, He Y. Multiple diffusion indices reveals white matter degeneration in Alzheimer's disease and mild cognitive impairment: a tract-based spatial statistics study. *J Alzheimer Dis.* (2011) 26(Suppl.3):275–85. doi: 10.3233/JAD-2011-0024
45. Fellgiebel A, Dellani PR, Greverus D, Scheurich A, Stoeter P, Müller MJ. Predicting conversion to dementia in mild cognitive impairment by volumetric and diffusivity measurements of the hippocampus. *Psychiatry Res.* (2006) 146:283–7. doi: 10.1016/j.pscychresns.2006.01.006
46. Van Bruggen T, Stieltjes B, Thomann PA, Parzer P, Meinzer HP, Fritzsche KH. Do Alzheimer-specific microstructural changes in mild cognitive impairment predict conversion? *Psychiatry Res.* (2012) 203:184–93. doi: 10.1016/j.pscychresns.2011.12.003
47. Mayo CD, Garcia-Barrera MA, Mazerolle EL, Ritchie LJ, Fisk JD, Gawryluk JR. Relationship between DTI metrics and cognitive function in Alzheimer's disease. *Front Aging Neurosci.* (2018) 10:436. doi: 10.3389/fnagi.2018.00436
48. Taoka T, Iwasaki S, Sakamoto M, Nakagawa H, Fukusumi A, Myochin K, et al. Diffusion anisotropy and diffusivity of white matter tracts within the temporal stem in Alzheimer disease: evaluation of the "tract of interest" by diffusion tensor tractography. *AJNR Am J Neuroradiol.* (2006) 27:1040–5. doi: 10.1016/j.jalz.2009.04.1162
49. Haller S, Montandon ML, Rodriguez C, Garibotto V, Lilja J, Herrmann FR, et al. Amyloid load, hippocampal volume loss, and diffusion tensor imaging changes in early phases of brain aging. *Front Neurosci.* (2019) 13:1228. doi: 10.3389/fnins.2019.01228
50. Mendonça CF, Kuras M, Nogueira FCS, Plá I, Hortobágyi T, Csiba L, et al. Proteomic signatures of brain regions affected by tau pathology in early and late stages of Alzheimer's disease. *Neurobiol Dis.* (2019) 130:104509. doi: 10.1016/j.nbd.2019.104509
51. Fernández-Miranda JC, Rhoton AL, Alvarez-Linera J, Kakizawa Y, Choi C, de Oliveira EP. Three-dimensional microsurgical and tractographic anatomy of the white matter of the human brain. *Neurosurgery.* (2008) 62(6 Suppl.3):989–1028. doi: 10.1227/01.neu.0000333767.05328.49
52. Hau J, Sarubbo S, Perchey G, Crivello F, Zago L, Mellet E, et al. Cortical terminations of the inferior fronto-occipital and uncinate fasciculi: anatomical stem-based virtual dissection. *Front Neuroanat.* (2016) 10:58. doi: 10.3389/fnana.2016.00058

53. Teipel SJ, Bokde AL, Meindl T, Amaro E, Soldner J, Reiser MF, et al. White matter microstructure underlying default mode network connectivity in the human brain. *Neuroimage.* (2010) 49:2021–32. doi: 10.1016/j.neuroimage.2009.10.067
54. Herbet G, Zemmoura I, Duffau H. Functional anatomy of the inferior longitudinal fasciculus: from historical reports to current hypotheses. *Front Neuroanat.* (2018) 12:77. doi: 10.3389/fnana.2018.00077
55. Douaud G, Menke RA, Gass A, Monsch AU, Rao A, Whitcher B, et al. Brain microstructure reveals early abnormalities more than 2 years prior to clinical progression from mild cognitive impairment to Alzheimer's disease. *J Neurosci.* (2013) 33:2147–55. doi: 10.1523/JNEUROSCI.4437-12.2013
56. Mielke MM, Okonkwo OC, Oishi K, Mori S, Tighe S, Miller MI, et al. Fornix integrity and hippocampal volume predict memory decline and progression to Alzheimer's disease. *Alzheimer Dement.* (2012) 8:105–13. doi: 10.1016/j.jalz.2011.05.2416

Conflict of Interest: The authors declare that the research was conducted in the absence of any commercial or financial relationships that could be construed as a potential conflict of interest.

frontiers in Neurology

ORIGINAL RESEARCH
published: 11 December 2020
doi: 10.3389/fneur.2020.546744

LesionQuant for Assessment of MRI in Multiple Sclerosis—A Promising Supplement to the Visual Scan Inspection

Synne Brune[1,2], Einar A. Høgestøl[1,2], Vanja Cengija[3], Pål Berg-Hansen[1,2], Piotr Sowa[3], Gro O. Nygaard[2], Hanne F. Harbo[1,2] and Mona K. Beyer[1,3]*

[1] Institute of Clinical Medicine, University of Oslo, Oslo, Norway, [2] Department of Neurology, Oslo University Hospital, Oslo, Norway, [3] Division of Radiology and Nuclear Medicine, Oslo University Hospital, Oslo, Norway

Edited by:
Deqiang Qiu,
Emory University, United States

Reviewed by:
Ronald Peeters,
University Hospitals Leuven, Belgium
Alexander Yuklun Lau,
The Chinese University of Hong Kong, China

***Correspondence:**
Mona K. Beyer
monbey@ous-hf.no

Specialty section:
This article was submitted to Applied Neuroimaging, a section of the journal Frontiers in Neurology

Received: 29 March 2020
Accepted: 23 November 2020
Published: 11 December 2020

Citation:
Brune S, Høgestøl EA, Cengija V, Berg-Hansen P, Sowa P, Nygaard GO, Harbo HF and Beyer MK (2020) LesionQuant for Assessment of MRI in Multiple Sclerosis—A Promising Supplement to the Visual Scan Inspection. Front. Neurol. 11:546744. doi: 10.3389/fneur.2020.546744

Background and Goals: Multiple sclerosis (MS) is a central nervous system inflammatory disease where magnetic resonance imaging (MRI) is an important tool for diagnosis and disease monitoring. Quantitative measurements of lesion volume, lesion count, distribution of lesions, and brain atrophy have a potentially significant value for evaluating disease progression. We hypothesize that utilizing software designed for evaluating MRI data in MS will provide more accurate and detailed analyses compared to the visual neuro-radiological evaluation.

Methods: A group of 56 MS patients (mean age 35 years, 70% females and 96% relapsing-remitting MS) was examined with brain MRI one and 5 years after diagnosis. The T1 and FLAIR brain MRI sequences for all patients were analyzed using the LesionQuant (LQ) software. These data were compared with data from structured visual evaluations of the MRI scans performed by neuro-radiologists, including assessments of atrophy, and lesion count. The data from LQ were also compared with data from other validated research methods for brain segmentation, including assessments of whole brain volume and lesion volume. Correlations with clinical tests like the timed 25-foot walk test (T25FT) were performed to explore additional value of LQ analyses.

Results: Lesion count assessments by LQ and by the neuro-radiologist were significantly correlated one year (cor $= 0.92$, $p = 2.2 \times 10^{-16}$) and 5 years (cor $= 0.84$, $p = 2.7 \times 10^{-16}$) after diagnosis. Analyzes of the intra- and interrater variability also correlated significantly (cor $= 0.96$, $p < 0.001$, cor $= 0.97$, $p < 0.001$). Significant positive correlation was found between lesion volume measured by LQ and by the software Cascade (cor $= 0.7$, $p < 0.001$. LQ detected a reduction in whole brain percentile >10 in 10 patients across the time-points, whereas the neuro-radiologist assessment identified six of these. The neuro-radiologist additionally identified five patients with increased atrophy in the follow-up period, all of them displayed decreasing low whole brain percentiles (median 11, range 8–28) in the LQ analysis. Significant positive correlation was identified between lesion volume measured by LQ and test performance on the T25FT both at 1 and 5 years after diagnosis.

Conclusion: For the number of MS lesions at both time-points, we demonstrated strong correlations between the assessments done by LQ and the neuro-radiologist. Lesion volume evaluated with LQ correlated with T25FT performance. LQ-analyses classified more patients to have brain atrophy than the visual neuro-radiological evaluation. In conclusion, LQ seems like a promising supplement to the evaluation performed by neuro-radiologists, providing an automated tool for evaluating lesions in MS patients and also detecting early signs of atrophy in both a longitudinal and cross-sectional setting.

Keywords: MRI, longitudinal lesions, brain atrophy, automatic lesion detection, multiple sclerosis

INTRODUCTION

Multiple sclerosis (MS) is a chronic inflammatory, demyelinating disorder of the central nervous system. Most frequently MS is characterized by a relapsing remitting disease course (RRMS) that over the years often converts to a secondary progressive disease course (SPMS). MS leads to variable degrees of physical and cognitive impairment. About 10 percent of the patients experience a progressive disease course from disease onset [primary progressive MS (PPMS)] (1, 2). A key challenge in MS care is to identify and develop prognostic biomarkers for the disease course (3). Magnetic resonance imaging (MRI) is still the most important tool for the diagnosis and monitoring of MS (4–6). MRI has a high sensitivity for the evaluation of inflammatory and neurodegenerative processes in the brain and spinal cord and it is the most commonly used method in the follow-up of MS patients (7).

Visual inspection of the MRI scans of people with MS is time consuming for the neuro-radiologist. Subjective measurements based on a radiologist's visual inspection may result in low reproducibility (8). In addition, the degrees of brain atrophy and MS-related pathology in the gray and white matter may be difficult to estimate, especially in early adulthood (9, 10).

Advanced tools have been shown necessary to detect early brain atrophy in MS (11). New MRI post-processing tools that automatically analyse complex brain volumetric information and lesion load have recently become commercially available. A study comparing two different software types for assessment of longitudinal whole brain atrophy in MS patients found a strong level of statistical agreement and consistency between the two programs in a real-world MS population (12). The authors conclude that automated measurements of atrophy show promise as biomarkers of neuro-degeneration in clinical practice and will enable more rapid clinical translation. If these types of programmes are to be introduced, in addition to showing their performance compared to competing programs or established research tools, we need to evaluate their use compared to clinical practice today. Do they perform as well, or better than current practice, and in what way can they be useful and valuable?

Although a neuro-radiological evaluation of structural brain MRI in MS patients can easily estimate the pathologic burden of abnormalities such as T2 hyperintense lesions, limited correlation exists between these measures and the clinical phenotype (13). This has been termed the "clinico-radiological paradox" and is well-described for both physical and cognitive impairments. Some explanations to this paradox have been suggested, including inappropriate clinical rating, and underestimation of damage to the normal appearing brain tissue (14). In a large meta-analysis including 2,891 patients, Mollison et al. found a modest correlation ($r = -0.30$) between MRI measures of total brain white matter lesions and cognitive function in people with MS (13).

LesionQuant(LQ) by CorTechs Labs is a software that automatically segments and measures volumes of brain structures and compares these volumes to norms based on the more established NeuroQuant(NQ) software (15). LQ was specifically designed for the evaluation of lesions and atrophy in MS patients. LQ also provides volumes and counts of new and enlarging brain lesions, and it automatically labels, visualizes and obtains the volumetric quantification of lesions based on brain MRI. LQ can therefore be used in the longitudinal follow-up of patients with MS. A recent study compared NQ to another software tool, Functional Magnetic Resonance Imaging of the Brain's (FMRIB's) Integrated Registration Segmentation Tool (FIRST), for estimating overall and regional brain volume in patients with clinically isolated syndrome (16). To our knowledge, no data is published that compares the LQ software in MS with visual evaluations performed by neuro-radiologists.

By using data from our prospective longitudinal study of newly diagnosed MS patients, results from longitudinal LQ analyses were compared to visual evaluations performed by neuro-radiologists in our hospital. We hypothesize that quantitative measurements of brain lesions and atrophy, using an unbiased automatic tool, may improve the correlation between clinical phenotype and MRI results.

Our aims were to evaluate (a) The performance of LQ at detecting brain lesions compared to a neuro-radiologist, and (b) brain atrophy as measured by LQ in comparison to the visual inspection by the neuro-radiologist. (c) The correlations of results from both visual assessment and LQ with clinically relevant variables and (d) the correlation between the segmented brain volumes and lesion volumes acquired from LQ and volumes from the two brain segmentation tools, FreeSurfer and Cascade.

MATERIALS AND METHODS

Participants

All analyses were based upon carefully phenotyped MS patients in an ongoing prospective longitudinal MS study in Oslo (17, 18). A total of 56 MS patients were included in this study, which had been examined on average 1 year after diagnosis. The inclusion criteria were a diagnosis of RRMS in the period 2009–2012 and age 18–50 years. The exclusion criteria were a history of psychiatric or other neurological diseases than MS, drug abuse, previous adverse Gadolinium reaction, pregnancy or breast-feeding at inclusion, or non-fluency in Norwegian. Data from two time-points after diagnosis of MS were included in this study; data from time-point 1 (TP1) was collected 13 months after diagnosis (± 9, $n = 56$) and data from time-point 2 (TP2) after 66 months (± 12, $n = 56$). At both time-points an expanded disability status scale (EDSS) score was calculated based on a standard neurological examination by trained clinicians (19, 20). For assessment of walking ability and upper extremity function we also performed timed 25-foot walk test (T25FT) and 9-Hole Peg Test (9HPT). A brain MRI scan for clinical and research setting, was performed at both time-points.

We classified the disease modifying treatments (DMTs) as follows; group 0: no treatment, group 1: Glatiramer Acetate, Interferons, Teriflunomide or Dimetylfumarate, group 2: Fingolimod, Natalizumab or Alemtuzumab.

MRI Acquisition

MS patients were scanned at both time-points with the same MRI scanning protocol in the same 1,5 T scanner (Avanto, Siemens Medical Solutions; Erlangen, Germany). The following two MRI sequences were required for the LQ analyses in this study;

(a) A Sagittal 3D T1 MPRAGE (FOV: 240 × 240 mm; slice thickness: 1.2 mm; voxel size: 1.3 × 1.3 × 1.2 mm; TR: 2,400 ms; TE: 3.61 ms; TI: 1,000 ms; flip angle: 8 deg.

(b) Pre-contrast sagittal 3D FLAIR (FOV: 260 × 260 mm; slice thickness: 1 mm; voxel size: 1 × 1 × 1 mm; TR: 6,000 ms; TE: 333 ms; TI: 2,200 ms.

The neuro-radiologist could in addition use all available other sequences in the study protocol, as mentioned in previous publications (17, 21).

LesionQuant Analyses of Lesion Count, Brain Volume, and Lesion Volume

The MRI data from the 56 patients were analyzed using the LQ tool (version 2.3.0), comparing data at TP1 and TP2. For each patient, T1-weighted and FLAIR sequences were uploaded to the LQ server from the PACS system in the hospital, without the need for pre-processing. Finalized LQ-reports were received after ∼10 min. The reports provided volumes and counts of all lesions, including new and enlarging lesions at TP2. A lesion was defined by LQ as being ≥ 4 mm^3. Volumes of brain structures in the MS patients were compared with age and sex matched healthy controls from the LQ reference database. To establish the normative LQ database, CorTechs Labs combined data from several thousand scans including publicly available studies, studies by collaboration partners, and other proprietary data sources (age range 3–100 years, acquired using Siemens, GE and Philips MRI scanners with both 1.5T and 3T field strength).

The LQ-reports provided information about volumes of different brain structures, including whole brain, thalamus, cerebral white matter, volume of white matter lesions and cortical gray matter. The results for each patient are illustrated both using percentiles and absolute values (**Figure 1**). A cut off for atrophy was defined as a 10 percentile drop in brain volume for LQ between TP1 and TP2 (= 5-year interval).

MRI Evaluation of Lesion Count and Brain Volume Presented by the Neuro-Radiologist

The brain MRIs from the included MS patients were systematically evaluated by a neuro-radiologist who carefully counted all lesions on the MRI scans of the patients at TP1 and TP2. A lesion was defined as having a high T2/FLAIR signal ≥ 3 millimeters in diameter. To evaluate the intrareader variability the neuro-radiologist read the data twice in 10 of the patients. A second neuro-radiologist also calculated the number of lesions in the same 10 patients to give information about the interrater variability. In addition to this, another method for evaluating the number of lesions was added. Two neuro-radiologists estimated a lesion number score at TP1. If the number of lesions were between 0 and 9 the lesion number score given was 1, if the number of lesions were between 10 and 19 the lesion number score given was 2, if the number of lesions were more than 20 the lesion number score given was 3.

A neuro-radiologist also assessed whether increased whole brain atrophy was visually evident between the two time-points or not (**Figure 2**). Visual evaluation of atrophy was done using the 3D T1 series, where increased CSF in the sulci or on the surface of the brain or volume loss of the gyri between TP1 and TP2, was regarded as atrophy.

The exact lesion number, lesion number score, and the evaluation of atrophy were then compared to the output from LQ. The assessment by the neuro-radiologist was used as the gold standard to compare the LQ data with.

MRI Evaluation of Brain Volume and Lesion Volume Using Freesurfer and Cascade

To compare LQ with other research methods for brain segmentation we compared LQ with the softwares FreeSurfer and Cascade (22). To compare brain volume between the different softwares we used the measure for whole brain volume from both LQ (including brain stem) and FreeSurfer (excluding brain stem) (23). To compare the lesion volume between the different softwares we used the measure for total lesion volume from both LQ and Cascade.

Statistical Analysis

We used R (R Core Team, Vienna, 2018, version 3.6.1) for statistical analyses. To assess reliability of the whole brain volumes from LQ and FreeSurfer we computed the intraclass correlation coefficient (ICC) using the R package "irr" (24). Figures were made using "ggplot2" (25) and "cowplot" (26) in R.

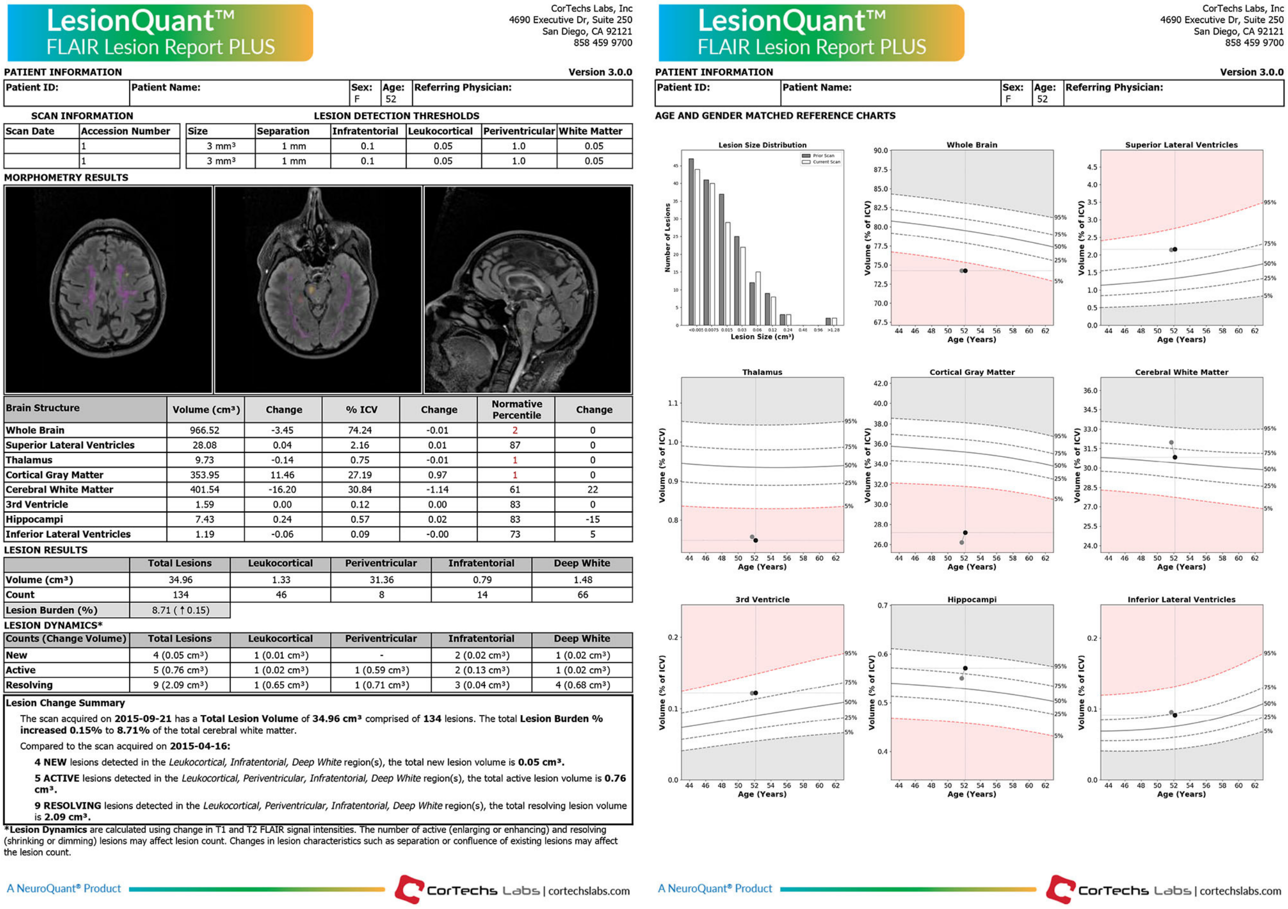

LesionQuant™
FLAIR Lesion Report PLUS

CorTechs Labs, Inc
4690 Executive Dr, Suite 250
San Diego, CA 92121
858 459 9700

PATIENT INFORMATION **Version 3.0.0**

Patient ID:	Patient Name:	Sex:	Age:	Referring Physician:
		F	52	

SCAN INFORMATION

Scan Date	Accession Number
	1
	1

LESION DETECTION THRESHOLDS

Size	Separation	Infratentorial	Leukocortical	Periventricular	White Matter
3 mm³	1 mm	0.1	0.05	1.0	0.05
3 mm³	1 mm	0.1	0.05	1.0	0.05

MORPHOMETRY RESULTS

Brain Structure	Volume (cm³)	Change	% ICV	Change	Normative Percentile	Change
Whole Brain	966.52	-3.45	74.24	-0.01	2	0
Superior Lateral Ventricles	28.08	0.04	2.16	0.01	87	0
Thalamus	9.73	-0.14	0.75	-0.01	1	0
Cortical Gray Matter	353.95	11.46	27.19	0.97	1	0
Cerebral White Matter	401.54	-16.20	30.84	-1.14	61	22
3rd Ventricle	1.59	0.00	0.12	0.00	83	0
Hippocampi	7.43	0.24	0.57	0.02	83	-15
Inferior Lateral Ventricles	1.19	-0.06	0.09	-0.00	73	5

LESION RESULTS

	Total Lesions	Leukocortical	Periventricular	Infratentorial	Deep White
Volume (cm³)	34.96	1.33	31.36	0.79	1.48
Count	134	46	8	14	66
Lesion Burden (%)	8.71 (↑ 0.15)				

LESION DYNAMICS*

Counts (Change Volume)	Total Lesions	Leukocortical	Periventricular	Infratentorial	Deep White
New	4 (0.05 cm³)	1 (0.01 cm³)	-	2 (0.02 cm³)	1 (0.02 cm³)
Active	5 (0.76 cm³)	1 (0.02 cm³)	1 (0.59 cm³)	2 (0.13 cm³)	1 (0.02 cm³)
Resolving	9 (2.09 cm³)	1 (0.65 cm³)	1 (0.71 cm³)	3 (0.04 cm³)	4 (0.68 cm³)

Lesion Change Summary

The scan acquired on **2015-09-21** has a **Total Lesion Volume** of **34.96 cm³** comprised of **134** lesions. The total **Lesion Burden % increased 0.15%** to **8.71%** of the total cerebral white matter.

Compared to the scan acquired on **2015-04-16:**

4 NEW lesions detected in the *Leukocortical, Infratentorial, Deep White* region(s), the total new lesion volume is **0.05 cm³.**

5 ACTIVE lesions detected in the *Leukocortical, Periventricular, Infratentorial, Deep White* region(s), the total active lesion volume is **0.76 cm³.**

9 RESOLVING lesions detected in the *Leukocortical, Periventricular, Infratentorial, Deep White* region(s), the total resolving lesion volume is **2.09 cm³.**

***Lesion Dynamics** are calculated using change in T1 and T2 FLAIR signal intensities. The number of active (enlarging or enhancing) and resolving (shrinking or dimming) lesions may affect lesion count. Changes in lesion characteristics such as separation or confluence of existing lesions may affect the lesion count.

A NeuroQuant® Product CorTechs Labs | cortechslabs.com

LesionQuant™
FLAIR Lesion Report PLUS

CorTechs Labs, Inc
4690 Executive Dr, Suite 250
San Diego, CA 92121
858 459 9700

PATIENT INFORMATION **Version 3.0.0**

Patient ID:	Patient Name:	Sex:	Age:	Referring Physician:
		F	52	

AGE AND GENDER MATCHED REFERENCE CHARTS

A NeuroQuant® Product CorTechs Labs | cortechslabs.com

FIGURE 1 | LesionQuant report. Example of a LesionQuant report from one MS subject comparing two MRI scans with a 5-month time interval between the two time-points.

To evaluate the associations between the assessment provided by LQ, the neuro-radiologist, analysis using the FreeSurfer and Cascade softwares and the clinical data, we used the "stats" package in R and calculated the Pearson's correlation coefficient and applied the student's *t*-test (27).

To adjust for multiple comparisons, we calculated the degree of independence between the four clinical variables available, making a 4 × 4 correlation matrix based on the Pearson's correlation between all pair-wise combinations of clinical data. Utilizing the ratio of observed eigenvalue variance to its theoretical maximum, the estimated equivalent number of independent traits in our analyses was 3.0 (28). To control for multiple testing, our significance threshold was therefore adjusted accordingly from 0.05 to 0.017 (28).

RESULTS

Participant Demographics and Characteristics

At TP1 mean age of the study participants was 36 years (range 21–49 years), 70% were females and 96% were classified as having RRMS. EDSS was stable between TP1 and TP2 with median EDSS 2.0 (range 0–6). Time since MS diagnosis was on average 12.9 months (SD = 9.3) at TP1 and 66.0 months (SD = 11.7) at TP2. At TP1, 25% did not receive any DMT for MS, 63% received a group 1 DMT (moderately effective treatment) and 12% a group 2 DMT (highly effective treatment). At TP2, 34% did not receive any DMT, 36% received a group 1 DMT and 30% a group 2 DMT (**Table 1**).

Cross-Sectional Comparison of Lesion Count Between the LesionQuant Reports and the Neuro-Radiological Evaluations

The lesion count assessments by LQ and the neuro-radiologist were significantly correlated at TP1 (cor = 0.92, $p = 2.2 \times 10^{-16}$) and TP2 (cor = 0.84, $p = 2.7 \times 10^{-16}$) (**Supplementary Figure 2**). The lesion counts were identical in only two and three patients at TP1 and TP2, respectively. While lesion counts were higher by the neuro-radiologist in 39 and 40 patients at TP1 and TP2, respectively. Lesion counts were lower by LQ in 15 and 13 patients at TP1 and TP2, respectively. In general, the differences in number of lesions evaluated by LQ and

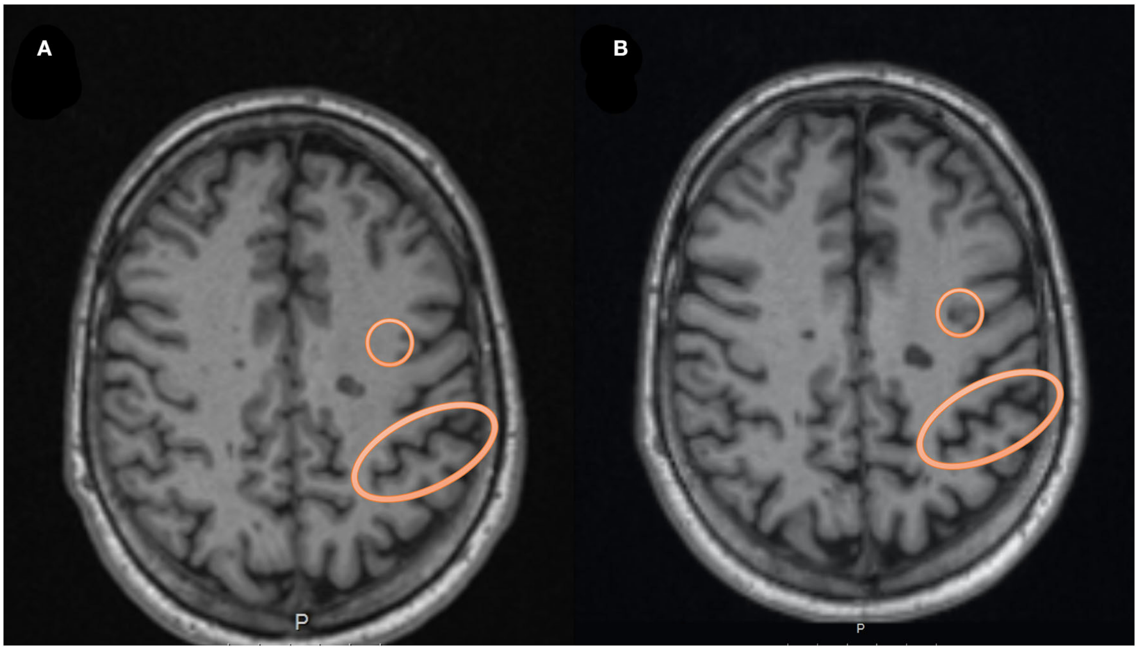

FIGURE 2 | An example of the visual assessment by the neuro-radiologist. In **(A)** we see an axial T1 MRI at time-point 1, while in **(B)** we see the MRI at time-point 2, highlighting a circle with an example of a new lesion evolving during the follow-up period. The oval circle is an example of an area showing increased CSF in the sulcus, which was evaluated as representing atrophy between the two time-points.

the neuro-radiologist increased with age. For patients with higher number of lesions the neuro-radiologist tended to count more lesions than LQ, and the opposite with lower number of lesions, see **Supplementary Figure 1**. To evaluate the intra and interrater variability the neuro-radiologist recounted the lesions in 10 of the patients, and a second neuro-radiologist counted lesions in the same 10 patients. Both the intra- and the inter-rater variability were significantly correlated (cor = 0.96, $p < 0.001$, cor = 0.97, $p < 0.001$). This was also the case for the lesion number scores estimated between LQ, and two different neuro-radiologists.

The lesion volume assessments by LQ and the Cascade software were significantly correlated (cor = 0.7, $p < 0.001$).

Longitudinal Evaluations of Atrophy and Lesions

We also compared the LQ software with the assessment by the neuro-radiologist in identifying whole brain atrophy at TP2. The neuro-radiologist classified 12 subjects to have brain atrophy. These 12 subjects also had significantly lower scores on whole brain atrophy by LQ (mean brain volume percentile 37.0, range 10–80), compared to the subjects that were not classified as having brain atrophy (mean brain volume percentile 48.7, range 2–99).

At TP2, LQ and the neuro-radiologist agreed in classifying 33% of the subjects with atrophy (four out of 12 subjects). In addition, the neuro-radiologist identified eight more subjects with brain atrophy (mean LQ whole brain percentile 31.3).

LQ detected a reduction in whole brain percentile >10 in 10 patients between TP1 and TP2, while the neuro-radiological evaluation identified six of these. The evaluation by the neuro-radiologist identified an additional six patients with increased atrophy between TP1 and TP2, all of whom displayed low whole brain percentiles at TP2 (median 11, range 8–28) and decreasing percentile between the time-points.

At TP2 we found that LQ showed reduced whole brain volume in 51 patients compared to TP1 with a mean reduction in volume of 20.5 ml/1.59% (range 0.4–109.4 ml/0.03–8.08%) of the whole brain volume. In the remaining five patients we found an increased volume with a mean increase in volume of 6.8 ml/0.56% (range 0.2–17.4 ml/0.02–1.44%).

To evaluate the sensitivity of LQ in detecting new lesions, compared to the neuro-radiologist, the difference in number of lesions assessed at the two time-points was analyzed in a 2 × 2 table (**Table 2**). The sensitivity of the LQ-analysis to correctly classify the patients according to the gold standard neuro-radiological evaluation was 53% (17/32 patients). The specificity of the LQ-analysis to correctly evaluate the MRI follow-up as stable according to the neuro-radiological evaluation was 75% (18/24). In total, 43 % of the patients were evaluated with no new lesions on MRI at TP2 by the neuro-radiologist. Also, 57% (32 patients) had new lesions according to the neuro-radiologist, and only 17 of these had new lesions according to the LQ-reports (**Table 2** and **Figure 3**).

Correlations Between MRI Features and Clinical Variables

We found significant positive correlations between T25FT and the lesion volume as measured by LQ at both TP1 ($t = 3.08$, p

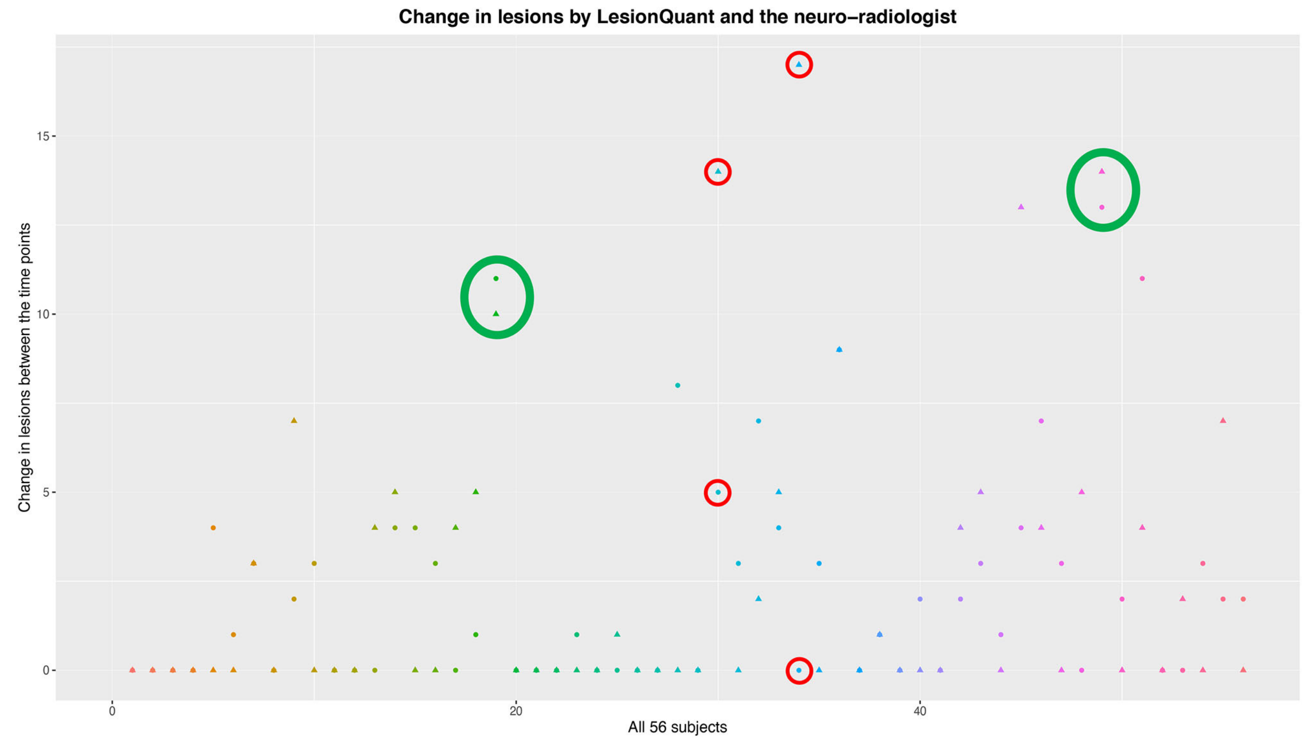

FIGURE 3 | An overview of the evaluations of change in lesions between the two time-points. The LesionQuant assessments are depicted with a circle, while the neuro-radiological evaluations are depicted using a triangle. Each subject is visualized with both assessments and with a unique color. The green circles show examples of assessments with good agreement between LQ and neuro-radiologist, while the red circles show assessments where the two methods differ a lot in the same patient.

$= 3.2 \times 10^{-3}$) and TP2 ($t = 3.72$, $p = 4.8 \times 10^{-4}$) (**Table 3**). These results also indicate slower test performance by T25FT in patients with a higher burden of lesion volume. In addition, we found a significant positive correlation between the 9HPT using the left hand and lesion volume at TP2 ($t = 5.34$, $p = 2.09 \times 10^{-6}$), indicating slower test performance with increased lesion volume. We also found a significant negative correlation with EDSS and whole brain volume at TP1 ($t = -2.68$, $p = 9.8 \times 10^{-3}$), indicating higher EDSS scores with lower brain volumes. We found no significant correlations between the number of lesions reported by the neuro-radiologist and the clinical variables. All significant correlations reported were adjusted for multiple testing.

Reliability of LesionQuant Volumes

To validate the LQ data with the established FreeSurfer output for brain segmentation we compared the measure for whole brain volume from both LQ (including brainstem) and FreeSurfer (excluding brain stem), (**Supplementary Figure 2**). At both TP1 ($t = 51.6$, cor = 0.99) and TP2 ($t = 45.2$, cor = 0.99), Pearson's correlations were highly significant. We also validated regional volumes for thalamus using both raw FreeSurfer data and data processed through the longitudinal stream compared to the LQ data, yielding less significant correlations ($t = 2.4$–2.8 and, cor = 0.32–0.35, $p = 0.02$–0.008).

LesionQuant Reports and Neuro-Radiological Evaluation

All longitudinal LQ-data yielded excellent concurrence. To evaluate the consistency and agreement of the longitudinal LQ-reports, we measured the Intraclass correlation coefficients (ICC) between TP1 and TP2 for brain volume (ICC = 0.97, $p = 2 \times 10^{-35}$), lesion count (ICC = 0.91, $p = 1.4 \times 10^{-23}$), lesion volume (ICC = 0.88, $p = 5.2 \times 10^{-20}$) and thalamus volume (ICC = 0.91, $p = 3.0 \times 10^{-23}$) (**Supplementary Table 1**). We found significant correlations between lesion volume and the number of lesions at both TP1 ($t = 6.32$, $p = 5.05 \times 10^{-8}$) and TP2 ($t = 4.21$, $p = 9.77 \times 10^{-5}$). We found no significant changes in the parameters between TP1 and TP2 (**Supplementary Table 1**). As a sanity check, the ICC for lesion counts reported by the neuro-radiologist was very high (ICC = 0.99, $p = 2.6 \times 10^{-50}$), as expected.

DISCUSSION

Magnetic resonance imaging is an important para-clinical tool for the diagnosis and monitoring of MS. Quantitative measurements of lesion volume and distribution of lesions have a significant value for evaluating disease progression in a clinical setting and brain atrophy is a possible new measurement to be used in future evaluation in MS patients. In this study we

TABLE 1 | Demographic and clinical characteristics of the multiple sclerosis patients.

	Time-point 1	Time-point 2
	n = 56	***n = 56***
Demographic and clinical characteristics		
Female, % (*n*)	70 (39)	70 (39)
Age, mean years (range)	35.8 (21–49)	40.3 (25–53)
Number of total attacks, mean (SD, range)	1.9 (1.0, 0–5)	2.6 (1.3)
Months since MS diagnosis, mean (SD, range)	12.9 (9.3, 0–34)	66.0 (11.7, 38–95)
Clinical classification		
EDSS, median (SD, range)	2.0 (1.0, 0–6)	2.0 (1.3, 0–6)
9-hole peg test, right hand, mean seconds (SD, range)	20.9 (3.4, 16.5–33.4)	21.3 (8.4, 15.3–73.7)
9-hole peg test, left hand, mean seconds (SD, range)	21.6 (3.0, 16.0–28.4)	21.1 (5.0, 16.6–45.5)
Timed 25-foot walk test, mean seconds (SD, range)	3.94 (0.75, 2.85–7.22)	4.05 (1.19, 2.49–9.49)
Multiple sclerosis classification		
RRMS, *n* (%)	54 (96)	53 (94)
PPMS, *n* (%)	1 (2)	1 (2)
SPMS, *n* (%)	1 (2)	2 (4)
Disease modifying treatments		
Group 0, *n* (%)	14 (25)	19 (34)
Group 1, *n* (%)	35 (63)	20 (36)
Group 2, *n* (%)	7 (12)	17 (30)

EDSS, Expanded Disability Status Scale; Group 0, No Treatment; Group 1, Glatiramer Acetate, Interferons, Teriflunomide or Dimetylfumarate; Group 2, Fingolimod, Natalizumab or Alemtuzumab; PPMS, Primary progressive; MS, RRMS, Relapsing-remitting MS, SD, Standard Deviation; SPMS, Secondary progressive MS.

TABLE 2 | A 2 × 2 table based on the ability to capture MRI activity based on the presence of new lesions in our longitudinal MS sample.

		LesionQuant report		
		New lesions	**Stable**	**In total**
Neuro-radiological evaluation	New lesions	17	15	32
	Stable	6	18	24
	In total	23	33	56

explored the use of the LQ software for evaluating cerebral MS lesions as well as brain atrophy in a clinical setting, and investigated if an automatic analysis of MRI scans using such software shows promise for use in the clinical follow-up of MS-patients.

We found a high correlation between lesions counted by the neuro-radiologist at TP1 and TP2 and the lesion count output from LQ. In evaluation of atrophy between TP1 and TP2 there was only agreement between the neuro-radiologist and LQ in 50% of the patients (6 out twelve). Differences in whole brain percentiles between TP1 to TP2 were detected with LQ in the majority of patients, ranging between 0.03 and 8.08%. Lesion volume from LQ analysis correlated with outcome of clinical tests of walking speed and upper extremity function. Significant positive correlation was identified between lesion volume measured by LQ and test performance on the T25FT both at 1–5 years after diagnosis. There was a significant correlation between the results of LQ and the segmented volumes by FreeSurfer, showing high reliability of LQ output for whole brain volume. The correlation between lesion volume estimated by LQ and by the Cascade software were also highly significant.

In order to evaluate treatment-effect, it is of importance to see if new or enlarging lesions appear on a follow-up MRI scan. The lesion counts of the LQ software and the neuro-radiologist were highly correlated at both timepoints. However, visual assessment revealed somewhat higher lesion counts than the LQ assessment, more so in patients with a high number of lesions. The explanation of this difference in lesion number could be explained in differences in the definition of a lesion. As mentioned in the materials and method chapter a lesion was defined as having a T2/FLAIR signal ≥ 3 millimeters in diameter when analyzed by visual evaluation, but the lesion size set by LQ was ≥ 4 mm^3. With the high correlation of lesion count overall, the LQ tool should be valuable for detecting lesions in routine follow-up MRI in MS. The resulting LQ report could then be controlled by a neuro-radiologist.

Regarding the detection of lesions, we used the assessment by the neuro-radiologist as the "gold standard." However, it is well-established that the detection of cortical lesions may be challenging using conventional brain MRI and these may be missed by radiologists (29). This is shown in a study comparing the number of MS lesions counted by radiologists and as analyzed by MSmetrix (today known as IcoBrain MS), a software comparable to LQ (30). This study showed a higher recount-difference when recounting was performed by radiologists than in MSmetrix (31). Therefore, the gold standard as we defined it in this paper, may be more variable than the automated software tool.

Reliable evaluation of atrophy is difficult with only visual inspection, although it is not a very time-consuming task. Results from studies comparing visual ratings of atrophy using GCA have shown Inter-rater reliability of > 0.6 and Intra-rater reliability of >0.7, which is considered moderate agreement (32). When the neuro-radiologist evaluated the MRI, images from TP2 was compared with the MRI scan at TP1 for each patient. In a clinical routine setting, the neuro-radiologists often compare to the previous MRI, which may be taken months or up to a year before. The changes in atrophy are rather small from year to year -0.2 to -0.3% per year in our patients' age range) (33) and it is not possible to detect such small changes in reduction of brain volume for the neuro-radiologist. A better approach may be to always compare the last scan to the first MRI in order to increase sensitivity of visual atrophy assessment. But even if there are several years between the MRI scans it could be difficult to estimate reduction in brain volume if the patients evaluated are young and stable. The discrepancy between the 12 patients found to have atrophy from visual inspection, to the 51 patients

TABLE 3 | Associations between LQ-variables and clinical variables.

	LesionQuant variables			
	Lesion volume			
	Time-point 1		**Time-point 2**	
Clinical variables	*t*-value	*p*-value	*t*-value	*p*-value
Expanded disability status scale	1.12	0.27	1.43	0.16
9-hole peg test, right hand	2.00	0.05	1.87	0.07
9-hole peg test, left hand	1.00	0.32	***5.34***	***2.09 x 10^{-6}***
Timed 25-foot walk test	***3.08***	***3.2 x 10^{-3}***	***3.72***	***4.8 x 10^{-4}***
	Lesion count			
Expanded disability status scale	0.85	0.40	0.42	0.68
9-hole peg test, right hand	2.35	0.02	0.50	0.62
9-hole peg test, left hand	−0.23	0.82	1.90	0.06
Timed 25-foot walk test	1.48	0.15	0.68	0.50
	Whole brain volume			
Expanded disability status scale	***−2.68***	***9.8 x 10^{-3}***	−1.45	0.15
9-hole peg test, right hand	0.94	0.35	0.86	0.40
9-hole peg test, left hand	−2.24	0.03	−0.20	0.84
Timed 25-foot walk test	−0.68	0.50	−1.22	0.23
	Whole brain percentile			
Expanded disability status scale	−0.11	0.91	−0.81	0.42
9-hole peg test, right hand	1.05	0.30	−0.33	0.74
9-hole peg test, left hand	−1.16	0.25	−0.69	0.49
Timed 25-foot walk test	1.06	0.29	0.18	0.86
	Lesion count by neuro-radiologist			
Expanded disability status scale	1.00	0.33	1.06	0.30
9-hole peg test, right hand	2.64	0.01	0.76	0.45
9-hole peg test, left hand	0.05	0.96	2.69	0.01
Timed 25-foot walk test	1.11	0.27	1.20	0.24

Results marked in bold and italics were significant after adjusting for multiple testing.

showing reduced brain volumes in the 5-year follow-up may indicate that LQ would be helpful in clinical practice. Never the less we should have in mind the risk of detecting reductions in whole brain volume with LQ which is not clinically relevant. Our MS population is young (mean age 36 years) and relatively stable (median EDSS 2,0). Finding small reductions in brain volume in such a population would not necessarily improve their general health condition. But overall, our results indicate that the automated method LQ performs better than the visual evaluation method in terms of atrophy evaluations, as discussed above.

Most of the MS patients were treated with moderately or highly efficacious disease modifying therapies at TP1 and TP2. In total, 10 MS patients changed to a more efficient MS treatment during the follow-up. We found no significant differences in brain volumes or change in brain volumes between the patients who increased treatment efficiency during the follow-up and those who either used the same treatment or reduced the efficacy of their MS treatment during the follow-up period. As a confounding factor we have to consider that switching to more efficacious treatments would impact the brain volumes by possible pseudoatrophy during the first 6 months (34). Although, during our observational period we did not find any significant differences. Other short term confounding factors affecting brain volume measurements are known, such as fluid restriction, the time of the day for MRI measurements, corticosteroids, antipsychotic treatment and short-term effects of pathological processes that decrease global brain volume (35).

LQ compared differences in brain volume during approximately a 5-year period (2012/2013 and 2016/2017). During this period the patients were scanned on several occasions, which were not part of the study. One of the main benefits of using automated methods for image analysis in MS patients, is the possibility to perform more reliable and quick evaluation of brain atrophy. As shown by Pareto et al. when comparing two different tools for automated volume analysis of different brain regions, the size of the brain region of interest seems to be important (16). We found an excellent correlation between the FreeSurfer and LQ software's in the assessment of whole brain atrophy (cor = 0.99). However, for thalamus we only found modest correlations between both the raw and processed volumes estimated by LQ and FreeSurfer (cor = 0.32–0.35, p = 0.02–0.008, respectively), confirming the results of Pareto et al. In a recent paper, Storelli et al. also studied reproducibility and repeatability using different software's for atrophy measurements (10). They concluded that an improved reproducibility between scanners is required for clinical application.

In our study the LQ software estimated an unexpected increased whole brain volume in six patients between TP1 and TP2. This could be due to variability in the MRI scanner or other technical reasons. Alternatively, changes in lesion load in the patient over time may affect the atrophy measurements (10).

We hypothesized that improved measurements of brain lesions and atrophy, using an unbiased automatic tool, may improve the correlation between clinical phenotype and MRI results. We found that only the automated LQ software was able to show significant correlation with the standard clinical tests (T25FT, 9HPT, and EDSS). We consider this to be a robust and expected finding as only LQ and not the neuro-radiologist could provide volumetric information. In line with this, the 9HPT was positively correlated with lesion volume at time-point two; although only significant for the left hand, the same trend was seen for the right hand. The EDSS scale, which is the most widely used method to grade disability in MS, was only associated with whole brain volume at TP1 ($t = -2.68$, $p = 9.8 \times 10^{-3}$). There were no correlations between lesion count, either from LQ or the neuro-radiologist and the EDSS, T25FT or 9HPT, also showing the value of having volumes of the lesions and whole brain available.

In general, we found very high levels of intraclass correlation coefficients (0.88–0.97), showing consistency and agreement among the longitudinal LQ-reports. A strength of this paper is the longitudinal design where the MS patients were examined clinically and with brain MRI both one and 5 years after diagnosis. The patient cohort is well-characterized by trained clinicians, performing the clinical and MRI assessments. The same MRI scanner and protocol was used for all patients at the two time-points of evaluation, and all patients were scanned in the afternoon/early evening. The neuro-radiological evaluation of the 56 patients at TP1 and TP2 was performed by the same neuro-radiologist, and in addition both inter and intrarater evaluations were performed. Thus, the quality of the data included in this study is suitable for addressing the research question. A weakness of the study is that we did not perform visual assessment by two independent raters for the visual evaluation of atrophy. Also, there was no control group.

The structured LQ report is acquired using fully automated MRI post-processing software, which requires only minimal effort and reduces bias of different raters, which is present when using visual inspection of images. Another advantage is the very short processing time of LQ compared to similar software used for research, with only about 10 min from the uploading of images to the final report is received. In comparison, software like FreeSurfer needs hours to process the data, cannot be interpreted for individual patients and is not feasible for clinical practice.

CONCLUSION

In conclusion, automatic analyses of MRI scans of MS patients may provide faster assessments than the traditional evaluation performed by the neuro-radiologist. LQ seems like a promising supplement to the evaluation by the neuro-radiologist, providing an automated tool for assessment of MS lesions and brain volume in MS patients.

DATA AVAILABILITY STATEMENT

The current dataset cannot be made publicly available for ethical reasons, and public availability would compromise patient confidentiality and participant privacy. The study was conducted in humans and the dataset includes sensitive and personal information on individuals. A portion of data can be made available upon request to interested, qualified researchers provided that an agreement is made up. The minimal data set will enable replication of the reported study findings. Requests to access the datasets should be directed to Hanne F. Harbo, h.f.harbo@medisin.uio.no.

ETHICS STATEMENT

The studies involving human participants were reviewed and approved by The South Eastern Regional Committee for Medical and Health Research Ethics. The patients/participants provided their written informed consent to participate in this study.

AUTHOR CONTRIBUTIONS

SB, EH, PB-H, HH, and MB contributed to the conception, design of the study, and drafted the text and figures. SB, EH, VC, GN, PB-H, HH, PS, and MB contributed to the acquisition and analysis of data. During review and editing of this manuscript, all authors contributed.

FUNDING

This project was supported by grants from The Research Council of Norway (NFR, grant numbers 240102 and 223273) and the South-Eastern Health Authorities of Norway (Grant Nos. 257955 and 2019111).

ACKNOWLEDGMENTS

We thank all the patients who participated in our study. We acknowledge the collaboration with members of the Multiple Sclerosis Research Group at the University of Oslo and Oslo University hospital, especially Professor Elisabeth G. Celius. We acknowledge the collaboration with the Regional Core Facility in Translational MRI with leader Frode A. Tuvnes, Lisa Kjønigsen and research assistant Eva B. Aamodt.

SUPPLEMENTARY MATERIAL

The Supplementary Material for this article can be found online at: https://www.frontiersin.org/articles/10.3389/fneur.2020.546744/full#supplementary-material

REFERENCES

1. Koch M, Kingwell E, Rieckmann P, Tremlett H. The natural history of primary progressive multiple sclerosis. *Neurology*. (2009) 73:1996–2002. doi: 10.1212/WNL.0b013e3181c5b47f
2. Lublin FD, Reingold SC, Cohen JA, Cutter GR, Sørensen PS, Thompson AJ, et al. Defining the clinical course of multiple sclerosis: the 2013 revisions. *Neurology*. (2014) 83:278–86. doi: 10.1212/WNL.0000000000000560
3. Katsavos S, Anagnostouli M. Biomarkers in multiple sclerosis: an up-to-date overview. *Mult Scler Int.* (2013) 2013:340508. doi: 10.1155/2013/340508
4. Wattjes MP, Rovira À, Miller D, Yousry TA, Sormani MP, de Stefano MP, et al. Evidence-based guidelines: MAGNIMS consensus guidelines on the use of MRI in multiple sclerosis–establishing disease prognosis and monitoring patients. *Nat Rev Neurol.* (2015) 11:597–606. doi: 10.1038/nrneurol.2015.157
5. Filippi M, Rocca MA, Ciccarelli O, De Stefano N, Evangelou N, Kappos L, et al. MRI criteria for the diagnosis of multiple sclerosis: MAGNIMS consensus guidelines. *Lancet Neurol.* (2016) 15:292–303. doi: 10.1016/S1474-4422(15)00393-2
6. Geraldes R, Ciccarelli O, Barkhof F, De Stefano N, Enzinger C, Filippi M, et al. The current role of MRI in differentiating multiple sclerosis from its imaging mimics. *Nat Rev Neurol.* (2018) 14:213. doi: 10.1038/nrneurol.2018.39
7. Kaunzner UW, Gauthier SA. MRI in the assessment and monitoring of multiple sclerosis: an update on best practice. *Ther Adv Neurol Disord.* (2017) 10:247–61. doi: 10.1177/1756285617708911

8. Dwyer MG, Silva D, Bergsland N, Horakova D, Ramasamy D, Durfee J, et al. Neurological software tool for reliable atrophy measurement (NeuroSTREAM) of the lateral ventricles on clinical-quality T2-FLAIR MRI scans in multiple sclerosis. *NeuroImage Clin*. (2017) 15:769–79. doi: 10.1016/j.nicl.2017.06.022
9. Eshaghi A, Marinescu RV, Young AL, Firth NC, Prados F, Jorge Cardoso M, et al. Progression of regional grey matter atrophy in multiple sclerosis. *Brain*. (2018) 141:1665–77. doi: 10.1093/brain/awy088
10. Storelli L, Rocca MA, Pagani E, Van Hecke W, Horsfield MA, De Stefano N, et al. Measurement of whole-brain and gray matter atrophy in multiple sclerosis: assessment with MR imaging. *Radiology*. (2018) 288:554–64. doi: 10.1148/radiol.2018172468
11. Filippi M. MRI measures of neurodegeneration in multiple sclerosis: implications for disability, disease monitoring, and treatment. *J Neurol*. (2015) 262:1–6. doi: 10.1007/s00415-014-7340-9
12. Beadnall HN, Wang C, Van Hecke W, Ribbens A, Billiet T, Barnett MH. Comparing longitudinal brain atrophy measurement techniques in a real-world multiple sclerosis clinical practice cohort: towards clinical integration? *Ther Adv Neurol Disord*. (2019) 12:1756286418823462. doi: 10.1177/1756286418823462
13. Mollison D, Sellar R, Bastin M, Mollison D, Chandran S, Wardlaw J, et al. The clinico-radiological paradox of cognitive function and MRI burden of white matter lesions in people with multiple sclerosis: a systematic review and meta-analysis. *PLoS ONE*. (2017) 12:e0177727. doi: 10.1371/journal.pone.0177727
14. Barkhof F. The clinico-radiological paradox in multiple sclerosis revisited. *Curr Opin Neurol*. (2002) 15:239–45. doi: 10.1097/00019052-200206000-00003
15. Brewer JB. Fully-automated volumetric MRI with normative ranges: translation to clinical practice. *Behav Neurol*. (2009) 21:21–8. doi: 10.1155/2009/616581
16. Pareto D, Sastre-Garriga J, Alberich M, Auger C, Tintoré M, Montalban X, et al. Brain regional volume estimations with NeuroQuant and FIRST: a study in patients with a clinically isolated syndrome. *Neuroradiology*. (2019) 61:667–74. doi: 10.1007/s00234-019-02191-3
17. Nygaard GO, Celius EG, de Rodez Benavent SA, Sowa P, Gustavsen MW, Fjell AM, et al. A Longitudinal study of disability, cognition and gray matter atrophy in early multiple sclerosis patients according to evidence of disease activity. *PLoS ONE*. (2015) 10:e0135974. doi: 10.1371/journal.pone.0135974
18. Høgestøl EA, Kaufmann T, Nygaard GO, Beyer MK, Sowa P, Nordvik JE, et al. Cross-sectional and longitudinal mri brain scans reveal accelerated brain aging in multiple sclerosis. *Front Neurol*. (2019) 10:450. doi: 10.3389/fneur.2019.00450
19. Kurtzke JF. Rating neurologic impairment in multiple sclerosis: an expanded disability status scale (EDSS). *Neurology*. (1983) 33:1444–52. doi: 10.1212/WNL.33.11.1444
20. Cutter GR, Baier ML, Rudick RA, Cookfair DL, Fischer JS, Petkau J, et al. Development of a multiple sclerosis functional composite as a clinical trial outcome measure. *Brain*. (1999) 122 (Pt 5):871–82. doi: 10.1093/brain/122.5.871
21. Nygaard GO, Walhovd KB, Sowa P, Chepkoech JL, Bjørnerud A, Due-Tønnessen P, et al. Cortical thickness and surface area relate to specific symptoms in early relapsing-remitting multiple sclerosis. *Mult Scler*. (2015) 21:402–14. doi: 10.1177/1352458514543811
22. Damangir S, Manzouri A, Oppedal K, Carlsson S, Firbank MJ, Sonnesyn H, et al. Multispectral MRI segmentation of age related white matter changes using a cascade of support vector machines. *J Neurol Sci*. (2012) 322:211–6. doi: 10.1016/j.jns.2012.07.064
23. Dale AM, Fischl B, Sereno MI. Cortical surface-based analysis. I. Segmentation and surface reconstruction. *Neuroimage*. (1999) 9:179–94.
24. Gamer ML, J. Singh. *Various Coefficients of Interrater Reliability and Agreement*. (2019).
25. Wickham H. *ggplot2: Elegant Graphics for Data Analysis*. 2 ed: Springer International Publishing (2016).
26. Wilke C. *cowplot: Streamlined Plot Theme and Plot Annotations for 'ggplot2' 2019*. [Available online at: https://wilkelab.org/cowplot/].
27. RCTTRSP. *The R Stats Package*. Available online at: https://stat.ethz.ch/R-manual/R-devel/library/stats/html/00Index.html~2019
28. Li J, Ji L. Adjusting multiple testing in multilocus analyses using the eigenvalues of a correlation matrix. *Heredity*. (2005) 95:221–7. doi: 10.1038/sj.hdy.6800717
29. Patel KR, Luo J, Alvarez E, Piccio L, Schmidt RE, Yablonskiy DA, et al. Detection of cortical lesions in multiple sclerosis: a new imaging approach. *Mult Scler J Exp Transl Clin*. (2015) 1:2055217315606465. doi: 10.1177%2F2055217315606465
30. Jain S, Sima DM, Ribbens A, Cambron M, Maertens A, Van Hecke W, et al. Automatic segmentation and volumetry of multiple sclerosis brain lesions from MR images. *NeuroImage Clin*. (2015) 8:367–75. doi: 10.1016/j.nicl.2015.05.003
31. D. Sima FP, N. Torcida, G. Wilms A, Lysandropoulos WVH, (editors). *Impact of MSmetrix Automatic Lesion Segmentation on the 32 Visual Count of Multiple Sclerosis Lesions. ECR* (2018).
32. Pasquier F, Leys D, Weerts JG, Mounier-Vehier F, Barkhof F, Scheltens P. Inter- and intraobserver reproducibility of cerebral atrophy assessment on MRI scans with hemispheric infarcts. *Eur Neurol*. (1996) 36:268–72. doi: 10.1159/000117270
33. Battaglini M, Gentile G, Luchetti L, Giorgio A, Vrenken H, Barkhof F, et al. Lifespan normative data on rates of brain volume changes. *Neurobiol Aging*. (2019) 81:30–7. doi: 10.1016/j.neurobiolaging.2019.05.010
34. De Stefano N, Arnold DL. Towards a better understanding of pseudoatrophy in the brain of multiple sclerosis patients. *Mult Scler*. (2015) 21:675–6. doi: 10.1177/1352458514564494
35. Dieleman N, Koek HL, Hendrikse J. Short-term mechanisms influencing volumetric brain dynamics. *NeuroImage Clin*. (2017) 16:507–13. doi: 10.1016/j.nicl.2017.09.002

Conflict of Interest: SB has received honoraria for lecturing from Biogen and Novartis. EH has received honoraria for lecturing from Biogen, Merck and Sanofi-Genzyme. PB-H has received advisory board and/or speaker honoraria from Biogen, Novartis, Merck, UCB, and Teva. PS has received honoraria for lecturing and travel support from Merck. HH has received travel support, honoraria for advice or lecturing from Biogen Idec, Sanofi-Genzyme, Merck, Novartis, Roche, and Teva and an unrestricted research grant from Novartis and Biogen. MB has received honoraria for lecturing from Novartis and Biogen Idec, Merck AB, Roche Norge, and Sanofi Genzyme.

The remaining authors declare that the research was conducted in the absence of any commercial or financial relationships that could be construed as a potential conflict of interest.

Advantages of publishing in Frontiers

OPEN ACCESS
Articles are free to read
for greatest visibility
and readership

FAST PUBLICATION
Around 90 days
from submission
to decision

HIGH QUALITY PEER-REVIEW
Rigorous, collaborative,
and constructive
peer-review

TRANSPARENT PEER-REVIEW
Editors and reviewers
acknowledged by name
on published articles

Frontiers
Avenue du Tribunal-Fédéral 34
1005 Lausanne | Switzerland

Visit us: www.frontiersin.org
Contact us: frontiersin.org/about/contact

REPRODUCIBILITY OF RESEARCH
Support open data
and methods to enhance
research reproducibility

DIGITAL PUBLISHING
Articles designed
for optimal readership
across devices

FOLLOW US
@frontiersin

IMPACT METRICS
Advanced article metrics
track visibility across
digital media

EXTENSIVE PROMOTION
Marketing
and promotion
of impactful research

LOOP RESEARCH NETWORK
Our network
increases your
article's readership